Numerical and experimental investigation of spectral domain vibration based indicators for structural health monitoring

Roger Serra Lopez

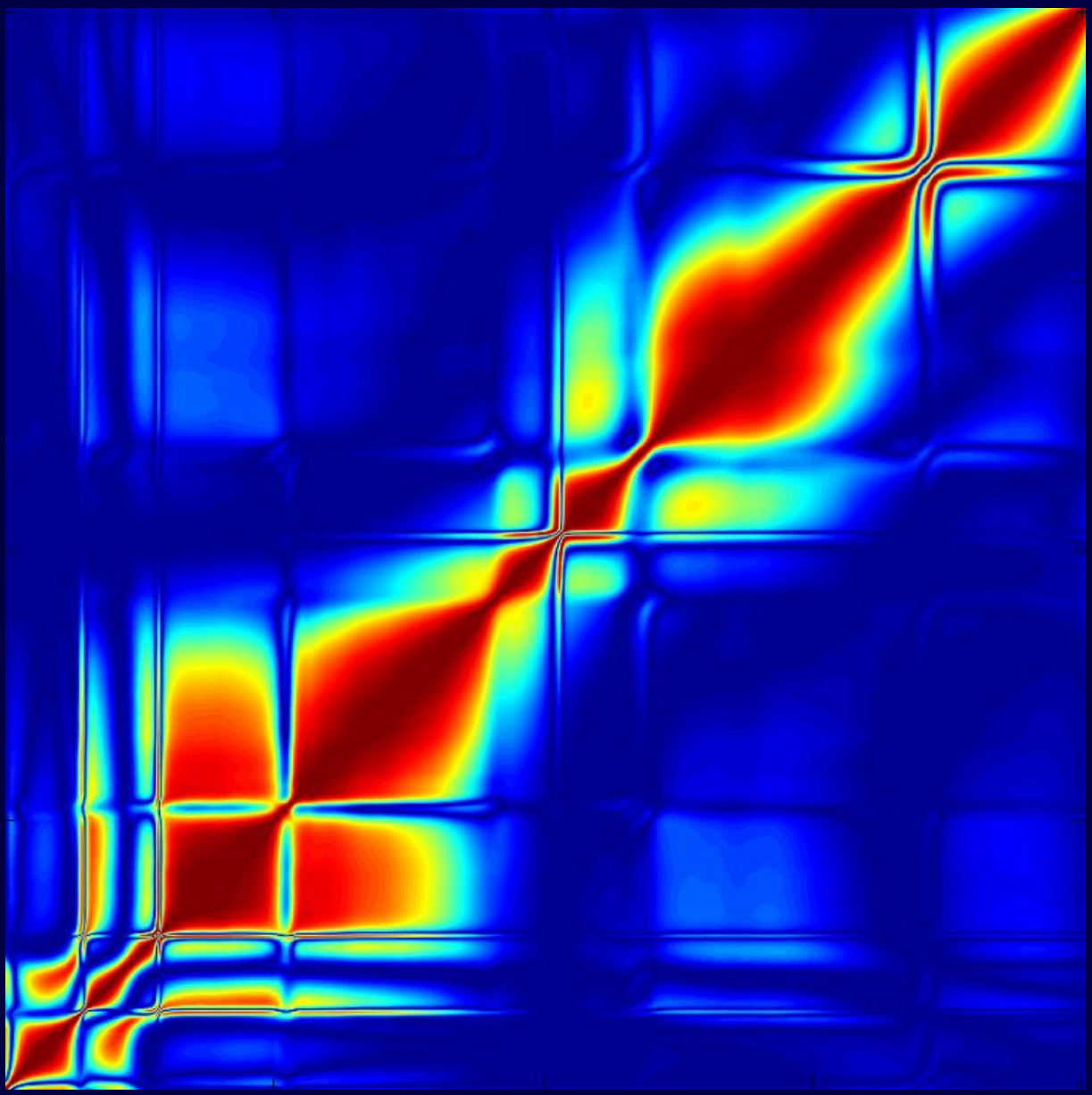

UNIVERSITAT POLITÈCNICA DE CATALUNYA
BARCELONATECH
Escola Superior d'Enginyeries Industrial, Aeroespacial i Audiovisual de Terrassa

UNIVERSITAT POLITÈCNICA DE CATALUNYA BARCELONATECH

Numerical and experimental investigation of spectral domain vibration based indicators for structural health monitoring

Roger Serra López

UNIVERSITAT POLITÈCNICA DE CATALUNYA
BARCELONATECH
Escola Superior d'Enginyeries Industrial,
Aeroespacial i Audiovisual de Terrassa

Doctoral programme in Mechanical, Fluids and Aerospace Engineering

Numerical and experimental investigation of spectral domain vibration based indicators for structural health monitoring

Author:
Roger Serra López

Advisors:

Lluís Gil Espert
Marco Antonio Pérez Martínez

A dissertation submitted in partial fulfilment of the requirements for the degree of Doctor of Philosophy at Universitat Politècnica de Catalunya - BarcelonaTech

November 2017

Contents: **Thesis Memoir**

UNIVERSITAT POLITÈCNICA DE CATALUNYA
BARCELONATECH
Escola de Doctorat

Acta de qualificació de tesi doctoral

Curs acadèmic:

Nom i cognoms

Programa de doctorat

Unitat estructural responsable del programa

Resolució del Tribunal

Reunit el Tribunal designat a l'efecte, el doctorand / la doctoranda exposa el tema de la seva tesi doctoral titulada

_____

_____.

Acabada la lectura i després de donar resposta a les qüestions formulades pels membres titulars del tribunal, aquest atorga la qualificació:

☐ NO APTE ☐ APROVAT ☐ NOTABLE ☐ EXCEL·LENT

(Nom, cognoms i signatura) President/a	(Nom, cognoms i signatura) Secretari/ària

(Nom, cognoms i signatura) Vocal	(Nom, cognoms i signatura) Vocal	(Nom, cognoms i signatura) Vocal

_____, _____ d'/de _____ de _____

El resultat de l'escrutini dels vots emesos pels membres titulars del tribunal, efectuat per l'Escola de Doctorat, a instància de la Comissió de Doctorat de la UPC, atorga la MENCIÓ CUM LAUDE:

☐ SÍ ☐ NO

(Nom, cognoms i signatura) President de la Comissió Permanent de l'Escola de Doctorat	(Nom, cognoms i signatura) Secretari de la Comissió Permanent de l'Escola de Doctorat

Barcelona, _____ d'/de _____ de _____

Diligència "Internacional del títol de doctor o doctora"

- Com a secretari/ària del tribunal faig constar que la tesi s'ha defensat en part, i com a mínim pel que fa al resum i les conclusions, en una de les llengües habituals per a la comunicació científica en el seu camp de coneixement i diferent de les que són oficials a Espanya. Aquesta norma no s'aplica si l'estada, els informes i els experts provenen d'un país de parla hispana.

(Nom, cognoms i signatura) Secretari/ària del Tribunal

A mi abuelo Juan

Acknowledgements

I would like to express my very great appreciation to Dr. Marco Antonio Pérez for his uncountable and constructive suggestions during the planning and development of this research. His willingness to give his time to solve my doubts is gratefully appreciated. It is worth acknowledging his contribution to the experimental testing campaign of the aluminium plate discussed in this thesis.

I am particularly grateful to Dr. Lluís Gil, one of the few people that gave me the opportunity to be in contact with the research environment. His advice has been a great help in the writing of this document and in the conceptual approach to the development of this investigation.

I would like to offer my special thanks to the "Laboratori per a la Innovació Tecnològica en Estructures i Materials (LITEM)" and all his staff for providing the support that has made this research possible. Co-workers at LITEM Dr. Ernest Bernat, Dr. Christian Escrig and Dr. Catalin Andrei Neagoe provided a most valuable support in the preparation of the experimental set-up and in FEM modelling. Assistance provided by Mr. Vicenç Andreu, laboratory technician at the Structural Engineering laboratory, is also much appreciated, specially with his contribution during the construction of the downscaled latticed model tower.

I also want to acknowledge the kind contribution of the Mechanical Engineering department of the IQS-URL university that allowed me to use its experimental testing equipment in some of the experimental tests in this investigation.

My deepest appreciation goes to my parents, Ángela and Jordi, my uncle Toni, my family and friends, who have suffered with me during this years. Without their support and encouragement I would have not accomplished this research.

Abstract

Structural health monitoring has been defined as the acquisition, validation and analysis of technical data to facilitate life-cycle management decisions. It is the result of a convergent path from many previous existing disciplines the two most influential being condition monitoring for rotary machinery and non destructive testing. From all the possible technologies, vibration based Structural health monitoring is the one which present a greater stage of maturity.

Spectral domain data is by nature more complete in information than modal condensed parameters. The use of spectral-domain measurements brings the need to develop new damage detection indicators, as much of the literature existing is focused on modal domain based damage indicators.

In this work, an integrated methodology for the evaluation of a spectral domain vibration based structural health monitoring is proposed. Results of this preliminary investigation show that spectral domain damage indicators present some advantages over modal domain and temporal domain based indicators such as convenient condensing procedures without loss of information through the Fourier transform, added post-process simplicity and enhanced sensitivity to degradation.

Contents

List of Figures

List of Tables

Symbols

a, a_{ij}, A, A_{ij}	Scalar (complex) value
$\boldsymbol{a}$	Vector of scalars
$\boldsymbol{A}$	Matrix of scalars
$a(\alpha)$	Scalar function of α
$\boldsymbol{a}(\alpha)$	Vector of scalar functions of α
$\boldsymbol{A}(\alpha)$	Matrix of scalar functions of α
a^*	Conjugated complex quantity
$\mathbb{A}$	Operator
$h_{ij}(\omega)$	(Inertance) frequency response function

Acronyms

A/D	Analogic-to-digital
ANN	Artificial neural network
APDL	ANSYS parametric design language
CAE	Computer assisted engineering
CFDAC	Complex frequency domain assurance criterion
CMIF	Complex mode identification function
DAQ	Data acquisition (systems)
DoF	Degree of freedom
DRQ	Relative damage quantification indicator
EMA	Experimental modal analysis
EMI	Electromagnetic interference
FEM	Finite element method
FDAC	Frequency domain assurance criterion
FFT	Fast Fourier transform
FRF	Frequency response function
MAC	Modal assurance criterion
NDT	Non-destructive testing
ODS	Operation deflection shape
OMA	Operational modal analysis
PCC	Pearson correlation coefficient
PTT	Power transmission tower
RMV	Residue modal vectors
SCI	Spectral correlation index
SVD	Single value decomposition
SVM	Support vector machine
SHM	Structural health monitoring
UMM	Unitary modal mass scaling

1. Prolegomenon

This chapter presents the fundamentals behind the Structural Health Monitoring (SHM) paradigm and the main challenges that arise when facing the implementation of these kind of systems in a real scenario. Arguments for the proposal of this investigation are presented based on a long-term research line in SHM applied to latticed structures. The discussion advances by exposing the problem formulation and the thesis statement to be assessed in this investigation. Problem formulation allows to set a general objective and a set of partial objectives to be accomplished during the development of this research. The chapter ends with the exposition of the investigation methodology that is adopted in this work and a general overview of the structure of this document.

1.1 Motivation

In March 9th, 2010 a freezing storm combined with strong winds stroke the landscapes nearby Girona, Catalonia. This caused the falling of several electrical power transmission towers which resulted in an extended power cut in the Girona region for over a week. The lack of a meshed power distribution network, combined with the ageing on steel supports were identified as the major causes of power transmission towers collapses and subsequent loss of electrical fluid for such an extended period of time. Local chambers of commerce estimated the economic impact of electric shortage to be of about 100 M€ and to have caused the loss of about 5 million work-hours [1]. Unusual low temperatures caused abnormal accretion of ice rods on transmission wires. This caused an increment in weight and aerodynamic drag over the lines which combined with fast cross winds derived from the snowstorm, resulted in a catastrophic failure of long segments of transmission links. Whip effect of failing cables of broken towers caused a cascade of propagating failures. Up to 14 high voltage towers and dozens of medium and low voltage ones became highly affected. In some cases, infrastructure spanned over 10 kilometres was affected. The cost of the power network

repair was estimated to be above 60 M€.

As the fall of a tower normally results in the rupture of the electrical carrier wires, cuts in the power supply are inevitable if structural failure happens on any of the components of distribution lines. Current maintenance procedures primarily focus on the state of the conduction lines and links. Structural maintenance programs are limited to a visual inspection. Towers are only replaced after the conclusion of a certain life cycle or when catastrophic collapse occurs. Both scenarios imply a degradation in the power distribution service.

In order to reduce unplanned maintenance shut downs in power supply, in service damage detection strategies arise as an interesting approach to explore in preventive maintenance. The large number of in-service towers, their relative long life cycles and its dimensions make field inspections procedures expensive. Consequently, the use of remote health monitoring techniques to estimate the presence of damage before the collapse, results in a reduction in the overall operational cost.

Early detection of damage in machinery and structures is one of the major research fields in present engineering. Damage evaluation and structural health monitoring techniques are essential to define the structural safety, stability and operational life of systems. The challenge of structural monitoring lies in the ability of getting information about the existence, location and magnitude of the damage using non-destructive techniques. Information extracted from these techniques can be effectively used for in service damage monitoring. When damage is detected by means of this strategy, corrective actions can be performed to avoid the complete failure of the system or, at least, to plan scheduled technical shut-downs which result in a reduction in the overall operational and maintenance costs.

With this record in mind, in 2011, a collaborative project between an electrical power sector leading company and the Technological Innovation in Structures and Materials Laboratory (LITEM) from UPC university was proposed. The SIDTE project had the aim of developing a remote structural health monitoring (SHM) system that allows operators to evaluate certain safety coefficients related with the global structural stability of power transmission towers (PTT).

1.2 Background

SHM is often defined as the process of using experimental technical data captured from a system in its operational environment in order to facilitate managing decisions during its operational life span. The process usually involves capturing experimental

data from a mechanical system, validating it using statistical manipulation or signal coherence practises, post-processing the experimental records using various signal processing tools, generating certain condensed and reduced damage indicators and assessing the degradation state using decision making algorithms. As the keystone of SHM systems is the experimental data in which the full cycle is based, one of the challenges of SHM systems is the election of the magnitude that will be sensed and how to relate the changes in that magnitude to the damage state of the system.

SHM has gained a lot of attention in recent years due to its potentiality to reduce operational costs on infrastructure. It is a well known fact that operational costs derived from maintenance, repairing or technical halts can account from 15% to 40% of the costs of the goods produced [2]. SHM allows to continuously monitor the progression of damage in mechanical systems so scheduled and convenient stops can be taken before undesired production chain interruptions happen. Continuous monitoring can also prevent catastrophic failures in large civil infrastructure, enhance operational safety and minimize maintenance costs derived from the substitution of completely damaged structures.

Vibration based SHM can be interpreted as a complex inverse problem. That problem is formulated as determining the causes (presence, location, severity of damage) which cause certain structural dynamics response modification. Each degraded state can be characterized by certain statistics derived from the dynamic response of the system to conform a statistical pattern. The process of tracing the changes in the statistical signature is known as the statistical pattern recognition paradigm. This approach is defined in terms of four stages: evaluation, data acquisition, condensation and damage assessment.

1.3 Problem statement

To the knowledge of the author, a problem which has not been yet addressed in the literature is the study of a structural health monitoring concept which utilizes Fourier-transformed vibration data to generate spectral domain based damage indicators, avoiding the use of modal condensation routines, so that those indices are able to assess structural alterations in the system, both interpreted as loss or gain of structural performance.

Structural health monitoring allows to reduce overall maintenance costs in all kinds of infrastructure. Although it is yet a matter of active investigation, current state of the art structural health monitoring technology shows certain maturity in using vi-

bration data condensed in the modal domain, both using active and operational excitation. Modal domain condensation is a relic of experimental to numerical correlation and modal harmonic analysis and it is not strictly necessary for damage identification. Spectral Fourier-transformed experimental data incorporates all the information available to the damage assessment cycle in a convenient and easily interpretable form. Although artificial neural networks seem to be the predominant trend in current research, this research is addressed using only statistical condensation techniques as it is a preliminary insight in newly developed spectral indicators. Further works could surely apply advanced data reduction and pattern recognition algorithms to damage detection using the indicators presented in this work.

1.4 Objectives

The objective of this work is to demonstrate the feasibility of utilizing vibration data to generate a set of spectral domain based damage indicators purposed to assess the degradation or reinforcement on structures. These indicators are proposed to be derived from the complex frequency domain assurance criterion (CFDAC) matrices corresponding to degraded and pristine states of the monitored structure. This indicator is referred as spectral correlation index (SCI).

To accomplish this main objective, several other specific objectives are identified:

1. Perform an exhaustive literature review to identify flaws and dark spots on current knowledge in vibration-based spectral-domain SHM.
2. Develop the formulation for the spectral domain structural assessment indices.
3. Perform a parametric analysis on the proposed spectral indicators using vibration data from numeric models. By doing so, the stability of the indicators in front of the most relevant sampling parameters can be evaluated. To do so, it is necessary to:
   - Generate a database of numeric FEM models in pristine state and with artificial structural alterations introduced to extract modal data from them.
   - Extract suitable damping models from reference pristine experimental tests.
   - Synthesize frequency response functions from numerical models and validate the synthesis methodology by comparing synthetic frequency response functions to experimentally determined ones.
4. Assess the structural condition of the used numerical models using the indicators

proposed.

5. Experimentally validate conclusions extracted from the numerical analysis, both in terms of dependencies and stability in front of acquisition parameters and in terms of structural assessment capabilities.

6. Evaluate if the numeric and experimental conclusions can be extended to more complex structural typologies, such as latticed 3D structures.

7. Apply the proposed indicators to structural assessment of a latticed structure in an operational environment.

This investigation is aimed to serve as a first step towards the development of a fully functional vibration-based SHM system based on spectral domain indices. Although real application of the indicators would include the use of output only experimental vibration data, this investigation uses input-output vibration data obtained through experimental modal analysis as this methodology allows for a better control of the experimental conditions. This way, an in depth assessment of the proposed damage indicators can be done minimizing the influence of the acquisition chain and environmental in-service conditions. Output-only measurements are usually captured using the so-called operational modal analysis technique which result in spectral data series analogue to those obtained through experimental modal analysis. The application of the techniques herein exposed is straightforward to operational data although the evaluation of the accuracy of the technique in such cases is out of the scope of this work.

1.5 Methodology

The methodology used in this investigation is based on the partial sub-objectives previously exposed and consist of a series of tasks grouped in three thematic lines. In first place, an initial bibliographic investigation, including the state of the art on structural health monitoring, mathematical formulation of the physical phenomena governing the vibration problem and definition the proposed spectral indicators. In second place a numeric campaign on two structural systems aimed to define sensitivity of the indicators in front of certain acquisition parameters and the relationship between the indicators and the structural alteration typology introduced. Finally, a block including three experimental studies on three real structural systems aimed to evaluate the performance of the indicators in real structural assessment scenarios. These eight work packages are sequentially discussed in following paragraphs.

The first stage of this investigation starts with a literature review on the state of the art in the topic of SHM. This serves as a starting point to get familiar with the concepts, tools and recent developments in the subject. The literature research is based in the topics of structural health monitoring, damage identification, condition monitoring, non-destructive testing, spectral correlation, modal analysis, signal processing and artificial neural networks in SHM among other tangential topics. This thematic area also addresses attempts made to identify damage in latticed structures.

The second work package includes the mathematical formulation of the spectral indicators involved in the investigation and structural dynamics concepts related with them. Numeric and experimental techniques used to obtain frequency response functions are presented. An effort is made to relate these newly proposed indicators with indices previously discussed in literature, such as the DRQ and ΔODS indicators (Maia, Urgueira, Sampaio et al. [3–5]). The Complex Frequency Domain Assurance Criteria, directly inspired by the Frequency Domain Assurance Criteria [6] is presented. A condensation and sign-decision algorithm is finally presented based on the Pearson correlation coefficient.

The second thematic area, involving numerical investigation on the indicators deals with an extensive numeric campaign on a square aluminium plate using simply-clamped boundary conditions. A first verification of the synthesis algorithm is executed by comparing experimental reference results to the numerically synthesized ones. This first experimental tests are also used to extract damping models to be later used. A progression of intentionally made structural modifications is introduced to the FEM base model. FRFs are generated from those modal results, and spectral indicators are extracted from FRF condensation. An exhaustive sensibility analysis is executed including the correlation of the indicators with the residual stiffness of the structure.

After the parametric numerical analysis on the aluminium plate is concluded, a mostly similar numerical campaign is executed on a downscaled version of a power transmission tower. The methodology involved is the same already mentioned with only one difference. Correlation of the residual stiffness of the structure with the indicator is put aside of the analysis as it is reasoned that its experimental replication would be impractical to reproduce.

The third and last thematic area tries to experimentally reproduce some of the structural alteration scenarios numerically modelled to validate or dismiss conclusions extracted using synthetic data. The first block includes an experimental campaign on a square aluminium plate equivalent to the numerical campaign. Equivalent sensibility analysis are performed for this experimental set of tests.

In a similar manner, the second work package of this area attempts to experimentally validate the conclusions extracted from the numerical campaign on the downscaled power transmission tower. A physical model is built and a set of intentionally made alteration scenarios are tested on it.

The investigation concludes with the application of the methodology presented to a full scale latticed structure in an operational environment. A series of experimentally and artificially introduced structural modifications are tested using experimental modal analysis. The performance of the proposed indicators in structural alteration detection is evaluated and discussed.

The methodologies involved in this investigation include both numerical and experimental approaches. Available tools used in the investigation consist on both software packages and experimental hardware. CAE software used for FEM modal simulations is ANSYS 14.5. Other post-processing and data manipulation tasks are done with the aid of Mathworks Matlab R2013b. Experimental vibration data acquisition is done using hardware by the manufacturer Bruel& Kjaær. Experimental data post-processing tasks are performed using Vibrant Technologies MEscope v4.1.

Methodology involved in the investigation directly translates into the organization of this document as it is depicted in figure 1.1.

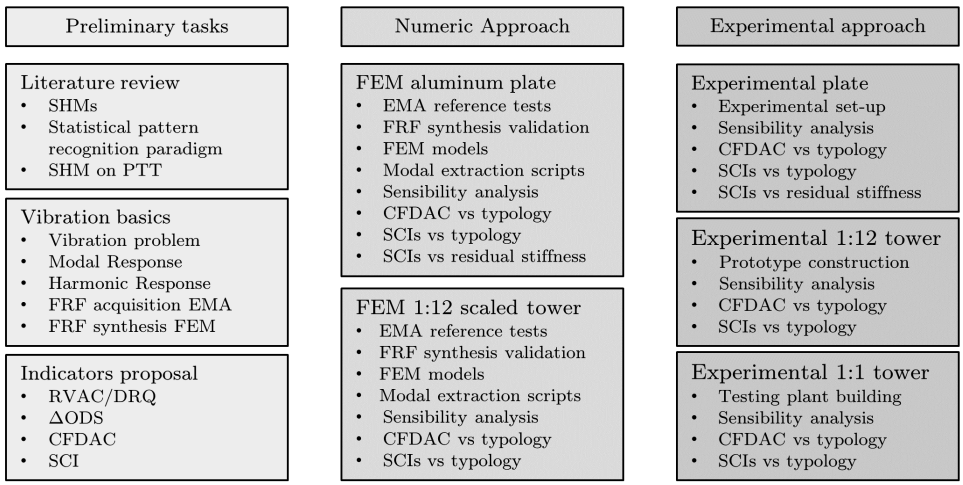

Figure 1.1: Flow diagram of the investigation

1.6 Outline

This document is organized following the subsequently exposed structure. In the first chapter, an introduction to the research topic is done, exposing the problem background, the problem itself and the proposed methodology to solve it. In Chapter 2 a review showing the state of the art in SHM is presented focusing on spectral domain derived damage indicators and statistical condensation techniques. Next, in Chapter 3, the Spectral Correlation Index (SCI) is proposed as a tool to detect and quantify structural shifts. The exposition is complemented with the basic formulation of the vibration problem, computational techniques used to address it and the equivalent experimental approach that allows to model vibrating systems. Numerical campaigns on two different structural typologies (an aluminium plate and a steel latticed structure) are addressed in Chapter 4. Chapter 5 deals with the application of the proposed indicator to experimentally acquired vibration series on an aluminium plate, on a 1:12 downscaled power transmission tower and on a real full scale in-service latticed tower.

2. State of the Art

In this chapter, a bibliographic research on structural health monitoring is presented. The exposition is presented under the statistical pattern recognition paradigm, identifying and categorizing up to the date developments under that approach. The chapter ends with a revision of the works in structural health monitoring of power transmission towers, both from the static approach and from the dynamic vibration-based point of view.

2.1 Structural health monitoring

SHM has been defined in the literature as the acquisition, validation and analysis of technical data to facilitate life-cycle management decisions [7]. More generally, SHM denotes a reliable system with the ability to detect and interpret adverse changes in a structure in order to improve reliability and reduce life cycle cost. SHM assesses the state of structural health and, through appropriate data processing and interpretation, predicts the remaining life of the structures. The greatest challenge in designing a SHM system is to identify what changes to search [8]. Farrar and Worden [9] defined SHM as the process of implementing a damage identification strategy for aerospace, civil and mechanical engineering. For the author, damage can be defined as changes introduced into a system that adversely affect its current or future structual performance.

SHM is a tool which allows for flaws in the structure to be characterized using the measured data for some known input. SHM has been used for both diagnosis and prognosis [10]. Through diagnosis, the presence damage, their location, and their extent in the structure is recognized. The prognosis uses the information in the diagnosis to determine the remaining life of the structure. SHM involves the observation of the system through time using periodic samples of certain magnitudes. The damage prediction is approached with a combination of current state measurements on the structure with the estimation of future operational loading conditions.

Several authors [11–13] agree on a classification for SHM based on the level of identification attempted:

- (Level 1) **Detection**: Affirmation that damage is present in the structure.
- (Level 2) **Location**: Determination of the geometrical locus of the damage.
- (Level 3) **Quantification**: Assessment of the severity of the damage.
- (Level 4) **Prognosis**: Prediction of the remaining service life of the structure.
- (Level 5) **Correction**: Adopted corrective actions and life enhancing measures. Self-healing and smart structures.

A multitude of techniques have been successfully used in the detection of damage in structures. Among others, the acquisition of displacements, strains or vibrations are common practise. Mechanical vibrations are usually divided in four categories depending on the physical phenomena involved and the frequency range of interest. Mechanical vibrations include conventional vibration of elastic structures, Lamb surface stress waves transferred along in-plane directions in thin shells or plates, ultrasonic waves which are transferred through the thickness of the material studied and acoustic waves. Displacement measurement requires the installation of auxiliary supporting systems to measure relative displacements. On the other hand, strain measurement requires the utilization of conventional adhered strain gauges or Bragg grating optical fibre arrays. Contrastingly, Lamb-wave based SHM uses surface piezo-transducer patches in order to generate and sense plain waves on the structure and requires high voltage amplifiers and high speed data acquisition hardware. Ultrasonic-based SHM includes the use of piezo-electric arrays for emission and transmission of waves in the MHz range. Acoustic inspection relies on speaker and microphone arrays for determining the acoustic transmissibility of the investigated component.

Whereas most of the mentioned techniques require complex sensing hardware, transverse vibrations present the fundamental advantage of only requiring the installation of a limited amount of cinematic transducers on the structure. Acceleration transducers are usually selected and mounted with magnetic attaches, glued unions or even with cable ties. Acceleration sensors are far more robust in terms of durability and stability than strain gages, optical fibre gratings or piezoelectric patches so its implementation on a SHM system is convenient. This investigation is routed to the low frequency mechanical vibrations of structures experimentally sampled using acceleration transducers.

Modern vibration-based SHM techniques are the direct successors of Condition Monitoring procedures used for rotary machine which started to flourish in the 1970s.

Rotary machine usually operates at stationary angular velocities which results in a fixed and well known vibration spectra. This vibration pattern is composed by harmonics resulting from all the moving components. Condition monitoring utilizes the changes in the vibration signature of rotating components to detect anomalies in the system. As rotary systems are designed to stand heavy vibration in operation, these excess of excitation energy is reused to assess the integrity of the system. This basic monitoring principle is vastly used in oil-drilling machinery and even in critical conventional production line hardware.

State-of-the art vibration-based SHM is applied to a wider range of mechanical systems with rotary machine included but not limited to. This introduces the need for an energy source that actively excites the system. First attempts to introduce SHM in civil structures included studies on latticed and concrete bridges. In that firsts studies, such as an extensive damage detection campaign over the I-40 Rio Grande bridge in the USA (Farrar et al. [14]), the structure was actively excited with vibrodynes (controlled rotary machines precursors of modern electrodynamic shakers) to mobilize the natural modes of vibration of the structure. First vibrodynes were heavy and difficult to transport and to install. Besides this, the set-up required was case-dependant for the typology of structure studied. Since then, many attempts have been made to detect damage on structures using active excitation such as impact hammers or modern shakers. The main drawback of this approach of needing active excitation still persists. Besides this, as the size of the civil structure increases the magnitude of excitation -and cost of the vibrodynes- also does.

All the difficulties encountered when performing active excitation vibration tests give room to the introduction of SHM systems that rely on the measurement of output-only acceleration histories on the structure. Therefore, there is no need to transport excitation equipment to field installations. Besides this, the structure can be kept in operational condition, investigation costs are reduced and tests better reproduce real operation states. Excitation on the structure is done by weather phenomena, such as wind or sea waving, or operational conditions such as road traffic over a bridge or ambient noise. However, the magnitude of operational excitation is not always high enough to allow the sensors to discriminate vibration signals from acquisition noise so there is need to generate statistical significant states by averaging a number of samples.

SHM developments with controlled active excitation rely on the determination of complete modal models of the structure studied. Experimental modal analysis (EMA) relies in the measurement of both input and output of the system to determine frequency response functions (FRFs) of a system and is a well known tool in industry

used to generate modal models of structures. EMA is not specially targeted to SHM as its main fields of application include the correlation between numerical models and real specimens and the development of modal models of structures to solve forced excitation problems using harmonic analysis.

The fact that experimental modal analysis has become a standard in industry caused that early attempts to identify damage were based on this tool. By tracing the variation in the modal model of a structure, an assessment of the damage state of a mechanical system can be done. These techniques rely on the identification of the parameters defining the modal model of a structure (natural resonant frequencies, associated dampings, and corresponding mass-normalized mode shapes). EMA requires the utilization of real-time FFT analysers, complex post-processing techniques and advanced curve-fitting tools on the raw temporal-series acquired. These tools are essential if a complete modal model of the structure is required. On the other hand, the main goal of vibration-based SHMs is to detect changes in the dynamic response of a structure and relate them to its degradation state. So then, a complete modal model identification is not strictly needed to damage assessment.

Recent developments in the topic discard the use of modal identification methods in order to face the damage detection problem using temporal-domain based or Fourier-transformed vibration-based damage indicators. Using filtered temporal-domain or spectral FFT-processed data suffices to perform such identification so modal extraction routines can be avoided. This way, post-processing complexity and potential sources of errors are reduced.

Conventional SHM systematically approaches detection of changes in structures as a loss of correlation with a reference pristine condition. This paradigm assumes that structural alteration is always and undesirable effect which reduces the structural performance of the system. However, in application scenarios it is possible to encounter certain structural modifications which positively influence the performance of the structure (i.e. a change in boundary conditions in a structure which increases the ballast coefficient in the surrounding ground and therefore increases the overall static stiffness of the structure). This work tries to overcome this limitation by considering the direction of the observed structural shift.

The last, and probably most complex topic to address in SHM, is the alteration identification from the indicators generated. Along the years in SHM investigation, alteration classification has been by far, the least studied aspect. Simpler approaches are based in the generation of a complete statistical database which relate the state of degradation of an specific structure with certain statistical indicators. This methodology presents the main drawback of requiring enough samples to generate the database

and of being highly case-dependant. More robust and general approaches to decision making have been developed based on Machine Learning Techniques such as Artificial Neural Network, Expert Systems or Support Vector Machines.

Bearing in mind all the developments proposed along the years, Farrar and Doebling [15] proposed to face the damage detection problem from the standpoint of a pattern recognition case. They suggested that pattern recognition methods are needed to overcome the limitation imposed by model based damage detection routines, so then purely experimental data can be use without the need of a numerical model to assess the integrity of the structure. In their opinion, the statistical pattern recognition paradigm can be sequenced in a series of consecutive steps. This paradigm is further expanded in the 2007 article by Farrar and Worden [9].

- **Operational evaluation:** The first step includes the operational evaluation, which consists on an executive assessment of the SHM system to be implemented. In this evaluation the costs of implementation are compared and balanced to the benefits resulting from life-safety enhancement and economic losses mitigation. In the operational evaluation step it is also where the damage to be detected is defined, multiple damaged possibilities are considered and the critical cases of most concern are set. Besides these aspects, this first analytic approach to a SHMs implementation also introduces the study of the operational conditions where the structure performs and the limitation arising from the data acquisition methodology in the operational environment. So as a summary, operational evaluation sets the operational envelope of the monitored structure. The process of selecting the possible excitation on the structure, the sensor selection, the number and location of them, the time interval between samples and the data acquisition, storage and transmission hardware are also involved in this executive step. This process is very case dependant and economic considerations usually play a major role in the decisions.

- **Data acquisition, normalization and cleansing:** Data acquisition involves three major concerns that must be addressed: data capture, data normalization and data cleaning. Normalization is the process of separating changes in readings caused by damage from that changes caused by varying environmental or operational conditions. Variability can not always be completely eliminated so its sources have to be statistically characterized and discounted from readings. Data cleansing includes the process of selecting or rejecting sampled data to be passed to the feature extraction procedure. Signal processing techniques such as filtering and re-sampling are a clear example of such procedure.

- **Feature extraction and information condensation:** This procedure involves the identification of data features that allow to distinguish between undamaged and

damaged states. A paradigmatic task in this step is the condensation of the data to reduce the amount of experimentally read samples to a smaller subset of significant information. A vast multitude of research papers are focused in the feature extraction portion of SHM [16–20]. A common approach is to use the amplitude of sampled signals and correlate the changes in its magnitude with the amount of damage accumulated in service. Diagnostic measurements included in SHM produce more data that traditional structural dynamic analyses so robust data reduction techniques must be developed retaining feature sensitivity and implementing appropriate operational variability reduction algorithms.

- **Damage assessment:** This portion of SHM has received the least attention in the technical literature reviewed. The statistical significance of the reduced features needs to be characterized in order to achieve a meaningful average state of degradation at a certain point of its operational span. Statistical model development uses algorithms that operate on top of the extracted features to quantify the state of damage of the structure. Sohn *et al.* [21] propose two main categories in which statistical model generation can be categorized: supervised learning and unsupervised learning. In supervised learning, degraded and pristine data is available so the pattern recognition algorithms can either correlate with reference cases or classify the degradation state in pre-set categories. On the other hand, in unsupervised learning algorithms pristine data is not available to be used as reference and only the experimentally determined current state is known. Through a novelty detection routine, the progression of certain indicators can be monitored until a certain established alarm threshold is reached. It is also common to apply engineered flaws, similar to those that would be encountered in real operation and develop an initial understanding of the parameters that are sensitive to change when damage appears. This damaged artificial system can also be used to assure that the diagnostic measurements do not throw false positives. Experimentally validated numerical models are very useful to perform such sensitivity analyses.

Farrar and Doebling [15] propose that SHM can only be explained as a convergent path of closely related previously existing disciplines. Condition monitoring has played a major role in the developement of SHM. Since late 1970s, when offshore oil drilling industry applied principles of spectra correlation to oil pump monitoring [22], condition monitoring has been successfully applied in multiple rotary machinery applications [23]. In second place, non-destructive testing (NDT) is essential to capture the experimental data that is used in structural health monitoring. Statistical process control [24] and damage prognosis [25] complete the four legs in which SHM is based.

In a more recent work, Worden, while collaborating with Farrar and coworkers [26], propose some axioms in which SHM is based after identifying these concepts from previous research published up to that time. Those axioms are further expanded in the their 2013 book "Structural Health Monitoring, a Machine Learning Perspective" [27]. These axioms are proposed to be:

- Axiom I: All materials have inherent flaws.
- Axiom II: Two system states are required to be compared to assess damage.
- Axiom III: Damage detection and damage location can be implemented using an unsupervised machine learning approach, but identification of the typology and severity of damage require to use supervised machine learning techniques.
- Axiom IVa: Sensors cannot detect damage. Feature extraction using signal processing tools can generate damage information.
- Axiom VIb: Without intelligent feature extraction, the increasing sensibility of a damage indicator is also an increasing sensibility to operational environment changes.
- Axiom V: Length and time scales of characteristic damaging mechanisms determine the requirements for the SHM system.
- Axiom VI: There is a comprise between sensitivity of a SHM system and robustness to environmental noise.
- Axiom VII: The size of the degradations to be detected is inversely proportional to the frequency range of excitation used by the SHM system.
- Axiom VIII: Damage increases the complexity of the mechanical system.

Structural alteration assessment of in-service structures is a recurrent topic in engineering. Several proposals have been presented to do so using spectral domain vibration based data. The issue has been addressed in the literature commonly from the standpoint of detecting degradations and damage in structures. This work tries to incorporate reinforcement detection in SHM investigation.

2.2 The statistical pattern recognition paradigm

2.2.1 Experimental data acquisition

Among the four aforementioned convergent disciplines which gave birth to SHM, NDT is the one that has the most direct impact on any SHM system. A comprehensive compendium on NDTs can be reviewed in the work by Shull [28]. In the work by Hung et al. [29], the authors suggest a classification of NDT techniques in eight major categories: visual inspection, penetrating radiation, electromagnetic methods, electrochemical methods, thermal techniques, other optical-based methods, mechanical strain based methods and vibration based methods. As visual inspection is highly human-dependant and can hardly be automatized, this category of NDT is not suitable for SHM.

Some of the successful examples of penetrating radiation techniques include the use of an automatic radiography system to detect cracks in welded components as accomplished by Liao and Li [30], the application of tomographic visualization techniques to detect inner defects and delaminations in fibre reinforced polymer matrix composites [31] and the development of neutron imaging procedures [32].

Examples using electromagnetic techniques include the use of magnetic particles for metallic structure evaluation [33] or eddy currents for corrosion detection [34]. Multiple examples on thermographic imagery for NDT can be found in literature as for example the work by Bagavathiappan et al. [35]. Concerning other optical-based methods, the main techniques falling in this category are Moiré holographic interferometry [36] and shearography [37].

Strain based methods rely on the fact that modifications in a structure due to damage or degradation modify the original load paths, stresses and strains distributions so then, by monitoring changes in the deformation in certain critical locations, an assessment of the integrity of the structure can be performed. Extensometry techniques have successfully applied to strain-based SHM either using static load monitoring through conventional resistive extensometry [38] or capturing dynamic deformation data using Bragg grating extensometry [39].

In recent decades, one of the main focus of interest in SHM has been in vibration-based NDT. A classification based on the frequency and physical characteristics of the mechanical waves involved in the phenomena is usually adopted differentiating between conventional mechanical vibrations, acoustic emission and reception, surface Lamb plain stress waves and ultrasonic inspection. Ultrasonic inspection has received

a lot of attention in the past 30 years. So is the case that nowadays, ultrasonic inspection has become a standard inspection procedure in aerospace engineering and material testing. Literature concerning this topic is very extensive so as a matter of exemplification the reader is routed to works by Dong et al., Pérez et al. or Ruzek et al. [40–42].

Several techniques focusing on the modification of the mechanical vibration response of structures have been developed along years. Even nowadays, this is a very active and vibrant area of research in SHM. Vibration methods are among the earliest and most common, mainly because they are of simple implementation on a real system. Structures can be excited by ambient data, an external shaker or embedded actuators and strain gauges or accelerometers can be used to monitor the structural dynamic response of the system. Changes in normal vibrational modes can be correlated to the loss of stiffness in a structure. The difficulty, however, comes in the interpretation of the data collected by the system. There are also detection limitations imposed by the resolution and range of the individual sensors chosen, and the density with which they are distributed over the structure.

There exists approaches that allow converting time domain data to modal domain data directly. Although time, frequency and modal domain data can be used for SHM, conversion between domains implies some compression of data and a possible loss of information. The loss of information between time and frequency domain is of little importance with the added benefit that frequency data can be easily averaged to reduce noise. Under linear behaviour hypothesis, there are also little loss of information in the modal condensation of the spectral domain if natural resonant frequencies are sufficiently spaced in the baseband. However, this affirmation is not shared by the entire SHM community. It has been suggested that the use of raw frequency data in form of frequency response functions (FRFs) presents greater completeness as modal data can be easily oversimplified by modal extraction procedures. This school of thought questions the suitability of modal data for damage detection due to the fact that modal parameters are a reflection of the structure as a whole while damage is a local phenomena. To date, arguments have been demonstrated in both sides for specific typologies of structures and damages but the underlying dichotomy has not been proven in a fundamental sense.

Works involving Surface stress Lamb waves for material inspection and damage assessment are also a commonplace in recent investigations. Lamb waves are usually depicted as in-plane stress waves propagating on surface directions on plates and shells. It is common to encounter in literature SHM developments using this physical phenomena. Some of the works in surface stress waves up to 2008 with piezoelectric transducer-

actuator patches can be found in the article by Wang et al. [43].

A few trends can be identified in the works dealing with Lamb waves for SHM applications. In first place, a research line trying to deepen the knowledge on the physical behaviour of this kind of waves, including the study of the influence of the temperature [44] and moisture content in CFRP [45] in the transmission of surface waves, a research paper by Baid et al. [46] where the authors propose a method for modelling non-linearities in Lamb waves propagation and a second paper by the same author [47] where the transmission of Lamb waves in honeycomb structures is assessed.

The second and most popular topic in state-of-the art investigations using Lamb waves and piezoelectric actuator-transducers are cases studies of this technology to actual SHM applications in a multitude of structural topologies. Some research has addressed the damage detection in an aluminium sheet as a paradigmatic case study [48–50]. The first work, by Clough and coworkers used near-field wave interactions to detect damage in the opposite face of the one measured. Investigation by Liu et al used an array of 16 piezoelectric elements to detect and locate single defects (single holes) but also multi-defects (multiple holes and added surface elements). The investigation by Nazarko and collaborators applied Artificial Neural Networks to the detection of damage on an aluminium plat. A second and vast group of research developments concert the use of Lamb waves in the detection of damage in composites [51–58]. Cracks, deboundings, delaminations, low and high energy impact damages and even fatigue damage have been identified using this technology. It is worth mentioning the work by Senyurek [59], where in contrast to simple plate-like structures used in literature, actual wing slats of a Boeing 737 aircraft were used for detection of typical damages observed at the normal operating conditions (cracks and cuts).

Some works have also addressed the algorithms used to look for damage in the Lamb Wave signals. As a matter of exemplification, the paper by Giridhara [60] proposed a method based on signal paths between neighbours in a circular array of piezo-trasducers to detect the direction in which signal similarity is lost.

Lamb waves are usually depicted as in-plane stress waves propagating on surface directions on plates and shells. However, longitudinal stress waves on less slender structures such as rods, bars or thick plates are not accurately described by the Lamb wave model but by conventional phonon-like longitudinal waves. Although mechanical and aerospace structures usually rely on plate-like structural sub-components, conventional transverse vibrations offer a wider flexibility in its application to structural modification assessment as they do not depend of the structure being a plate nor a shell. In addition, Lamb waves usually inhabit in the ultrasonic frequency range so longitudinal surface-mounted piezoelectric transducers are needed. Accelerometer technology used

to sense and acquire transverse vibrations is by far, much more mature and robust that Lamb wave transducers. Acquisition parameters required to record acceleration and the hardware costs derived from those requirements are also much more affordable for mechanical vibration acquisition so its implementation in a real scenario is much more convenient.

2.2.2 Feature extraction and condensation

Several reviews dealing with vibration-based damage detection methodologies have been published. The following exposition is extracted from the review articles by Carden and Fanning [11], Yan et al. [61] and Fan and Qiao [62] which at the same time are deeply inspired and sourced on the works by Doebling et al. [63], Salawu [64], Zou et al. [65] and Sohn et al. [21]. Readers interested in a deeper insight in the topic are referred the aforementioned articles.

The methods presented herein are only a short and non-exhaustive selection of all the indicators that have been presented in the literature. For a vast and complete enumeration of all the damage indicators presented along the years, the reader is encouraged to revise Appendix B in the book by Ooijevaar "Vibration based structural health monitoring of composite skin-stiffener structures" [66].

2.2.2.1 Modal domain methods

Early literature on vibration-based SHM focused on modal domain. Since initial development of condition monitoring, researchers have used modal parameter monitoring approach as natural frequencies, dampings and characteristic mode shapes are easily interpreted and initially more attractive than spectral or time domain feature extraction. Damage detection and severity can be determined by finding differences in the structural response of the system between intact and degraded configurations. Since any change in the mass or stiffness in the structure is reflected in its equivalent discretized mass and stiffness matrices, these changes translate in a variation of the natural frequencies and mode shapes (eigenvalues and eigenvectors) of the system.

Modal domain based methods differ in the number of sensors needed to generate damage identification information. Natural frequencies and dampings can be measured using a single or very few sensors on the structure whereas mode shape extraction requires multiple sensors distributed in well known positions over the structure. However, even with a large number of sensors the measurement is incomplete due to the discrete nature of the experimental mesh used. Eigenfrequency measurements are, on

the other hand, less sensitive to noise than modal vectors.

Fan and Qiao [62] revise some modal based methods which are divided in two categories depending on the approach adopted towards the damage detection problem. In first place the forward problem formulation is presented. This kind of methodology has the aim of determining natural frequencies, dampings and modal shapes of a given damaged structure in certain locations with certain severities. On the other hand, the inverse problem is presented. The objective in this case is to determine the presence, location and severity of damage (Levels 1 to 3) whether evaluating only a damaged configuration or comparing degraded with pristine states.

Despite having proved their value, modal domain derived procedures are directly dependent on the quality of the modal parameter extraction algorithms. In fact, modal identification from measured Frequency Response Functions is a process which inevitably introduces inaccuracies and errors to those already intrinsic to real experimentation.

a. Natural frequency and damping methods

Firsts attempts to use natural vibration data to detect damage used natural frequency shifts between pristine and damaged configurations. An extensive collection of the literature published to his time is presented in the work by Salawu [64]. In those works, natural frequency changes are expressed as unitary or absolute percentages of variation in the natural frequencies with respect to reference pristine cases.

Other more complex approaches using natural frequency changes also have been proposed. In first place, Kim and Stubbs [67] propose a frequency based damage indicator, namely the single damage indicator (SDI) that shows to be able to locate and quantify local damage in a beam. A numerical simulation is used to correlate experimental frequency shifts with known locations of cracks in it. Then, this correlated indicator is successfully used to locate unknown defects in a beam.

Authors focusing in frequencies shifts seem to agree that frequency based damage identification methods can be successfully applied to detect damage in simple structures with small damages, typically artificially induced cracks in controlled laboratory conditions (Salawu, [64]). Location capacities are also possible when experimental frequency shifts are correlated with full field numerical simulations. On the other hand, there exists consensus that they are not reliable in real and complex structures or in multiple or severe damage scenarios as some studies focused in real scale bridges have shown small variations in first vibrations modes (near ambient variance) when severe damages close to collapse conditions are artificially induced to the structure [11].

When compared to frequencies, damping properties have not been used as extensively for damage diagnosis. However damping variation has been used in crack detection on beams under the premise that defects introduce additional non-linear dissipation effects in the structure [21]. Changes in damping have been used to detect cracks in conventional reinforced concrete beams, in pre-stressed hollow concrete panels and to detect irregularities in metallic blanks to be stamped into computer hard-drive disks.

b. Characteristic vector methods

The first systematic attempt to locate damage from experimental data without the aid of a correlated numerical model dates back to early 80s with the use of mode shape vectors [63]. The basic concept underlying the use of experimentally determined modal vectors is that a variation in the mechanical characteristics of a system can locally affect modal vectors in certain locations nearby the damaged regions. This statement, however, has been put into doubt by some authors as stated in the review by Carden et al. [11]. Major criticism comes from the fact that although modal vectors are spatially distributed over a discrete mesh, mode shapes are directly related to natural frequencies, thus being damage sensitive only global scale wise. Measurement of the mode shapes of a structure requires either exciting the structure in multiple locations of interest and measuring the response in a single point or measuring the structure in the points of interest and exciting at a single locations. In both cases, complex modal estimation techniques are required to convert temporal series in modal domain data.

Doebling et al. first introduce the use of modal vectors as damage indicators in the form of mode shape shifts and complementary mode shape first derivative shifts [63]. Mode shapes are normalized with its corresponding natural frequency to account for its relatively lower participation factor in the vibrational response of the structure in real operation as depicted in equations 2.1a and 2.1b.

$$\boldsymbol{\delta\phi}_k = \frac{1}{\varpi_k}\boldsymbol{\varphi}_k - \frac{1}{\omega_k}\boldsymbol{\phi}_k \tag{2.1a}$$

$$\boldsymbol{\delta\phi}'_k = \frac{1}{\varpi_k}\boldsymbol{\varphi}'_k - \frac{1}{\omega_k}\boldsymbol{\phi}'_k \tag{2.1b}$$

Along the years, techniques based on orthogonality checks in a set of modal vectors have been extensively investigated and subsequently have been introduced in most vibration fundamentals textbooks (i.e. Harris' Shock and Vibration Handbook [68]). The two most widely and commonly used mode shape based indicators are the Modal

Assurance Criterion (MAC) and Coordinate Modal Assurance Criterion (CoMAC). Initially MAC and CoMAC indicators were used to compare two sets of vectors corresponding to a numeric and an experimental equivalent case. Orthogonality checks are used to quantify the degree of correlation between numerical models and experimental tests. They are also used in correlations between different numerical cases and even in EMA testing to discard linear dependant mode shapes.

When introduced to damage assessment scenarios these indicators are usually computed from a pristine well known state and a damaged state. The computation can as well be made for numerical pristine simulation and an experimental degraded conditions. The function of the modal assurance criterion (MAC) is to provide a measure of the degree of linearity between estimates of modal vectors. It is commonly described as the square product of a conventional orthogonality check between vectors using the scalar inner product. The MAC matrix comparing two sets of modal vectors can be obtained through expression 2.2.

$$MAC_{kl} = \frac{\left(\boldsymbol{\phi}_k \cdot \boldsymbol{\varphi}_l^T\right)^2}{(\boldsymbol{\phi}_k \cdot \boldsymbol{\phi}_k^T)(\boldsymbol{\varphi}_l \cdot \boldsymbol{\varphi}_l^T)} \tag{2.2}$$

Where $\boldsymbol{\phi}_k$ corresponds to the k^{th} reference modal vector and $\boldsymbol{\varphi}_l$ corresponds to the l^{th} compared modal vector. This results in a $M \times M$ matrix with M the number of eigenvectors used in the modal model. It is well known that if the modal assurance criterion has a value near unity, the pair of modal modal vectors compared are consistent whereas if the modal assurance criterion has a value near zero, modal vectors are not consistent. Thus, equivalent mode shapes in two different stages must approach a MAC value of 1. If these values significantly shift from 1, subsequent stage is considered to present damage. MAC indicator has been extensively used as an indicator of the presence of damage. MAC components have also been used as the condensed Trace MAC (TrMAC) indicator used by Pérez et al. [69].

$$TrMAC = \frac{1}{M} \sum_{k=1}^{M} MAC_{kk} \tag{2.3}$$

The coordinate modal assurance criterion (CoMAC) is an extension of the modal assurance criterion. The CoMAC matrix relates two sets of modal vectors and can also be computed from a pristine well known state and a damaged state or between the results of a numerical reference simulation and an experimental degraded condition. The formulation for the CoMAC is:

$$CoMAC_{ij} = \frac{\left(\sum_{k=1}^{M} \phi_{ik}\varphi_{jk}\right)^2}{\left(\sum_{k=1}^{M} \phi_{ik}\phi_{ik}\right) \cdot \left(\sum_{k=1}^{M} \varphi_{jk}\varphi_{jk}\right)} \tag{2.4}$$

This results in a $N \times N$ matrix with N the number of degrees of freedom used in the modal model. Indices i and j refer to the coordinates compared in each component of the matrix. The CoMAC attempts to identify which measured DoF contributes negatively to a low value of MAC. As it is the case with the MAC indicator values near 1 indicate a perfect correlation between coordinates. As the value decreases towards 0, so does the correlation of the compared DoFs. CoMAC indicator has been proposed as both a damage detector and locator.

From the compilation works by Doebling et al. [63] and Sohn et al. [21], it seems to be consensus on the fact that MAC and CoMAC methods are more sensible to global damage detection than direct comparison of mode shapes using simple procedures. Further manipulation of these indicators, as in TrMAC computation, increase the sensitivity to damage by accounting for the variations in all mode shapes. Whereas frequency shift methods indicate the change in global stiffness of the structure as a whole, MAC methods indicate changes in the degree of similarity in the modal shapes with scalar quantities. MAC has shown to be quite effective in the identification of damage in the structure as a whole and in the tracing of equivalent mode shapes as degradation occurs. On the other hand, few attempts in using CoMAC as a localizer of damage have succeed. This is the case only in controlled laboratory conditions, in specimens with prescribed degradation zones or in structures with simple boundary conditions. When mixed boundary conditions are investigated, for example with flexible supports modelled with ballast coeffcients, CoMAC is not able to correctly indicate damage in a direct manner (Serra-Lopez and Pérez [70]). It is common knowledge that that higher frequency modes are usually the most affected when damage is present so high frequency data is usually more inclined to show damage.

Other methods involving mode shapes have been used for damage detection. Messina et al. [71] define a correlation coefficient coined MDLAC (multiple damage location assurance criterion) as a statistical correlation between analytical predictions of the mode shapes changes and the real measured changes. This MDLAC is similar to the Modal Assurance Criterion (MAC) and only requires the measurement of a few modal vectors changes between undamaged and damaged states of the structure. The accuracy of damage prediction is concluded to be further improved by including pseudo mode shapes extracted from antiresonances.

In contrast to actual mode shapes which represent the core of the modal model used to describe a dynamic system, Operational Deflection Shapes (ODS) are captured from the experimental response of the structure when certain excitation is applied to the structure. This excitation may comprise a linear combination of multiple excitation at diverse points and frequencies ranges and thus, may or may not excite all frequencies in the frequency of interest in the structure. If a structure is excited near any resonance (or in a white noise pattern as in EMA, at all resonances in equal amount) ODS will be very similar to modal vectors. In their compilation work, Carden et al. [11] review a method for the location of cracks in a beam excited with piezoelectric actuators and sensed though Laser Doppler Vibrometry (LDV). Discontinuities in the ODS are used by the original authors to locate cracks in the beam.

Ritz vectors represent an alternative to mode shapes and operational deflection shapes to describe the response space of dynamic systems. Ritz vectors (also referred as Lanczos vectors) have been shown to be very effective for dynamic and earthquake analyses, eigenvalue problems, and model reductions. However, very few studies have applied these vectorial space to damage detection or system identification problems because of the difficulty of extracting Ritz vectors from vibration testing. Sohn [21] presents some of the few analytical attempts that utilize this approach.

c. Curvature and modal stain methods

Mode shapes curvatures use in structural damage assessment assumes that changes in modal curvatures are localized near regions where damage is present and that these changes are greater in magnitude that changes in the displacement mode shapes. That statement is still unclear particularly for structures with load path redundancy such as truss structures (Carden, [11]). The modal curvature is calculated from modal vectors and from geometrical relative distances between nodes. The expression for curvature is:

$$\phi''_{ik} = \frac{\partial^2 \phi_{ik}}{\partial x^2} = \frac{\phi_{(i+1)k} - 2\phi_{ik} + \phi_{(i-1)k}}{0.5^2 (d_{i-1,i} + d_{i,i+1})^2} \tag{2.5}$$

Where ϕ''_{ik} and ϕ_{ik} are the curvature and mode shape components at DoF i and corresponding to mode k, and the denominator of the expression corresponds to the mean squared distance between adjacent nodes. A common approach used by many authors (i.e. Pérez et al. [69]) is to generate a distributed Curvature Damage Factor (CDF) based on the summation of the absolute differences in curvatures for each mode shape between pristine and damage states as in equation 2.6.

$$CDF_i = \sum_{k=1}^{M} \left| \frac{\phi''_{ik} - \varphi''_{ik}}{\phi''_{ik}} \right| \tag{2.6}$$

When a particular vibration mode stores a large amount of strain energy in a particular load path, the frequency and shape of the eigenvector are very sensitive to structural changes in that load path. The strain energy is computed from the second derivative of mode shapes, so then, strain energy is closely related to modal curvatures. The general expression for modal curvature is shown in Equation 2.7a. Sohn et al. prefer the use of accumulated modal strain energy from the reference support [21]. The indicator generated in each DOF is a unitary fraction of the total energy accumulated by each mode. Fang and Qiao [62] refer to this indicator as fractional Modal Strain Energy (fMSE). Its general expression is exposed in 2.7b. Radzieski et al. [72] propose a methodology to condensate this fractional Modal Strain Energy in a Strain Energy Damage Index (SEDI) to have an indication of the amount of damage accumulated in each DoF. The SEDI indicator is calculated via equation 2.7c.

$$U_k = \frac{1}{2} \int_0^L EI \left(\frac{\partial^2 \phi_k}{\partial x^2} \right)^2 dx \tag{2.7a}$$

$$f_{ik} = \frac{1}{2U_k} \int_0^{l_i} EI \left(\frac{\partial^2 \phi_k}{\partial x^2} \right)^2 dx \tag{2.7b}$$

$$SEDI_i = \frac{\sum_{k=1}^{M} f_{ik,d}}{\sum_{k=1}^{M} f_{ik,p}} \tag{2.7c}$$

2.2.2.2 Spatial domain methods

Spatial domain methods are based in the evaluation of the shift in the dynamic matrices of the system (mass, stiffness or damping contributions) to assess structural modifications in the structure. These methods can directly attempt to quantify the variation in the matrix terms or generate certain indicators which are a direct measurement of the cahnge in the whole transfer matrices as a whole

a. Modal flexibility methods

The static stiffness matrix relates the static displacements in the DoFs of the structure with the external forces applied on the structure that caused them. If the mechanical system is in static rest, these external forces have to be in perfect equilibrium with

the internal forces developed in the materials. The flexibility matrix is the inverse of the stiffness matrix, relating forces to nodal displacements. The flexibility matrix for the damaged structure $\boldsymbol{F}_d$ can be represented using the stiffness matrix of the baseline structure $\boldsymbol{F}_p$ plus the unknown change of stiffness caused by damage $\boldsymbol{\Delta F}$. By means of tracing the changes in the damaged modal flexibility matrix calculated through the modal vectors and eigenvalues matrices, the amount of change in the flexibility of the structure can be traced as shown in Equation 2.8 with $\boldsymbol{\Gamma}$ being the diagonal matrix created from the squared ordered modal frequencies -the modal stiffness matrix-.

$$\boldsymbol{\Delta F} = \left(\boldsymbol{\phi}\boldsymbol{\Gamma}_p^{-1}\boldsymbol{\phi}^T\right)^{-1} - \left(\boldsymbol{\varphi}\boldsymbol{\Gamma}_d^{-1}\boldsymbol{\varphi}^T\right)^{-1} \tag{2.8}$$

b. Residual force vector methods

If the mode shapes, natural frequencies and initial discrete numerical model is available, it is possible to assemble the Residual Force Vector (RFV). Natural frequencies and mode shapes satisfy the eigenvalue problem, so for each natural mode and degraded operational condition, equation 2.9 is satisfied.

$$\left(\boldsymbol{K}_d - \omega_{k,d}^2\boldsymbol{M}_d\right)\boldsymbol{\phi}_{k,d} = 0 \tag{2.9}$$

With ω_k being the k^{th} natural frequency, ϕ_k are the associated modal vectors and the subscripts (d) and (p) refer to the condition of the structure, degraded or pristine. If the pristine dynamic matrices of the system are utilized in the equality, the result is unbalanced and the residue vector $\boldsymbol{r}_k$ arises for each eigenvalue of the system (Equation 2.10).

$$\boldsymbol{r}_k = \left(\boldsymbol{K}_p - \omega_{k,p}^2\boldsymbol{M}_p\right)\boldsymbol{\phi}_{k,d} \tag{2.10}$$

Carden et al. [11] suggests a physical interpretation for RFV as the harmonic force excitation that would have to be applied to the undamaged structure at damaged frequency $\omega_{k,d}$ so that the structure would response with mode shapes $\phi_{k,d)}$. Juxtaposing the residue for each mode shape a RFV can be assembled with each row corresponding to a DoF. When damage occurs components of RFV near the damage location become very large. The evaluation of those terms provides a method for both detection and localization of the damage.

c. Model updating with experimental retrofitting

Modal updating is a technique which allows to modify an initial and correlated numerical model of a structure as the degradation occurs in the experimental structure monitored. When degradation appears, mass, stiffness and damping matrices representing the structure are susceptible to change. Reproducing these changes in the numerical model would require to manually modify the definition of the simulated model for each stage. Modal updating solves this issue by continuously monitoring and extracting modal parameters of the structure in order to capture incremental differences in the dynamic matrices representing the pristine state of the system. The algorithm automatically changes the predefined variables in the model to achieve convergence. Common parameters used in modal updating are those representing global properties such as Young modulus, density, damping coefficients or ballast constants.

A rich source of damage identification methods, such as matrix updating methods, has come from the finite element model updating knowledge corpus. This can be clearly comprehended as model updating with experimental retrofitting rely on an initial correlated numerical model of the structure in its original state. With this methodology damage is assessed by mean of tracing the variation in the components of the dynamic matrices of the system. Then, these methods can be said to present damage detection, location and even quantification capabilities (Levels I to III). Although real damage in a structure usually appears on a single location, damage events could happen in a distributed manner. Modal updating techniques are one of the few methodologies capable of detecting damage in such distributed flaws scenarios.

Literature on model updating is vast both in purely numerical cases and experimental retrofitted ones. As a matter of exemplification two recent studies are exposed. Kraaij et al. [73] conducted a thorough investigation using an in-house coded computational tool in order to fit experimental data with the results provided by the software. In their work, the authors proceed by minimizing an error function calculated from the differences in modal parameters (frequencies, mode shapes and MAC values) between the experimental data and the results of the simulation for each updating loop.

Foti et al. [74] adopted a different approach using output-only acceleration records. In first place, the authors numerically modelled the system in terms of a sensibility matrix $\boldsymbol{S}$ relating changes in the modal parameters $\boldsymbol{\Delta p}^{num}$ with changes in the dynamic response of the system $\boldsymbol{\Delta r}^{num}$.

$$\boldsymbol{\Delta p}^{num} = \boldsymbol{S}\boldsymbol{\Delta r}^{num} \tag{2.11}$$

The sensibility matrix was obtained for linear variations in the elastic modulus and density of the studied structure around its nominal value. The objective of the work

is set to obtain an experimental determined $\boldsymbol{\Delta p}^{exp}$ indicator showing the changes in modal parameters by means of sensing the output only responses $\boldsymbol{\Delta r}^{exp}$.

2.2.2.3 Response domain methods

Response methods rely on the utilization of raw or processed vibration data to generate certain structural modification indicators. The main difference with other approaches lies in the fact that the series are no longer condensed into simplified sets of data, so then, potentially, there is not any loss of information in the indicators generation besides the numerical limitations from the mathematical operators used to transfmorm the signals.

a. Spectral domain methods

Modal domain indicators present the main disadvantage of requiring arduous post-process to extract the modal parameters. By using complete FRFs in the spectral domain that intermediate step can be skipped, post-process errors reduced and completeness of available diagnosis data increased.

The methodologies reviewed up to this point are based on the manipulation and transformation of information in the modal domain, which require a condensation procedure. This reduction allows to convert frequency domain data, namely FRFs, to modal domain data, that is, natural frequencies, dampings and modal vectors. Some authors state that this transformation can suppose a loss of data that theoretically could be used in the damage evaluation [75]. The use of modal domain data is inherited from the well known modal testing experimental techniques. Modal testing and structural health monitoring are not equivalent terms, as the later is a more general term which can or cannot use modal testing techniques (as well as other NDTs).

Some approaches using spectral domain data also use modal testing techniques to capture data although the modal extraction routines are not applied to the data available. One of the advantages of using spectral domain data is that the procedures are adaptable from FRFs data to Fourier-transformed output-only time measurements. So then, this kind of approach endows the structural evaluation problem with more flexibility.

Sohn et al. [21] revisit works using frequency domain methods up to 2002. The most primitive approach involves the direct comparison of FRFs corresponding to equivalent degrees of freedom by computing the absolute value of the subtraction between pristine and damaged FRFs, even averaging the value of each FRF along the fre-

quency sampling. A second common proposal shown in the review is to use FRF to extract mass, stiffness and damping matrices not only corresponding to mode shapes but extended to the whole spectral domain measured. By comparing these extracted values to the original pristine ones, changes in these matrices are related to damage introduced in experimental specimens.

Zhong et al [76] discuss another damage detection procedure, the spectral center correction method (SCCM), which relies on the identification of output-only acceleration versus time histories when an auxiliary mass is attached as a probe to certain locations of the structure. The verification of this procedure is purely numerical and the practical applicability is proposed as a further work.

A more complex approach is presented by Schulz et al. [77] using a spectral-equivalent of the residual force vector. The FRF matrix of the structure $\boldsymbol{H}(\omega)$ is assumed to be known for the undamaged state. Then, a damage vector $\boldsymbol{d}$ equivalent to the difference between the force vector applied to the structure $\boldsymbol{f}$ and the inverse of FRFs matrix $\boldsymbol{H}(\omega)^{-1}$ multiplied by the displacement vector $\boldsymbol{x}$ (the dynamic force vector) is introduced (Equation 2.12). This vectorial damage index shows non-zero elements in the DoFs connected to damaged elements.

$$\boldsymbol{d} = \boldsymbol{H}(\omega)^{-1}\boldsymbol{x} - \boldsymbol{f} \tag{2.12}$$

When the excitation forces are unknown (a common case in SHM of large structures) a new damage indicator is developed using only the monitored responses. This second indicator is the sum of two contributions, the unbalanced damage force and the unknown external force. Its formulation is shown in equation 2.13.

$$\boldsymbol{r} = \boldsymbol{d} + \boldsymbol{f} = \boldsymbol{H}(\omega)^{-1}\boldsymbol{x} \tag{2.13}$$

As the excitation force is unknown, it becomes necessary to introduce a damage indicator matrix $\boldsymbol{D}$ calculated from the statistical expectation of the $\{r\}$ vector as in equation 2.14 with f_1 and f_2 defining the range of frequencies of the FRFs conforming $\boldsymbol{H}(\omega)^{-1}$, $\mathbb{E}$ operator being the Expectancy of the vector enclosed and $\circ$ being the outer product of two matrices. This results in a $i \times j$ matrix with each D_{ij} element showing damage if its value is non-zero. So then, this indicator is capable of both detecting and locating damage.

$$\boldsymbol{D}^2 = \frac{1}{f_2 - f_1}\int_{f_1}^{f_2} \left[\mathbb{E}(r \times r^*)\right] \circ \left[\mathbb{E}(r \times r^*)^*\right] df \tag{2.14}$$

The philosophy behind the following spectral indicators is equivalent to the one used in the modal damage indicators but considering the full range of frequencies of interest in the FRFs functions. The correlation between two sets of FRFs can be obtained using the Spectral Correlation Criterion (SCC) reviewed in [68]. SCC is an operator parallel to the CoMAC but formulated in the spectral domain instead of the modal domain. SCC is usually interpreted as a covariance map in the geometrical domain showing the amount of similarity of all the available FRFs spectra together. The indicator results in a $N_{dof} \times N_{dof}$ matrix with N_{dof} the number of degrees of freedom considered in the test. Its formulation is shown in Equation 2.15. Heylen and Lammens [78] referred to this indicator as the Frequency Response Assurance Criterion (FRAC) in its 1996 work where they successfully used it in the comparison of FRFs.

$$SCC_{ij} = \frac{\left(\sum_{\omega_1}^{\Omega} h_{ij}^{(p)}(\omega) h_{ij}^{*(a)}(\omega) \right)^2}{\left(\sum_{\omega_1}^{\Omega} h_{ij}^{(p)}(\omega) h_{ij}^{*(p)}(\omega) \right) \left(\sum_{\omega_1}^{\Omega} h_{ij}^{(a)}(\omega) h_{ij}^{*(a)}(\omega) \right)} \tag{2.15}$$

Based on the same philosophy, Pascual et al. [6] proposed to use the Frequency Domain Assurance Criterion operator (FDAC) to quantify the degree of correlation between two numerical sets of FRFs numerically generated and aimed to perform modal updating studies in simualted models. In his work, Pascual uses the conjugated product of FRFs to avoid the appearing of imaginary part of the results as:

$$FDAC_{fg} = \frac{\left| \sum_{i=1}^{N} \sum_{j=1}^{N} h_{ij}^{(p)}(\omega_f) h_{ij}^{*(a)}(\omega_g) \right|^2}{\left(\sum_{i=1}^{N} \sum_{j=1}^{N} h_{ij}^{(p)}(\omega_f) h_{ij}^{*(p)}(\omega_f) \right) \left(\sum_{i=1}^{N} \sum_{j=1}^{N} h_{ij}^{(a)}(\omega_g) h_{ij}^{*(a)}(\omega_g) \right)} \tag{2.16}$$

Where i denotes the DoF in which the FRF is captured, $h_{ij}^{(p)}(\omega_f)$ corresponds to the reference pristine FRF excited at DoF i, measured at DoF j and sampled at frequency f, $h_{ij}^{(a)}(\omega_g)$ refers to the value of the altered FRF at frequency g. This results in a $N_f \times N_e$ matrix with N_f and N_g being the number of lines of frequency in the spectral sampling of both FRFs.

Zhang et al. [79] proposed both the First Global Shape Correlation function (GSC) and Global Amplitude Correlation function (GAC) to detect damage in a structure. GSC is an equivalent to the original SCC formulation. Although the GSC indicator is exactly equivalent to the SCC operator, the main singularity of the GAC lays in the fact that that second index is a linear combination of FRFs at the same DoF for

each frequency available in the spectral domain. The formulation of the GCA rests as shown in eq. 2.17.

$$GCA_{ij}(\omega) = \frac{2\left|h_{ij}^{(p)}(\omega)h_{ij}^{*(a)}(\omega)\right|}{h(p)_{ij}(\omega)h_{ij}^{*(p)}(\omega) + h_{ij}^{(a)}(\omega)h_{ij}^{*(a)}(\omega)} \tag{2.17}$$

Palacz et al. [80] proposed the use of frequency response curvature method for damage detection in a cantilever beam. This damage assessment technique is based on the extension of the mode shape curvature for a given and continuous frequency range. The frequency response curvature is estimated using the same central difference scheme as in the mode shape curvature. An equivalent damage index can be computed in a similar fashion to the modal domain indicator using the magnitude of the FRFs (eqs. 2.18 and 2.19. Reddy et al. also used this methodology to asses damage in plate like structures [81].

$$h''_{ij}(\omega) = \frac{h_{i+1,j}(\omega) - 2h_{i,j}(\omega) + h_{i-1,j}(\omega)}{0.25(d_{i-1,i} + d_{i,i+1})^2} \tag{2.18}$$

$$\Delta h''_{ij}(\omega) = \sum_{\omega_1}^{\Omega}\left|h_{ij}^{\prime\prime(a)}(\omega) - h_{ij}^{\prime\prime(p)}(\omega)\right| \tag{2.19}$$

In the same line of investigation in spectral correlation derived indicators, Maia, Urgueira, Sampaio an co-workers [3–5] propose the use of both mobility matrix components and transmissibility matrix components in damage detection. Authors claim that the use of the transmissivity matrix allows to obtain FRFs in inaccessible points in the experimental mesh by using available FRFs to generate equivalent transmissibility components H_{ij} which cannot be directly measured using FRFs. The concept is then further extended to damage detection using those transmissibility functions. The Response Vector Assurance Criteria (RVAC) is computed from FRFs measured with a fixed excitation point and multiple measurement points with the following expression:

$$RVAC_{\omega} = \frac{\left(\sum_{i=1}^{N}\sum_{j=1}^{N} h_{ij}^{(p)}(\omega)h_{ij}^{*(a)}(\omega)\right)^2}{\left(\sum_{i=1}^{N}\sum_{j=1}^{N} h_{ij}^{(p)}(\omega)h_{ij}^{*(p)}(\omega)\right)\left(\sum_{i=1}^{N}\sum_{j=1}^{N} h_{ij}^{(a)}(\omega)h_{ij}^{*(a)}(\omega)\right)} \tag{2.20}$$

Their investigation progress by extending this RVAC indicator to the full $\boldsymbol{H}$ compliance matrix with all available mesh nodes and proposes the condensation of all the

values in the RVAC/FDAC matrix in a single Detection and Relative damage Quantification indicator (DRQ) which is defined as the mean of the full RVAC indicator along the spectral domain.

$$DRQ = \frac{1}{N_\omega} \sum_{\omega_1}^{\Omega} \frac{\left(\sum_{i=1}^{N} \sum_{j=1}^{N} h_{ij}^{(p)}(\omega) h_{ij}^{*(a)}(\omega) \right)^2}{\left(\sum_{i=1}^{N} \sum_{j=1}^{N} h_{ij}^{(p)}(\omega) h_{ij}^{*(p)}(\omega) \right) \left(\sum_{i=1}^{N} \sum_{j=1}^{N} h_{ij}^{(a)}(\omega) h_{ij}^{*(a)}(\omega) \right)} \tag{2.21}$$

In a more recent development [5], Sampaio proposes to directly use Operational Deflection Shapes in the spectral domain (mobility FRF functions) to generate an Operational Deflection Shape difference indicator ΔODS as a damage indicator. This indicator is defined as a inner comparison of a set of measurements m as:

$$S_m = \sum_{k=1}^{N_\omega} \sum_{j=1}^{N} \sum_{i=1}^{N} |h_{ij}^{(a)}(\omega_k) - h_{ij}^{(p)}(\omega_k)| \tag{2.22a}$$

$$\Delta ODS_m = 1 - \frac{S_m}{max(\{S_m\})} \tag{2.22b}$$

This background is considered to be of vital importance to this research as authors adopt the same spectral domain approach that proposed in this investigation. Newly proposed indicators in this document are a direct response to some observations made about these indices. A first limitation is identified as both DRQ and ΔODS are unable to discern losses from gains in structural performance of the system. Although in real scenarios structural performance loss is the most common phenomena, an increase in it may also appear as a result of material hardening or reinforcement intervention. An upwards shift in spectral series can also appear due to changes in in-service loads. If these loads increase due to environmental factors, vibration spectra is susceptible of positively shifting in the spectral domain, as a string rises its pitch when its working tension is increased.

The indicator derived from shift in ODSs is always normalized with respect to the highest value of the indicator in the progression studied. So then, this indicator is highly dependant on the number and severity of the tests executed on the structure and can not be systematized for different structural typologies or even different damage mechanisms. However Δ ODS indicator is much more sensible to damage than the DRQ.

DRQ and Δ ODS are further analysed considering its interpretation in relation with changes in the FRFs. Figure 2.1 shows two sets of FRFs (in black and grey), each

composed of three FRFs and with only the first harmonic peak visible in the spectra. The first set of FRFs corresponds to the reference state of system while the second one corresponds to a reduction the stiffness in the structure. Reduction in stiffness translates in a downwards shift in the resonant peak in the frequency axis and a possible increment in the amplitude of the FRF (more elastic elements presents bigger mobility).

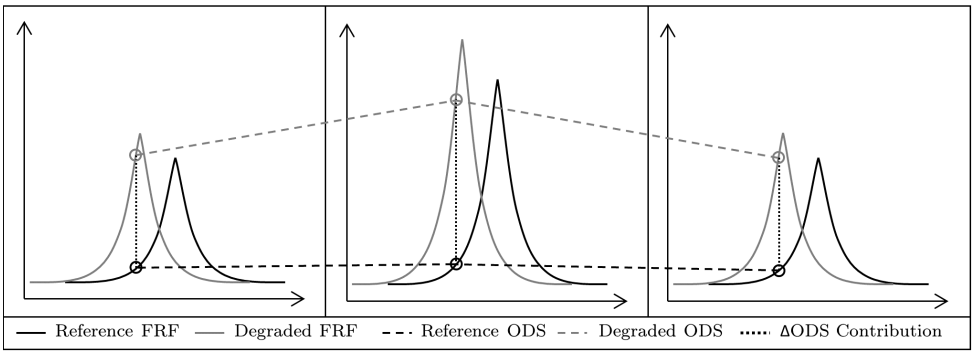

Figure 2.1: Concept behind the RVAC and ΔODS.

The ΔODS indicator then is an accumulated difference between magnitudes of spectral ODS. On the other hand, the RVAC, precursor of the DRQ indicator, can be interpreted as a measure of the loss of orthogonality between ODS corresponding to each line of frequency. As it can be easily interpreted from the figures, DRQ is much more stable in front of spectral shifts than ΔODS as the loss of orthogonality in ODS is very small in the neighbourhood of the resonant peak.

On the contrary, ΔODS accumulates damage even when frequency shift introduced is very small and equivalent resonances are very close to each other. Even for peaks at the same frequency position, but with different amplitudes damage levels keep accumulating. RVAC on the other hand, non-dimensionalizes with local magnitudes of FRFs and do only account for orthogonality losses. However, the DRQ keeps the limitation being unable to discriminate increase from decrease in stiffness.

Same authors also proposed a Transmissibility Damage Indicator (TDI) with a similar approach and formulation as that applied to calculate the DRQ but using transmissibility functions $\tau_{ij}(\omega)$ instead of FRFs $h_{ij}(\omega)$. The formulation is exactly equivalent to the DRQ but the fact that the indicator is computed from trasmisibility functions makes the use of this indicator very suitable to apply it to FRFs obtained using Operational Modal Analysis.

The transmissibility matrix is defined as the matrix of spectral functions which relates a sub-set of displacement responses in the system measured in certain locations of the

system with the responses measured in a different sub-set of locations. So then, the transmissibility matrix is defined in a similar matter as Operational Modal Analysis is executed: by only relating displacements in the system due to unknown (or not measured) excitations. If two partial transfer matrices are defined for each subset relating excitation forces and responses as:

$$\boldsymbol{X}_B = \boldsymbol{H_{BA}}\mathbf{F}_A \tag{2.23a}$$

$$\boldsymbol{X}_C = \boldsymbol{H_{CA}}\mathbf{F}_A \tag{2.23b}$$

Then, the transmissibility matrix is defined as the operator which can relate two sets of distinct displacements through the equalization of the external force vector $\boldsymbol{F}_A$

$$\boldsymbol{X}_B = \boldsymbol{H}_{BA}\boldsymbol{H}_{CA}^{-1}\boldsymbol{X}_C \tag{2.24a}$$

$$\boldsymbol{\mathcal{T}}_{BC} = \boldsymbol{H}_{BA}\boldsymbol{H}_{CA}^{-1} \tag{2.24b}$$

So then the TDI is formulated as:

$$TDI = \frac{1}{N_\omega}\sum_{\omega_1}^{\Omega}\frac{\left|\sum_{i=1}^{N}\sum_{j=1}^{N}\tau_{ij}^{(p)}(\omega)\tau_{ij}^{*(a)}(\omega)\right|^2}{\left(\sum_{i=1}^{N}\sum_{j=1}^{N}\tau_{ij}^{(p)}(\omega)\tau_{ij}^{*(p)}(\omega)\right)\left(\sum_{i=1}^{N}\sum_{j=1}^{N}\tau_{ij}^{(a)}(\omega)\tau_{ij}^{*(a)}(\omega)\right)} \tag{2.25}$$

As the TDI is computed from transmissibility functions obtained by applying a known force in an exciting point and measuring all FRFs at all possible receiving driving points of the experimental mesh, the index is then a quantifier of the amount of mechanical energy transmitted from each location to other points of the structure.

Both indicators are applied to the detection of damage in a beam-like structure with artificially introduced damage scenarios using experimentally acquired FRF data. The authors, however, claim that the DRQ indicator is neither very sensitive to damage detection.

However the the TDI index shows to be much more sensitive to damage than DRQ, so authors conclude that this transmissibility derived index is much more sensitive to damage. Indicators proposed in these two papers, although very sensitive, are only capable of detecting damage and cannot differentiate between reinforcement or degradation scenarios. The current investigation attempts to overcome this limitation starting only from the detection point of view.

b. Time domain methods

Temporal domain methods are based on a common concept that is also shared by Fourier decomposition methods. However, the historical sounds of Fourier methods and their widespread applications in many fields of science, physics and engineering form by themselves a differentiated analysis paradigm. Temporal methods rely on the projection of temporal continuous data series to a subspace of well defined functions with fixed geometry and temporal scales (characteristic frequencies). The most used continuous temporal method is the Wavelet Transform. The Continuous Wavelet Transform (CWT) (or its discrete implementation, the Discrete Wavelet Transform -DWT-) decompose a continuous signal in time in a scaleogram which shows the coefficients of each wavelet scale along the time (this is somewhat equivalent to a frequency vs. time 2D map, as each wavelet scale corresponds to an increasingly growing number of oscillations in the fixed period of the Wavelet). Although Wavelet analysis can detect progressive changes in the scalogram map of a structure, it has been most successfully applied to the detection of abrupt changes in the frequency response of the system. The increasing complexity of wavelet analysis in front of Fourier analysis is not justified by any increase of the sensibility or applicability when compared with conventional Fourier Transforms. The results obtained from both methodologies are essentially equivalent with the added benefit that the FFT discrete algorithm is by far more computationally efficient that DWT. Periodic snapshots of the vibration response of the structure processed through FFT are then the most cost-efficient solution for an in-service application of a SHM system.

Time series methods are one the most rapidly evolving methods of vibration-based structural health monitoring. As opposed to modal domain based methods, time domain methods are a recent and very active field of investigation in SHM. In real applications, the spectral composition of a signal is prone to experiment changes along time. The main advantage of temporal domain derived indicators is that time varying spectral components of signals can be traced. This spectral shift phenomena is of great importance if these changes suddenly happen and are needed to be accounted for.

Kopsaftopoulos and Fassois [17] propose the use of three main elements when dealing with time domain vibration based damage assessment: random excitation and vibration, statistical model representing the mechanical system monitored and adequate statistical decision making tool for inferring the health state of the structure. These components are very similar to the Statistical Pattern Recognition problem formulated by Farrar and Doebling [15]. In their work, the authors compare degraded to pristine state of a structure by generating a set of statistical indicators (mean value

and standard deviation) calculated from time series of acceleration in a structure. If a residual function derived from these statistical indicators surpass certain threshold, the structure is assumed to present some kind of damage.

Straszewsky and Robertson [20] present a review of some of the time-domain based techniques for SHM. In the work, the Gabor transform, the Wigner-Ville Distribution, the Pseudo Wigner-Ville distribution, the Choi-Williams distrbution and the Continous Wavelet Transform are presented. The following discussion is based on this review article.

The original approach for time-domain analysis of vibration relies on the Fourier transform. If this transform is applied to sections of the sampled signal, an indication of the time-varying spectral characteristics of the signal can be obtained. Usually, the Fourier transform is not directly applied to the raw sampled signal, but calculated on its product to a windowing function which allows to reduce noise influence, leakage and aliasing effects of the sub-sampling. If a Gaussian window is selected to be applied to the Fourier transform, the transformation is then referred to as the Gabor transform and its expression lays as

$$X(t,\omega)) = \int_{-\infty}^{\infty} \frac{e^{-\left(\frac{(t-\tau)^2}{4\alpha}+j\omega\tau\right)}}{2\sqrt{\pi\alpha}} x_t(\tau)d\tau \qquad with \qquad \alpha > 0 \tag{2.26}$$

The Gabor transform present some limitations in the size of the window which is used to compute it. The Wigner-Ville Distribution (WVD) attempts to increase the limits of this windowing procedure by weighting the temporal signal with time and frequency translations of itself instead of a fixed window function. The WVD is a measure of the signal overlapping with itself at past and future temporal points and it is computed from the instantaneous auto-correlation function of the signal as:

$$WVD(t,\omega) = \frac{1}{2\pi}\int_{-\infty}^{\infty} x^*\left(t-\frac{\tau}{2}\right) x\left(t+\frac{\tau}{2}\right) e^{-j\omega\tau}d\tau \tag{2.27}$$

The most important drawback of WVD is that it introduces highly oscillating residua cross-interference terms which can lead to misinterpretations. To solve that issue, the Pseudo Wigner-Ville Distribution applies a windowing function to the original Wigner-Ville expression. The windowing functions helps to empathize the signal at each time and to smooth residual cross terms. Some different windowing functions can be selected but the most common is again, a Gaussian peak. Its expression rest as:

$$PWVD(t,\omega) = \frac{1}{2\pi}\int_{-\infty}^{\infty} h(\tau)x^*\left(t-\frac{\tau}{2}\right) x\left(t+\frac{\tau}{2}\right) e^{-j\omega\tau}d\tau \tag{2.28}$$

If the windowing function selected to compute PWVD is selected to be

$$\phi(\theta, \tau) = e^{-\theta\tau^2/\sigma} \tag{2.29}$$

then the Choi-Williams distribution is obtained. The parameter σ controls the attenuation of cross terms of the correlation whereas θ controls the peak height in the windowing function.

Laplace and Fourier derived transforms can be viewed as a decomposition of signals in the harmonic base space defined by trigonometric functions. This decomposition do not show any kind of local information function as the geometrical distribution of the signals is composed by a linear combination of the harmonic base functions (which at the same time are infinite, so truncation is always an issue to be considered). To solve this problem, Wavelet analysis was introduced in the late 80s.

Wavelets are a class of basis functions that have well defined and specific properties very different from Fourier base space functions. Wavelet base functions are localized both in time and in spectral domain, so dilation of the base functions gives a description both in the temporal and in the spectral domain. In the other hand, short time Fourier analysis requires the use of windowing functions which can introduce residual error contributions to the data processed. Wavelet analysis appears as a more direct approach to the analysis of time-varying spectrum of signals.

The work of Taha et al. [82] is a good starting point as the authors present an comprehensive introduction to wavelet analysis formulation for SHM applications. A case study of the wavelet analysis of a bridge is depicted and results are discussed. Radzienski and his colleagues [72] also present the results of using wavelet analysis in the detection of cracks in an experimentally tested beam in clamped-free boundary conditions.

The Continous Wavelet Transform uses scales s which are directly related to frequencies. Scales in the time are defined by the time parameter u which computes for a time translation forward or backward in the time domain. The squared amplitude of the Wavelet Transform map as a function of time is called scalogram and can be transformed to time-frequency map straightforward. The expression for the base wavelet from where the dilations in time and frequency are generated is

$$\psi_{u,s}(\tau) = \frac{\psi}{\sqrt{s}}\left(\frac{\tau - u}{s}\right) \tag{2.30}$$

So the Continous Wavelet Transform for specific s and u scales is calculated as:

$$W_\psi(u,s) = \frac{1}{\sqrt{s}} \int_{-\infty}^{\infty} f(\tau)\psi^*_{u,s}(\tau)d\tau \tag{2.31}$$

The result of a wavelet analysis results in a two dimensional map consisting in a scalogram and a time-frequency map.

One of the latests signal processing tools to come to the SHM scene has been Hilbert-Huang Transform (HHT). The Hilbert-Huang method was first introduced in a US Patent (Huang, U.S. Patent No. 09/210.693, 1998) and two companion papers by Huang et al. [83], [84]. Hilbert-Huang method uses Empirical Mode Decomposition (EMD) to decompose vibration signals in intrinsic mode functions (IMF). Authors claim that EMD is able to decompose a signal in the frequency-time domain more precisely that wavelet analysis. Consequently, it is capable of detecting discontinuities in the recorded acceleration time-series and is capable of dealing with non-stationary data.

Yang et al. [85] present their works using HHT and EMD in the field of damage detection on a benchmark problem proposed by the American Society of Civil Engineering Task Group on SHM. When sudden damage events occur during the recording period of health monitoring systems, the HHT is able to locate that discontinuity in the time domain. With this in mind, a method based on EMD is proposed to detect the damage time instants and damage locations. However, the capability of detecting damage spikes in the signal depends on the severity of damage, the level of noise pollution among others. In general, if the damage is small or the level of noise pollution is high, the proposed method do not produce satisfactory results.

2.2.3 Damage detection paradigms

Model identification based on experimental information in Structural Health Monitoring is the part of the pattern recognition problem which has received the least attention in technical literature. Model identification is concerned with three main tasks in SHMs, pattern processing, situation assessment and decision making. These three aspects aims to solve Levels I to III of the SHM problems of detection, location and assessment of damage in a structure.

Worden and Manson [86] argue that the Machine Learning Theory (MLT) offers a natural and comprehensive framework to address these tasks in an integrated procedure. MLT is a body of knowledge that attempts to construct computational relationships between data observed using prescribed rules. This rules are acquired dynamically, or learned, taking into account the experimental data available. This computational

paradigm is essentially opposed to conventional computation, where algorithmic rules are imposed in a sequential manner.

MLT embraces both supervised and unsupervised procedures presented in introductory section 2.1. Learning theory is specially useful when dealing with classification problems in sets, if regression maps between inputs and outputs in a system are to be done and to estimate probability densities characterizing a physical system. As these three aspects are the defining characteristics of SHM problem, Learnig Theory approach is specially suitable to be applied to the condensed information extracted from monitored systems to assess the degradation state of the structure.

Machine Learning algorithms fall into the unsupervised and supervised categories. Supervised learning requires examples of inputs and outputs to postulate relationships from them. These inferred laws, allows errors in the model to be corrected along progression. When the system is well trained it can be used to perform classification and regression problems. On the other hand, unsupervised learning can statistically characterize a system on the basis of a set of measurements. This second approach is suitable if the causes in the variations of the response do not need to be characterized and if only a novelty recognition is required.

Decision making procedures in degradation assessment of a structure range from very simple routines where a threshold in statistical indicators derived from condensed information is used to trigger a damage alarm to much more complex systems where an adequately trained Artificial Neural Network (ANN) is used to classify the type or locate the damage in a structure monitored. In the following sections, some works involving decision making in damage assessment will be presented.

2.2.3.1 Unsupervised learning: Novelty detection

Novelty detection is based in statistical modelling of structural systems. This approach is among the earliest methods of damage detection through the analysis of vibration data. This methodology uses condensed data captured from the monitored specimen to generate certain statistic indicators. If the values of these statistical indicators are well characterized for damaged and degraded conditions, the current state of operation of the system can be inferred by direct comparison with an available database.

Statistical approach to damage detection is based in the statistical pattern recognition paradigm already presented. This school of thought tries to identify damage from a non-model based standpoint by applying principles of novelty detection to sampled signals. Non-model statistical pattern recognition is not based in a correlated numerical model, which is not always easy to converge. This kind of approaches are also suited

to the post-process of data from ambient excitation (wind, traffic loads or other). In the words of Carden in its 2004 review [11]:

> Novelty detection is concerned with the identification of any deviations in measured data relative to data measured under normal operating conditions. Features derived from measurements taken from a structure in its undamaged state will have a distribution with an associated mean and variance. If the structure is damaged, then there may be a change in the mean, the variance, or both. Statistical process control provides a framework for monitoring the distribution of the features and identifying new data that is inconsistent with the past outlier analysis. If all other variables can be eliminated then a change in the distribution characteristics of the features will indicate damage. It is important to note that the detection of damage, rather than location and quantification, is the objective of using statistical pattern recognition.

Works using statistical description of mechanical systems are vast. As a matter of exemplification, in the 2000 article by Sohn et al [87], the authors use Statistical Processing Control principles (SPC) to detect damage in concrete columns. Applying Control Chart Analysis, the existence of degradations are investigated. This method presents the advantage of being very suitable for continuous automatic monitoring. The authors concluded that when the system of interest experiences abnormal conditions, the mean and variance of the extracted features surpass the established pristine configuration threshold values.

The statistical approach to novelty detection is based in the basic statistical descriptors of random signals. Those are the statistical mean of a sample μ, the standard deviation σ and mostly residual, the skewness γ, the statistical kurtosis κ and the covariance between two data sets σ_{xy}. The formulation for those descriptors can be rapidly recovered from any basic statistics textbook (i.e. [88]). Whereas the mean of a signal measures the central tendency of the data set, the standard deviation measures how far a set of numbers is spread out. A STD of zero indicates that all the values are identical. STD is always non-negative so small values indicate that the data points tend to be very close to the expected value, while a high variance indicates that the data points are very spread out around the mean and from each other. Skewness is a measure of the asymmetry of the probability distribution of a real-valued random variable about its mean. The skewness value can be positive or negative, or even undefined. For a one-dimensional distribution, negative skew indicates that the tail on the left side of the probability density function is longer or wider than the right side. Conversely, positive skew indicates that the tail on the right side is longer or wider than

the left side. Kurtosis is a measure of the lack of tails in the probability distribution of a random variable from its central expected value. Several conceptual descriptions of the kurtosis are encountered in bibliography such as the relative tail weight, the peakedness of a distribution (width of peak), or the lack of shoulders (distribution primarily accumulated near central peak peak and near tails, not in between).

On the other hand there are the statistics which relate two sets of data. In first place, the covariance, that is a measure of how much two random variables change together. If greater values of one variable mainly correspond with the greater values of the other variable, and the same holds for the smaller values, the covariance is positive. When greater values of one variable mainly correspond to the smaller values of the other, the covariance is negative. The sign of the covariance therefore shows the linear relationship between the variables. The Pearson correlation coefficient is a normalized version of the covariance and shows the strength of the linear relation between two variables. The Pearson correlation coefficient r is a measure of the linear correlation between two variables X and Y, giving a value between 1 and 1 inclusive, where 1 is total positive correlation, 0 is no correlation, and 1 is total negative correlation. It is widely used in sciences as a measure of the degree of linear dependence between two variables.

The bibliographic Work by Farrar and Worden [27], again, serves as a guideline to identify the statistical approaches used to novelty detection using unsupervised machine learning methodologies and statistical descriptors. Those are basically grouped in four categories:

- **Gaussian normal description** of the vibratory phenomena. The mean and the standard deviation of the process is calculated and deviations from this distribution are assessed with certain confidence thresholds.
- **Auto Associative Neural Networks** (AANN) which are input statistical descriptors of a process so they output the confidence threshold for the intactness of the structure.
- Non-parametric probability functions estimation. The Probability Density Function (PDF) of the vibratory phenomena is generated from experimental data and deviations in those PDFs are used to assess the presence of structural degradation.
- **Statistic Process Control**. Derived from industrial Statistic Quality Control and Assurance, this methodology uses normal Gaussian probability distributions to perform a series of statistical systematized tests over the models to assess the degradation state of the system. Most simple tests may include Student t-Distribution tests or ANOVA tests.

2.2.3.2 Supervised learning

a. Artificial Neural Networks

An Artificial Neural Network (ANN) is a set of interconnected elements, called neurons, that provide a response, namely the output, from a series of inputs. These inputs are linearly combined in each neuron through a relative weight coefficient for each. The neural network output is obtained through the result of the linear combination of transfer functions (the activation function) that can be either linear or non-linear [89]. By the words of his original inventor, Dr. Robert Hecht-Nielsen, an ANN is a computing system made up of a number of simple, highly interconnected processing elements, which process information by their dynamic state response to external inputs [90].

Dr. David Kriesel presents a comprehensive introductory text to Artificial Neural Networks [91]. The principles involved in this computational paradigm are briefly discussed here. The reader is addressed to that text if further interested. Connections between neurons are directed (meaning that only one direction of information flow is allowed) and weighted through the weight strength of each connection w_{ij}. These weights in connections can be implemented in a square weight matrix [W] with the row number indicating where the connection begins and the column number indicating where the connection is targeted. This matrix is known as a Hinton diagram and can be represented using graph theory.

In each neuron, a propagation function receives the output of other neurons o_i and transforms them according to the weight of each connection to generate the overall Network Input to that neuron $net_j = \sum_i o_i \cdot w_{ij}$. Neurons have also an activation threshold value at which the neuron is considered to activate (and deactivate if lower). The function which sets the state of activity of a neuron is called activation function and is dependent on the previous activation state of the neuron $a_j(t-1)$, on the network input net_j and on the threshold value Θ_j. Some of the most simple activation functions used are the Heaviside function, the Fermi function and the hyperbolic tangent. Finally, the output of the neuron is computed from an output function which is directly a function of the activation state of the neuron $o_j = f(a_j)$. In the simplest approximation, the output function is assumed to be equal to the activation function of the neuron so $o_j = a_j$.

Once the basic components of an ANN are set, there is need to adopt a learning strategy. Learning is defined as the process used to fine tune the strengths w_{ij} of each connection in order to reproduce known outputs to a set of well defined training

examples. So then, after training, the network will prodcue desired ouputs for given inputs.

Although there exists a great diversity of topologies used in ANN, one of the most common is the feed-forward ANN. In this type of topology, neurons are grouped in different layers: an input layer, n hidden processing layers and an output layer. Hidden layers are 'invisible' from the outside (from input and output data ports). In this kind of network, each neuron in one layer has only direct output connections to the next towards the output layer. If all possible connections to the next layer are materialized, the term completely linked ANN is adopted. Neurons in the input layer are referred as i_j, hdden layer neurons as h_j and output layer neurons as Ω_j. When the number of intermediate layers in the ANN increases, the term Deep Neural Network (DNN) arises. DNNs allow to model complex non-linear relationships.

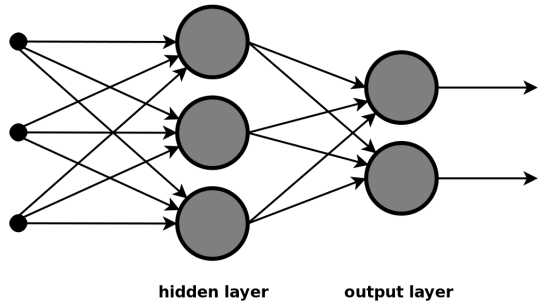

Figure 2.2: Feed-forward artificial neural network topology. Reproduced from Wikimedia Commons

Neural network based damage detection generally consists of a training phase and a recognition phase. In the training phase a set of already known solutions are used to generate an adequate ANN capable of outputting the same solutions given the known inputs. Each of the training steps can be done using the back-propagation principle. The process of sequentially modifying an ANN until convergence with the database results is commonly executed using Evolutionary Algorithms. Among them, the most popular and robust is the algorithm known as Evolutionary Genetic Algorithm which is an optimisation tool aimed to fit an objective function by randomly changing design parameters in an initial population. By selecting the most successful specimens in the population (those that maximize the objective function), and applying crossover and mutation principles on the selected most able specimens, the residual error between the fitted ANN and the database solutions can be minimized. The objective of this investigation is far from being even an summary of ANN developments as literature on ANNs is extremely vast and with multiple ramifications and applications in and infinitude of engineering and science problems.

ANN have been successfully employed in several engineering fields as for instance, in structural engineering. Hakim et Razak [75] discuss how artificial intelligence approaches to computation, such as ANN, Genetic Algorithms or Fuzzy Logic, are very attractive in the inverse SHM problem as they present proven performance and robustness when dealing with incomplete, uncertain or noisy data.

The effectiveness of ANN for solving inverse problems as damage detection in structural systems have been widely proven in literature, as for example the work by Mehrjoo et al. [92], where damage is successfully detected in a truss bridge using ANN. Other cases of success using ANN to damage detection include the work by Facchini et al. [93], where an ANN is used to assess the degradation state on a numerical 1-bay 5-storey building using some damage indicators previously computed that act as the inputs of the ANN.

In the research paper by Fang et al. [94], the authors explore the structural damage detection using frequency response functions (FRFs) as input data to a back-propagation neural network (BPNN) with three different learning algorithms. The authors claim that the ANN trained with the different algorithms can assess damage conditions with very good accuracy and that their proposed method is non-model based and thus can have advantage in many practical applications.

Artificial Neural Networks have been in constant development in SHM since the maturation of Evolutionary Genetic Algorithms (EGA). EGA are a keystone in modern unsupervised machine learning as they allow to recurrently fit an ANN to a set of known solutions for a given problem in an approach without the need of a complex physics-based model of the phenomena. Although this is undoubtedly a very promising field in SHM and almost certainly, the essential tool to be used in model identification applied to SHM, ANN are usually an abstract layer resting in top of conventional well characterised damage indicators. So then, ANN are trained to identify structural modifications based in certain input data that is, commonly, a set of modal-domain derived damage indicators. As the objective of this research is to propose and validate damage indicators based the spectral domain, the top-layer ANN-based model identification phase of a SHM is considered out of scope. Statistical tools are considered to be enough to perform the sensibility analysis on the studied spectral indicators.

b. Support Vector Machines

Support Vector Machines (SVM) are algorithms supported on the Statistical Learning Theory (SLT), a generalized evolution of Machine Learning Theory [86]. Widodo and Yang provide an introductory work to SVM theory [2] for machine condition monitor-

ing and fault diagnosis. Whereas classic machine learning techniques (such as Artificial Neural Networks) are designed to evolve a model by minimizing the prediction error of its output in base of a set of previously known training examples until the error is neutralized, SVM is based on the Structural Risk Minimization principle (SRM) rooted in SLT. The basic idea behind it is that to find a good model, one must select the simplest one minimizing training error (error between the fitted model and experimental samples). In other words, it is preferable to have a simple model over complex one as the complex one makes more assumptions about the data without factual evidences that support the increase in complexity. By utilizing SRM principle over-fitting errors (common in Artificial Neural Networks) are avoided.

c. Expert systems

All the previous concepts and developments have to be implemented in a real system if this technology is required to be applied in a real scenario. In traditional Condition Monitoring of rotary machinery, if a faulty condition is developed, the frequencies emitted by the machine, the amplitudes at resonant peaks and the peak distribution along the spectra are sensible to change. By tracing these fault signatures, damage identification can be performed. This kind of analysis has been traditionally executed by experienced maintenance engineers by manually examining the vibration time histories of the mechanical system in question. This human interaction factor can be avoided and automated with the aid of Expert Systems.

An expert system is a computer program that uses artificial intelligence technologies (for example, statistical pattern recognition algorithms, artificial neural networks or other more complex approaches) to simulate the judgement and behaviour of a person that has expert knowledge and experience in a particular field. Expert Systems can solve complex problems using artificially introduced reasoning rules rather than procedural conventional code. Expert systems are among the first truly successful forms of AI software.

An expert system is divided into two sub-systems: the inference engine and the knowledge base. The knowledge base represents facts and rules. The inference engine applies the rules to the known facts to deduce new ones by means of applying if-else rules to the captured experimental data. Expert systems in vibration analysis develop rules relating physical fault conditions to changes in frequencies emitted by the rotary machine monitored.

Ebersbach and Peng [95] present a case study where an Expert System is applied to the monitoring and damage identification on an oil drilling assembly. They develop a

27 case knowledge base for that specific system and test the system for real damaged scenarios corresponding to the designed knowledge base. Damage identification and classification is successfully achieved and a software application is designed for that specific application.

2.3 Damage detection in power transmission towers

Electrical power transmission towers are slender metallic truss structures quite sensitive to dynamic excitations. Dynamic properties of the system can be correlated with the physical properties of the different components of the structure. On the other hand, deformations on the elements of the structure can be related to the loads and stresses applied to it. With this two sets of data, and applying certain damage indicators, an inference about the presence of damage can be done.

Works on damage detection in power transmission towers are scarce. Most of investigation to date in these structure focus in the evaluation of static or dynamic structural performance and not in the damage detection itself. Damage identification is approached in a general way, as the change of structural performance of the system. Many numerical and analytical studies have been performed over transmission towers by means of finite element analysis. On the other hand, experimental approaches to study such phenomena are less prevalent. In addition, whereas transmission lines coupling has been punctually investigated using numerical procedures, experimental wired set-ups have been rarely evaluated.

The following exposition attempts to expose the works in structural performance evaluation of transmission towers. Structural health monitoring paradigm is rare to encounter in latticed tower evaluation so the range of this exposition is widened more generally to the dynamic and static assessment of these kind of structures.

Some numerical works on tower structures coupled with transmission lines have been carried out. Existing investigations will be presented in five conceptuals blocks: numerical investigation concerning general static or dynamic structural performance, investigation including the aerolastic coupling with transmission lines, works dealing with the dynamic response to seismic events, investigation on the effect of cable ruptures in the transient response of the structure and research on the effects of ice accretion on the cables due to severe weather conditions.

Albermani et al. [96] proposed a non-linear technique for simulating the ultimate structural load of latticed transmission towers. A design-case and several reinforcements over existing towers were studied. The failure mechanism of known failed towers was

successfully reproduced. Eslamlou and Asgarian [97] also investigate the structural sensitivity of a power transmission tower in front of various loads. A nonlinear dynamic analysis of the tower is performed considering the buckling of compressed members and the plasticity effects n materials. A progressive collapse analysis is performed. A capacity-to-demand ratio is calculated for different failure scenarios and structural progressive damage sequences adn compared to a proposed Relative impact factor for each member damaged in the structure. The authors conclude that this impact factor correlates with the capacity-to-demand ratio in 41 % of the cases.

Yasui et al. [98] described a method for analysing wind-induced vibrations of latticed towers coupled with power lines. Buffeting was studied on suspension and tension towers showing that boundary conditions in transmission lines had great influence on the response characteristics. In a similar way, Battista et al. [99] proposed an analytical-numerical model of transmission line towers under wind actions to reproduce the mechanism of collapse of a typical power transmission tower. A simplified two DoF analytical model was proposed as a useful tool for evaluating the fundamental frequency of the system in early design stages. Computational simulations were also carried out by Fei et al. [100] where the natural frequencies of a tower without transmission cables, its ultimate non-linear buckling wind load and the evolution of the natural frequencies of the tower versus different wind loads were calculated. Conclusions showed a decrease of the natural frequencies as the wind load increased towards its ultimate value. Authors claimed that frequency decrease as a structural instability indicator. Working in the aerolastic coupling as well, Takeuchi et al. [101] studied the influence of the aerodynamic loads on the damping ratio of different modes of vibration of a power transmission tower for different wind speeds. Single degree-of-freedom damping estimation methods were found to be insufficient to this aim. The damping ratio for each aerodynamically excited mode was determined.

Staying in the aerolastics field, Pengyun et al. [102] described a method for evaluation on dynamic characteristics of power transmission towers coupled with power lines under wind load. Energy evaluation criteria was effectively utilized in the examination on structural dynamic performance. Qin et al. [103] researched the the effects of conductor wires on transmission tower under wind load. The vibration equations of transmission towers-line system under wind load were deduced and several configurations were studied using such derived equations of motion. These configurations included an isolated tower, a tower coupled with transmission lines, three coupled towers and five coupled towers. In each case, the displacements of the middle tower were studied. Mara and Hong [104] investigated the inelastic response of a self-supported lattice transmission tower under different wind events, including traditional atmospheric boundary layer

wind (ABL) and downburst wind, and for wind loading at different directions relative to the tower. The nonlinear static pushover (NSP) analysis was used to obtain the capacity curve of the tower, defined by the force and deformation relationship, at each considered wind direction. Results showed that the yield and maximum capacities vary with wind direction. Moreover, the results indicated that the capacity for ABL and rectangular (uniform) winds could provide an approximate envelope for the capacity estimated for different sizes of downburst events.

Structural performance in front of earthquake events has also attracted research efforts. Li et al. [105] proposed a simplified model to study the dynamic behaviour of power transmission latticed towers coupled with its carrier lines. In-plane and out-of-plane vibrations caused by seismic excitation were studied by solving the equations of motion of the coupled system. The model was validated using experimental results captured in shake table tests. This correlation served to propose a simplified calculus method for the design of power transmission towers under earthquake loading. Wu et al. [106] investigated the seismic response of Large Crossing Transmission Tower-line System (LCTL) to near-fault ground motions using equivalent pulse solicitations. Results showed that equivalent impulsive near-fault ground motions imposed a larger seismic response to LCTL compared to far-field ground motions.

Kaminski et al. [107] study and predict the dynamic response of latticed steel towers subjected to cable rupture. The predictions of various models are compared with the aim of quantifying mechanical model uncertainty. The authors state that there exists an underlying problem of evaluating the uncertainty in response predictions, once all parameters that define the external actions and the system itself have been unequivocally prescribed. Conclusively the authors outline some strategies to model uncertainty and reliability assessment.

Yang et al. [108] studied the effect of unbalanced tension caused by the accretion of ice rods over the transmission lines, broken wires, ice shedding and galloping over Ultra High Voltage (UHV - 1000kV) power transmission towers. FEM was used and compared with the constant conductor length method. The calculated values of the unbalanced tension were compared with those of applicable regulations and some suggestions on the design criteria for unbalanced tension values were proposed.

Regarding experimental works, studies have been focused on both static and dynamic structural tests. Moon et al. [109] performed a half-scaled substructure test on a 154 kV transmission tower to evaluate its failure mode subjected to wind loads. The design loads on leg members resulted to be between an 80 and 90 percent of the allowable actual buckling loads.

Yin, Lam et al. [110] [111] reported and validated a tailored method for electrical transmission towers which used ambient vibration data from a limited number of sensors in the structural damage detection applied to this kind of structures. By means of Damage detection was successfully simulated and experimentally accomplished using modal identification and sub-structuring.

In 2008, an ice disaster in South China caused the collapse of thousands of power towers. Xie et al. [112] conducted an experimental study on subassemblages of typical failed 500 kV electrical transmission towers in order to study the failure mechanisms on them under extreme load of freezing rain conditions. The study concluded that buckling on the main legs members was the main failure mechanism and that the addition of sufficient diaphragms reinforcement substructures significantly increased the load capacity of the structure.

Other attempts to use vibration data in the detection of damage in transmission towers have replaced the utilization of Frequency Response Functions calculated via the Fast Fourier Transform (FFT) by the use of other signal processing methods such as the Hilbert-Huang Transform (HHT). Cheng-Zhong et al. [113] proposed a method that used empirical mode decomposition based on the HHT to quantitatively analyse the response function of various intrinsic modes. Damage detection was achieved by comparing those responses between damaged and reference pristine states.

In this research damage detection through changes in the dynamic properties is based on the acquisition (or generation) of vibration responses to known excitations. The basic assumption is that structures reveal a change in its frequency, modal and geometrical domain parameters, that is, in its frequency, modal deformation vectors, and mass, stiffness and damping values under the presence of damage. Many theoretical analysis and studies along with modal testing have confirmed this relationship and detected the presence of cracks, changes in geometry and other types of macroscopic damages. Nevertheless, at the same time these methods result non effective for the detection of microscopic damages.

3. Formulation

This chapter serves as an exposition on the methodologies involved in the generation of the indicators analysed in this investigation. Frequency response functions are obtained both from experimental modal analysis and from synthesis using numeric modal results. Spectral indices are obtained from correlation between a reference condition and altered states.

3.1 Mechanical vibrations

The problem of determining the vibration response of a complex system given certain excitation commonly arises in many fields of engineering and applied sciences. It is a conventional practise to express excitation forces on a structure in terms of its spectral decomposition using Fourier or Laplace analysis. This domain remapping allows to have an in-depth knowledge on the amount of force which is mobilized at each frequency in the spectral domain of interest. The problem of determining the response of a system in front of certain dynamic excitations with a certain spectral signatures is usually referred as response analysis (RA).

Vibration in structural systems is the result of the interaction between elastic, inertial and dissipative characteristics of the materials integrating the structure studied. Those three contributions are commonly referred as stiffness, mass and damping properties. Stiffness is usually modelled using a variety of constitutive equations describing the relationship between deformations and forces needed to generate them. Mass properties and inertia moments and products are obtained from volumetric, surface and even linear densities that describe mass distribution in the object. Damping properties include the dissipative effects on the structure which cause mechanical energy losses and movement attenuation. Multiple physical phenomena affect the damping characteristics of structures and materials. Such phenomenology is of a complex nature and is still matter of present investigation. However, this contribution is usually neglected

in front of stiffness and mass contribution as it is significantly smaller in front of them. Damping sources will be carefully discussed in section 3.2.5.3.

In structural dynamics, the mass and stiffness properties are key ingredients to formulate mathematical relations between mechanical inputs and outputs in the system. These relationships aim to describe the displacement of the structure along the time $\boldsymbol{x}(t)$ given an input force exciting it $\boldsymbol{f}(t)$. This descriptive model can be formulated from dynamic balance considerations in an euclidean vectorial space using Newton's Second Law of motion or from energy conservation principles applying Lagrangian Mechanics. The mathematical description of the system is referred as 'model' and is the central aspect in mechanical vibration analysis.

An exact analysis of structures involves the generation and solution of a system of partial differential equations as a function of space and time coordinates. For elemental structures, such as bars, plates or shells with simple geometries and boundary conditions, closed forms of such differential equations exist. For real structures, the problem becomes intractable. If closed analytically exact solutions can not be found, there exists the possibility of using assumed functions satisfying the boundary conditions (i.e. harmonic functions) to approximate the solution as a summation series. Although this procedure was convention up to 1950s, the introduction of finite element methods (FEM) in late 1950s and 1960s caused this assumed functions solution methodology to become obsolete. Maturity of FEM software caused that these approaches become the convention tool to solve vibration problems. FEM models differ in the number of degrees of freedom (DoFs) used to describe systems. Real structures are usually continuous and of complex geometry, so there is need for discretization techniques. Formulation in this work assumes that the FEM representation of the mechanical systems described is know, so the continuous domain formulation of the vibration problem is skipped. The reader is routed to comprehensive introductory text books on vibration theory by Harris [68] and De Silva [114] for further and in depth discussion of vibratory phenomena in such continuous systems.

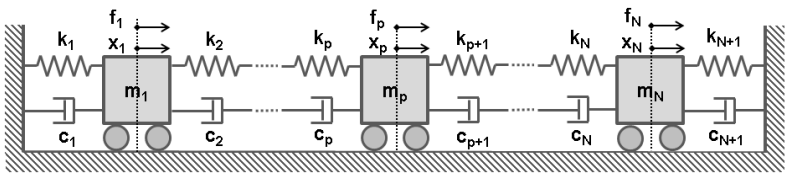

Figure 3.1: Discrete N-dimensional vibration problem

Problems in engineering involving the computation of dynamic responses are extremely difficult to solve using analytical methods. A preliminary approach to the solution can be made by substituting the structure by an equivalent system of rigid body with

lumped representations of springs, mass and dampers (figure 3.1). This simplification, however, allows only to gain insight for few modes of the structure.

Alternatively, the vibration problem of continuous systems can be solved using approximate numerical techniques such as FEM. Structural dynamics equations of a mechanical system are usually expressed as a geometrical-domain discretization of the model expressed in matrix form. In FEM, the physical domain is divided in small regions called elements. The response of each element can be analysed individually accounting for the mass, stiffness and dissipation contributions and the influence of the elements around it. Elements are interconnected in nodes to surrounding neighbours. The set of nodes interconnecting elements is known as mesh. The accuracy of the solution is determined by the size and amount of elements included in the modelization of the problem.

Given an idealised representation of a system in N DoFs corresponding to the defining nodes of elements forming the whole physical domain, the most general form of Newton's second law can be written in terms of inertial forces contribution $\boldsymbol{i}(t)$, internal material resisting forces (elastic forces) $\boldsymbol{r}(t)$ and external dissipative contributions $\boldsymbol{d}(t)$. These contributions must satisfy the equilibrium condition with external forces applied on the system $\boldsymbol{f}(t)$:

$$\boldsymbol{i}(t) + \boldsymbol{r}(\boldsymbol{x}(t), \dot{\boldsymbol{x}}(t)) + \boldsymbol{d}(t) = \boldsymbol{f}(t) \tag{3.1}$$

In this formulation, all magnitudes are 1D vectors corresponding to the discrete degrees of freedom in the model and do not assume any kind of constitutive equation for its components. As the main objective of the model is to relate the cinematic responses of the system $\boldsymbol{x}(t)$, $\dot{\boldsymbol{x}}(t)$ and $\ddot{\boldsymbol{x}}(t)$ with the dynamic excitations $\boldsymbol{f}(t)$ on the system, it becomes necessary to express inertial, elastic and dissipative terms as a function of nodal displacements, velocities and accelerations. Inertial forces are simply expressed using the time derivatives of both the linear momentum of the system and the angular momentum of the system. The simplest and most common approach to the problem is adopted in terms of mass times acceleration. The resisting forces are governed by the constitutive model adopted for the material. If the material is assumed to present a linear elastic behaviour coupled with velocity dependant hysteretic characteristics, the expression rests as:

$$\boldsymbol{M}\ddot{\boldsymbol{x}}(t) + \boldsymbol{K}\boldsymbol{x}(t) + \boldsymbol{K}'\dot{\boldsymbol{x}}(t) + \boldsymbol{d}(t) = \boldsymbol{f}(t) \tag{3.2}$$

If the external damping $\boldsymbol{d}(t)$ is also considered to be linear dependant to the velocity,

that is, to assume a viscous-like model, this external damping contribution together with the histeretic energy loss in the material can be grouped in a single term. So then, the expression can be simplified to the well-known structural dynamics simplified equation.

$$\boldsymbol{M}\ddot{\boldsymbol{x}}(t) + \boldsymbol{C}\dot{\boldsymbol{x}}(t) + \boldsymbol{K}\boldsymbol{x}(t) = \boldsymbol{f}(t) \tag{3.3}$$

Where $\boldsymbol{M}$ is the equivalent inertial components of the system (masses and inertias), $\boldsymbol{C}$ is the velocity-dependant energy dissipation term known as damping, $\boldsymbol{K}$ represents the elastic stiffness of the structural system, $\boldsymbol{x}(t)$ are the nodal displacements and $\boldsymbol{f}(t)$ is the vector containing the assembled equivalent external nodal forces. As the dynamic problem can also be interpreted as a mechanical energy conservation balance, the general governing equation can be obtained using Lagrangian mechanics. Then, $\boldsymbol{K}\boldsymbol{x}(t)$ can be interpreted as the amount of elastic energy accumulated in the structure, $\boldsymbol{C}\dot{\boldsymbol{x}}(t)$ as the quantity of energy dissipated per time unit and $\boldsymbol{M}\ddot{\boldsymbol{x}}(t)$ as the amount of linear and angular momentum present in the system. This matrix representation of the system can be understood as a global assembled system of equations each of them governing the behaviour of a single element in relation with its neighbours.

Equation 3.3 denotes a system of N linear ordinary differential equation with constant coefficients expressed in vectorial form. These dynamic equilibrium equations are valid for a condition around the static response of the structure at rest $\boldsymbol{x}(t = 0)$. The solution of the homogeneous differential equation describes the steady-state harmonic response of the system. The forced response of the system can be solved by assuming solutions in the form of $\boldsymbol{x}(t) = \boldsymbol{x}e^{j\omega t}$ and expressing external excitation forces $\boldsymbol{f}(\omega)$ as Fourier series in the form $\boldsymbol{f}(t) = \boldsymbol{f}e^{i\omega t}$. This harmonic assumption in the solution space is equivalent to express the structural dynamics equation in the Fourier spectral domain. This proceeding allows to linearise the derivatives of the differential system of equations, so the expression rests as:

$$\left(-\omega^2\boldsymbol{M} + j\omega\boldsymbol{C} + \boldsymbol{K}\right)\boldsymbol{x}(\omega) = \boldsymbol{f}(\omega) \tag{3.4}$$

So then, as both the exciting force $\boldsymbol{f}(\omega)$ and the response vector $\boldsymbol{x}(\omega)$ have been remapped to the Fourier domain, it is possible to express the structural dynamics equation as a summation of each of the spectral components of the exciting force as:

$$\sum_{\omega_1}^{\Omega}\left(-\omega^2\boldsymbol{M} + j\omega\boldsymbol{C} + \boldsymbol{K}\right)\boldsymbol{x}_\omega\, e^{j\omega t} = \sum_{\omega_1}^{\Omega}\boldsymbol{f}_\omega\, e^{j\omega t} \tag{3.5}$$

Where $\boldsymbol{x}_\omega$ and $\boldsymbol{f}_\omega$ refer to the value of the force and response vectors at certain spectral position in the Fourier domain.

So finally, the response vector can be obtained as:

$$\boldsymbol{x}(\omega) = \left(-\omega^2 \boldsymbol{M} + j\omega \boldsymbol{C} + \boldsymbol{K}\right)^{-1} \boldsymbol{f}(\omega) \tag{3.6}$$

Which can be also expressed as a summation of Fourier spectral terms:

$$\sum_{\omega_1}^{\Omega} \boldsymbol{x}_\omega \, e^{j\omega t} = \sum_{\omega_1}^{\Omega} \left(-\omega^2 \boldsymbol{M} + j\omega \boldsymbol{C} + \boldsymbol{K}\right)^{-1} \boldsymbol{f}_\omega \, e^{j\omega t} \tag{3.7}$$

The inverse matrix of inertial, damping and stiffness terms is usually referred as the transfer matrix of the system, the frequency response function matrix of the system, or the compliance matrix, and it is commonly denoted as $\boldsymbol{H}(\omega)$:

$$\boldsymbol{H}(\omega) = \boldsymbol{X}(\omega)\boldsymbol{F}^{-1}(\omega) = \left(-\omega^2 \boldsymbol{M} + j\omega \boldsymbol{C} + \boldsymbol{K}\right)^{-1} \tag{3.8}$$

Alternative expressions exist for the Compliance matrix, namely the Mobility matrix $\dot{\boldsymbol{H}}(\omega)$ when relating nodal velocities with excitation forces and the Inertance matrix $\ddot{\boldsymbol{H}}(\omega)$ when relating nodal accelerations with excitation forces. In addition, it is possible to express the same quantities in its inverse form as the Dynamic Stiffness matrix $\boldsymbol{H}^{-1}(\omega)$, the Mechanical Impedance matrix $\dot{\boldsymbol{H}}^{-1}(\omega)$ and the Apparent Mass matrix $\ddot{\boldsymbol{H}}^{-1}(\omega)$. Their formulation rest as:

$$\dot{\boldsymbol{H}}(\omega) = j\omega \boldsymbol{H}(\omega) \tag{3.9a}$$

$$\ddot{\boldsymbol{H}}(\omega) = -\omega^2 \boldsymbol{H}(\omega) \tag{3.9b}$$

Direct representations of the transfer matrix (compliance, mobility and inertance) are usually indistinctly referred in literature as frequency response functions (FRFs). The use of this nomenclature does not allow to indentify which cinematic variable is being used to describe the system. To keep things as clear as possible, in this work the term FRFs is only used to refer inertance $\ddot{\boldsymbol{H}}(\omega)$ matrices.

Forced response analysis of mechanical systems is for most of the cases, computationally expensive when performed in the form of equation 3.3. The structural dynamics community has developed multiple numerical schemes to solve the equations of motion. This approach is known as general transient analysis (GTA) and can be approached using multiple schemes. An infinitude of works dealing with the solution of vibration

on a system using the full form of the dynamic equations have been presented along the years.

A second, and somewhat lighter approach to forced vibration problem is the solution of the dynamic equation in its Fourier form as shown in equation 3.4. This is commonly known as harmonic response analysis (HRA). Solution of the problem involves the calculation of the dynamic stiffness matrix $\boldsymbol{H}^{-1}(\omega)$ at each frequency point of interest in the domain (which requires the inversion of the compliance $\boldsymbol{H}(\omega)$ matrix determined from mass, stiffness and damping matrices), the Fourier decomposition of the excitation force and a matrix inner product for each frequency line to determine the spectral response in the nodes of interest. This procedure is commonly computationally expensive due to the inversion of the compliance matrix.

The complexity of GTA and HRA can, however, be overcome by analysing the system using the modal analysis paradigm. This approach is commonly known as modal response analysis (MRA). The basic idea behind this approximation is that the transient response of a system can be described in terms of a linear combination of simpler solutions. This base space of simpler solution is conformed by the modal parameters of the system: modal frequencies, modal dampings and modal vectors. By reducing the dynamic matrices to its modal decoupled equivalent form, and by expressing the external excitations on a system in terms of a summation of harmonic contributions (Fourier decomposition), the transient analysis of structures becomes computationally much lighter than GTA or HRA.

This work focused on spectral response analysis of systems using inertance frequency response functions. GTA and HRA are put aside this discussion for concision. The reader is referred to references [115] for a comprehensive review of GTA methods in structural dynamics, and [68] for a discussion on modal decomposition methods for dynamic analysis of systems.

3.2 Structural assessment using spectral correlation

The central topic of this investigation is the identification of structural modifications using condensed indicators directly derived from frequency response functions. FRF mobility functions are directly related to the dynamic stiffness measured between some excitation and receiving points thought the inverse of these functions. So then, if all available FRF data is condensed in a single index, it is possible to identify the changes in the global mobility (or dynamic stiffness) of the studied structure.

This idea can be further developed thinking in terms of mass, stiffness and damping

properties of the structure. Any modification in the restoring forces, energy dissipation or inertial characteristics of the structure results in a modification in the characteristic FRFs of the system, and therefore, in the condensed parameter representing the whole set of FRF functions. The question then can be formulated as which is the best way to condensate FRFs in order that a univoque relationship is obtained in front of equivalent structural changes.

This section presents the mathematical formulation of a vibration-based spectral-domain structural assessment indicator based on condensation through correlation of frequency response functions defining a system, between its pristine condition and its current status. The proposed indicator uses all information available in the Fourier domain to generate an index capable of discerning damages from reinforcements, with quantifying potentiality ranging from a 0 (no alteration) to 1 (maximum alteration) and with enhanced sensibility and stability characteristics in front of sampling parameters.

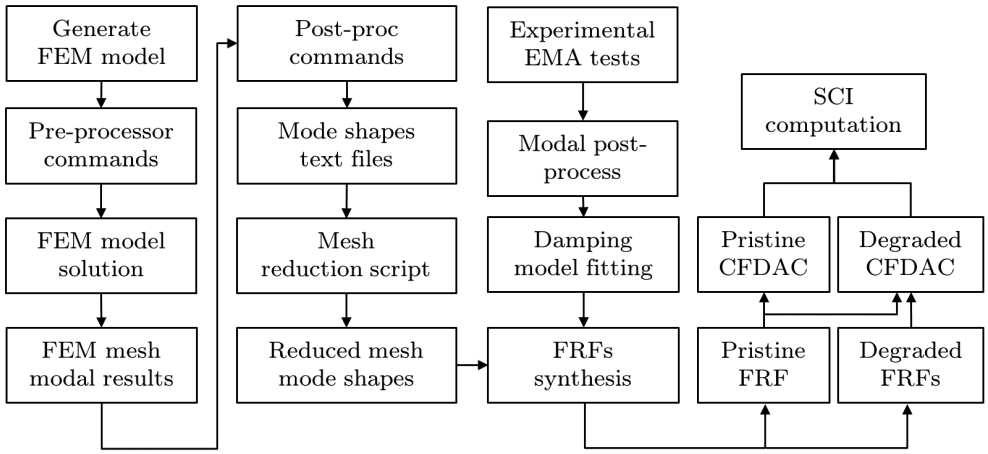

Figure 3.2: Flowchart used to generate SCI indicator

Inspired in the FDAC indicator [6], this research uses a slight modification in the formulation of this matrix indicator that extends the result to the complex domain using non-conjugated FRFs in its formulation. Extension of the FDAC to the complex FDAC (CFDAC) enhances the sensibility of alteration detection while keeping desirable stability properties, as it is later discussed. Linear correlation of two CFDACs, one corresponding to pristine-to-pristine conditions, and the second one corresponding to pristine-to-altered states, calculated for the real parts, for the imaginary parts, and for the magnitudes of the two complex matrices allows to generate three condensed indicators referred as spectral correlation indexes (SCIs).

The use of CFDAC matrix as an indicator of the current state of a structure allows to

have a two-dimensional spectral map of the relationships between frequency response functions of a system. In contrast, other spectral indicators such as the RVAC [3] only permit to have insight in the loss of correlation between sets of FRFs at each spectral line. This way, the direction of the shift in FRFs can be traced as the two-dimensional spectral clearly indicates spectral correspondences of operational deflection shapes even if frequency shift occurs.

3.2.1 CFDAC

The complex FDAC (CFDAC) is computed for pristine-to-pristine and pristine-to-altered combinations and is defined for each pair of frequency lines in the spectra ω_g and ω_g over a set of N_p measured frequency response functions as follows:

$$CFDAC_{fg}^{p,p} = \frac{\left(\sum_{i=1}^{N_p} \sum_{j=1}^{N_p} h_{ij}^{(p)}(\omega_f) h_{ij}^{(p)}(\omega_g) \right)^2}{\left(\sum_{i=1}^{N_p} \sum_{j=1}^{N_p} h_{ij}^{(p)}(\omega_f) h_{ij}^{(p)}(\omega_f) \right) \left(\sum_{i=1}^{N_p} \sum_{j=1}^{N_p} h_{ij}^{(p)}(\omega_g) h_{ij}^{(p)}(\omega_g) \right)} \tag{3.10}$$

$$CFDAC_{fg}^{p,a} = \frac{\left(\sum_{i=1}^{N_p} \sum_{j=1}^{N_p} h_{ij}^{(p)}(\omega_f) h_{ij}^{(a)}(\omega_g) \right)^2}{\left(\sum_{i=1}^{N_p} \sum_{j=1}^{N_p} h_{ij}^{(p)}(\omega_f) h_{ij}^{(p)}(\omega_f) \right) \left(\sum_{i=1}^{N_p} \sum_{j=1}^{N_p} h_{ij}^{(a)}(\omega_g) h_{ij}^{(a)}(\omega_g) \right)} \tag{3.11}$$

Indices i and j correspond to the exciting and receiving locations for each FRF, h_{ij}^{p} refer to pristine state FRFs, h_{ij}^{a} refer to altered FRFs, f and g are the indices referring to each pair of spectral lines compared from the two sets of mobility functions and N_p is the number of sampled points in the specimen. For mathematical consistency it is essential that all the FRFs h_{ij} involved in the computation of the CFDAC have the same amount of lines and resolution, namely $N_f = N_g$. CFDAC results in a complex two-dimensional array of dimension $N_f \times N_f$. CFDAC indicator is defined as a inner product of two $N_p \times N_f$ matrices so its algorithmic implementation has a large impact in the required computational time.

Some basic treats of the CFDAC are herein exposed concerning its significance, basic structure and general behaviour when structural alteration appears. CFDAC is a complex valued, two-dimensional indicator of the covariance between two sets of FRFs compared for each pair of spectral-lines. Resulting values are confined in the $[-1, 1], [-i, i]$ region of the complex plane. The qualitative discussion on the significance of this values is done in terms of absolute value of the real and imaginary part

of the indicators. Negative valued elements arise from the fact that FRFs are complex in nature and imaginary products and imaginary to real crossproducts can potentially land in those negative quadrants of the domain.

Real part of the CFDAC is the joint contribution of the products of the real parts and the imaginary parts of the FRFs involved in the computation. In the other hand, imaginary part of the CFDAC results of the product of imaginary to real parts of the FRFs. So then, representation of the real part of the CFDAC shows correlation of the resonant peaks and its adjacent frequencies (the imaginary peaks in the FRFs contribute the the correlation at the central frequency of the peaks, the real part correlation contribute to the correlation at lateral frequencies of each lobe as real part is strictly null at resonant frequency). Complementary, the imaginary part of the CFDAC is the result of the product of real parts to imaginary parts. This results in a mostly empty matrix with correlation twin lobes around central natural frequencies and with a null correlation zones coincident to each peak frequency - due to the fact that real part of the FRFs are zero at resonances-. Magnitude of the CFDAC is the combined modulus of these two contributions. The general form of a pristine to pristine CFDAC is shown in Figure 3.3.

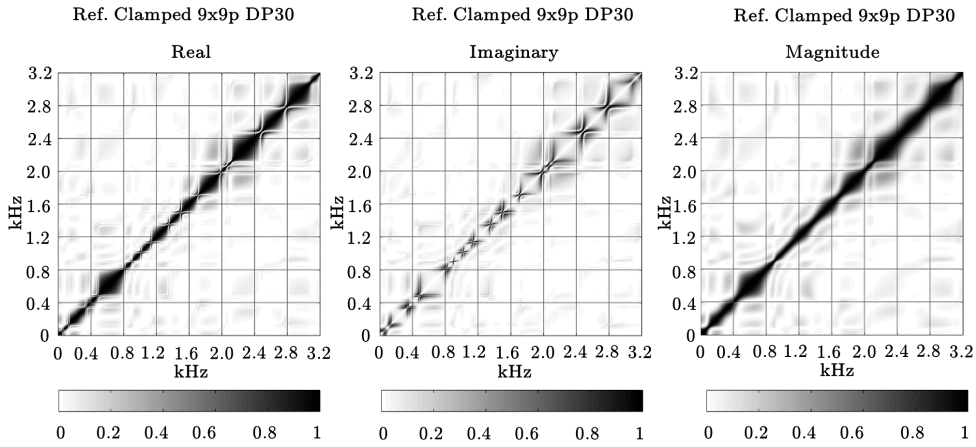

Figure 3.3: Pristine to pristine CFDAC

Auto-CFDACs (which compare one set of FRFs with itself) always show a perfect diagonal unitary structure, as shown in Figure 3.3. When a set of pristine FRFs and another set of altered FRFs are condensed to a CFDAC, degradation appears in the diagonal signature of the matrix indicator so the symmetric diagonal pattern diffuses. Figure 3.4 shows the real part of CFDACs calculated between pristine and altered states. The shift appearing in the CFDAC indicator (either real part, imaginary part and magnitude) depends on the typology of alteration present in the structure. When global damage is present in the structure (for example artificiality reducing the

elasticity modulus of materials to simulate ageing), the shift introduced in the CFDAC indicator shows a global decreasing tendency, shown in the left image of figure 3.4 as a lowering in the main CFDAC diagonal. This phenomena is due to the fact that modal shape correlation is maintained for all equivalent mode shapes but natural frequencies suffer a decrease, thus shifting the correlation downwards in the spectral domain. On the other hand, when local modifications are introduced in the system (for example adding a stringer or introducing a crack) the distortion in the CFDAC is observed to be non-linear, showing different amount of shift in different regions in the spectral domain.

These general observations lead to the proposal of two hypothesis:

- The global shift in the CFDAC diagonal signature is a measure of the change in the global stiffness of the structure.
- The pattern of the shift in the CFDAC diagonal signature is characteristic of the typology of damage present in the structure.

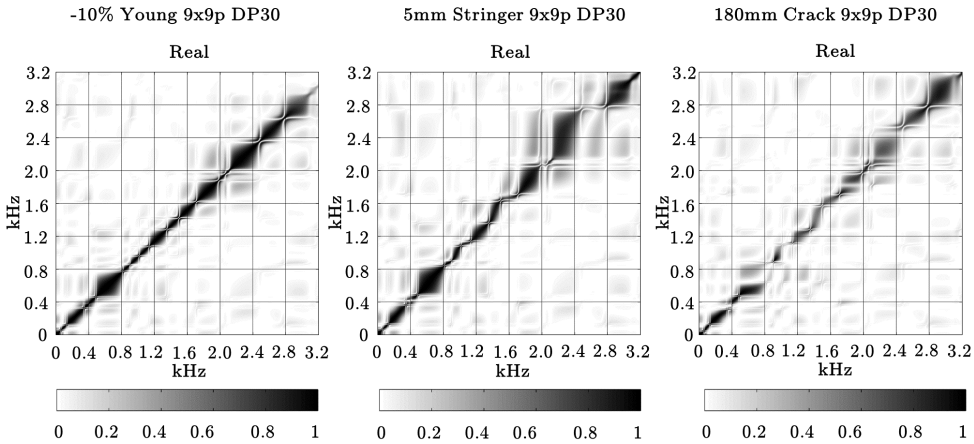

Figure 3.4: Real part of CFDAC. Left: pristine - pristine. Center: pristine - linear damage. Right: pristine - non-linear damage

As this research is the first step into the subject, the demonstration of the first hypothesis is chosen to be the core of this investigation. Future works could address the matter of damage classification based on the pattern observed in the CFDAC shift. A derived issue from this first hypothesis arises then concerning how the global shift in the CFDAC matrix can be quantified.

3.2.2 Structural similarity quantification

The approach adopted in this research is rooted in cognitive arguments. The problem of recognizing when structural alteration is present in the system is translated to a problem of determining how different or similar are two CFDACs, one corresponding to the auto CFDAC between the reference state with itself, and the second CFDAC corresponding to the comparison between an altered state with and the reference condition. The second CFDAC shows some shift if alteration is present in the structure. The identification of this shift is faced reproducing cognitive processes on human perception from an image recognition and comparison standpoint. Assessment on the dissimilarity of CFDACs is used using a quantitative values based on a image-structure modification indicator generated from the two matrix indicators (reference-to-reference and altered-to-reference).

Perception and comparison is a recurrent topic in image processing research. The methodology adopted is inspired by the work of Wang et al. [116], which serves as a basis to understand the principles involved in image recognition and contrast. The mentioned research paper is based around the concept of Structural Similarity. In the context of image processing, structural similarity has nothing to do with mechanical arguments. The term structural is used as a concept referred to the basic form, shape, color distribution and in general, distinctive characteristics which make an image different of another one. Structural similarity is what makes two pictures depicting the same scene but with different contrasts, luminosities, saturations or even color filters, identifiable as the same picture although the pixel-by-pixel information is not the same.

Authors review the conventional image comparison methodology, which is based in the computation of the mean square error (MSE) of two images pixel by pixel. Authors identify a series of limitations in this approach, and by detecting some cognitive patterns in human perception propose a new approach. This new philosophy is based in the fact that natural images present a very structured distribution of pixel information. Citing the authors:

> [...] pixels exhibit strong dependencies, especially when they are spatially close, and these dependencies carry important information about the structure of the objects in the visual scene. [...].

With this in mind, the work suggest to use a structural similarity index (SSIM) to assess if two images represent the same scene. The index is a linear combination involving the luminosity of the two images (the mean value of the pixels), the contrast of the two images (the Standard Deviation of pixel values in the two images) and

the structural similarity of the two images (defined from covariances and correlation of pixel values of the two images). Authors demonstrate that this approach is much more robust that common MSE error computation between two images.

With this developments in mind, a similar approach is adopted to compare two CFDAC matrices. However in the current case of study, luminosity of the two images is expected to be very similar (although not exactly equal), as the mean value in the whole CFDACs matrices is almost the same and very close to zero. Change in STD of CFDACs have been observed to be derisory so a dereferenced damage indicator between the two signals is proposed. The Pearson correlation coefficient (PCC), which is the normalized form of the covariance, is adopted in this investigation, so the statistical index obtained is bounded in the $[-1...1]$ domain.

PCC results in a real number, with values in the range $[-1...1]$ with 1 corresponding to a perfect direct correlation, 0 indicating total lack of correlation and -1 indicating and inverse or indirect correlation between the sets of data compared. Image structural characteristics of the two images are always kept. The diagonal structure of the CFDACs always arises (in a more or less degraded form). That means that this diagonal structure will allways appear from small values of frequency to big values of frequency in a direct correlation. Negative correlation will never appear in these kind of post process as this would signify an inversion of the main diagonal structure in the CFDAC representation. Image Structural Similarity arguments allow to reduce the domain which the PCC of two CFDACs is expected to occupy. This argument further bounds the PCC in the $[0...1]$ range. In each case of structural alteration, two evaluations of the CFDAC are required to generate each PCC indicator.

$PCC^{\mathbb{R}e}_{p,a}$ is the correlation between real parts of reference-to-reference and a reference-to-altered CFDACs (p and a indicate the stages compared). Similarly, $PCC^{\mathbb{I}m}_{p,a}$ is the PCC of the imaginary parts and $PCC^{|\mathbb{C}|}_{p,a}$ corresponds to the correlation of the absolute values of CFDACs compared. If reference-to-reference CFDAC is denoted $CFDAC^{p,p}$ and reference-to-altered CFDAC is denoted $CFDAC^{p,a}$ each Pearson correlation coefficient for each of the parts is computed using equations 3.12 to 3.16 as:

$$\begin{aligned} \mathcal{A}^{\mathbb{R}e} &= \mathbb{R}\mathrm{e}(CFDAC^{p,p}) \\ \mathcal{A}^{\mathbb{I}m} &= \mathbb{I}\mathrm{m}(CFDAC^{p,p}) \\ \mathcal{A}^{|\mathbb{C}|} &= |(CFDAC^{p,p})| \end{aligned} \tag{3.12}$$

$$\begin{aligned}\mathcal{B}^{\mathbb{R}\mathrm{e}} &= \mathbb{R}\mathrm{e}(CFDAC^{p,a}) \\ \mathcal{B}^{\mathbb{I}\mathrm{m}} &= \mathbb{I}\mathrm{m}(CFDAC^{p,a}) \\ \mathcal{B}^{|\mathbb{C}|} &= |(CFDAC^{p,a})|\end{aligned} \tag{3.13}$$

$$PCC_{\mathcal{A},\mathcal{B}} = \frac{\sum_{f=1}^{N_f}\sum_{g=1}^{N_g}\mathcal{A}_{fg}\mathcal{B}_{fg} - N_f N_g \bar{\mathcal{A}}\bar{\mathcal{B}}}{(N_f N_g - 1)\sigma_{\mathcal{A}}\sigma_{\mathcal{B}}} \tag{3.14}$$

$$\bar{\mathcal{A}} = \frac{1}{N_f N_g}\sum_{f=1}^{N_f}\sum_{g=1}^{N_g} A_{fg} \tag{3.15}$$

$$\sigma_{\mathcal{A}} = \sqrt{\frac{1}{N_f N_g - 1}\sum_{f=1}^{N_f}\sum_{g=1}^{N_g}(\mathcal{A}_{fg} - \bar{\mathcal{A}})^2} \tag{3.16}$$

Perfect correlation of two CFDAC results in unitary values of PCCs. Therefore if a value very close to one is obtained between pristine-to-pristine CFDAC and a pristine-to-degraded CFDAC that implies that degraded state is very close to the intact conditions. For convenience a value of 0 is assigned when the structure is not altered and values near 1 indicate whenever the correlation is completely lost.

3.2.3 Sign-decision algorithm

The correlation coefficient by itself presents an important drawback. This coefficient is not capable of discerning if the loss of correlation is due to an increase of the stiffness in the system or a reduction of it. Although most SHM systems are aimed to detect degradation, this work tries to include positive shifts in the study of cases. To do so, it is important to have a preliminary insight in the behaviour of the CFDAC in front of over-stiffening and under-stiffening. This behaviour is shown Figure 3.5.

CFDAC diagonal signature tends to shift towards smaller values of frequency when damage is present in the system. On the contrary a positive shift is observed when there is an increase in the stiffness of the system. This work takes advantage of this behaviour to assign a proper sign to the proposed indices. These indicators are intended to be negative-valued if damage is present in the system and positive-valued if reinforcement is introduced in the system. So then, indicators are ranged between $[-1...1]$ with a value of -1 corresponding to a complete lack of correlation due to degradation (negative shift) and a value of 1 corresponding to a complete lack of correlation due to over-stiffening of the system.

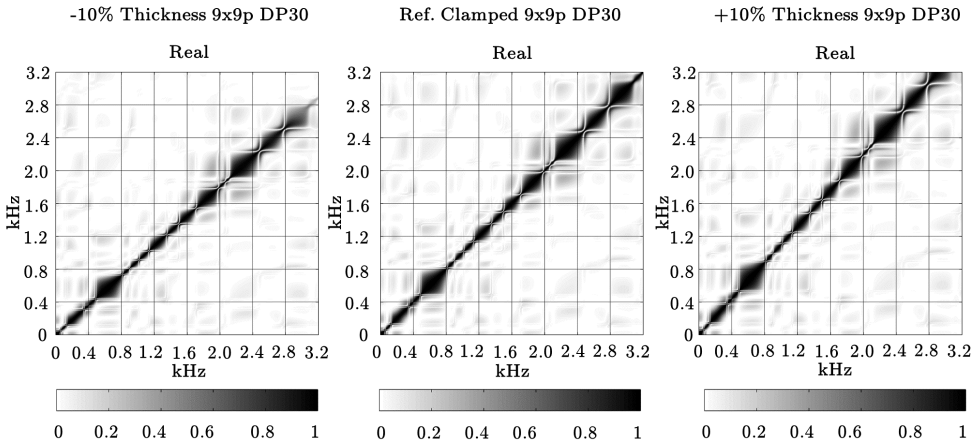

Figure 3.5: Real part of CFDAC behaviour in front of under-stiffening (left) and over-stiffening (right).

This alteration direction sign is assigned taking into account that when shift is present in the CFDAC, the mean values of the two sub-triangular (upper and lower) matrices of the CFDAC lose the symmetry. Figure 3.6 shows the equivalence between the matrix formulation of CFDACs and its pictographic representation to facilitate the comprehension of the upper and lower diagonal matrix concepts. If the CFDAC shifts positively, the mean of the lower triangular matrix increases and the mean of the upper triangular matrix decreases. This fact is used to define the sign of the indicator κ as shown in equations 3.17 3.18 and 3.19 with $\hat{B}$ and $\check{B}$ being respectively the mean of the absolute value of the upper and lower triangular matrices of the pristine-to-altered CFDAC part (each of them ignores the main diagonal of the component of the CFDAC matrix). This two values are computed for each of the three parts of the CFDAC: real and imaginary parts and magnitude of the variable.

$$\hat{\mathcal{B}} = \frac{1}{N_f N_g} \sum_{f=1}^{N_f} \sum_{g=1}^{N_g} B_{fg} \quad \text{for} \quad f < g \tag{3.17}$$

$$\check{\mathcal{B}} = \frac{1}{N_f N_g} \sum_{f=1}^{N_f} \sum_{g=1}^{N_g} B_{fg} \quad \text{for} \quad f > g \tag{3.18}$$

$$\kappa = \begin{cases} 1 & \text{if } \hat{\mathcal{B}} < \check{\mathcal{B}} \\ -1 & \text{if } \hat{\mathcal{B}} > \check{\mathcal{B}} \end{cases} \tag{3.19}$$

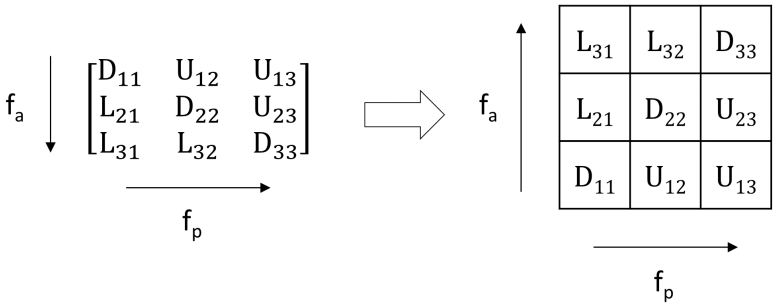

Figure 3.6: Triangular sub-matrices and its graphic representation

3.2.4 Spectral correlation index (SCI)

Once the statistical correlation between pristine-to-pristine and pristine-to-altered CFDACs is calculated using the Pearson correlation coefficient, the spectral correlation indices (SCIs) are computed. Although based on the PCC, some transformations are applied to ease up the interpretation of the indicators. As already mentioned, PCC range from -1 to 1, with the former indicating a perfect inverse correlation, the later indicating direct correlation and 0 being a total lack of correlation between compared series. PCC applied to CFDACs are usually bounded between 0 and 1. Additionally, and to ensure that the final indicator is always bounded in the same interval, the PCC is absolute-valued and re-referenced to the 1 to 0 domain, with 0 indicating a perfect correlation and 1 indicating a total lack of correlation. The final transformation consist of the application of appropriate estimated sign from equation 3.19. The formulation of SCIs rests as:

$$\begin{aligned} SCI^{\mathbb{R}\mathrm{e}} &= \kappa^{\mathbb{R}\mathrm{e}} \left(1 - \left|PCC_{p,a}^{\mathbb{R}\mathrm{e}}\right|\right) \\ SCI^{\mathbb{I}\mathrm{m}} &= \kappa^{\mathbb{I}\mathrm{m}} \left(1 - \left|PCC_{p,a}^{\mathbb{I}\mathrm{m}}\right|\right) \\ SCI^{|\mathbb{C}|} &= \kappa^{|\mathbb{C}|} \left(1 - \left|PCC_{p,a}^{|\mathbb{C}|}\right|\right) \end{aligned} \tag{3.20}$$

3.2.5 Frequency response functions

Frequency response functions representing the inertance matrix of a system $\ddot{\boldsymbol{H}}(\omega)$ can be experimentally determined using experimental modal analysis (EMA) or generated from (numeric) modal results using re-synthesis techniques. This section discusses the experimental and numerical methodologies used to obtain such transfer functions.

3.2.5.1 FRF acquisition using EMA

Most indicators presented in first pages of section 2.2.2 are based to more or less extent in vibration data captured through experimental modal analysis. This technique uses Fourier transformed captured data from accelerometers and load cells (usually piezoelectric). In the technique, the structure is excited with a white-noise-like uniform force spectra. The final target of EMA is to experimentally extract the modal model of a structure. To do so, it is enough to experimentally determine only a small subset of the full inertance matrix. Usually modal testing is performed in terms of force and acceleration measurements.

Peter Avitabile provides an excellent conceptual and formal introduction to EMA in his 2001 paper [117] and in his series of divulgative articles "Modal Analysis - Back to Basics" published in the magazine "Experimental Techniques" between 1999 and 2003 [118–125].

Each term in the inertance matrix relates response displacements to external excitations and can be conceptually interpreted as shown in equation 3.21. However, experimental determination of inertance functions require some additional signal processing approaches as this form of the inertance formulation is prone to introduce noise and additional artefacts in the results.

$$h_{ij}(\omega) = \ddot{x}_i(\omega) f_j(\omega)^{-1} \tag{3.21}$$

In the expression of inertance, $x_i(\omega)$ and $f_j(\omega)$ are the Fourier transforms of acceleration response and force input, respectively, ω is the frequency variable, $h_{ij}(\omega)$ is the inertance FRF function corresponding to excitation at DoF j measured in the i position. To completely determine the modal model of a system, it is not necessary to capture all terms in the inertance matrix $\ddot{\boldsymbol{H}}(\omega)$. This is explained by the fact that each transfer function between two DoFs is calculated from pairs of modal vector coordinates. So then, each column, or each row of the inertance matrix contains enough information to fully determine the transfer model of the mechanical system.

Inertance FRFs are not directly calculated from the Fourier transforms of input force and output acceleration but from cross-Spectral densities (CSD) and power spectral densities (PSD) of signals [68]. $CSD_{x_i,f_j}(\omega)$ is formulated from the Fourier transforms of cross-correlation between excitation and responses whereas $PSD_{x_i,x_i}(\omega)$ is computed from the raw response signal:

$$CSD_{x_i,f_j}(\omega) = \int_{-\infty}^{\infty} \left(\int_{-\infty}^{\infty} \ddot{x}_i^*(t) f_j(t+\tau) d\tau \right) e^{-2\pi i t\omega} dt \tag{3.22}$$

$$PSD_{x_i,x_i}(\omega) = \left| \int_{-\infty}^{infty} \ddot{x}_i(t) e^{-2\pi i t\omega} dt \right|^2 \tag{3.23}$$

Where $x_i(t)$ is the time-domain nodal response in i and $f_j(t)$ is the force series applied at node j. CSD operator allows to assure that responses are directly correlated to the actions that cause them. For example, random vibration harmonics that are not directly correlated with an spectral harmonic in the excitation action are not accounted for. Each component of the inertance FRFs can be approximated using the $h1$ operator:

$$h_{ij}(\omega) \simeq h1_{ij} = \frac{CSD_{x_i,f_j}(\omega)}{PSD_{x_i,x_i}(\omega)} \tag{3.24}$$

3.2.5.2 FRF synthesis from modal models

This section discusses the procedure used to synthesize FRFs from modal models. Experimentally determined modal models usually include natural frequencies, dampings and mode shapes. However, numerically determined modal models do not include damping in most of the cases.

Modal results are usually expressed under the UMM paradigm. Modal vectors are adimensionalized in order to get a unitary and diagonal modal mass matrix. Numeric simulations in this research determine the UMM scaling from arbitrarily scaled mode shapes by computing the total elastic energy of each mode shape, by deriving the modal stiffness per mode from this elastic energy and by calculating associated modal mass to every mode. This approach allows to be in control of the modal scaling in all stages of the simulation and further manipulation.

A first set of points $\boldsymbol{P} = (\boldsymbol{x}, \boldsymbol{y}, \boldsymbol{z})$ is defined as the coordinates which define the elements discretized in the numerical FEM model of the structure to be simulated. On the other hand, a second and smaller set of points $\boldsymbol{P'} = (\boldsymbol{x'}, \boldsymbol{y'}, \boldsymbol{z'})$ is defined as the locations in which FRFs are resynthesised. This second coarser subset tries to reproduce an experimental acquisition mesh that would be used in an EMA test

The set of modal vectors got from FEM is defined for $\boldsymbol{P}$ in all the spatial directions, namely $\boldsymbol{\Phi}_k = (\boldsymbol{\phi}_x, \boldsymbol{\phi}_y, \boldsymbol{\phi}_z)_k$ for each of mode k. Modal vectors are only necessary in the locations of interest where the FRFs are synthesised and only in certain directions (in a plate-like structure, for example, only fot the transverse direction, $\boldsymbol{\phi} = \boldsymbol{\phi}_z$).

So then, a reduction procedure is required to map synthesis locations to numerical nodes in the FEM mesh. A simple minimum distance location routine is implemented to do so. If sampling locations do not coincide with numerical nodes of the FEM mesh, an interpolation routine is required. In this investigation, however, all synthesis locations are exactly coincident with locations in the FEM mesh. Reduced modal vectors required to perform FRF synthesis are stacked in a reduced modal matrix as $\boldsymbol{\Phi} = \{\boldsymbol{\phi}_{z,1} ... \boldsymbol{\phi}_{z,k} ... \boldsymbol{\phi}_{z,M}\}$

Formulation for FRFs re-synthesis between a point i acting as an exciting location and point j acting as the response location is commonly expressed as

$$h_{ij}(\omega) = \sum_{k=1}^{M} \frac{r_{ijk}}{j\omega - \lambda_k} + \frac{r_{ijk}^*}{j\omega - \lambda_k^*} \tag{3.25a}$$

$$r_{ijk} = \frac{\phi_{ik}\phi_{jk}}{2j\omega_k m_k} \tag{3.25b}$$

With M the total number of modes, k the mode indexer, m_k the modal mass associated to each mode (if the modal vectors are expressed in its UMM form, $m_k = 1$), λ_k each complex eigenvalue corresponding to each natural frequency, ϕ_{ik} the modal vector component correspondent to excitation location i and mode k, idem for ϕ_{jk} with the j response location, and ω the independent variable of the function. The numerators of the synthesis equation are directly the residual modal vectors ψ_{ijk} (RMV).

In this investigation numerical simulations in Ansys use the APDL scripting language to export full mesh numeric modal vectors and mesh coordinates to text files. Mapping algorithms are implemented in Matlab.

3.2.5.3 Damping modelling

Although damping is usually neglected in front of other terms when performing numerical modal analyses, it is of vital importance to properly generate a representative dynamic model of the mechanical system under in-service loads. Knowledge of the sources of damping is also very useful if design modifications are to be introduced to improve structural behaviour once set in service.

Damping causes mechanical energy dissipation usually in form of internal thermal energy and is one of the most complex phenomena to describe in the field of vibrations. A thorough discussion on damping can be found in the book by Silva [114] where the author presents an entire chapter dedicated to the topic.

Several types of damping are inherently present in mechanical systems although external damping devices can also be dynamically coupled to the structure. Four mech-

anisms of damping are important in the study of mechanical vibrations:

1. **Internal damping** of structures results from mechanical energy dissipation within the material due to grain or crystal dislocations or sliding, relocation of defects in the microstructure, thermoelastic effects caused by internal temperature gradients, eddy current effects due to electromagnetic interference, polymeric macromolecule chain motions in plastics or fluency effects. Effects related with the microstructure of the material can be modelled using visco-plastic hysteretic constitutive equations.

2. **Dissipation at interfaces and joints** may arise from the rubbing friction interaction due to the relative movement between structural components, from the intermittent contact at the joints in the mechanical system or from local deformations in the joints. This relative interaction can also appear in composite materials as friction caused by relative movement between laminae in a composite lay-up with internal delaminations or defects. Energy dissipation caused by relative rubbing can be described using the Couloumb friction model.

3. **Fluid-structure interaction** couples mechanic vibrations with transient harmonic oscillations in the fluid flow. Transverse drag on the object moving though the flow field is usually the biggest source of fluid-generated damping. These forces arise both from pressure gradients and from shear stresses in the fluid-object interface.

4. **External damping devices** are accounted using its equivalent damping coefficient. This value is obtained from manufacturer or through experimental characterization.

Damping is usually treated using an equivalent simplified model as it is not practical to incorporate detailed microscopic representations it. In structural dynamics, it is common practise to assume a proportional damping model in the modal analysis of vibratory systems as shown in 3.26.

$$[C] = \alpha[M] + \beta[K] \tag{3.26}$$

The first term in the equation is referred as inertial damping matrix and it is proportional to the momentum in each equivalent lumped mass, whereas the second term is the stiffness damping matrix, proportional to the rate of change resisting forces on structural nodes. This damping matrix is introduced to the structural dynamics equation as a viscous linear term proportional to the velocity of the nodes of the structure. This simplified proportional damping model has the only benefit of becoming diagonal when expressed in the modal domain using the modal matrix of the system so it is

possible to incorporate decoupled damping terms for each modal coordinate individually. However, the model has been heavily criticized for not being representative of the physical phenomena undergoing energy dissipation. In this investigation, proportional damping is assumed due to the fact that by doing so, damping can be introduced in the modal coordinate in a decoupled form. Proportional damping models the damping coefficient at each natural mode of the structure as:

$$\xi_k = \frac{\alpha}{2\omega_k} + \frac{\beta\omega_k}{2} \tag{3.27}$$

This investigation uses modal results from numeric models to synthesise inertance FRFs. However, modal results from FEM do not incorporate dissipation characteristics of the system. However, as the light damping hypothesis is embraced, damping can be introduced *a-posteriori* either as a fixed percentage of the natural frequency at each resonance or adjusting a linear damping model to experimentally determined damping values. Experimental damping coefficient is fit through a least-squares error minimization procedure to equation 3.27. In a damped system, eigenvalues become then complex-valued and are approximated as:

$$\lambda_k = 2\xi_k\omega_k + j\omega_k^2 \tag{3.28}$$

Experimentation on specimens usually results in an estimated ξ_k for each mode of vibration. In order to reconstruct the proportional model coefficients α and β of the system, a least-squares optimization of these coefficients is used in this investigation to fit a proportional damping function to experimental data.

4. Numerical approach

This chapter presents a numeric parametric study on the behaviour of the SCI indicators in front of certain damage scenarios and FRF synthesis parameters. Vibration data utilized in this section is generated from FEM models. Initial stages in this chapter deal with the validation of FRFs synthesised from numerical FEM models. An extensive parametric study is then performed to characterize the behaviour of the indicator in front of the acquisition and sampling parameters. The chapter progresses by relating the structural alteration indexes with the alteration typology and residual stiffness in the structure. Structural deviation indexes from literature are finally compared with the newly proposed indicators.

4.1 Aluminium plate

4.1.1 FRF synthesis verification

4.1.1.1 Reference state characterization

The first task to be addressed is the validation of the methodology used to synthesize FRFs from numerical modal models calculated through FEM. To do so, it is necessary to establish a set of experimental acquisitions that are used as a reference to be compared with synthetic results. The experimental tests are also used to fit a damping model that is later used in the FRFs synthesis from numeric results.

Reference tests are executed on two specimens of an square aluminium plate. Nominal dimensions for both plates are $300 \times 300 \times 5$ mm. Aluminium used is a T5083 alloy with an approximate Young modulus of 69.0 GPa. Table 4.1 summarizes the main characteristics of the two specimens.

id	width (mm)	height (mm)	thickness (mm)	mass (g)
PAL1	300.0	300.0	5.0	1199.1
PAL2	300.0	300.0	5.0	1202.6

Table 4.1: Experimental specimens

Accuracy of the FRFs synthesis algorithm has to be demonstrated if reasonable conclusions are wanted to be extracted from this numeric investigation. The FRF synthesis validation for the aluminium plate is done comparing synthetic FRFs to free and clamped boundary conditions with 4 experimental modal analysis acquisitions equivalent to the numeric cases. These experimental boundary condition configurations are exposed in figure 4.1.

Reference EMA tests are performed on the two aforementioned specimens. Four different EMA test are executed, two corresponding to quasi-free boundary conditions and two more corresponding to quasi-clamped boundary conditions. Clamped EMA tests give an insight on the influence of flexible clamping boundary conditions on the results, so the same specimen is used in both tests. PAL2 specimen is arbitrarily selected to do so.

It is commonly known that ideal boundary conditions are not possible to be reproduced in laboratory conditions -pure free boundary conditions can only be achieved in microgravity whereas infinitely rigid clamping supports do not exist by definition, as boundary elements have certain associated stiffness-. Common practice to simulate free boundary conditions include the execution of EMA tests with a hanged specimen using connecting elements with a stiffness much lower than the first modes of interest in the studied component. That way, low frequency vibration harmonics derived from the linking element can be easily decoupled from structural dynamics of the specimen whereas link-structure interference upper harmonics are effectively minimized.

A slightly different approach has been adopted to reproduce free boundary conditions. Sound absorbing sponge is used as a supporting element for the specimens. This kind of foam presents a spike-valley characteristic pattern which causes that contacts between the aluminium plate and the foam are reduced to a limited number of sponge peaks. As the foam is several orders of magnitude less stiff than the aluminium, vibratory behaviour of the plate is very similar to the one numerically observed for perfectly free boundary conditions. Results agree closely with numeric modal analysis once the low frequency resonance caused by the foam support is ignored.

Boundary Condition	Specimen	Tag
Free	PAL1	PAL1 Free
Free	PAL2	PAL2 Free
Clamped	PAL2	PAL2 Clamp1
Clamped	PAL2	PAL2 Clamp2

Table 4.2: EMA tests on aluminium plate specimens

On the other hand, clamped boundary conditions are reproduced with two auxiliary steel plates imprisoning the edge of the aluminium plate and keeping it in place using two steel cramps. Both configurations are shown in figure 4.1. A summary of the tests executed is depicted in table 4.2.

Vibration acquisition hardware is by the manufacturer Bruel & Kjaær. Equipment available include a DAQ Type 3050-B-060 connected via an ethernet link to a 32-bit architecture Windows XP Laptop Computer running Pulse LabShop v13.1.0.246 acquisition software. A model 4518-003 accelerometer is used for all cases. Excitation is done with the aid of a 8206-003 impact hammer. All the connections to the sensors are done with low-noise double-screened coaxial 10-32 UNF to BNC cables. Post-process aimed to extract the complete modal model from the raw EMA captured data is made using the software by Vibrant Technologies MEScope v4.1.

All EMA tests are post-processed using MEscope modal extraction software in order to obtain the full modal model for each case. Additionally, a linear damping model (which formulation is exposed in section 3.2.5.3) is adjusted for each boundary condition. These experimental acquisitions are compared to a set of response functions that are generated from numerical simulations using the procedure described in section 3.2.5.2.

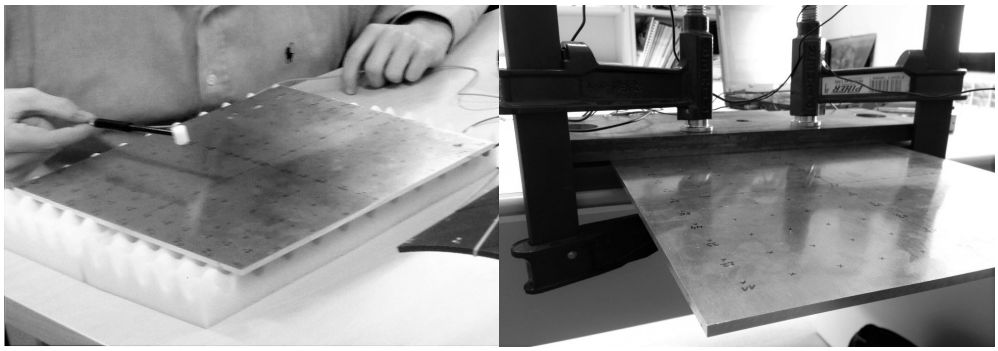

Figure 4.1: Left: Quasi-free boundary conditions equivalent. Right: Clamping boundary condition

The experimental acquisition mesh used in the EMA tests is common for all 4 cases. A mesh of 9×9 evenly distributed points is selected in order to have abundant geomet-

rically distributed modal data on the plate to capture higher mode shapes. The mesh is defined from the intersection of the two symmetry axes on the specimens so point 41 always is coincident with the ortocenter of the plates. All the tests are performed using the roaming excitation technique.

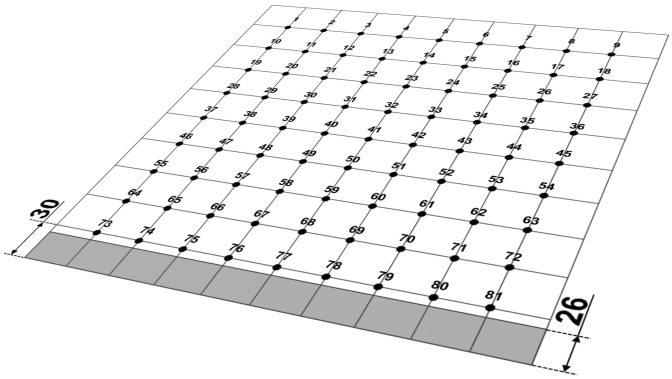

Figure 4.2: Experimental Modal Analysis acquisition mesh. Dimensions in mm

As the objective of this set of tests is not to extract an accurate modal model of the structure, but to generate a set of experimental FRFs to validate the synthesis procedure, the driving point location is not critical (on the contrary, a well refined EMA test aimed to extract modal shapes is highly dependant of the acquisition point selected). Point 1 is selected for the FRF validation tests. The mesh used for this test, as well as the location of the clamping in correspondent cases, are shown in figure 4.2.

Acquisition parameters are set to the following for all the EMA tests executed. 6400 acquisition lines are used, with a maximum frequency of interest of 3200 Hz. Frequency resolution resulting from this combination is 0.5 Hz. The FFT of the force signal sampled with the hammer is calculated using a rectangular window. Accelerometer signal is windowed using and exponential function.

Response functions captured using EMA are meant to be compared to the synthetic FRFs. For clarity, only FRFs corresponding to three acquisition points are shown in figures 4.4 and 4.5 for each EMA test. Figures show magnitudes in a logarithmic scale for convenience. Modal extraction is applied to the full set of FRFs in order to extract modal frequencies and dampings associated to each test. The objective of this experimental modal condensation is to extract the associated damping models. Resonances are identified using the CMIF function on the imaginary part of the FRFs. Residues are identified from the CoQuad expression of the FRFs. Results from modal condensation routines and mode shapes corresponding to those natural frequencies are shown in table 4.3 and figures 4.6 and 4.7 respectively.

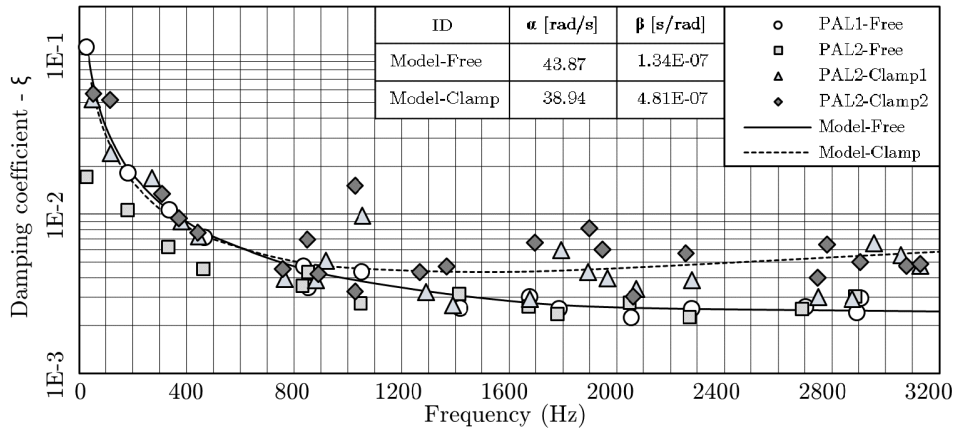

Figure 4.3: Experimental and adjusted damping vs. frequency

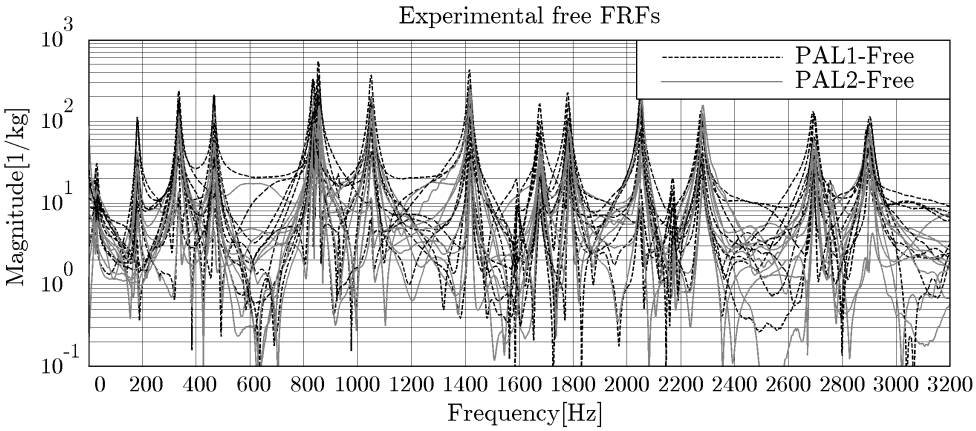

Figure 4.4: Experimental free boundary conditions FRFs

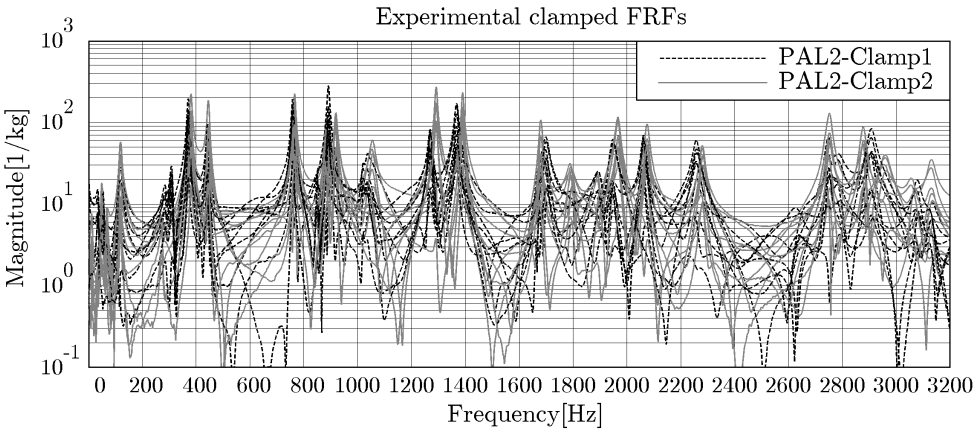

Figure 4.5: Experimental clamped boundary conditions FRFs

Although materials used and geometry of specimens are very similar for all the cases, boundary conditions play a key role in the equivalent damping properties of the mechanical system so it becomes necessary to set an appropriate damping fitting for each boundary condition. Figure 4.3 shows experimental results relating damping coefficients with associated natural frequencies for the four EMA tests corresponding to two different boundary conditions. Proportional damping models (equation 3.27) for both types of boundary conditions are fitted to experimental data using a least squares algorithm and are also depicted in the same figure.

PAL1-Free		PAL2-Free		PAL2-Clamp1		PAL2-Clamp2	
f [Hz]	ξ	f [Hz]	ξ	f [Hz]	ξ	f [Hz]	ξ
31.31	1.12E-01	28.76	1.11E-01	53.54	5.69E-02	49.23	5.23E-02
181.88	1.70E-02	181.93	1.81E-02	117.10	5.20E-02	119.03	2.41E-02
335.38	1.05E-02	335.95	1.06E-02	309.14	1.34E-02	271.99	1.68E-02
466.46	6.15E-03	467.34	7.12E-03	370.64	9.37E-03	380.66	8.96E-03
834.50	4.48E-03	836.73	4.68E-03	442.48	7.65E-03	445.47	7.26E-03
853.73	3.51E-03	855.65	3.44E-03	758.51	4.53E-03	765.72	3.93E-03
1049.37	4.28E-03	1051.74	4.32E-03	850.09	6.95E-03	881.74	3.86E-03
1414.98	2.72E-03	1418.00	2.56E-03	890.94	4.21E-03	918.28	5.07E-03
1674.81	3.12E-03	1678.75	3.02E-03	1026.94	3.26E-03	1055.15	9.71E-03
1780.51	2.61E-03	1785.52	2.54E-03	1269.35	4.34E-03	1291.17	3.23E-03
2049.67	2.33E-03	2054.87	2.23E-03	1366.89	4.68E-03	1389.50	2.69E-03
2274.77	2.76E-03	2280.48	2.54E-03	1695.88	6.62E-03	1678.97	2.94E-03
2693.31	2.24E-03	2704.43	2.62E-03	-	-	1792.71	5.94E-03
2889.45	2.52E-03	2895.77	2.41E-03	1898.63	8.17E-03	1894.13	4.32E-03
2902.66	3.00E-03	2909.46	2.96E-03	1947.25	5.97E-03	1966.74	3.93E-03
				2061.44	3.05E-03	2073.40	3.39E-03
				2257.48	5.65E-03	2279.84	3.85E-03
				2747.12	3.97E-03	2750.95	3.02E-03
				2781.46	6.43E-03	2876.56	2.93E-03
				2906.62	5.01E-03	2957.58	6.53E-03
				3078.11	4.72E-03	3058.77	5.51E-03
				3130.00	4.86E-03	3130.56	4.75E-03

Table 4.3: Natural frequencies and damping for each EMA test

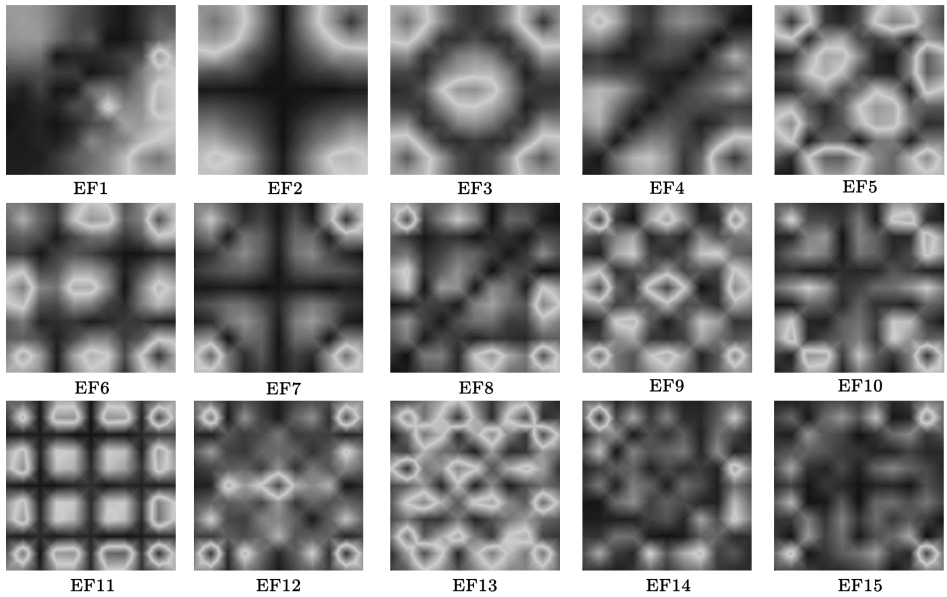

Figure 4.6: Modal shapes for experimental free test.

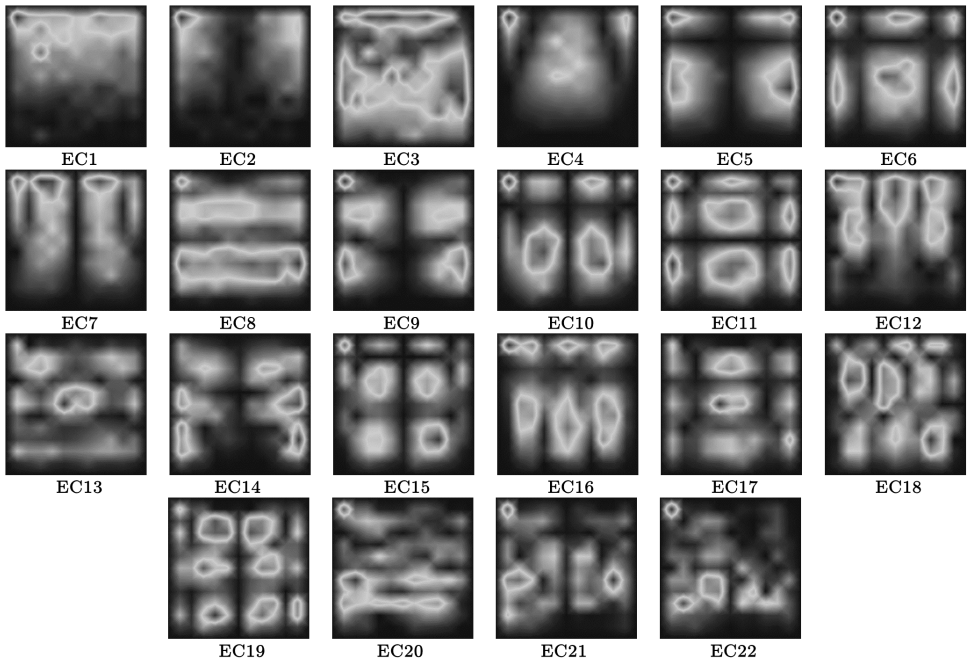

Figure 4.7: Modal shapes for experimental clamped test.

4.1.1.2 FEM modal analysis

Synthesis of the FRFs from numerical modal FEM results requires the generation and solution of an accurate modal model of the structural component studied. In order to reproduce experimental modal analysis results for the free and clamped boundary conditions, a model is generated in the commercial FEM software Ansys 14.5. The same reference geometry of $300.0 \times 300.0 \times 5.0$ mm used in the experimental reference tests is modelled in FEM. Geometry is modelled in two regions: the first one including the clamped surface of the plate and the other including the rest of the plate. This geometry definition allows to introduce both free and clamped boundary conditions by changing only few parameters in the model. The region subdivision of the geometry is shown in figure 4.2.

Material used in these simulation consist of an isotropic linear elastic material with young modulus E = 69 GPa, Poisson ratio $\nu = 0.29$ and a density of $\rho = 2655$ kg/m^3. The material is modelled without dissipative effects in order to improve computational speed of the solution. As the structure studied is lightly damped, damping can be introduced *a posteriori* in the FRFs synthesis.

The solver is configured to range from 0.1 Hz to 3200 Hz with a maximum of 50 modes to extract using a direct method. Using the APDL scripting language, the solver is required to extract modal masses and modal stiffnesses to be in control on the normalization of mode shapes. Modal stiffness is calculated from the total elastic energy mobilized by each mode shape. Modal frequency relates this quantity with the modal mass.

Geometry is the same free and clamped boundary conditions. However, whereas in the free case, the model has all the movements allowed, in the clamping simulation, the region shown in light grey in Figure 4.2 is restrained in all its linear displacements and rotations. One of the critical points of the FRFs synthesis is to sub-sample modal results from the full numerical mesh in a smaller subset of nodes defining to the sampling or experimental mesh. To do so, it is necessary that experimental points of interest are contained in the numerical mesh as well to avoid the need for interpolation procedures.

To ensure that the sampling mesh is coincident with some nodes in the numeric mesh, the simulated plate is discretized in $2 \times 2 \times 5$ mm elements using a perfectly structured mesh with regular Reissner-Mindlin plate elements (Element SHELL181 in Ansys, which include both bending and shear contributions to stiffness). This results in a mesh consisting of 22500 regular perfectly structured elements and 22801 nodes.

Free boundary conditons					Clamped boundary conditions				
FEM		EMA			FEM		EMA		
ID	f[Hz]	ID	f_1[Hz]	f_2[Hz]	ID	f[Hz]	ID	f_1[Hz]	f_2[Hz]
-	-	EF1	31.31	28.76	NC1	56.14	EC1	53.54	49.23
NF1	182.49	EF2	181.88	181.93	NC2	127.65	EC2	117.10	119.03
NF2	267.92	-	-	-	NC3	335.41	EC3	309.14	271.99
NF3	339.46	EF3	335.38	335.95	NC4	393.95	EC4	370.64	380.66
NF4	473.85	EF4	466.46	467.34	NC5	474.67	EC5	442.48	445.47
NF5	473.85	-	-	-	NC6	801.37	EC6	758.51	765.72
NF6	845.85	EF5	834.50	836.73	NC7	898.80	EC7	850.09	881.74
NF7	845.85	-	-	-	NC8	984.96	EC8	890.94	918.28
NF8	865.79	EF6	853.73	853.73	NC9	1106.78	EC9	1026.94	1055.15
NF9	941.96	-	-	-	NC10	1338.46	EC10	1269.35	1291.17
NF10	1064.64	EF7	1049.37	1051.74	NC11	1468.51	EC11	1366.89	1389.50
NF11	1434.48	EF8	1414.98	1418.00	NC12	1705.49	EC12	1695.88	1678.97
NF12	1434.48	-	-	-	NC13	1926.80	EC13	-	1792.71
NF13	1611.31	-	-	-	NC14	2020.30	EC14	1898.63	1894.13
NF14	1694.83	EF9	1674.81	1678.75	NC15	2069.57	EC15	1947.25	1966.74
NF15	1804.32	EF10	1780.51	1785.52	NC16	2122.76	EC16	2061.44	2073.40
NF16	1804.32	-	-	-	NC17	2424.02	EC17	2257.48	2279.84
NF17	2075.10	EF11	2049.67	2054.87	NC18	2772.81	EC18	2747.12	2750.95
NF18	2195.72	-	-	-	NC19	2856.14	EC19	2781.46	2876.56
NF19	2302.98	EF12	2274.77	2280.48	NC20	3030.16	EC20	2906.62	2957.58
NF20	2725.01	EF13	2693.31	2704.43	NC21	3163.97	EC21	3078.11	3058.77
NF21	2725.01	-	-	-	NC22	3172.71	EC22	3130.00	3130.56
NF22	2785.67	-	-	-	-	-	-	-	-
NF23	2923.51	EF14	2895.77	2889.45	-	-	-	-	-
NF24	2923.51	EF15	2902.66	2909.46	-	-	-	-	-
NF25	2938.55	-	-	-	-	-	-	-	-

Table 4.4: Natural frequencies numerics vs experimentals

Modal results for both free and clamped simulations are shown and compared to experimentally determined natural frequencies in table 4.4. Modal shapes corresponding to those natural frequencies are shown in figures 4.8 and 4.9. Some modal shapes in figure 4.8 appear shaded in lighter gray. Those correspond to mode shapes that are not visible in experimental modal analysis test due to the accelerometer being placed on a nodal line of that mode. Companion symmetric double modes are not explicitly shown but indicated with double tags under mode shapes representation in the figures. An experimental to numerical comparison of mode shapes for the free boundary conditions case is shown in figure 4.10 using the MAC matrix yielding very good agreement.

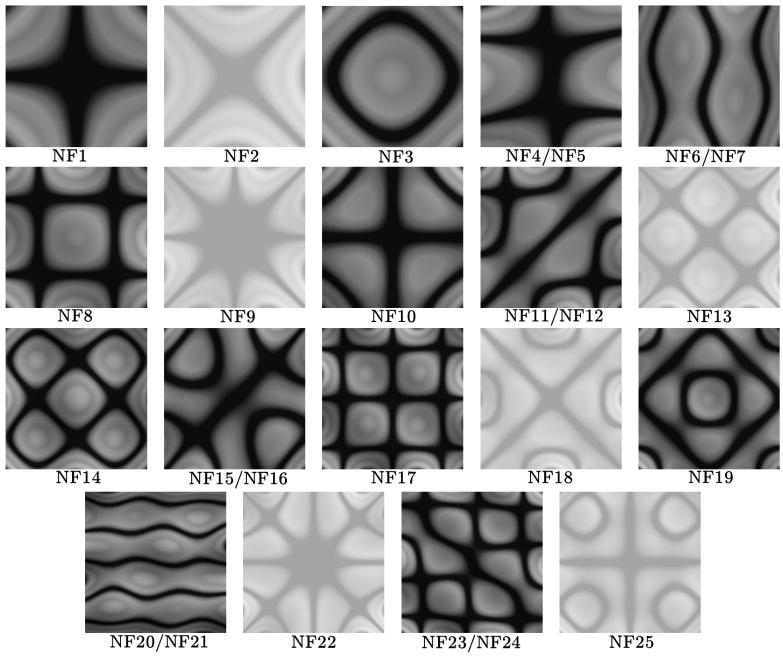

Figure 4.8: Modal shapes for FEM free test.

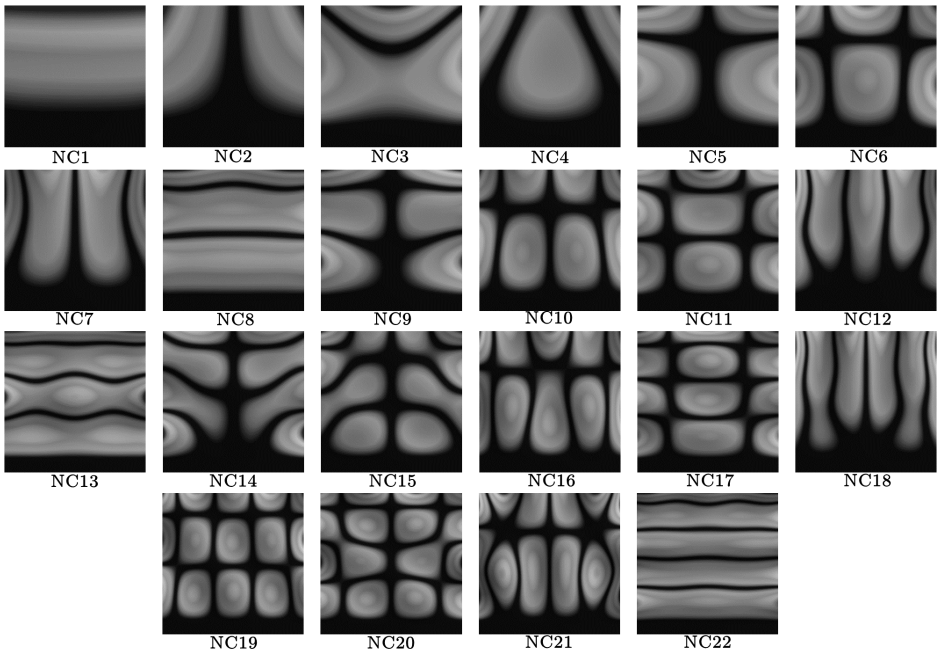

Figure 4.9: Modal shapes for FEM clamped test.

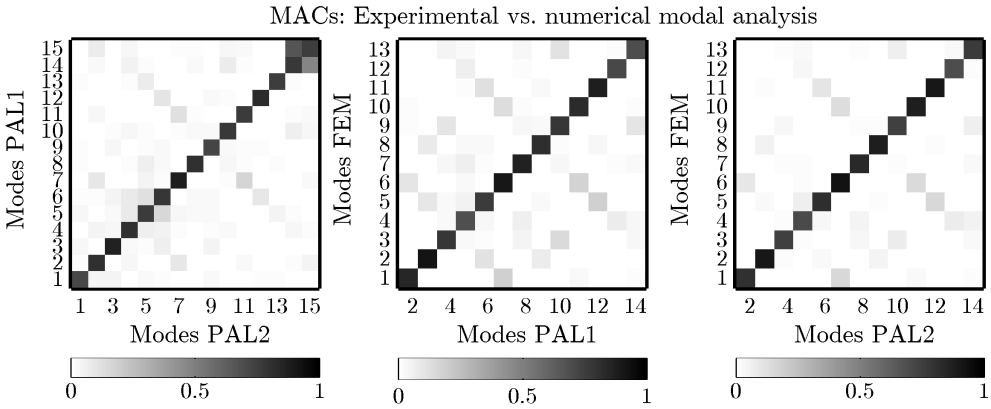

Figure 4.10: MAC comparing experimental with synthetic mode shapes for free boundary conditions

4.1.1.3 FRFs comparison

Synthetic FRFs are generated from numerical modal results using equation 3.25a. Functions are scripted in Matlab using the procedure exposed with detail in section 3.2.5.2. The main idea behind this is to reduce the modal results corresponding to the full numeric mesh to a mesh equivalent to the one used in experimental acquisition so a reduced set of modal vectors is obtained. That set of reduced modal vectors is used to compute residual operational deflection shapes which at the same time act as the governing terms of the polynomial expansion of the FRFs approximations.

For each of the cases, comparison between functions will be discussed from a qualitative point of view. Modal estimation techniques can incorporate little pole shifts in the resonant peaks of the FRFs. Simulated natural frequencies can be closely matched but not exactly overlapped to experimental results, usually due to mixed boundary conditions in the experiment. If quantitative comparison methods would be used such as a mean squared error comparison would be adopted, slight shifts in the poles of the FRFs would introduce large increments in those quantifiers.

Using the reduced modal results from the FEM modal simulations of the free and clamped aluminium plates, synthetic FRFs can be calculated. Synthesis is performed for driving point 1 and 81 roving points. Figures 4.11 and 4.12 show the comparison for the magnitude of synthetic free and clamped boundary conditions for roving points 9 to 79 in steps of 10.

Synthesis for free boundary conditions agrees almost identically with experimentally acquired FRFs functions. Small discrepancies can be observed in the magnitude of the resonances which are attributed to the small differences introduced by the fitted

damping model. Experimentally determined damping coefficients present small deviations from the central fitted damping model, so the amplitude of the resonant lobes varies. However, magnitude order is kept for all cases and the overall shape of the FRFs shows good agreement. Small shifts in peak frequencies are observed. Those are attributed to slight differences between the numerical model and the experimental specimen in geometric and material properties. Results are considered to present an almost perfect correlation with experimentally captured FRFs

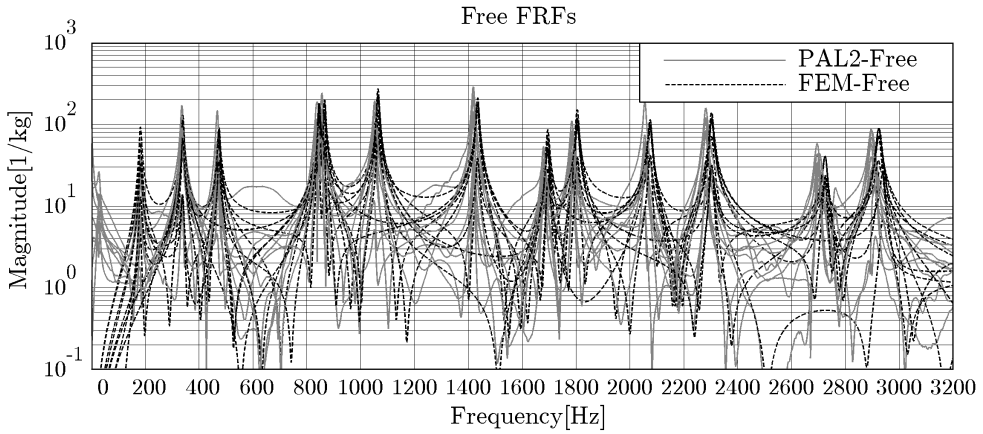

Figure 4.11: Experimental to numeric comparison of FRFs corresponding to free boundary condition

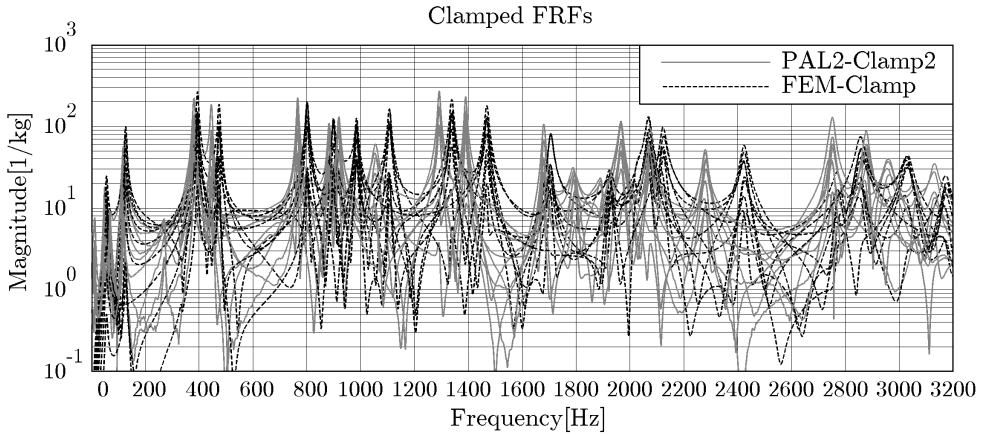

Figure 4.12: Experimental to numeric comparison of FRFs corresponding to clamped boundary condition

Synthesis for the clamped boundary condition presents a slightly more erratic correlation. FRFs present good agreement in the magnitude value of the peaks, corresponding to the relative influence of the driving and roving points contributions to the residual operational deflection shapes. However, peaks positions present an appreciable shift between the experimentally measured values and the FEM-synthesized functions. As

peak magnitudes are similar, this differences in the natural frequencies are attributed to the presence of a soft clamping boundary condition. That means that the real implemented clamping condition introduces additional stiffness in the boundary comparable in order of magnitude to the stiffness of the specimen, modifying then, the values of the natural frequencies. However, as already discussed, as magnitudes of the FRFs are similar between cases, synthesis procedure is also considered to be reliable for this case.

4.1.2 Numerical campaign

Characterization of the proposed spectral domain structural alteration indices involves a comprehensive parametric study and sensibility analysis in front of several acquisition (and generation) parameters concerning the FRFs. To try and generalize this parametric study, multiple structural modification scenarios are included in the analysis. These artificially introduced damages and reinforcements are utilized as a virtual testing campaign database that is later used to carry out a sensibility and characterization study on the indicators.

Reference pristine case is set as an ideal clamping scenario -equivalent to the already used in the FRFs validation stage of this work-. This clamped configuration is selected as it is the most simple boundary condition representative of a real operational condition of a structural component (free and simple supported boundary conditions are not suitable for load-bearing applications). Geometry, clamping and synthesis mesh definitions are the same as in FRF validation cases. Numerical models are meshed using a 2 mm characteristic length structured grid (already depicted in subsection 4.1.1.2). Materials are the same used before, except in degradation scenarios where it is explicitly referenced. The cases corresponding to structural modifications are shown in tables 4.5 and 4.6.

Structural modifications consist of seven families of cases, each representing certain damage typology. These families include global, local and boundary condition modifications. The first and second families introduce changes in the Young Modulus and in the thickness of the aluminium plate in a range between -10% and +10% of the nominal values. These cases are not realistic, but serve as tendency estimators.

	#	Familiy	Tag	Description	Value
-	00	Clamped	00Clamp	Baseline reference pristine state	-
Global modification	01	Young Modulus	01YM-10	10% Young modulus reduction	62.100 GPa
	02		02YM-5	5% Young modulus reduction	65.550 GPa
	03		03YM-2	2% Young modulus reduction	67.620 GPa
	04		04YM-1	1% Young modulus reduction	68.310 GPa
	05		05YM-0.5	0.5% Young modulus reduction	68.655 GPa
	06		06YM+0.5	0.5% Young modulus increase	69.345 GPa
	07		07YM+1	1% Young modulus increase	69.690 GPa
	08		08YM+2	2% Young modulus increase	70.380 GPa
	09		09YM+5	5% Young modulus increase	72.450 GPa
	10		10YM+10	10% Young modulus increase	75.900 GPa
	11	Thickness	11T-10	10% Thickness reduction	4.500 mm
	12		12T-5	5% Thickness reduction	4.750 mm
	13		13T-2	2% Thickness reduction	4.900 mm
	14		14T-1	1% Thickness reduction	4.950 mm
	15		15T-0.5	0.5% Thickness reductions	4.975 mm
	16		16T+0.5	0.5% Thickness increase	5.025 mm
	17		17T+1	1% Thickness increase	5.050 mm
	18		18T+2	2% Thickness increase	5.100 mm
	19		19T+5	5% Thickness increase	5.250 mm
	20		20T+10	10% Thickness increase	5.500 mm
	21	Edge pre-stress	21PS-99	Compression at 99% P_{crit}	-7330.5 N
	22		22PS-75	Compression at 75% P_{crit}	-5553.4 N
	23		23PS-50	Compression at 50% P_{crit}	-3702.3 N
	24		24PS-25	Compression at 25% P_{crit}	-1851.1 N
	25		25PS-10	Compression at 10% P_{crit}	-740.5 N
	26		26PS+10	Tension at 10% P_{crit}	740.5 N
	27		27PS+25	Tension at 25% P_{crit}	1851.1 N
	28		28PS+50	Tension at 50% P_{crit}	3702.3 N
	29		29PS+75	Tension at 75% P_{crit}	5553.4 N
	30		30PS+100	Tension at 100% P_{crit}	7404.5 N

Table 4.5: Cases analysed in the parametric study of the indicator

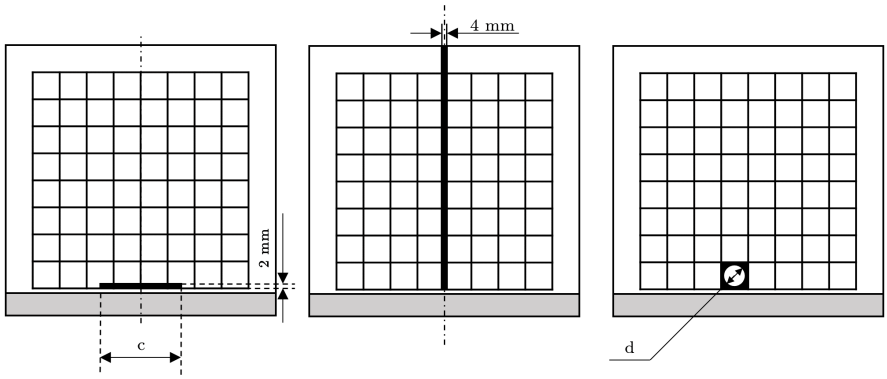

Figure 4.13: Structural modification scenarios.

	#	Familiy	Tag	Description	Associated value
Local modification	31	Crack analogy	31C4	4 x 2 x 0.5 mm slot	4mm wide
	32		32C8	8 x 2 x 0.5 mm slot	8mm wide
	33		33C12	12 x 2 x 0.5 mm slot	12mm wide
	34		34C16	16 x 2 x 0.5 mm slot	16mm wide
	35		35C20	20 x 2 x 0.5 mm slot	20mm wide
	36		36C40	40 x 2 x 0.5 mm slot	40mm wide
	37		37C60	60 x 2 x 0.5 mm slot	60mm wide
	38		38C100	100 x 2 x 0.5 mm slot	100mm wide
	39		39C140	140 x 2 x 0.5 mm slot	140mm wide
	40		40C180	180 x 2 x 0.5 mm slot	180mm wide
	41	Stringer	41S0.5	4 x 270 x 0.5 mm stringer	0.5 mm thick
	42		42S1.0	4 x 270 x 1.0 mm stringer	1.0 mm thick
	43		43S1.5	4 x 270 x 1.5 mm stringer	1.5 mm thick
	44		44S2.0	4 x 270 x 2.0 mm stringer	2.0 mm thick
	45		45S2.5	4 x 270 x 2.5 mm stringer	2.5 mm thick
	46		46S3.0	4 x 270 x 3.0 mm stringer	3.0 mm thick
	47		47S3.5	4 x 270 x 3.5 mm stringer	3.5 mm thick
	48		48S4.0	4 x 270 x 4.0 mm stringer	4.0 mm thick
	49		49S4.5	4 x 270 x 4.5 mm stringer	4.5 mm thick
	50		50S5.0	4 x 270 x 5.0 mm stringer	5.0 mm thick
	51	Holes	51HD1	Circular hole	1 mm diameter
	52		52HD2	Circular hole	2 mm diameter
	53		53HD5	Circular hole	5 mm diameter
	54		54HD10	Circular hole	10 mm diameter
	55		55HD15	Circular hole	15 mm diameter
	56		56HD20	Circular hole	20 mm diameter
	57		57HD25	Circular hole	25 mm diameter
	58		58HD27	Circular hole	27 mm diameter
	59		59HD29	Circular hole	29 mm diameter
	60		60HS30	Square hole	30 mm side
Boundary modification	61	Elastic support	61ES1.0E6	Elastic soft clamping	1.0E6 N/mm^3
	62		62ES2.5E5	Elastic soft clamping	2.5E5 N/mm^3
	63		63ES1.0E5	Elastic soft clamping	1.0E5 N/mm^3
	64		64ES1.0E4	Elastic soft clamping	1.0E4 N/mm^3
	65		65ES2.5E3	Elastic soft clamping	2.5E3 N/mm^3
	66		66ES1.0E3	Elastic soft clamping	1.0E3 N/mm^3
	67		67ES7.5E2	Elastic soft clamping	7.5E2 N/mm^3
	68		68ES5.0E2	Elastic soft clamping	5.0E2 N/mm^3
	69		69ES2.5E2	Elastic soft clamping	2.5E2 N/mm^3
	70		70ES1.0E2	Elastic soft clamping	1.0E2 N/mm^3

Table 4.6: Cases analysed in the parametric study of the indicator(continued)

The third family of global modification involves the application of certain pre-stressing loads on the structure before the execution of the modal simulations. Pre-stresses modify the equilibrium reference condition around which the vibration problem is solved and thus, modal parameters get affected. This fact can be easily identified when considering an example of a vibrating string. If the tension in a string is increased or decreased, its modal frequencies shift. This pre-stressing loads are incorporated to the model by solving a static problem with second-order displacement effects enabled for the same model later used in modal analysis. A constant line distributed load is applied at the farthest free edge of the plate (the one parallel to the clamping line) in the in-plane direction perpendicular to the clamping line. This load ranges from a tensile load of 100% of the compressive buckling load, to a compressive load of 99% of the compressive buckling load. The first buckling mode load is determined from the same numerical model by solving the equivalent bifurcation problem. A unitary load in the free edge is applied in the direction already mentioned and a linear buckling solution is found for the first buckling eigenvector of the structure. The compressive in-plane buckling load for this 1-edge clamping condition is determined to be $P_{crit} =$ 7404.5 N.

The first family of local distortions includes cracking analogy cases. To keep mesh requirements low, and ensure the same mesh quality for all cases, the cracks are modelled as 2 mm width slots so the numeric mesh do not present element distortions from the pristine one. The parameter governing the progression of the alteration is the length of the slot representing the crack. This slot is always symmetric from the symmetry line of the clamped system. As the characteristic length of elements is 2 mm, the minimum slot possible under this restrictions is a 2 mm width, 4 mm long, 2 mm depth slot. Slots progress up to 180 mm long (that is up to 60 mm from each lateral edge). The slot shares one of its long edges with the experimental mesh line defined by points 73-81. The slot is positioned inwards the plate, so its other long edge is located 2 mm towards the 64-72 point line.

The second family of local modifications includes the introduction of a stringer in the central symmetry line of the plate. Stringers are 4 mm wide, 2 mm at each side of the symmetry line and spanning from the 73-81 nodal line up the furthest edge to the clamping. Parameter governing the progression of alteration is the thickness of the stringer, composed of the same aluminium material than the rest of the plate.

The third family of local modifications includes the introduction of a circular hole in the plate. The parameter governing the progression of damage in this family is the diameter of the hole. The orifice is centred in the ortocenter of the element defined by experimental points 67, 68, 76 and 77. As the experimental typical element is of

30×30 mm, this is the upper limit case of the family, with the full square element removed.

The last family of damage is defined as a progression in the elasticity of the boundary condition, ranging from an ideal clamped condition (equivalent to infinite stiffness) to a value that causes an approximate increment in half of the static stiffness of the plate measured at its free tip. All artificially induced modifications on the structure are summarized in tables 4.5 and 4.6. Local alterations are schematized in figure 4.13.

4.1.3 Parameter sensibility

4.1.3.1 Driving point

The influence on the SCIs of the driving point used to synthesise FRFs is studied in this section. To understand its the dependency, it is important to firstly clarify the concept of modal visibility. FRFs functions are defined as quotient between the acceleration response on a sampled point (where the accelerometer is mounted) and the excitation force applied in a certain node of the experimental mesh. Reception point is referred as driving point and excitation point is referred as roving excitation point. So then, FRFs values are influenced by the position of these two locations for each acquisition and the relative mobility of each point at a certain modal frequency and its spectral surroundings.

For a given structure, ideal numeric mode shapes (or experimental ODS approximations to modal shapes) define the relative mobility of each point of the structure at each resonant frequency. So then, the effective mobilities observed in FRFs are defined by linear combinations of individual mobilities of the excited and receiving points and accounting for the modal scaling factor for each mode. As FRFs involve the mobility of both the exciting and the receiving point, the selection of a driving point determines the amount of visible nodes and the scaling factor of each of them (For example, if the driving point is located on a nodal line of a certain mode, that mode is not visible in the measurements).

The influence of the driving point on the SCI is a consequence of the modal visibility of driving point(s) used to sample FRFs. Consequently, when executing EMA tests, it is convention to select an appropriate receiving point which presents adequate values of mobility (mode shape amplitude) in all the natural modes of interest. The effect of selecting driving points with different modal visibilities can be observed in the imaginary part of the CFDAC shown in figure 4.14. When there exists more modal visibility,

imaginary part of the CFDAC shows greater amount of cross-shaped maximums, corresponding to resonant peaks in the spectra. On the contrary, driving points with less modal visibility present less cross-structures indicating less visible modes.

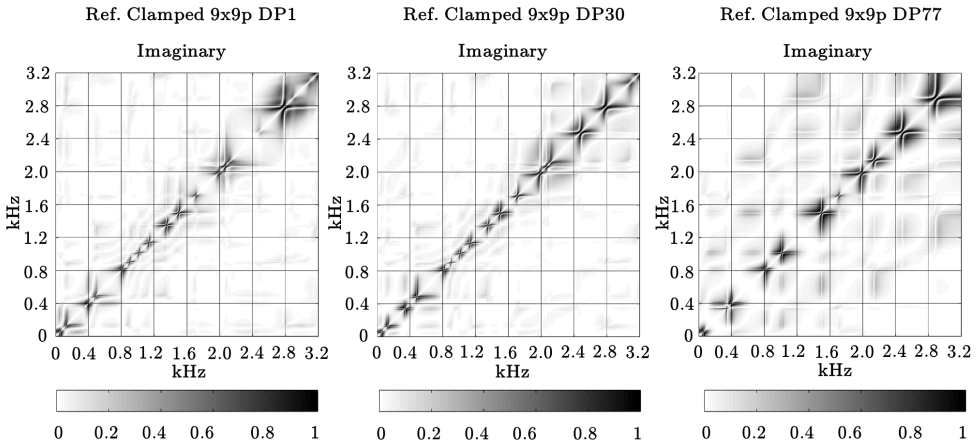

Figure 4.14: CFDAC imaginary part. DP1, DP30, DP77, 81-node mesh, BW = 3200 Hz, Δf = 0.5 Hz

The influence of the driving point is studied by varying the selected reference used to synthesize the FRFs. Although this first analysis is performed for all structural alteration families, only results corresponding to the Young modulus modification are shown in this section using the full 81 points sampling mesh with a total bandwidth of 3200 Hz and a frequency resolution of 2 Hz. This resolution has been selected to reduce computational time (there is a total number of 71 structural alteration cases, each consisting of 81 FRFs and with 81 driving point evaluations required for each) and to keep stability requirements acceptable (see section 4.1.3.2). Results show SCI values for the real part, imaginary part and magnitude for each structural modification included in the Young modulus alteration family. The result of this extensive sensitivity study in front of the driving point is shown in figure 4.15. Driving point deviations are also computed for other structural modification families but are not shown in this section for constriction. Figures A.1 to A.6 in annexes show results for those remaining cases.

The observation of figure 4.15 shows that the variation introduced by different driving points is quite noticeable. However, a clear trend cannot be identified, So then, the influence of the reference point is observed to introduce an erratic and seemingly random variability. As degradation and stiffening increases, so does the scattering of the indicators.

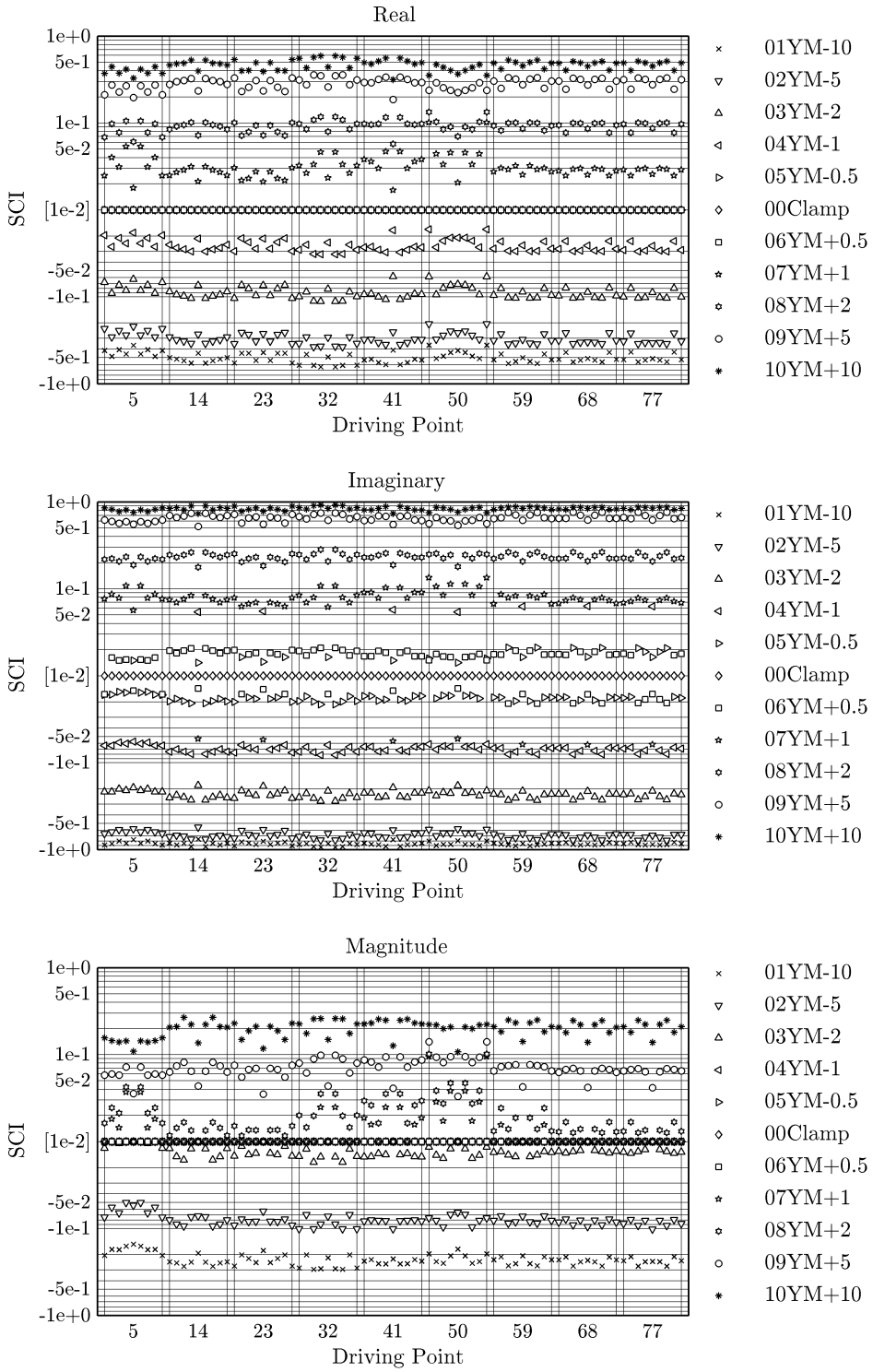

Figure 4.15: SCI evaluated for different driving points. Full 9x9 mesh, $\Delta f = 2Hz$, f_{max} = 3200 Hz

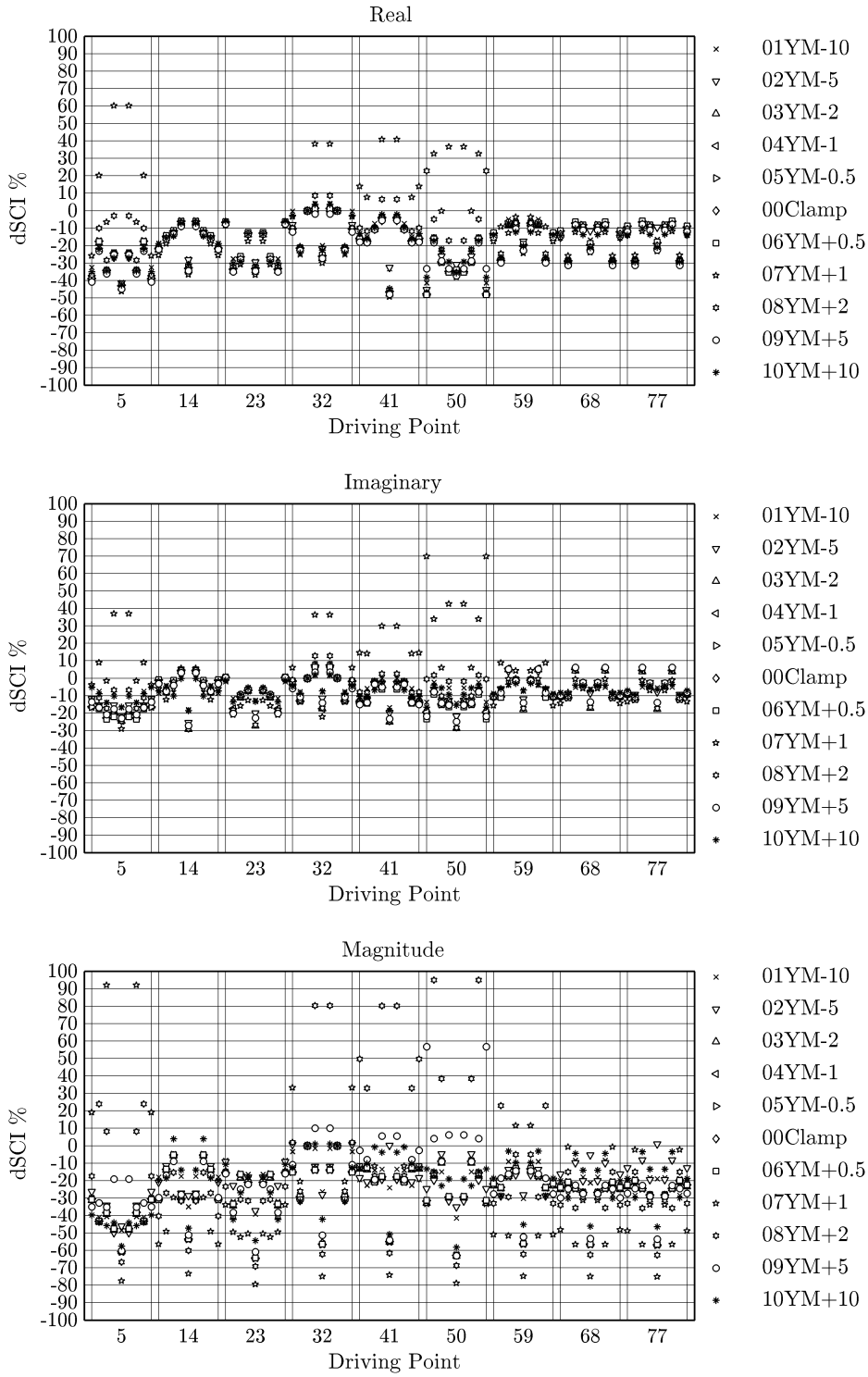

Figure 4.16: SCI variation from optimal driving point selected. Full 9x9 mesh, $\Delta f = 2Hz$, $f_{max} = 3200$ Hz

With those results in mind, it becomes necessary to establish a systematic criterion to select an appropriate driving point. It is proposed to select a reference point which gives a CFDAC as close as possible to the CFDAC generated from the full set of FRFs that compose the full inertance matrix $\mathbf{H}(\omega)$ (Roving excitation correspond to only one column of the full inertance matrix $\mathbf{H}(\omega)$), the CFADC matrix generated from the complete inertance matrix is set as reference). This methodology is based in the concept of modal visibility as it is assumed that the full inertance matrix for a given sampling mesh presents the maximum modal visibility possible for that grid.

The driving point selection is performed on the pristine state as this is the only *a-priori* information that can be readily known for a given structure. The degree of similarity between full inertance matrix CFDACs and single-driving-point CFDACs is evaluated using the Pearson correlation coefficient for the real and imaginary parts, and for the magnitude of CFDACs. Results for this evaluation are depicted in figure 4.17 and show that the driving point that better reproduces the modal visibility of the full FRF matrix is driving point 30. The same figure also shows that the nodes coincident with the symmetry axis of the plate present the least modal visibility. This methodology arises as a very powerful tool to select optimal driving points to perform EMA from equivalent FEM models. Dispersion in SCIs caused by the selection of different driving points is shown in figure 4.16 as relative magnitudes to the values of SCIs measured at driving points 30.

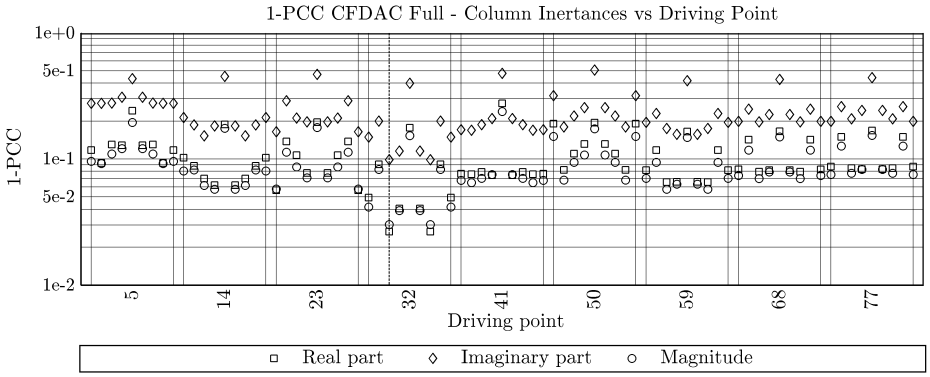

Figure 4.17: 1-PCC between CFDACs corresponding to a virtual EMA for each DP and the CFDAC computed with all the complete FRF matrix functions.

4.1.3.2 Frequency resolution

The second sampling parameter analysed in front of SCIs convergence is the frequency resolution used to synthesize FRFs (or to experimentally acquire if using EMA). All the damage and reinforcement cases are included in this study, with a maximum

frequency of interest 3200 Hz, keeping the driving point at node 30 (DP30) and with the full experimental mesh of $9 \times 9 = 81$ nodes experimental mesh. Synthesis frequency resolution is swept through values of 0.5, 1, 2, 4, 6, 8, 12, 14 and 16 Hz in order to study the behaviour of the SCI indices as frequency resolution decreases. SCIs values corresponding to 0.5 Hz of resolution are selected as the baseline reference for this analysis.

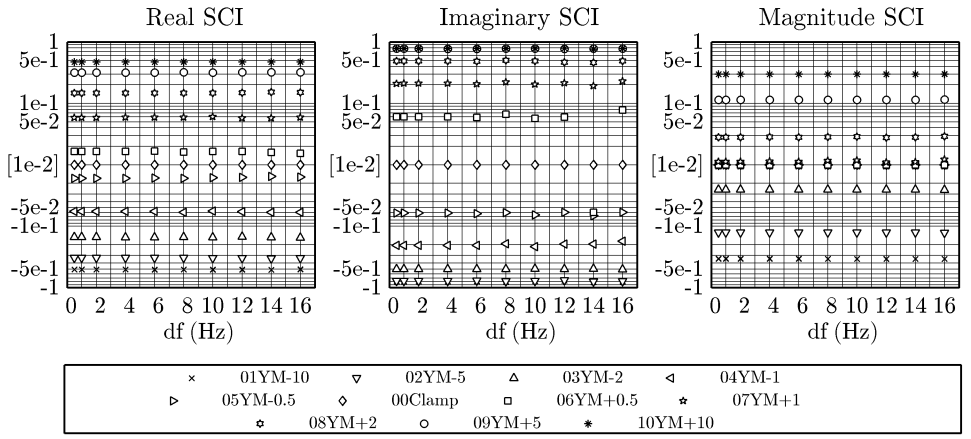

Figure 4.18: SCI vs frequecny resolution. Family of Young modulus alteration. 81-node mesh, DP30, $f_{max} = 3200$ Hz.

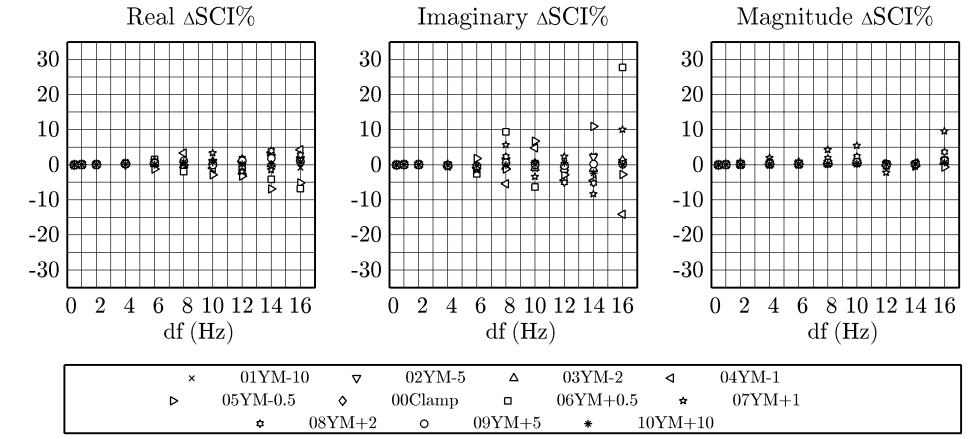

Figure 4.19: SCI variation vs frequecny resolution. Family of Young modulus alteration. 81-node mesh, DP30, $f_{max} = 3200$ Hz.

Discussion on the influence of the frequency resolution is only explicitly shown for the Young Modulus modification family for economy arguments. Tendencies in this analysis are shared for all the families of structural changes and do not present exceptions of interest, so the discussion here presented is valid for all other casuistic. Results for other structural modification families are available in figures A.18 to A.13 in annexes. Observation of figure 4.18 do not shown visible variations in the SCI values as fre-

quency resolution decreases. To have a more in-depth insight, results are presented in figure 4.19 as relative values to the maximum 0.5 Hz frequency resolution. Results in this second figure indicate that SCIs are very stable in front of the frequency resolution for values up to 4 Hz. This behaviour is justified as the proposed indicator is a measure of the shift in the diagonal structure of the CFDAC matrix. Despite decreasing the frequency resolution, the shift in the diagonal is visible for large frequency resolutions. By having few, but enough samples, the shift can be equally quantified. This reduced sensitivity to frequency resolution is a beneficial characteristic as it is usually one of the most expensive acquisition parameters to increase as it involves the use of faster DAQs.

4.1.3.3 Mesh density

The baseline synthesis mesh used in previous sections consist of 81 sampling points defining a grid of 9 x 9 equally distributed points and spaced by 30 mm in both planar directions. This mesh is selected to adequately capture operational deflection shapes with enough spatial resolution. However, the methodology here presented can be applied to cases with relatively coarser meshes as it does not require to capture operational deflection shapes with precision. This section evaluates the behaviour of the indicators in front of the number of FRFs used for computing the CFDAC matrix. The reduction in the number of acquisition points would drastically reduce time and cost requirements in a real operational deployment of the technology.

Multiple sub-sampled meshes are used in this section to study the influence of the number of sampled points in the stability of the SCI indicators. Driving point is kept at position 30 of original mesh. However, this point is not always part of the sub-sampled meshes. In a real EMA modal test, this would be a problem as the driving point plays a key role in the determination of modal scaling. In the current case of study, FRFs are not used to extract modal data but to generate CFDAC matrices so this aspect does not invalidate conclusions drawn.

Coarser meshes in this study are always subsets of the original 81-node mesh. The goal of this analysis is to determine the minimum number of FRFs needed to generate relatively invariant CFDACs (and therefore invariant SCIs). This is analogous to a convergence study when evaluating the quality of a FEM simulation in front of the number of mesh elements in the model. This way, adequate (and minimum) number of FRFs can be selected to reduce computation cost of the evaluation of the SCIs. Sub-meshes involved in this sections are shown in table 4.7.

Mesh ID	Nodes IDs
4p	10 18 64 72
9p	10 18 21 34 37 45 58 64 72
16p	11:2:17 29:2:35 47:2:53 65:2:71
25p	1:2:1:9 19:2:27 37:2:45 55:2:63 73:2:81
34p	2:2:10 18:2:64 72:2:80
40p	2:2:80
48p	2 4:1:7 10:2:18 20 22:1:24 26 28:2:36 38:1:44 46:2:54 56 58:1:60 62 64:2:72 74 76:1:78 80
55p	2:1:8 10:2:18 20:1:26 28:2:36 38:1:44 46:2:54 56:1:62 64:2:72 74:1:80
65p	1:1:9 10:2:18 19:1:27 28:2:36 37:1:45 46:2:54 55:1:63 64:2:72 73:1:81
73p	1:1:10 12:1:16 18:1:28 30:1:34 36:1:46 48:1:52 54:1:64 66:1:70 72:1:81
81p	1:1:81

Table 4.7: Sub-sampled meshes in the numerical study.

The influence of the number of FRF series used to generate the CFDAC and SCIs is attributed to the off-diagonal terms in the CFDAC matrix. When few FRFs are used, terms outside the main diagonal of the CFDAC tend to increase in value, showing greater correlation. As mesh gets finer, off-diagonal terms in the CFDAC matrix are reduced due to each spectral shape being more distinguishable from others. This growth in the off-diagonal terms is caused by the fact that when less FRFs are available to the computation, operational deflection shapes (ODS) at each frequency are described by less spatial points. If ODS at each frequency are poorly spatially sampled it becomes much easier that correlation in the CFDAC appears for frequency pairs which would present very different ODS if richer spatial sampling was used. This phantom correlations between spectral segments which do not share equivalent ODS dilutes when more FRFs are introduced in the computation of the FRFs, giving as a result a much more diagonal CFDAC matrix. This phenomena is equivalent to the one that appears in the MAC matrix when ODS approximating mode shapes are described by few spatial samplings.

CFDACs for coarser meshes have in general bigger image structural similarity, so altered-to-pristine PCCs result in lower correlation values as alteration shifts values in the whole matrix. CFDACs for finer meshes present less structural similarity between them (as much of the regions in the matrix are near-zero values). Altered-to-pristine PCCs are then greater as structural alterations only shift regions corresponding to the diagonal pattern in the CFDAC. Much of the zero-valued elements in the matrix are not altered, so the correlation is bigger due to these terms. This phenomena is observed for all the damage families proposed but is only shown for the CFDAC comparing the pristine state with itself in figure 4.20.

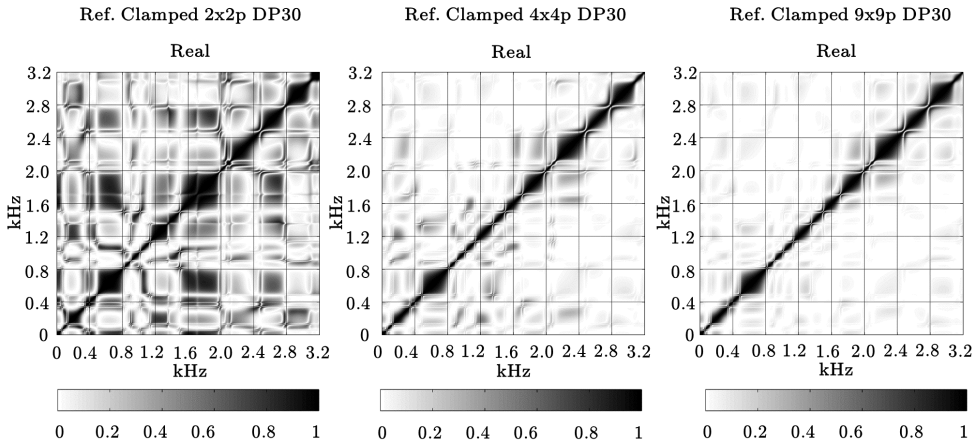

Figure 4.20: Evolution of the real part of the CFDAC in front of number of available FRFs. From left to right, top to bottom: 4 FRFs, 9 FRFs, 16 FRFs, 25 FRFs, 55 FRFs, 81 FRFs

SCIs are evaluated from CFDACs ranging from 0 to 3200 Hz with a spectral resolution of 0.5 Hz. SCI indices convergence in front of mesh density is done for the three real, imaginary and magnitude parts of the CFDAC when the mesh is modified from coarser meshes to finer node distributions. The evaluation of the sensitivity of the mesh is done for all the structural modification families but only shown for the Young modulus modification family to avoid redundancy. Results of the SCI convergence for Young modulus modification family is shown in figure 4.21 as absolute values and in figure 4.22 as relative values to the finer 81-mesh to make shifts more visible.

A clear trend can be identified for real, imaginary and magnitude correlation. SCI indicators seem to stabilize around 40 sampled nodes and tend to show higher values of degradation or reinforcement when few FRFs are use. This tendency is explained bearing in mind that the CFDAC becomes fuller with less FRFs used, as off-diagonal terms increase their values (due to spectral shapes being more similar to each other as spatial resolution is coarser). When the pristine-to-altered PCC is calculated, frequency pairs compared tend show higher divergences in its values. In the other hand, with cleaner and more diagonal CFDAC matrices corresponding to denser sets of FRFs, correlation at each frequency pair tends to include a large number of near-zero elements. Structural similarity of CFDACs plays a major role in the SCI indicators: richer sets of FRFs result in more diagonal CFADCs which present less structural similarity when altered so its pristine-to-altered PCCs are bigger and its SCIs smaller in comparison with coarser sets of FRFs. Results for other structural modification families are depicted in figures A.7 to A.12 in annexes. Large values of damage or reinforcement cause little ripples in the stabilization of the indicators. However, these

phenomena are considered to be residual to the general tendencies observed.

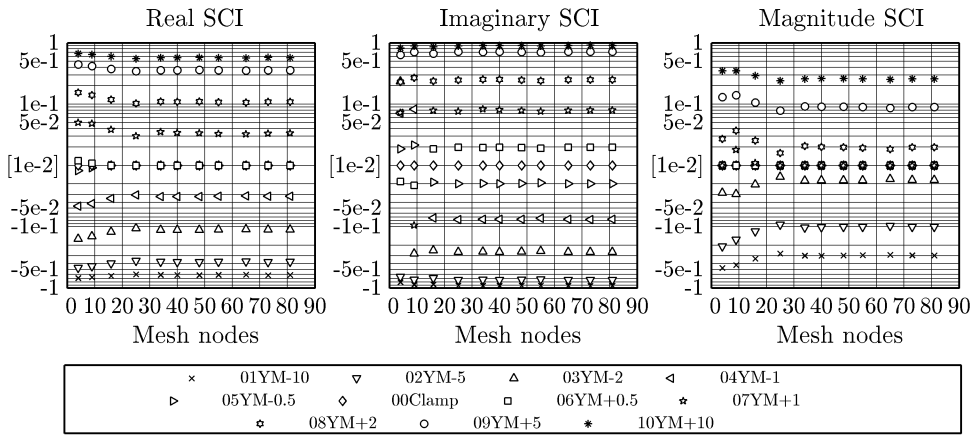

Figure 4.21: Convergence of the SCI indicator as a function of sampled points for Young variations family. DP30, $f_{max} = 3200$ Hz, $\Delta f = 2$ Hz

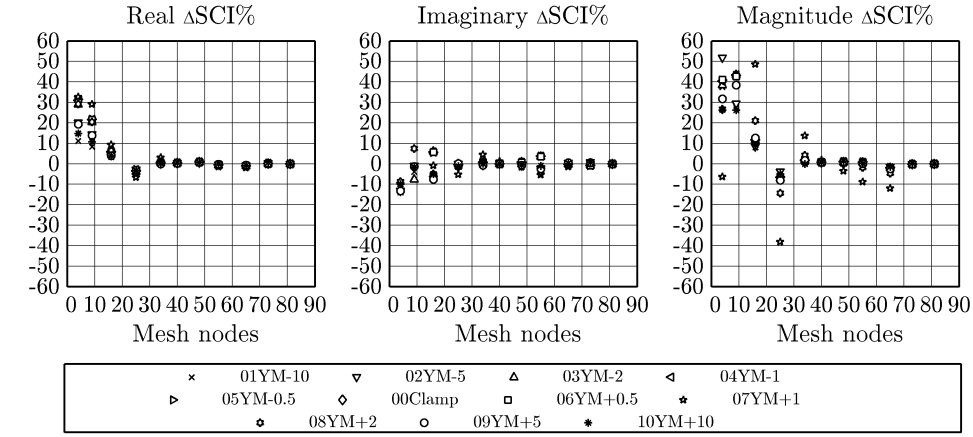

Figure 4.22: Convergence of the SCI indicator as a function of sampled points for Young variations family. DP30, $f_{max} = 3200$ Hz, $\Delta f = 2$ Hz

Real application of the indicators would involve operational modal analysis (OMA), where the full FRFs matrix is acquired in terms of cross-PSD functions of accelerations without capturing the excitation. OMA includes a relatively small number of measured points as each of them would is sensed using an individual accelerometer. So then, for an experimental mesh of 9 locations, inertance matrix for a EMA test has 9×1 FRFs as only one driving point is used. On the other hand, and equivalent OMA test includes 9 accelerometers the equivalent transmissibility matrix has 9×9 FRFs. The author recognizes the promising possibilities of the CFDAC correlation damage index in damage detection using data series from an OMA technique, but investigation scope in this work is limited to EMA acquisitions with only one driving point. However, the methodology is straightforwardly adaptable to multiple driving points measurements

and output-only measured transfer functions.

4.1.3.4 Bandwidth

Next parametric analysis stability of SCI indicators in front of the sampled bandwidth in FRFs. Although the definition of bandwidth is usually understood as a relative measure between the upper and lower frequencies in the spectral domain of interest, in this investigation spectral intervals are always considered to start at 0 Hz. This parameter is one of the major experimental decisions when designing EMA tests and, in combination with the frequency resolution required, it has a major impact on the sampling frequency and buffer capacity required for the DAQ system. These two parameters, at the same time, influence the sampling clock required to capture experimental data, the bits required to have enough acquisition lines in the converter and impact the most on the monetary cost of hardware. The range of frequencies sampled has also great impact on the number of natural modes and associated operational deflection shapes that are captured in an experimental test.

Study of the influence of bandwidth is done for all the families of structural modifications keeping the frequency resolution at 0.5 Hz, for the full 81-node mesh and positioning the driving point at node 30. Bandwidths involved in this parametric analysis range from 200 Hz to 3200 Hz with increments of 200 Hz. Number of samples in each case are always double the maximum frequency as resolution is always 0.5 Hz. Figure 4.23 shows the effect of using different bandwidths in the SCIs computation. In the figure, two cases belonging to the thickness modification family are used to illustrate the effect of this variable. For the global structural alteration scenario shown, it is clear that the amount of shift in the diagonal structure of the CFDAC is greater as the bandwidth increases. Consequently, SCI values are expected to correlatedly grow as bandwidth is increased.

Expected behaviour is confirmed by results here shown. The Young modulus alteration family is again used to illustrate the behaviour of the SCI indicators in front of different bandwidths. Figure 4.24 shows the dependency between SCI indicators and the maximum frequency of interest sampled. Results show a monotonically growing correspondence between SCIs and bandwidths involved in the analysis. Results corresponding to other structural modification families are depicted in figures A.19 to A.24 in annexes and also show direct correlation between SCIs and bandwidths involved in the analysis. Family of thickness alteration presents a very similar trend to the one observed for the Young modulus changes. Other families including local degradations or reinforcements show looser correlation between alterations and SCIs changes.

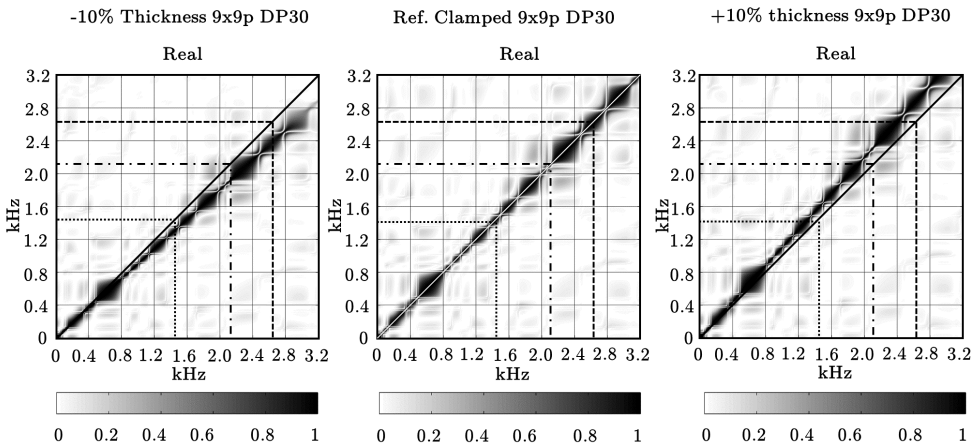

Figure 4.23: Influence of the spectral lines in the CFDAC

Bandwidth dependency is clearly an undesired behaviour if systematization is required in the indicators. Further experimental investigation shows that this effect is heavily mitigated in real acquisition scenarios including real effects. Numeric FRFs are much smoother than their experimental equivalents as they do not include effects such as noise or narrow-band excitation. When using FEM modal data, FRFs can be synthesised up to an arbitrarily large frequency of interest if that particular modal result is available so synthetic FRFs are then much smoother functions even at high frequencies in the spectral domain, a behaviour that is far from the experimental observations.

The maximum frequency of interest when performing EMA acquisitions is usually set as a comprise between two physical phenomena in the vibrating system. In first place, the combination of structural damping, sensor limitation and limited narrow range of excitation of hammers and shakers (even narrower is ambient excitation is used) causes that FRFs dilute in the higher part of the spectra. In those regions, resonances are not accurately captured and noise starts to dominate the spectral series. In second place, EMA tests rely on a geometrically distributed experimental acquisition mesh that allows to obtain distributed modal shapes corresponding to each resonance. As the frequency of interest increases, the modal shapes tend to be more complex and intricate, so much finer spatial resolution is required to correctly describe mode shapes. This fact, combined with the reduced excitation on higher modes, causes that the modal description of the mechanical system at high frequencies becomes poorer. In an experimental case, these phenomena usually translate in an inability to accurately describe higher mode shapes despite resonant peaks being identifiable in the FRFs. In such cases, modal shapes at these high frequencies tend to be very similar in shape to lower modes (as the spatial resolution is not enough to describe more complex

forms). These phenomena usually arises as a mode shape correspondence between higher frequency mode shapes when using the MAC matrix.

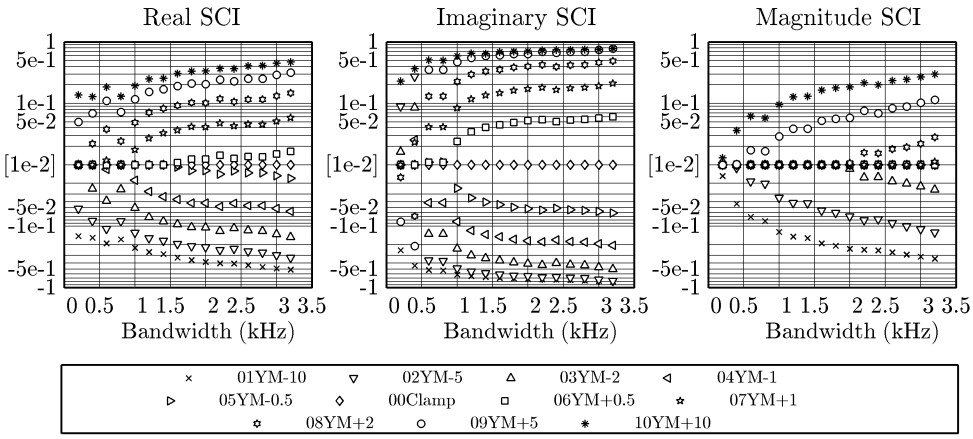

Figure 4.24: Influence of the spectral lines in the SCI. 81-node mesh, DP30, $\Delta f = 0.5$ Hz

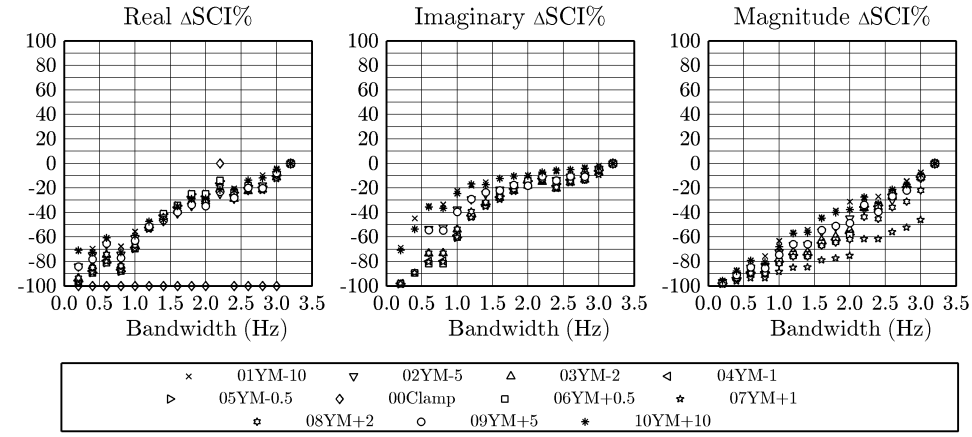

Figure 4.25: Influence of the spectral lines in the SCI. 81-node mesh, DP30, $\Delta f = 0.5$ Hz

The CFDAC is the spectral equivalent of the MAC matrix. Thus, the phenomena exposed for modal vectors also reproduce in the spectral domain: spatial resolution is not enough to differentiate spectral shapes at higher frequencies. This causes the appearance of regions of correlation in the higher frequencies of experimental CFDACs as it can be seen in figure 4.26 for the region comprised between 150 Hz and 400 Hz. When this phenomena appears, the PCC and, thus, the SCI shows a completely different behaviour from the ideal numerical one already exposed before. The higher correlation region in higher parts of the spectra causes that the PCCs grow in value as the bandwidth is increased. This is due to the better values correlation in higher regions of the spectra. SCIs indicators then, decrease due to the rescaling nature of this indicators respect the PCCs.

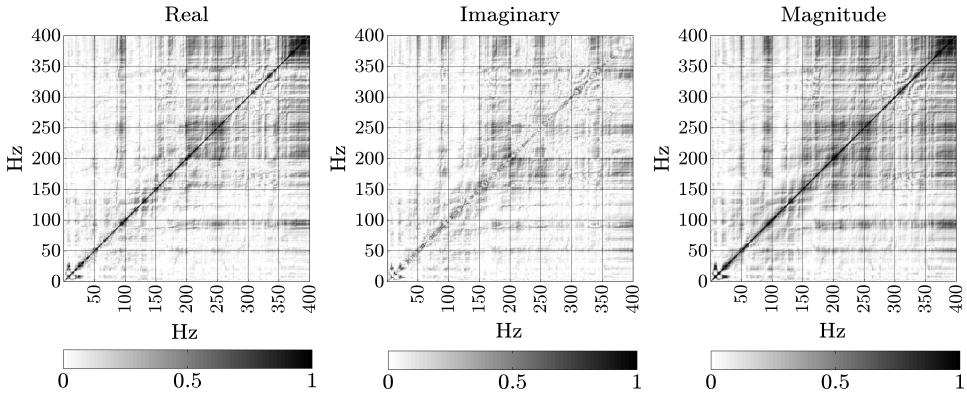

Figure 4.26: Auto CFDAC for a reference EMA test of a full scale latticed power transmission tower

If spatial resolution is enough to differentiate spectral shapes, the absolute value of the SCI indicator increases with the bandwidth. However, either when spatial resolution of acquisitions is not enough to differentiate spectral shapes or either when the attenuation characteristics of the structure and acquisition hardware causes noise to mask significant vibration data, SCIs stabilize and even decrease as bandwidth increases. This effect acts a soft upper convergence limit for the SCI -to a certain maximum if reinforcement is present, or to a minimum if damage is present- and can be used to systematize SCIs for each specific application by setting adequate convergence bandwidths. This behaviour is exploited in experimental investigation of the indicators in sections 5.2 and 5.3.

4.1.3.5 Damping

This investigation uses a proportional damping model adjusted to experimental data to model the dissipation characteristics of the structure. The proportional damping model has been criticised for not being representative of the physical phenomena undergoing the dynamic behaviour of the system. As a matter of fact, the only benefit of this model is that simplifies to a diagonalized form when treated in the modal domain. This is used in this investigation to introduce damping *a posteriori* on FEM derived modal results. A more representative model of the physical phenomena governing the dynamics of the system is the structural damping, which is proportional to the displacements and in phase with velocities.

However, this work is faced from the standpoint of being a comparative study. If the same model is adopted for all the cases, consistent conclusions can be extracted without loss of generality. This section tries to address the influence of the damping in the results of the CFDAC and in the SCI indices. To do so, a constant damping

coefficient is adopted and the sensibility of the SCI indicator is observed for variations in that damping coefficient. Analysis is made using the 81-node mesh, for a total bandwidth of 3200 Hz, with a frequency resolution of 0.5 Hz and driving point set at point 30.

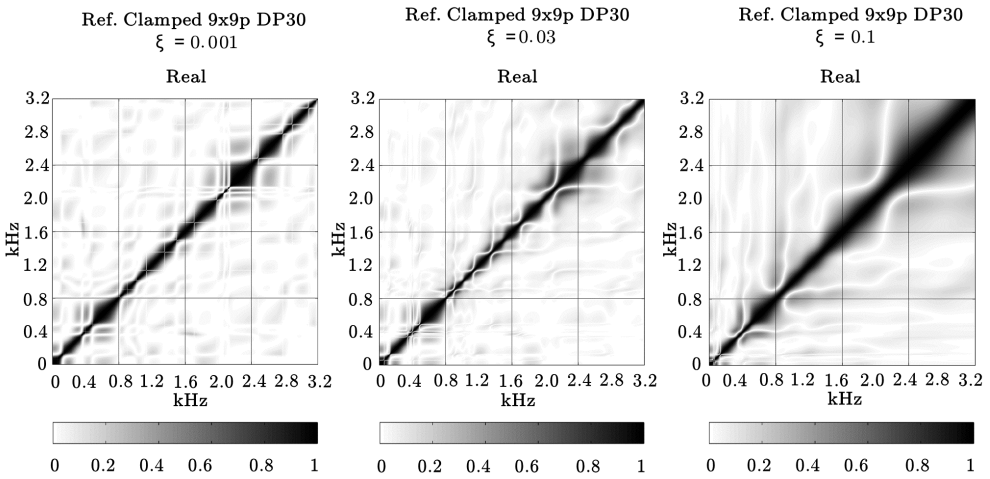

Figure 4.27: Effect of the damping in the CFDAC. FEM plate.

Figure 4.27 shows the influence of the variation in the damping coefficient in the real part of the CFDAC indicator. Values around the experimentally determined damping coefficients (of about $\xi = 0.001$) result in a CFDACs very similar to the ones obtained using a proportional damping model in the synthesis. As the value of the constant damping coefficient increases, the main diagonal structure in the real part of the CFDAC thickens and cross-like structures showing resonances become more difficult to identify. This is credited to the fact that increasingly big damping coefficients cause the peaks in the FRFs to lower its value and to increase its width, causing overlapping of modes and camouflaging other relatively lower peaks.

Figure 4.28 shows the dependency of the SCI indicator in front of the damping in the structure. The reader is encouraged to focus his attention on results involving damping coefficients in the range 0.001 to 0.01. Higher values of damping are not very common to encounter in light structures are are characteristic of monolithic structures such as concrete, masonry or hybrid builds. It is worth noting that such high values of damping would invalidate the hypothesis of low damped system. However, they serve as tendency indicators. In this section results corresponding to the Young modulus alteration family are exposed. Results corresponding to other families of structural alterations are exposed in annexes in figures A.25 to A.30.

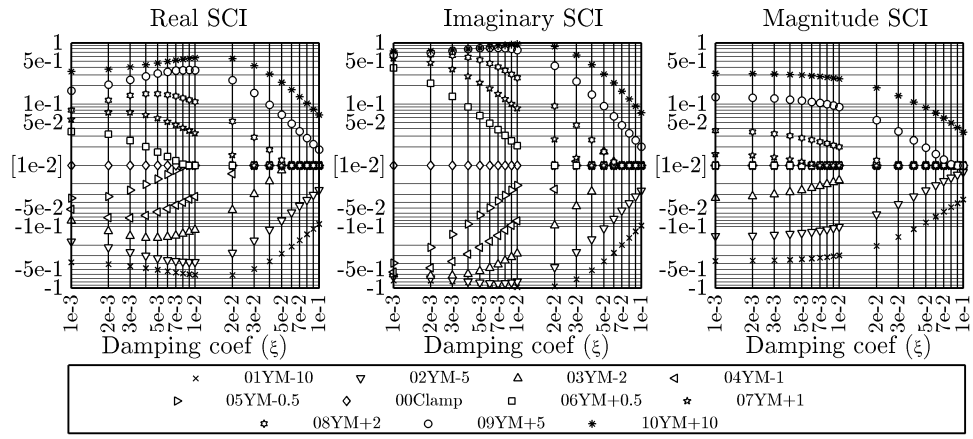

Figure 4.28: Convergence of the SCI indicator as a function of the damping present in the system. Young modulus family. DP30, BW = 3200 Hz, $\Delta f = 0.5$ Hz

Analysing the magnitude SCI, it becomes clear that this is more stable in front of changes in the damping. SCIs derived from real and imaginary parts of the CFDAC present a much higher dependency on the damping coefficient. As the structural changes increase, the sensibility of the indicators in front of damping variation decreases. The inverse is also true, as the structural alteration is relatively smaller, the sensibility of the indicator in front of of the damping increases.

Results show that SCIs derived from synthetic FRFs are heavily influenced by values of the damping coefficients. However, the damping model used in all analyses is the same so there is inner consistency in the comparison that allows to extract valid conclusions. Additionally, in a real scenario, damping is an almost constant characteristic of the system so changes in its values do not occur spontaneously and are usually a sign of alteration. This sensibility in front of damping can be used to detect structural alterations which modify the dissipative characteristics of the structure

4.1.3.6 Noise

Noise in experimentally acquired FRFs arises from three main sources: mechanical noise, electromagnetic interference (EMI) and processing noise. Mechanical noise include the effect of self interaction of subcomponents of the structure, structural or mechanical non-linearities, fluid-structure interactions and ambient sound. EMI effects can be imputed to power grid instabilities, electromagnetic inductions on acquisition wiring, connectors influence or even noise introduced by inner electronics such as A/D converters. Least but not last, parameters selected to process raw temporal signals can also influence the amount of noise present in the readings and introduce processing artefacts as for example leakage and aliasing.

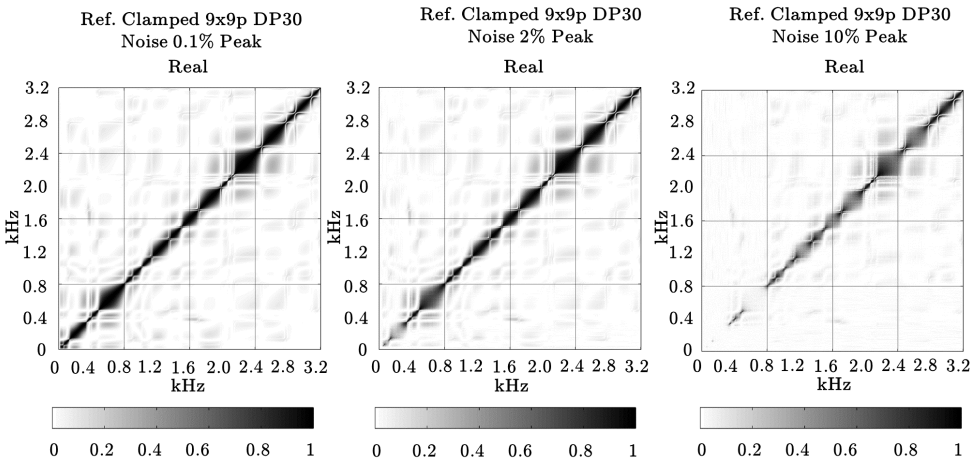

Figure 4.29: Effect of the acquisition noise on the CFDAC. FEM plate.

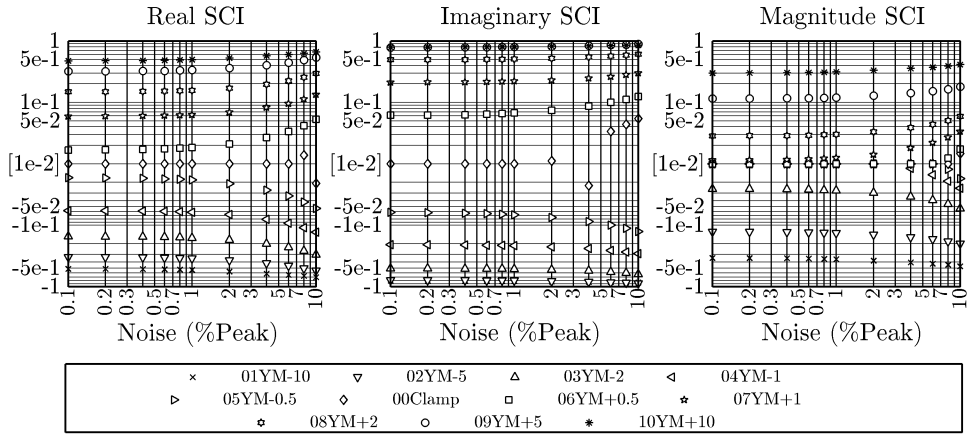

Figure 4.30: Convergence of the SCI indicator versus acquisition noise. Young modulus family. DP30, BW = 3200 Hz, $\Delta f = 0.5$ Hz

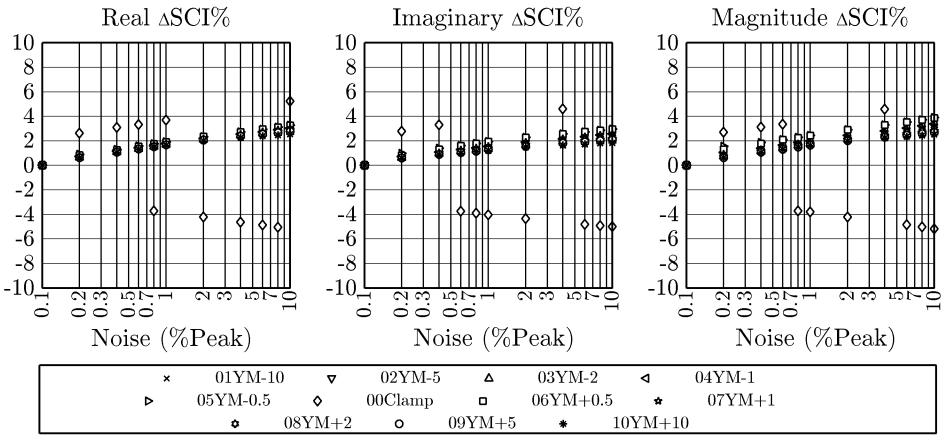

Figure 4.31: Relative convergence of SCIs versus acquisition noise. Young modulus family. DP30, BW = 3200 Hz, $\Delta f = 0.5$ Hz

The presence of random noise in FRFs affects the CFDACs by diluting the main diagonal structure in the matrix indicator as shown in figure 4.29. This is caused by the fact that random noise introduces decoherences between equivalent FRFs for the structural scenarios compared. These decoherences are translated to regions with lowered values of the CFDAC compared to low-noise-level CFDACs.

A sensibility study is executed by varying the percentage of random noise present in the signal. This noise is modelled as a random signal overlapped to the original FRF series with an amplitude equal to the percentage of the maximum peak value in magnitude for each FRF. Analysis is made using the 81-node mesh, for a total bandwidth of 3200 Hz, with a frequency resolution of 0.5 Hz and driving point set at point 30. In this section only results corresponding to the Young modulus alteration family are exposed. Results depicted in figure 4.30 do not show an explicit trend so the same results are depicted as relative values in figure 4.31. Results corresponding to other families of structural alterations are exposed in annexes in figures A.31 to A.36.

From the observation of figure 4.31 it can be stated that SCIs are almost insensitive to noise in the signals. Divergences in the results appear for values of noise above 1% of the peak value of the FRFs, which are far from being acceptable noise-to-signal ratios in common practise. This fact is clearly beneficial as it allows to apply this methodology to in-field applications where signal-to-noise ratios are much lower than in controlled environment applications.

4.1.4 Structural modification assessment

At this point sensibility of the indicators in front of synthesizing (or acquisition) parameters has been thoroughly studied. This section uses some information in the convergence analysis of the SCIs to study the influence of structural alteration typologies on the indicators. All structural alteration families are included in this evaluation. CFDACs and SCIs are evaluated for the artificial modifications introduced in the structure. As in the previous segment of the investigation, indicators are generated from synthetic FRFs from FEM modal analysis results. The final goal of this segment is to demonstrate if the SCIs can be used as a global evaluators even if non-linear alterations or local modifications are present in the structure.

4.1.4.1 Damage typology and the CFDAC

In first place, the effect that the different typologies of damage have in the CFDAC matrix is evaluated. For simplicity, only the real part of the CFDAC matrix is shown as it contains the greater amount of spectral information -imaginary part, on the other hand, consist mainly of an empty matrix whereas magnitude of the CFDAC is exactly equivalent to the FDAC formulation [6].

Frequency resolution is set at 0.5 Hz and maximum frequency of interest is set at 3200 Hz. FRFs for all available 81 nodes in the mesh are used to generate the indicator. This parameter selection is used to mimic the experimental EMA acquisitions done in the FRF validation segment of this chapter and further experimental analysis. The driving point used for the generation of the CFDACs is set at node 30 of the experimental sampling mesh. Characteristic behaviour of the real part of the CFDAC computed from altered and reference cases is shown in figure 4.32.

Changes in Young modulus and in thickness of the specimens introduce a linear proportional shift in the diagonal structure of the CFDAC. The shift in the diagonal is proportional to the position in the spectral domain with growing shifts as the frequency increases. This behaviour is symmetric for structural modification scenarios around a central reference value (as Young modulus modification and thickness alteration). A similar behaviour is also observed for the edge pre-stressing cases: compression introduces negative global shift whereas as tractions introduce a positive global shift. It is worth mentioning that for the first two compressing cases of the family, the observed shift is positive. That is because at low values of compressive loads, first order deformations dominate in front of second order terms so the global effect is to increase the tangent stiffness in that regime. When second order deformation contributions grow, the effect inverts and the tangent stiffness in the structural component start to decrease until it becomes null at 100% of the compressive buckling load. This is why the maximum compressive load is only a 99% of the buckling load. This first compressive buckling load is determined using the same FEM model used for the modal analysis and performing an instability bifurcation-point analysis. First buckling mode corresponds in shape with the first natural mode shape of the structure.

The effect of introducing cracks (slots) in the system presents two differentiated regimes. For the cases up to a slot growth of 100 mm, the loss of correlation due to this degradation is consistent with the longitude of the crack-analogue slot. However, when the slots grow above this value, that is for cases including 140 mm and 180 mm, the effect of the damage in the CFDAC changes. The distortion becomes more important at lower frequencies so previous distortions in higher frequencies become

less noticeable. The real effect however is that as degradation in the CFDAC moves to lower frequencies, the overall PCC correlation increases so the SCI values decrease. This shouldn't be viewed as an inconsistency of the indicator in front of damage typology but as a global change in the response mechanism due to slot growth.

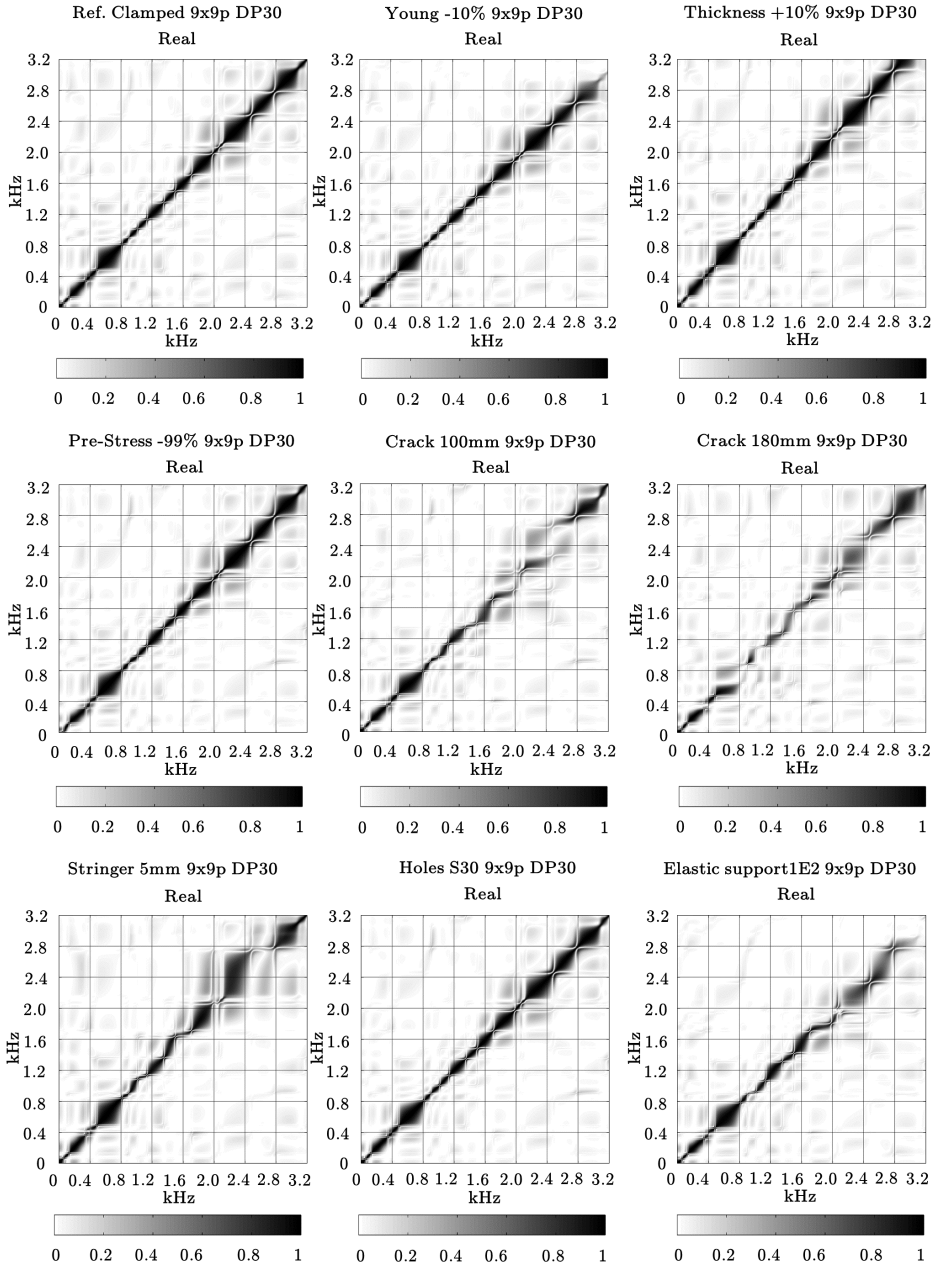

Figure 4.32: Behaviour of the magnitude of the CFDAC as a funtion of he typology of structural alteration. $3.2kHz$, $\Delta f = 0.5Hz$, 81 node mesh, DP30

Reinforcement due to the introduction of a stringer presents a similar trend to the introduction of cracks, but in the reinforcement direction. That means that this kind of modification affects in a limited region of the spectral domain coincident with the frequency region around 2.4 kHz. The over-stiffening distortion is clearly shown in the figure. Introduction of holes in the structure has not a naked-eye visible effect in the CFDAC matrix at first sight, but numerical post-process of the information shows a small negative shift consistent with the loss of stiffness in the plate.

Finally, the introduction of a flexible boundary condition in the structure clamping has a clear effect in the loss of correlation of the CFDAC matrix. This loss of correlation is very clear in high regions of the frequency spectra where a clear dilution of the correlation is observed.

4.1.4.2 Damage typology and the SCI

The influence of damage typology in the SCI indices is thereafter studied. This methodology follows the progression of damage in a similar manner that would occur in a real monitoring case. The results are presented as an alteration progression with tags C1 to C11 referring to each of the cases in each family. The correspondences for cases of each structural alteration family are shown in table 4.8.

SCI indicators are generated from FRFs with frequency resolution of 2 Hz as it has been demonstrated that this parameter has little effect of the convergence behaviour of the indicator as long as kept below 4 Hz. This resolution allows to reduce computational and memory requirements for the SCI computation. The CFDAC is generated for the 81 available nodes in the sampled mesh keeping the driving point in position 30. The whole available 3200 Hz range of modal results are used to the FRFs synthesis. Although it has been shown that the indicators depend on the range of frequencies used, in this analysis only the 3200 Hz bandwidth is analysed to show damage progression for each family as clear as possible.

Results in figure 4.33 are consistent with the alterations introduced in the structure. Alteration detection threshold is set at an absolute value of SCIs of 0.01 based on the test-retest repeatability achieved in subsequent experimental analysis of equivalent cases to the ones here studied (section 5.1.3). Young modulus and thickness modifications present a symmetrical trend around the reference C6 case as it would be expected. Pre-stressing family of cases shows an interesting trend. Traction cases show a monotonic growing trend in the indicator, consistent with a pre-stressing stiffening of the structure. However, when compressing the plate, the first two cases also show a stiffening in the structure (C4, C5). As second order deformation effects start to

appear in the system and the load reaches the buckling limits, the structure starts to show more flexibility (cases C1, C2, C3) and the indicator shows damage. The family of cracks and stringers are consistent with the damage and over-stiffening introduced in the structure. The minimum level of crack damage detected is for a slot of 40mm. Smaller defects are not detected. The family of damages including holes also present a consistent tendency. Minimum diameter of hole detected is 20mm. Lastly, the introduction of an elastic boundary condition is clearly detected for all cases.

Case	Young modulus	Thickness	Pre-stress	Cracks	Stringer	Holes	Elastic Support
C1	01YM-10	11T-10	21PS-99	00Clamp	00Clamp	00Clamp	00Clamp
C2	02YM-5	12T-5	22PS-75	31C4	41S0.5	51HD1	61ES1.0E6
C3	03YM-2	13T-2	23PS-50	32C8	42S1.0	52HD2	62ES2.5E5
C4	04YM-1	14T-1	24PS-25	33C12	43S1.5	53HD5	63ES1.0E5
C5	05YM-0.5	15T-0.5	25PS-10	34C16	44S2.0	54HD10	64ES1.0E4
C6	00Clamp	00Clamp	00Clamp	35C20	45S2.5	55HD15	65ES2.5E5
C7	06YM+0.5	16T+0.5	26PS+10	36C40	46S3.0	56HD20	66ES1.0E3
C8	07YM+1	17T+1	27PS+25	37C60	47S3.5	57HD25	67ES7.5E2
C9	08YM+2	18T+2	28PS+50	38C100	48S4.0	58HD27	68ES5.0E2
C10	09YM+5	19T+5	29PS+75	39C140	49S4.5	59HD29	69ES2.5E2
C11	10YM+10	20T+10	30PS+100	40C180	50S5.0	60HS30	70ES1.0E2

Table 4.8: Structural modification scenarios corresponding to each family for the aluminium plate

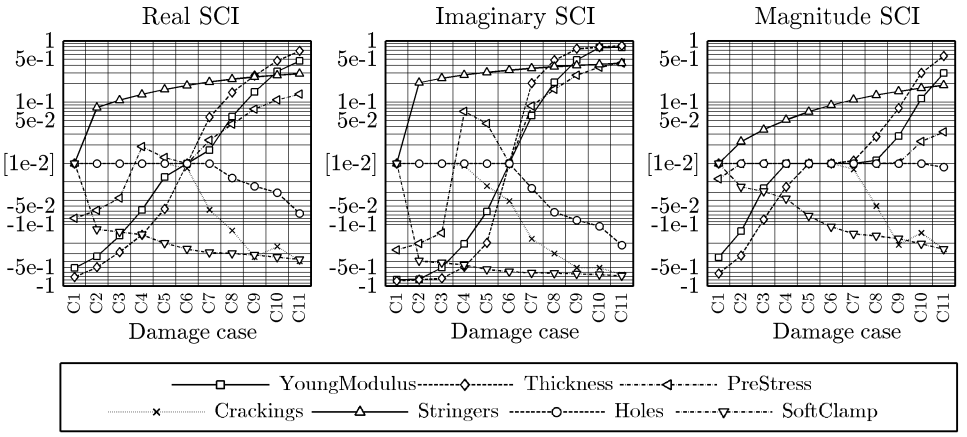

Figure 4.33: SCI vs numerical damage scenarios. FEM plate.

In general, the SCI indicator corresponding to the real part of the CFDAC is less sensitive to damage that for the imaginary part. However, its tendency in front of damage is much more linear that for the imaginary SCI. This is possibly due to the emptiness of the imaginary part of the CFDAC matrix. Even with little shifts in the imaginary part of the CFDAC, the PCC correlation quickly degrades. This fact

suggests that both parts can be used in damage detection with different objectives: whereas the real SCI can be used to establish a damage progression that can be related with the amount of damage accumulated, the imaginary part SCI can be used as an early detector of changes in the system due to its increased sensibility.

4.1.4.3 Residual stiffness and the SCI

This sections aims to relate the evolution of SCI indicators in front of structural alterations with the residual stiffness in the structure. As it has been shown before, the SCIs present relative stability in front of most acquisition parameters once certain thresholds are reached. However this is not the case for the bandwidth (at least from a numeric standpoint without considering experimental effects). So then, this relationship between the residual stiffness and the indicators is done accounting for the variability in the SCIs due to different bandwidths used for computation.

To do so, it is necessary to establish a procedure to evaluate the static structural stiffness of each degraded configuration. FEM models for structural alteration scenarios are already available as they are used to extract its modal data. Therefore, these numerical models are also used to evaluate the stiffness at each altered stage by applying adequate static loads and measuring the displacement caused by them.

The numerical model is exactly the same used in the modal analysis except for the application of an static load and the solver used to resolve the problem. Mesh considerations are equivalent to those modal cases. Boundary conditions are also maintained. In all the structural modification scenarios, static stiffness is evaluated from numerical models applying a 100 N force on a position equivalent to node 5 in the experimental mesh. Stiffness is obtained by probing the vertical displacement in the same location where the force is applied.

Static structural simulations include second order deformation effects and are solved using a direct scheme. Evaluation of the structural stiffness is obtained in each case as its flexibility S expressed in mm/kN which is latter inverted to the stiffness, K expressed in kN/mm for convenience. Stiffness allows a more direct insight than the flexibility in the structural alteration in the structure.

Flexibility and stiffness results are obtained from the application of a 100 N force in the node number 5 of the aluminium plate and sampling the displacement in the same location. Results are shown in tables 4.9 and 4.10 for all the structural alteration families and scenarios. The change in stiffness is computed as a stiffness shift from the reference measured value.

SCI indicators are generated from FRFs with frequency resolution of 2 Hz as it has been demonstrated that this parameter has little effect of the convergence behaviour of the indicator as long as kept below 4 Hz. This resolution allows to reduce computational and memory requirements for the SCI computation. The CFDAC is generated for the 81 available nodes in the sampled mesh keeping the driving point in position 30. In this case it has been decided to show the results for different bandwidths as the multiplicity of data series do not hinder the identification of the tendencies in the indicator. Selected bandwidths range from 400 Hz to 3200 Hz in 400 Hz steps. The relationship between the SCI indicators and the residual stiffness obtained for node 5 is shown in figures 4.34 to 4.40 for each damage family.

	#	**Familiy**	**Tag**	**S (mm/N)**	**K (mm/N)**	**Δ S (%)**	**Δ K (%)**
-	00	Clamped	00_Clamp	22.45	44.54541	0	0
Global modification	01	Young Modulus	01YM-10	24.93	40.1075	-9.96	11.07
	02		02YM-5	23.63	42.3263	-4.98	5.24
	03		03YM-2	22.91	43.6576	-1.99	2.03
	04		04YM-1	22.68	44.1014	-1.00	1.01
	05		05YM-05	22.56	44.3233	-0.50	0.50
	06		06YM+05	22.34	44.7668	0.50	-0.49
	07		07YM+1	22.23	44.9893	1.00	-0.99
	08		08YM+2	22.01	45.4329	1.99	-1.95
	09		09YM+5	21.38	46.7650	4.98	-4.75
	10		10YM+10	20.44	48.9345	9.85	-8.97
	11	Thickness	11T-10	30.72	32.5505	-26.93	36.85
	12		12T-5	26.18	38.1971	-14.25	16.62
	13		13T-2	23.84	41.9402	-5.85	6.21
	14		14T-1	23.13	43.2292	-2.95	3.04
	15		15T-05	22.79	43.8837	-1.49	1.51
	16		16T+05	22.12	45.2131	1.50	-1.48
	17		17T+1	21.79	45.8873	3.01	-2.92
	18		18T+2	21.18	47.2077	5.98	-5.64
	19		19T+5	19.42	51.4893	15.59	-13.49
	20		20T+10	16.90	59.1891	32.87	-24.74
	21	Edge pre-stress	21PS-99	318.84	3.1364	-92.96	1320.26
	22		22PS-75	82.84	12.0715	-72.90	269.01
	23		23PS-50	41.98	23.8209	-46.52	87.00
	24		24PS-25	29.38	34.0315	-23.60	30.89
	25		25PS-10	24.77	40.3657	-9.38	10.35
	26		26PS+10	20.54	48.6796	9.28	-8.49
	27		27PS+25	18.25	54.7915	23.00	-18.70
	28		28PS+50	15.46	64.7040	45.25	-31.16
	29		29PS+75	13.47	74.2501	66.68	-40.01
	30		30PS+100	11.98	83.4516	87.34	-46.62

Table 4.9: Stiffness of cases analysed in the parametric study

	#	Familiy	Tag	S (mm/N)	K (mm/N)	Δ S (%)	Δ K (%)
Local modification	31	Crack analogy	31C4	22.51	44.4277	-0.26	0.27
	32		32C180	22.54	44.3584	-0.42	0.42
	33		33C180	22.59	44.2693	-0.62	0.62
	34		34C180	22.64	44.1608	-0.86	0.87
	35		35C180	22.71	44.0344	-1.15	1.16
	36		36C180	23.17	43.1602	-3.11	3.21
	37		37C180	23.85	41.9226	-5.89	6.26
	38		38C180	25.95	38.5416	-13.48	15.58
	39		39C180	29.24	34.2044	-23.21	30.23
	40		40C180	34.33	29.1273	-34.61	52.93
	41	Stringer	41S0.5	22.38	44.69174	0.33	-0.33
	42		42S1.0	22.23	44.98122	0.98	-0.97
	43		43S1.5	22.05	45.34839	1.80	-1.77
	44		44S2.0	21.83	45.80642	2.83	-2.75
	45		45S2.5	21.57	46.36284	4.08	-3.92
	46		46S3.0	21.27	47.02452	5.57	-5.27
	47		47S3.5	20.92	47.80000	7.31	-6.81
	48		48S4.0	20.54	48.69260	9.31	-8.52
	49		49S4.5	20.12	49.70797	11.59	-10.39
	50		50S5.0	19.67	50.84660	14.15	-12.39
	51	Holes	51HD1	22.49	44.4622	-0.19	0.19
	52		52HD2	22.50	44.4514	-0.21	0.21
	53		53HD5	22.53	44.3794	-0.37	0.37
	54		54HD10	22.65	44.1423	-0.90	0.91
	55		55HD15	22.84	43.7838	-1.71	1.74
	56		56HD20	23.07	43.3482	-2.69	0.91
	57		57HD25	23.33	42.8679	-3.77	3.91
	58		58HD27	23.44	42.6621	-4.23	4.41
	59		59HD29	23.55	42.4619	-4.68	4.91
	60		60HS30	23.91	41.8226	-6.11	6.51
Boundary modification	61	Elastic support	61ES1.0E6	23.24	43.0274	-3.41	3.53
	62		62ES2.5E5	23.31	42.8991	-3.70	3.84
	63		63ES1.0E5	23.40	42.7414	-4.05	4.22
	64		64ES1.0E4	23.80	42.0097	-5.69	6.04
	65		65ES2.5E3	24.24	41.2558	-7.38	7.97
	66		66ES1.0E3	24.64	40.5852	-8.89	9.76
	67		67ES7.5E2	24.79	40.3429	-9.43	10.42
	68		68ES5.0E2	25.02	39.9712	-10.27	11.44
	69		69ES2.5E2	25.50	39.2134	-11.97	13.60
	70		70ES1.0E2	26.52	37.7145	-15.33	18.11

Table 4.10: Stiffness of cases analysed in the parametric study (continued)

Accepting the SCI dependence in front of the bandwidth, tendencies are fairly consistent. Stiffness reductions correlate well with negative values of the SCIs whereas stiffness growths correlate well with positive values of the SCIs. Figure 4.36 shows results corresponding to the pre-stressing family. Previous discussions have exposed that

compressing the plate at low percentages of the buckling load (Compression at 20% of its value) shows positive values of the SCI, indicating rigidization before the second order contribution to deformations appear. However, when the effective bandwidth is reduced from 3200 Hz, SCIs show negative values corresponding to flexibilization. These reversed tendencies for low compressions, do not translate to the numerically evaluated stiffness. These cases show negative values of stiffness shift when directly evaluated. This is attributed to the procedure used to evaluate the static stiffness with a simple clamped bending test. The application of the 100 N transverse force causes the second order deformation phenomena to fully develop, thus showing reduction in stiffness when numerically evaluating it. Modal models including the pre-stress without the introduction of the transverse forces cause that the second order terms keep undeveloped and that the SCIs show slightly positive values showing over-stiffening when little compression is introduced.

Another interesting aspect to comment is that low amounts of damage or small ranges of bandwidths used for the SCIs computation have the similar effect of invalidating the sign-decision algorithm in the SCI computation as seen in figures 4.37, 4.38 and 4.39. Either when the amount of alteration is low or the maximum frequency of interest is small, the sign of the SCI indicator diverges from its expected behaviour, specially for imaginary SCIs. Young modulus and thickness variation families present a almost equal SCIs - stiffness shift slope whereas each other families present other characteristic curves relating the two parameters. The slope relating residual stiffness and SCIs values is characteristic of the typology of alteration being analysed so could eventually be used as a structural modification classification parameter.

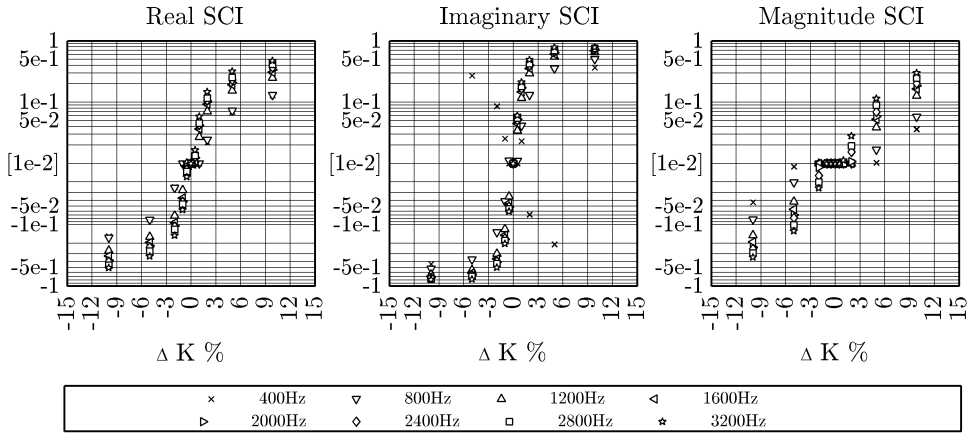

Figure 4.34: SCI vs Stiffness shift (DP30). Young modulus family. FEM plate.

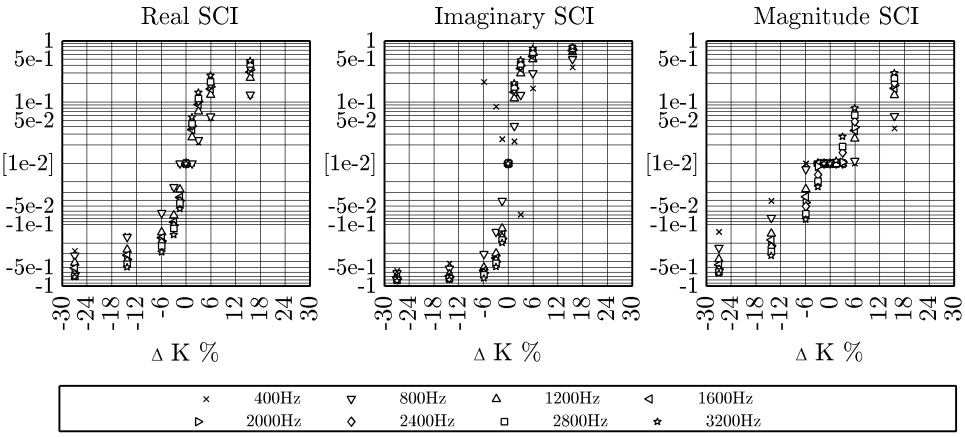

Figure 4.35: SCI vs Stiffness shift (DP30) for the thickness alteration family. FEM plate.

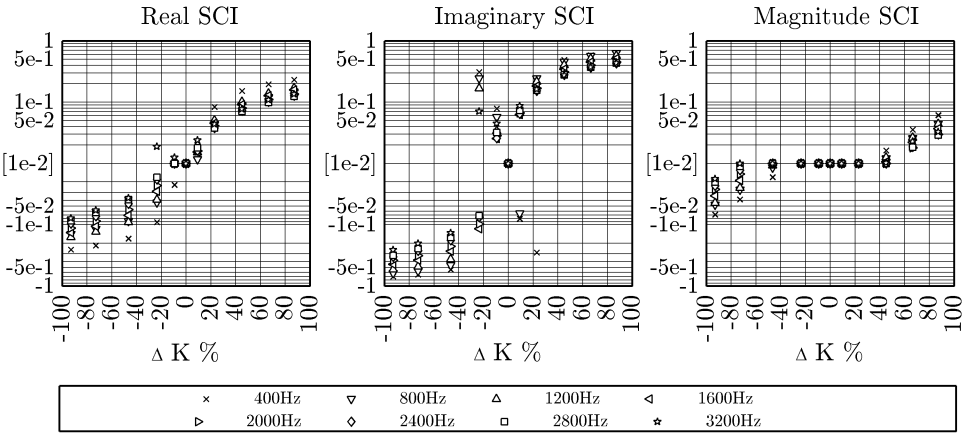

Figure 4.36: SCI vs Stiffness shift (DP30) for pre-stress family. FEM plate.

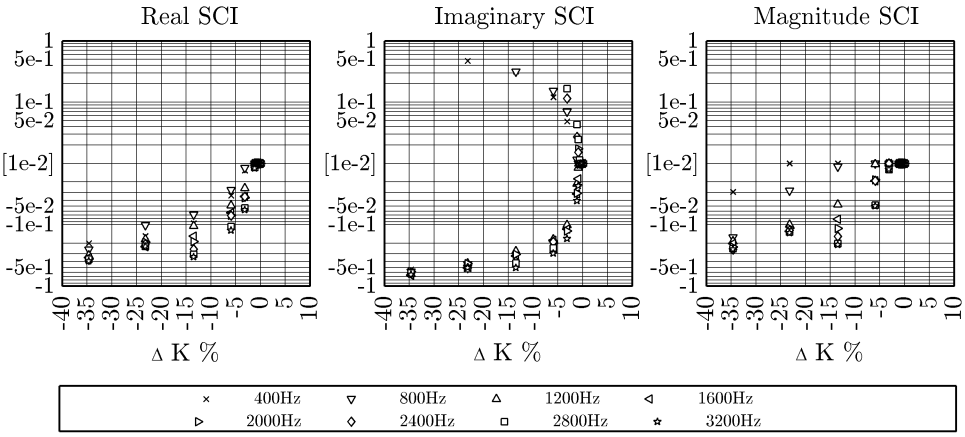

Figure 4.37: SCI vs Stiffness shift (DP30) for crack analogy family. FEM plate.

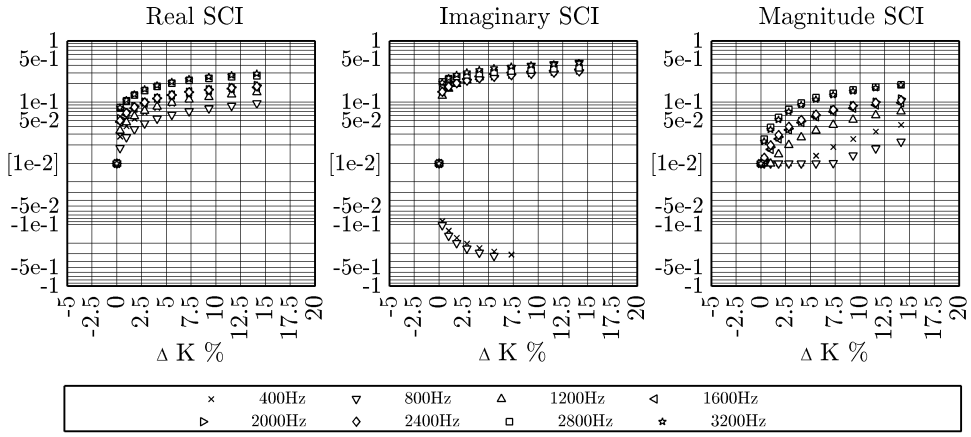

Figure 4.38: SCI vs Stiffness shift (DP30) for the stringer family. FEM plate.

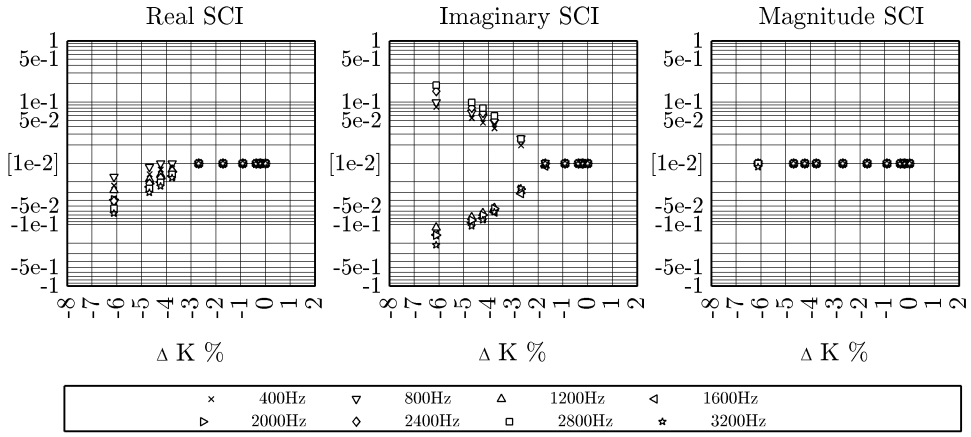

Figure 4.39: SCI vs Stiffness shift (DP30) for the holes family. FEM plate.

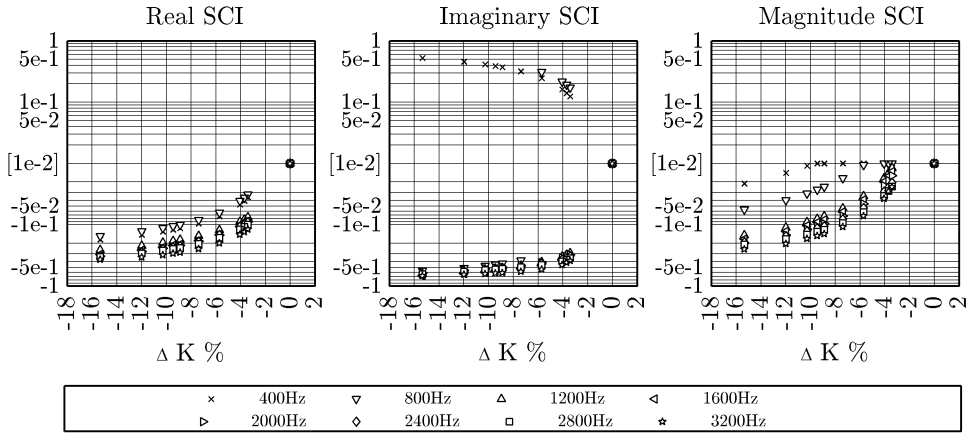

Figure 4.40: SCI vs Stiffness shift (DP30) for the boundary condition family. FEM plate.

4.1.5 Comparing numeric SCIs with DRQ and ΔODS

As already exposed in the literature review chapter of this investigation, Maia, Urgueira, Sampaio an co-workers [3] [4] [5] propose the use of certain spectral indicators to asses the damage in structures using vibration data. As this is the most similar approach to the topic of this research in the literature, this section tries to establish a parallelism between proposed indicators and previous works.

Spectral data is derived from the cases for the alteration families already exposed. Two indicators are evaluated and compared to the SCIs: the DRQ (which is based in a condensation of the RVAC indicator) and the ΔODS indicator. The results are shown per each of structural alteration families in figure 4.41. The DRQ indicator is reescaled to 1-DRQ so a perfect correlation (no damage present) is represented by a 0, and a total discorrelation (large amount of damage)is represented by a 1.

From the figure 4.41, it can be observed that both indicators are formulated with damage detection in mind as they do not differentiate reinforcements from degradations in the structure. That is due to the fact that the sign of the shift in the indicators is not accounted for. This limitation is tried to be overcome by the SCI indicator, which includes the sign of the shift in the CFDAC indicator. Besides the sign of the degradation, the DRQ indicator shows tendencies very similar to the SCI indicator in front of the damage typology and severity. This is an expected behaviour as both indicators are based on a direct correlation of FRFs. ΔODS presents the higher sensibility followed by the imaginary SCI and then the real part SCI. The DRQ presents slightly less sensibility than the real part SCI. The less sensible of the compared indicators is the magnitude SCI. However, experimental analysis of the sensibility of indicators (section 5.1.6) will show that the sensibility of the ΔODS is so high that even test-retest repeatability analysis show a large amount of accumulated damage. This is clearly a disadvantage in the use of the ΔODS as a damage indicator.

A second aspect that limits the application of the ΔODS indicator is that it is always defined relative to the most degraded state in the family. Therefore, it cannot be systematized in front of other damage indicators. Usually, damage indexers are ranged between 0 and 1, with one being a total lack of correlation between states. This total discorrelation is hardly achieved so damage indicators do not usually exhibit values too close to 1. The relative scale of the ΔODS indicator becomes clear when observing the cases dealing with the detection of damage in form of holes. DRQ indicator exhibits values very close to zero (detection is very difficult) whereas the ΔODS present s unitary values for the extreme case of the family. So then, this indicator is not directly comparable to other damage indicators conventionally used in literature.

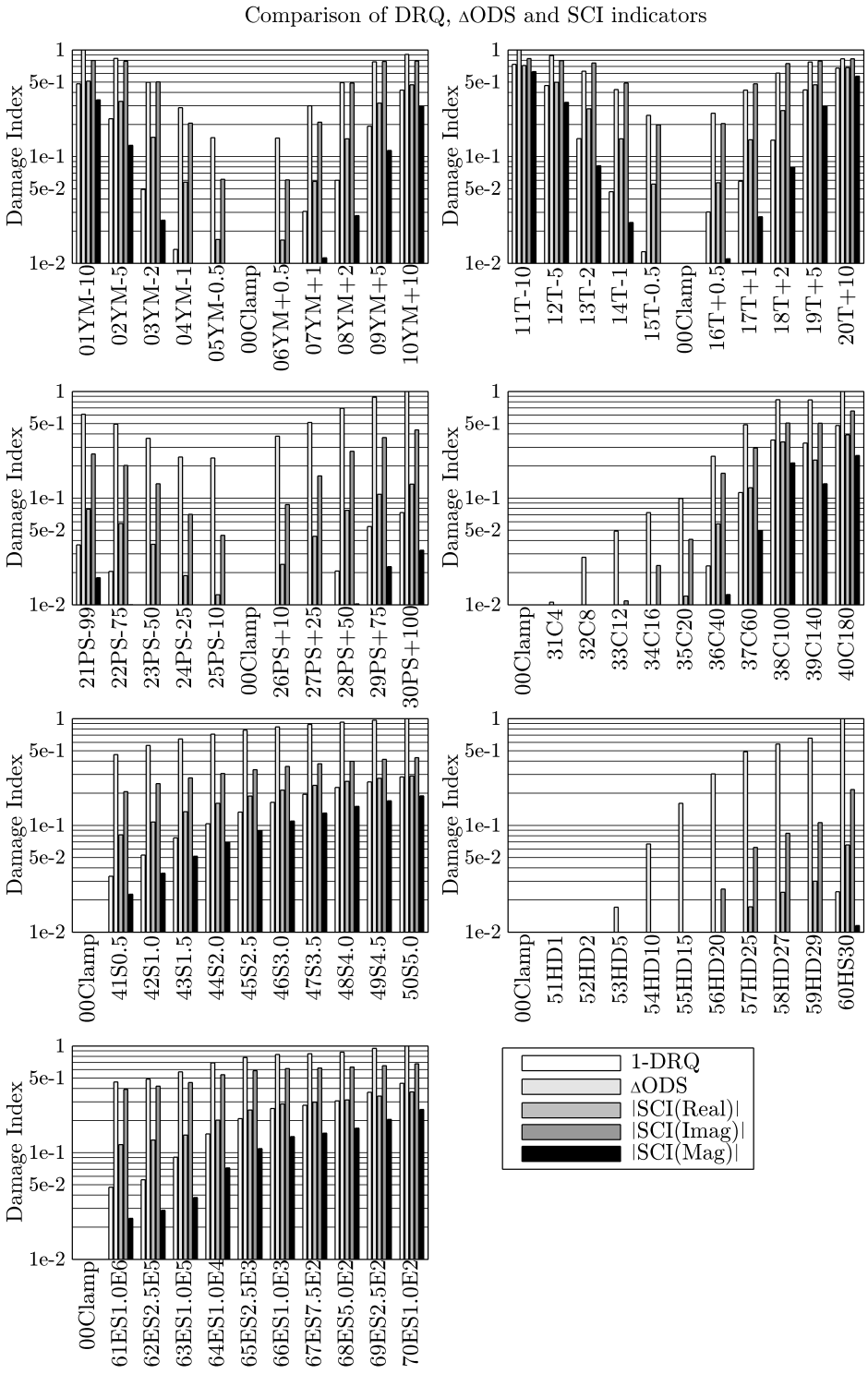

Figure 4.41: Comparison of structural alterations indices: DRQ, ΔODS and SCIs.

4.2 Model tower

After studying the behaviour of the SCI indicator on a modelled FEM aluminium plate, a numerical study is also performed on a downscaled model of a power transmission tower. The final aim of this research is to serve as a guiding line for the implementation of the SCI indicator to a SHM system monitoring real-scale latticed structures. This second numerical campaign serves as a first step to show the validity of the SCI indicator when applied to a different typology of structure from the already analysed plate-like one.

A downscaled version of a full power transmission tower (PTT) is numerically modelled and studied using the SCI indicators. Further works in this investigation deal with the experimental investigation on the same indicators on a real-scale structure using EMA captured FRFs so it becomes necessary to keep geometric, static and dynamic scaling of the structure. Dynamic scaling is always very difficult to keep as the frequency range of interest for a full-scale tower is very different from a model one (equivalent natural modes of structures are very distant in the spectral domain). However, the possibility to have an easy access an control over environmental condition easily justifies the use of a laboratory down-scaled prototype.

This investigation on a 1:12 downscaled model of a power transmission tower uses an equivalent procedure to the one used in the parametric study executed on the aluminium plate. Numerical simulations include certain cases of artificially introduced structural alteration in the models, both in the parameters defining the global performance of the structure (Young modulus members cross-section) and in localized regions of the structure in order to reproduce local degradations.

The modelled structure consist in a 1:12 downscaled version of a GE19 2-circuit LA455 110 kV latticed power transimission tower. Baseline geometry is courtesy of COMSA-EMTE R&D department. Some simplifications are adopted to the full-scale geometry as dimension reduction reduces the possibility of fitting certain members in the lattice. Simplifications in the geometry are shown in figure 4.42. Most of these modifications are adopted keeping in mind that the modelled downscaled geometry has to be experimentally replicated in a testing prototype.

Geometric changes in the geometry include the addition of some dimensional clearance in the connecting members to the foundations of the structure. Another change introduced consist in the omission of certain secondary reinforcement trusses as their relative size would make its physical installation very difficult or almost impossible. This is the case for certain transverse torsional horizontal reinforcements in the first

three levels of the structure. Although these slight modifications, the main load bearing components are kept in the original configuration.

The trusses in the model structure consist of L profiles. The steel used is assumed to be compliant with the ASTM-A36 grade so median values for its properties are adopted. Direct geometrical scaling of cross-sections is not possible as L bars come from manufacturer in a gradation of normalized sections. So then, model tower trusses are remapped to available commercial L profiles. This assignation of profiles results in:

- L30.3 for all the trusses in the lower section of the main body of the tower (the one with variable cross-section). This includes all 4 vertical main columns, primary horizontal reinforcements, primary diagonals and primary torsion reinforcements.
- L15.1 for the secondary and tertiary diagonals in the lower body.
- L30.3 in the main 4 columns of the upper body of the tower.
- L20.2 for all the main transversal elements forming the arms of the tower.
- L15.1 for all diagonals, and torsion reinforcement trusses in the upper part of the tower.

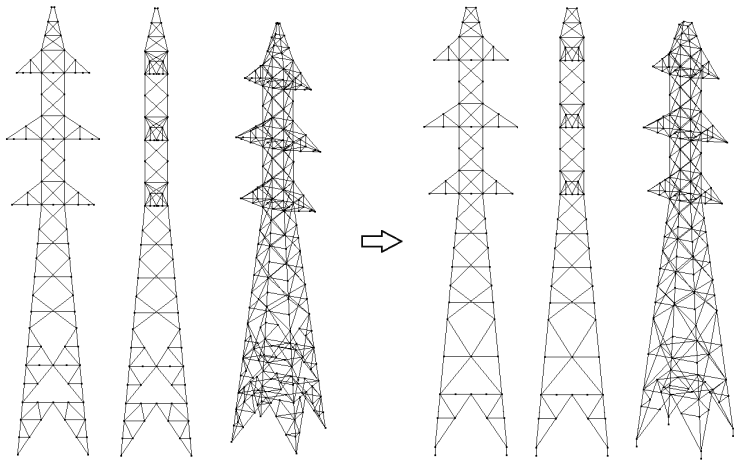

Figure 4.42: Full size geometry and downscaled simplification of the GE19 2-circuit LA455 110 kV power transmission tower

Although this chapter deals with the numerical study of the SCI indicators using a FEM model of a downscaled power transmission tower, this firsts paragraphs discuss some aspects of the experimental specimen built that strongly influence some modelling decision taken in the FEM characterization. The numeric analysis was performed after the execution of the experimental acquisitions on the prototype. Original purpose of EMA acquired experimental FRFs was to asses degradation in structures using

modal domain derived damage indicators. The same FRFs database is used in this investigation to assess the viability of using spectral domain indices in structural assessment. Two different experimental configurations were originally used in boundary conditions of the model tower. These two boundary conditions differ in the restrained number of degrees of freedom in the base block of the structure. These divergences in the allowed movements were a consequence of the irregular interface between the supporting concrete block and the testing floor.

Boundary conditions are identified to be one of the most critical aspects to be taken into account in the downscaled experimental campaign as they dramatically alter the natural frequencies and dynamic responses of the coupled system. First approach focused on assuring a good compatibility between the lower surface of the supporting concrete block and the ground, avoiding any kind on relative rotation between them. To do so, an elastomeric bed was inserted between the two surfaces. As initial purpose of the investigation (using modal domain derived indicators) did not include the numerical modelling of the system, the solution was considered to be acceptable.

However, when facing the numerical modelling of the system, elastomeric boundary conditions were encountered to be complex to reproduce. A second experimental campaign was then proposed with the aim of simplifying the system-to-ground interaction. To do so, the elastomeric support was discarded from the experimental setup. Interaction between ground and concrete block was tried to be minimized by using wedges along the interface perimeter.

In spite of all the efforts put in improving interaction between the system and the ground, simple boundary are not able to reproduce experimental observations. However, a somewhat more complex model for the ground support is consistent with the dynamic response of the coupled system for the low and mid regions of the spectral domain. This boundary conditions model includes:

- A complete pinned connection between the tower legs and the concrete base (the real structure is not pinned, but screwed to a metallic support embedded in the concrete)
- Vertical axis (Z) rotation completely restrained in the concrete base
- One horizontal direction rotation of the concrete base allowed, the other one restrained. Experimental results show asymmetries in the modal shapes so the allowed rotation and fixed axes are considered to be a linear rotation of 45 degrees in the Z direction of the main XY axis in the counter-clockwise positive direction. This leads to the conclusion that wedging the interface perimeter between the base and the ground is not enough to restrain both rotations.

- Previous mechanism implies that the system becomes a somewhat 'coupled pendulum' between the structural dynamics of the tower and the pendular motion allowed for the concrete base. As a result, it is critically important to correctly model the weight of the concrete slab and the resisting forces acting on it.
- The coupled pendulum motion of the concrete slab requires that the resisting reaction of the ground is fine tuned. An elastic boundary support is needed to fit experimental results to numerical model solutions

In the experimental discussion of this investigation concerning the results for the downscaled model tower, this aspect is further developed and quantitative characterization of the boundary conditions is exposed.

The correct modelling of boundary-to-structure interface is important to validate the FRF synthesis procedure of FEM derived FRFs. Preliminary numeric analysis on the model tower included the concrete block and elastic boundary conditions in the sensitivity analysis of the SCI indicators. Initial results showed that the dynamics of the system is dominated by the concrete block to ground interaction so the influence of changes in the latticed structure is heavily masked by the main vibration modes (those including a heavier modal mass, thus mobilizing the concrete slab base). In order to have a cleaner insight on the structural shifts using SCI indicators, a simplified model was decided to be used in the numerical analysis of the SCIs. Although this decision causes that direct comparison of numeric and experimental is meaningless , the isolation of the effect of alterations in the structure allows to extract more significant conclusions.

With that in mind, simple boundary condition is adopted to execute the parametric study. This simplified boundary condition tries to replicate the mode shapes and frequencies that are considered to be dominated by the latticed steel structure and not by the concrete slab dynamics. The experimental boundary conditions used in this investigations as well as the equivalent simplified elastic boundary condition are shown in figure 4.43 and further developed in section 4.2.1.2 of this chapter.

The reference directions for the structure are defined respect to certain elements of the tower. Z direction is coincident with the height of the tower, with zero level defined in the first element connecting the tower to the concrete base. X direction is defined as the perpendicular vector to Z, which at the same time is perpendicular to the plane defined by the 6 tip points of the tower arms. As the tower is symmetrical respect to this plane, further orientation of the X axis is not required (at this point two possible orientations of the X vector are possible, further discussion assumes that one direction is selected). The Y direction is defined by completing the trihedral, so

then it is perpendicular to the Z direction, and contained in the plane defined by the 6 tip-points of the tower arms. The tower then presents four visible pseudo-surfaces in the four projection directions perpendicular to the Z axis. This faces are symmetrical in pairs and are indistinctly referred to in this investigation. Frontal plane refers to the faces directly and inversely perpendicular to the X direction of the tower. Lateral plane refers to the faces directly and inversely perpendicular to the Y direction of the tower. Numerical structural modifications in the tower are always introduced in the faces with most positive values of its perpendicular axis in the FEM model. Only one of each faces is used during the experimental campaign of the tower. These two faces are physically labelled and traced for all experimental tests.

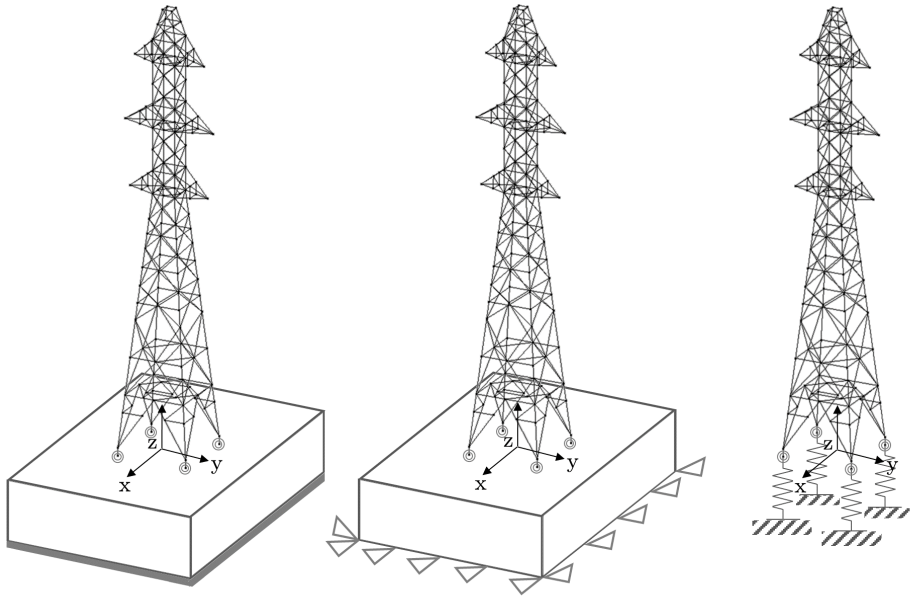

Figure 4.43: Used boundary conditions for the prototype. Left: Initial elastic support, Mid: Reworked wedged support, Right: Simplified FEM model

4.2.1 FRF synthesis verification

4.2.1.1 Reference state characterization

In the same fashion that is done for the aluminium plate, the first step in the parametric analysis including the model tower is to validate the FRFs synthesis using a different structural typology. Although accuracy of the methodology has already been demonstrated for the plate, this second iteration on the issue allows to have additional confirmation.

The approach adopted is exact to the one adopted for the plate: in first place, a series of reference experimental modal analysis are executed on reference configurations of the studied structure using an experimental specimen. These initial experimental reference tests are part of the experimental campaign that is exposed in subsequent chapters of this investigations and correspond to two reference tests on the model structure with elastic boundary conditions and to two additional tests on the model structure under wedged boundary conditions. These four experimental sets of results are used as a baseline to firstly adjust a damping model representative of the mechanical system, secondly to fine tune the numerical model until numerical to experimental convergence is achieved and finally as reference acquisitions to assess the validity of the FRFs synthesis methodology.

Four experimental FRFs are shown in figure 4.44 corresponding to some of the reference pristine cases that are comprehensively presented in section 5.2.2. Tags for the series refer to unwired elastic boundary conditions (EBC-UW-Ref1 and EBC-UW-Ref2) and unwired wedged boundary conditions (WBC-UW-Ref1 and WBC-UW-Ref2). Results herein shown only correspond to the frontal YZ plane, measuring the vibration in the X direction of the tower. So then, the acquisitions for the two boundary conditions are directly comparable (as this document progresses, it is further explained that the experimental tests made with the elastic boundary conditions include acquisitions for both YZ -frontal- and XZ -lateral- planes). The lateral acquisitions for the elastic boundary condition tests have not been taken into account in the current discussion. The acquisition meshes for both planes are depicted in figure 4.46.

Modal post-process results consist of modal frequencies and corresponding dampings are shown in table 4.11. Modal shapes corresponding to EMA tests with wedged boundary conditions are shown in figure 4.45. Modal deformations corresponding to elastic boundary conditions have been omitted for redundancy. Shape results for this first type of support are almost identical to the second support typology. The only difference observed lays in the frequency shift observed in natural frequencies. Correspondences between mode shapes shown in table 4.11 serve as a guiding line to match equivalent mode shapes. Additionally, modal shapes are only depicted up to a frequency of interest of 210 Hz, as higher modes do not appear clearly in the post process mostly due to the fact that spatial resolution of the EMA test is not enough to accurately capture their modal deformations (although the resonant peaks clearly appear in the acquisitions). It is also clearly shown that the boundary conditions have a considerable impact on bending modes whereas torsion mode shapes are quite stable in front of boundary condition alterations.

With these experimental acquisitions, a damping model is adjusted using the least-

squares algorithm to the damping equation shown in expression 3.27. This results allow to fit a representative proportional damping model to be used in the numerical FRF synthesis. This adjusted damping model is shown in figure 4.47.

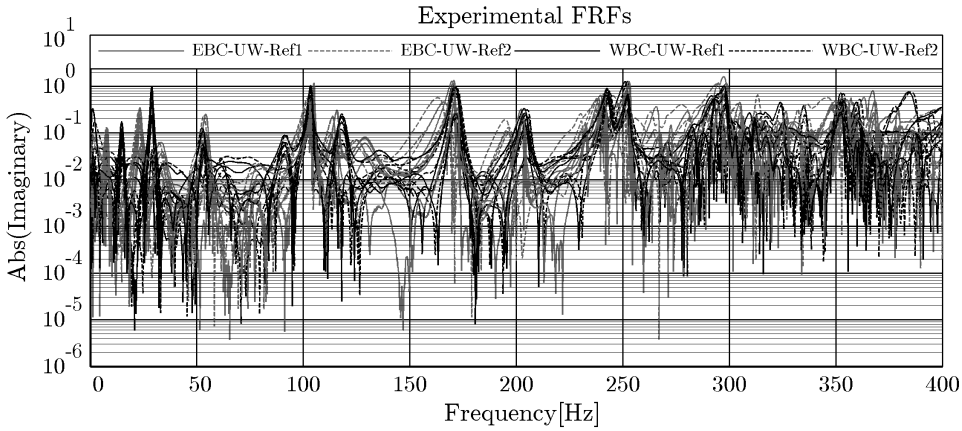

Figure 4.44: Experimental FRFs for references without cables for elastic and wedged BCs.

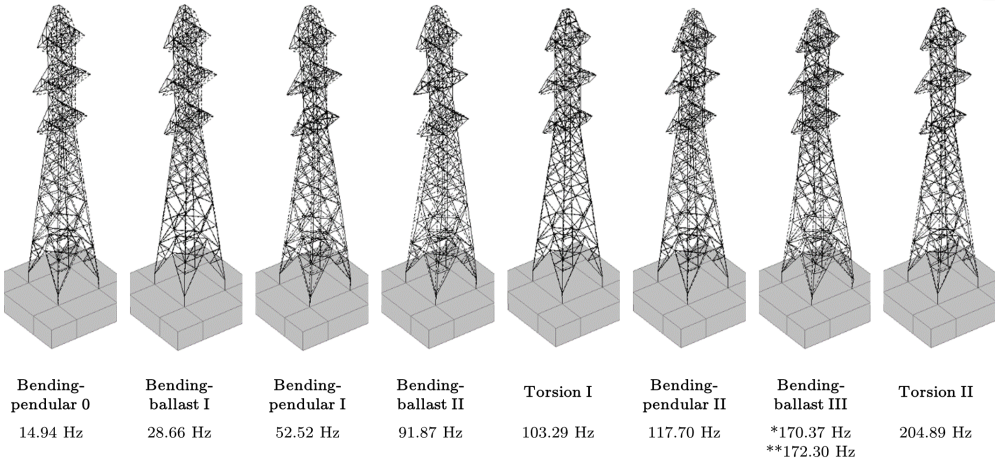

Figure 4.45: Experimental operational mode shapes for wedged boundary condition.

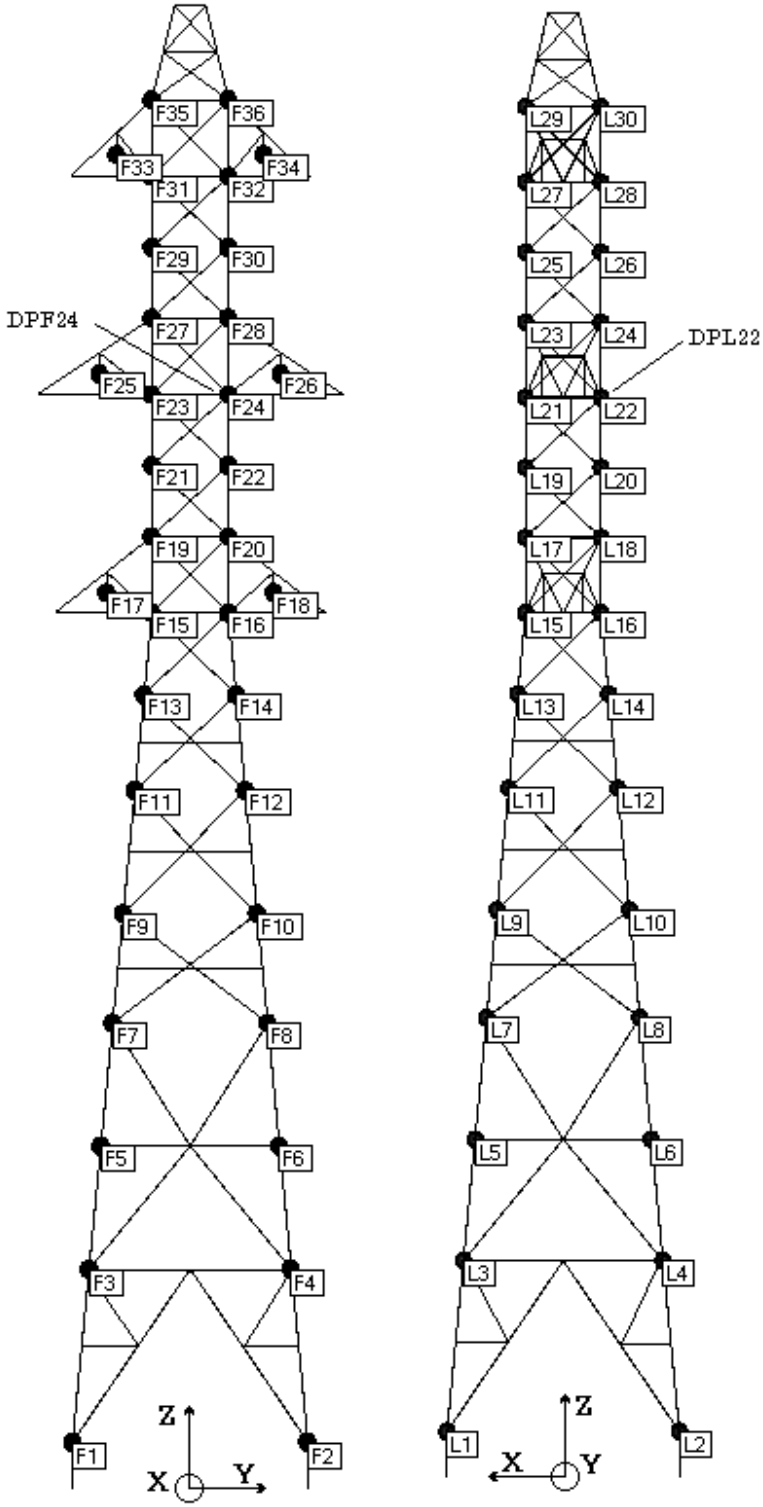

Figure 4.46: Left: frontal test plane view. Right: lateral test plane view

EBC-UW-Ref1		**EBC-UW-Ref2**		**WBC-UW-Ref1**		**WBC-UW-Ref2**	
f (Hz)	ξ	f (Hz)	ξ	f (Hz)	ξ	f (Hz)	ξ
8.10967	3.90E-02	7.59237	4.11E-02	14.435	2.49E-02	14.9602	2.46E-02
23.1865	1.83E-02	22.583	1.97E-02	28.6184	9.26E-03	28.6579	9.10E-03
33.674	3.27E-04	32.6008	3.28E-02	-	-	-	-
54.2705	1.05E-02	53.3478	1.11E-02	53.0384	1.29E-02	52.5862	1.09E-02
104.608	2.67E-03	102.349	7.38E-03	90.9227	1.37E-02	91.9403	1.17E-02
-	-	103.36	1.29E-03	102.932	4.37E-03	103.345	3.88E-03
115.632	4.47E-03	113.684	6.09E-03	117.917	1.16E-02	117.648	8.65E-03
128.853	1.70E-02	124.015	1.63E-02	169.467	4.41E-03	170.337	3.66E-03
170.15	3.39E-03	166.247	7.99E-03	171.638	4.50E-03	172.288	4.35E-03
203.147	1.78E-03	196.958	5.08E-03	203.812	5.16E-03	205.02	4.90E-03
232.322	1.94E-03	233.476	6.89E-03	-	-	-	-
240.063	3.60E-03	237.609	2.07E-03	242.159	3.19E-03	243.238	3.21E-03
252.853	1.38E-03	250.112	3.40E-03	251.553	2.59E-03	252.399	2.53E-03
266.43	2.46E-03	263.36	3.87E-03	-	-	-	-
298.961	2.78E-03	276.952	3.86E-03	-	-	-	-
305.571	7.73E-04	295.842	2.82E-03	297.311	2.69E-03	298.346	2.15E-03
312.978	5.52E-04	312.984	1.99E-03	-	-	-	-
326.774	1.13E-03	322.065	1.02E-03	-	-	-	-
353.536	1.82E-03	349.472	3.73E-03	352.571	2.60E-03	353.828	2.48E-03
368.158	1.95E-03	-	-	360.189	2.65E-03	361.452	2.57E-03
377.425	1.06E-03	-	-	-	-	-	-

Table 4.11: Identified modes from EMA on four tests corresponding to two different boundary conditions

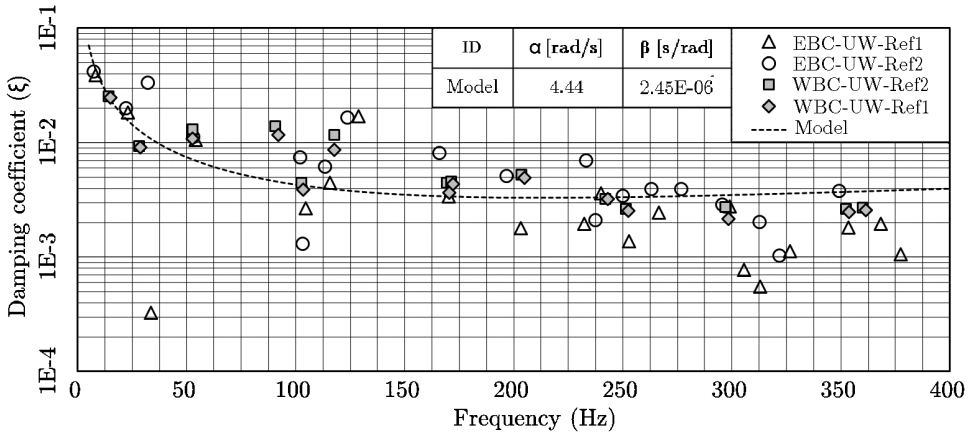

Figure 4.47: Adjusted damping model for the model tower EMA

4.2.1.2 FEM modal analysis

The execution of the numerical parametric analysis requires the use of a FEM model to which artificial induced alterations are applied. Modal solutions are obtained from that model, FRFs are synthesized from those modal results and damage indicators are generated from those FRFs. It is then necessary to generate a model that is both representative of the model experimental structure and simple enough to allow flexibility and computational efficiency in the progression of the successive damage stages.

Models developed in Ansys use BEAM188 3-D linear finite strain beam elements. Material used for all sections is linear structural steel compliant with the ASTM-A36 standard, with a Young modulus of E = 200 GPa and a Poisson ration of $\nu = 0.3$, and an equivalent density of $\rho = 8623$ kg/m^3. This density is far above its nominal value of $\rho = 7850$ kg/m^3 as it has been calibrated to account for additional weight in the structure caused by screws, nuts, washers and rivets. This value has been obtained by matching the Torsion I and Torsion II modes of the structure, which have been observed to be boundary condition invariant (as long as a pinned link is kept between the truss structure and the concrete block). Thermal expansion coefficient is set at 1.2E-5 1/^{o}C and the reference temperature for all thermal stresses tests is set at $T_{ref} = 20$ ^{o}C. Elements in the mesh have a characteristic length of 10 mm. The concrete base block is treated as a monolithic rigid element with rigid motion movements allowed and a density of $\rho = 2100$ kg/m^3.

During the verification of FRF synthesis, experimental acquisitions obtained for the elastic boundary condition reference tests were tried to be replicated. However, although several attempts were made, those were unfruitful in matching the FEM model to experimental results. The interaction between the floor, the elastic support and the concrete block in the base could not be numerically reproduced. Although torsional modes (Torsion II and Torsion II) could be accurately reproduced with a pinned connection of the tower with the base, bending modes were far from the experimentally observed ones. So then, a second experimental campaign was then proposed using wedged boundary conditions.

In the second experimental campaign, the base concrete block is simply supported on the ground. All its perimeter is wedged to avoid relative displacements. However, this restrain is not perfect and relative movements are identified in post-process. However, this second boundary condition can be successfully reproduced in a FEM model as already stated before. This second FEM model accurately reproduces the interaction with the boundary conditions and the ground and is referred as *FEM-Fit* model.

The concrete base block is modelled as a rigid solid of dimensions 1000 x 1000 x 200 mm with an equivalent density of $\rho = 2100$ kg/m^3 and with an elastic support of $K_{sup} = 5 \cdot 10^7$ N/m^3 extended to all the lower interface plane between the concrete block and the ground. Mode shapes obtained for this configurations are shown in figure 4.48 and accurately reproduce natural frequencies and mode shapes experimentally determined using EMA.

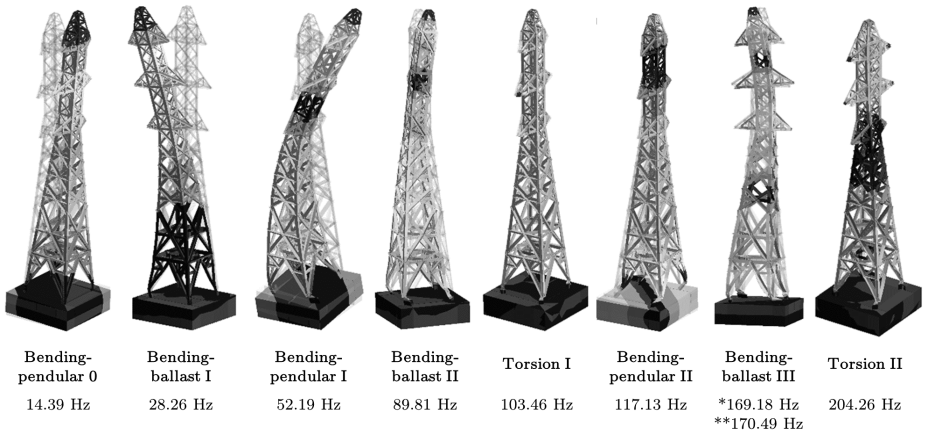

Figure 4.48: Mode shapes for the FEM model with experimentally fitted boundary conditions

This FEM-Fit model is used to verify the FRF synthesis. However, and in favour of simplicity in the structure and reduce computational time required for each case, a second FEM model is generated with simplified boundary conditions. This simplified boundary condition tries to replicate the mode shapes and frequencies that are considered to be dominated by the latticed steel structure dynamics. The simplified boundary conditions consist of four springs connected to each of the legs of the tower an allowing only vertical displacement (so lateral and transverse movements in the legs are restrained). The rotations are also freed, so the four supports are consistent with an spherical bearing with vertical displacement coupled to a spring. The equivalent stiffness of the springs is found to better reproduce the experimental results with a value of $K_s = 5 \cdot 10^7$ N/m per each of them. A comparison between the FRFs obtained from the second experimental boundary condition, its modelled numerical equivalent (FEM Fit) and the simplified boundary condition is shown in figure 4.53. The modal shapes of this second FEM model, referred as *FEM-Simple* are depicted in figure 4.49. A comparison between EMA determined natural frequencies, modal results from the FEM-Fit model and additional numeric results corresponding to the FEM-Simple model are depicted in table 4.12. Correlation between mode shapes depicted in table 4.12 is shown in figure 4.50 using the MAC matrix.

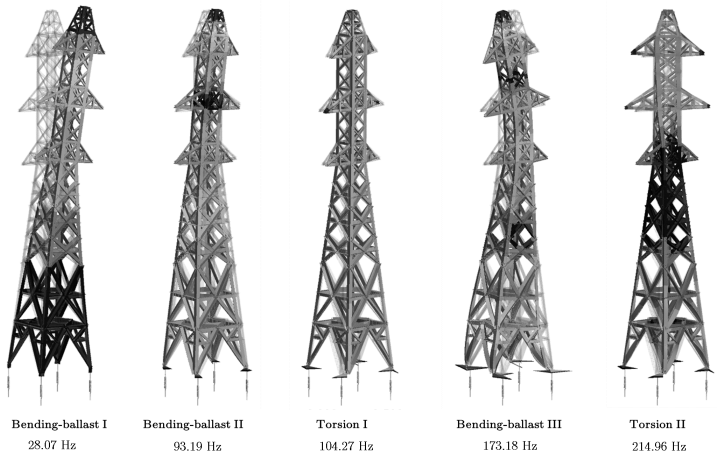

Figure 4.49: Mode shapes for the FEM model with simplified boundary conditions

	EMA		**FEM - Fit**	**FEM - Simple**
Name	f (Hz)	f (Hz)	f (Hz)	f (Hz)
Bending-pendular 0	14.53	14.94	14.39	-
Bending-ballast I	28.62	28.66	28.26	28.07
Bending-pendular I	53.01	52.52	52.19	-
Bending-ballast II	90.91	91.87	89.81	93.19
Torsion I	102.97	103.29	103.46	104.27
Bending-pendular II	117.80	117.70	117.13	-
Bending-ballast III	169.52	170.37	170.49	173.18
Bending-ballast III	171.65	172.30	170.49	-
Torsion II	203.90	204.89	204.26	214.96

Table 4.12: Results for experimental wedged unwired tests, fit FEM model and simple FEM model

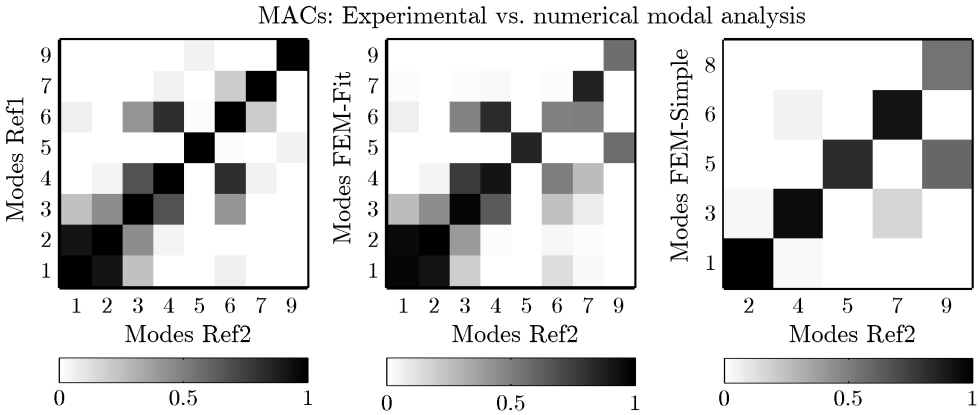

Figure 4.50: Experimental to numerical MACs.

Modal results from FEM are extracted from Ansys in a series of discrete points corresponding to the nodes of the real latticed structure (connections between bars of the structure) in a similar way of what is done with the aluminium plate (where a sub-mesh of 81 nodes is sampled from the numerical model). This numerical sampled mesh contains points in two different vertical faces of the tower, namely the fronatal and lateral planes already exposed. Locations in the frontal YZ plane define nodes where the X component of vibration is measured. Points in the XZ lateral plane define nodes in which the Y component of vibration is sampled. So then, the vibration is always sampled perpendicularly to the plane studied. The frontal plane includes a total of 65 sampled nodes, whereas the lateral one, 59. The sampled mesh, including nodes from both planes is shown in figures 4.51 and 4.52.

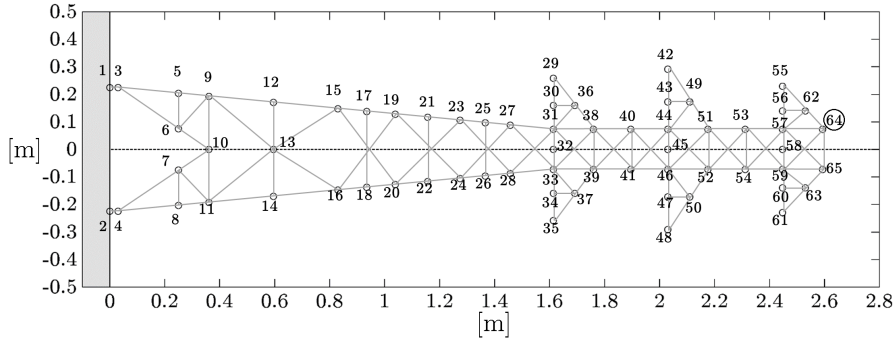

Figure 4.51: Numeric sub-sampled mesh. Frontal plane. YZ plane normal (X-direction)

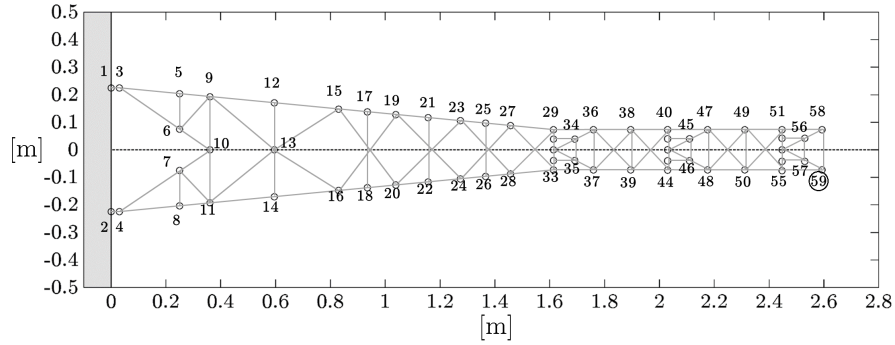

Figure 4.52: Numeric sub-sampled mesh. Lateral plane. XZ plane normal (Y-direction)

4.2.1.3 FRF comparison

FRFs synthesis verification is performed on modal results corresponding to nodes of the frontal plane. Modal results from models FEM-Fit and FEM-Simple are sampled to the mesh depicted in figure 4.51 corresponding to the frontal plane. The objective is to be able to assess the degree of similarity between the results synthesized from FEM modal data and the ones obtained via EMA so the procedure can be said to be

trustworthy.

Figure 4.53 shows a comparison between the two reference EMA tests for a wedged boundary conditions on the tower substructure without cables and the results obtained from synthesis from the FEM-Fit and FEM-Simple models. Acquisition mesh used is much coarser that the numerical sampling mesh. However, equivalent locations in the numerical mesh have been selected to coincide with those of the EMA mesh. FRFs correspond to numerical locations 8, 21, 38, 52 and 60 in the frontal plane and its correspondent experimental positions F4, F12, F20, F28, F34 (figure 4.46).

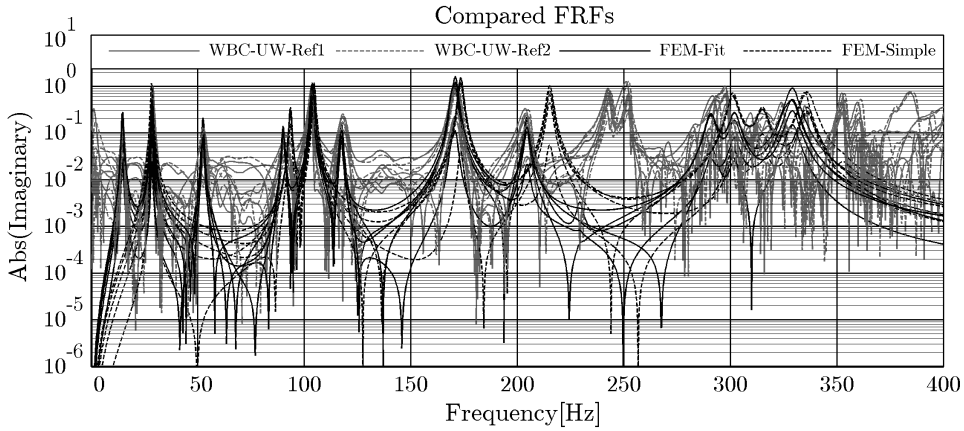

Figure 4.53: Comparison between experimental FRFs and synthetic FRFs for the model tower structure.

From the observation of figure 4.46) it becomes clear that the synthesis algorithm correctly reproduces the magnitude of the peaks in the FRFs. This is specially clear when focusing in the FEM-Fit synthetic FRFs which almost perfectly reproduce experimental FRFs up to 220 Hz. From that spectral point and onwards, some modes are not correctly reproduced by the FEM-Fit model although some others appear in their supposed locations. This facts suggests that the numerical model is still incomplete and lacks the description of additional phenomena. As the objective of this section in the discussion is not strictly to model the experimental behaviour of the tower, but to validate the synthesis methodology, and due to the fact that a simplified FEM-Simple model has already been adopted to perform the sensibility analysis, this discrepancy is considered to be of minor importance to further discussions.

Keeping the focus of interest in the same figure, and when comparing the synthetic FRFs obtained from the simplified FEM-Simple model, results shows that only certain modes are correctly reproduced by the simple model. However, this mode shapes coincide with the main bending and torsional modes. Only lattice-concrete coupled pendulum modes are not correctly reproduced by this simplified model. As the para-

metric analysis to be performed in subsequent sections of this research is faced from a comparative and relative point of view, the validity of this simplified model is considered enough to extract conclusions on the general behaviour and trends of the proposed structural shift indicators.

4.2.2 Numerical campaign

The parametric analysis on the SCI indicator using FEM derived data requires to introduce a series of intentionally made structural alterations to the baseline structure. The structural alterations on the modelled power transmission tower are divided in families of interventions, each corresponding to a typology of modification on the structure. These families include two families of global modifications on the structure (-10% to a +10% modification of the Young modulus and the effect of the thermal pre-stresses caused by temperatures in range -30^{o}C to 70^{o}C), two families of pre-stressing scenarios where the structure is progressive loaded up to Y-lateral and Z-axial buckling loads, one family corresponding to the progressive removal of trusses near the Z-zero level, another family involving the softening and hardening of the springs representing the flexible boundary condition, and a final family of cases representing the unbalances caused by the falling of cables that are originally suspended on the structure. The entire progression of damages in each family is depicted in tables 4.13 and 4.14.

Cases involving modification of the Young modulus are not realistic but serve as a guiding line of the behaviour of the indicator. Thermal pre-stresses are included in the analysis using the same base model that in the reference condition. A linear thermal analysis is executed on the structure (the reference temperature is always set at $T_{ref} = 20\ ^o$C). The deformed configuration induced by thermal gradients causes residual loads on members of the structure and is used as a pre-stressing condition. The linear modal analysis is solved atop this pre-stressed state. Second order displacement terms are active for these cases.

Z-axis (vertical) and Y-axis (lateral) pre-stressing families try to answer whether the damage indicator proposed is capable of detecting the progression of increasing growing loads that could approach buckling design limits. This is the case when heavy winds interact with power lines (specially with additional accretion ice rods on the lines due to extreme cold temperatures) or when external elements, such as fallen trees on the lines vertically overload the structure. Although axial buckling failure of power transmission towers is extremely rare, it has been included in the analysis for completion.

Buckling loads are determined from the same FEM model used in modal computations. To do so, unitary point loads are applied in all 6 tips of the arms in the direction studied

in each case, so the load is always symmetrical and uniformly distributed in all nodes. Values shown in this exposition refer to the total force applied to the 6 nodes (so the contribution to each arm is one sixth of this total value).

The first buckling mode critic load in the vertical direction (Z) is obtained applying a vertical unitary force at the mentioned nodes and is determined to be 174230 N. The first buckling mode critic load for the transverse direction (Y) is obtained similarly by applying a unitary force evenly distributed in the six arm tips and is found to be 9687 N. Buckling load in the X axis direction is found to be almost identical to the Y axis one. This s clearly justified by the geometrical symmetry on the tower. It is worth mentioning that the elastic boundary condition used for the model plays a major role in the absolute value of this first buckling mode. These alteration progression scenarios are depicted in the two initial diagrams in figure 4.54.

The family of damages involving trusses removal is referred using the nomenclature exposed in figure 4.55. Southern face of the structure is considered to be quasi-parallel to the YZ plane and thus is considered to be part of the frontal plane. So then, the removal of trusses always happens in elements in the front plane and in the east (lateral) plane. Symmetry arguments would suggest that equivalent removal of trusses in complementary planes to the frontal and lateral ones, would result in the same outcome. However this affirmation is not addressed in this work.

Family of structural alteration involving the boundary conditions tries to reproduce the effect of changing the supporting characteristics of the soil around the foundations of the tower, a phenomena that is usually encountered in real operation scenarios.

Finally, the last family tries to reproduce the imbalance effect caused by the loss of some cables in the structure. The dynamic interaction between the cables and the structure is left out of scope of this investigation, as its modelling is arduous and has a far from straight-forward implementation. Some research works [98] solely focus on the cable-to-tower dynamic interaction and it is not the intention of the author to face this phenomena. Cable interaction is modelled as the arising of certain unbalanced forces that act on the tips of each arm. If the reference tower is considered to be perfectly balanced, a complete disconnection of the middle right cable from the tower induces a vertical unbalance in the three other left arm tips equal to the vertical load that the middle right link was supporting. The tension for each cable is estimated for a worst case scenario as one sixth of the transverse buckling load with a safety factor of 1.5. This unitary unbalanced tension is determined to be F_{pull} = 1076 N. This means that if the 6 cables were pulling the tower from its 6 links from only one side, with a force of 1.5 times that tension, the structure would undergo a buckling failure. The damage scenarios here presented suppose that the cables in one of the two symmetry

planes of the structure are always intact and in place, whereas the cables in the other semi-space are the ones that fall causing unbalances. It is worth noting that this is not a realistic scenario of a cable breaking but serves as a tool to assess the ability of the indicator to detect unbalanced loads on the structure. Those cases are depicted in figure 4.54.

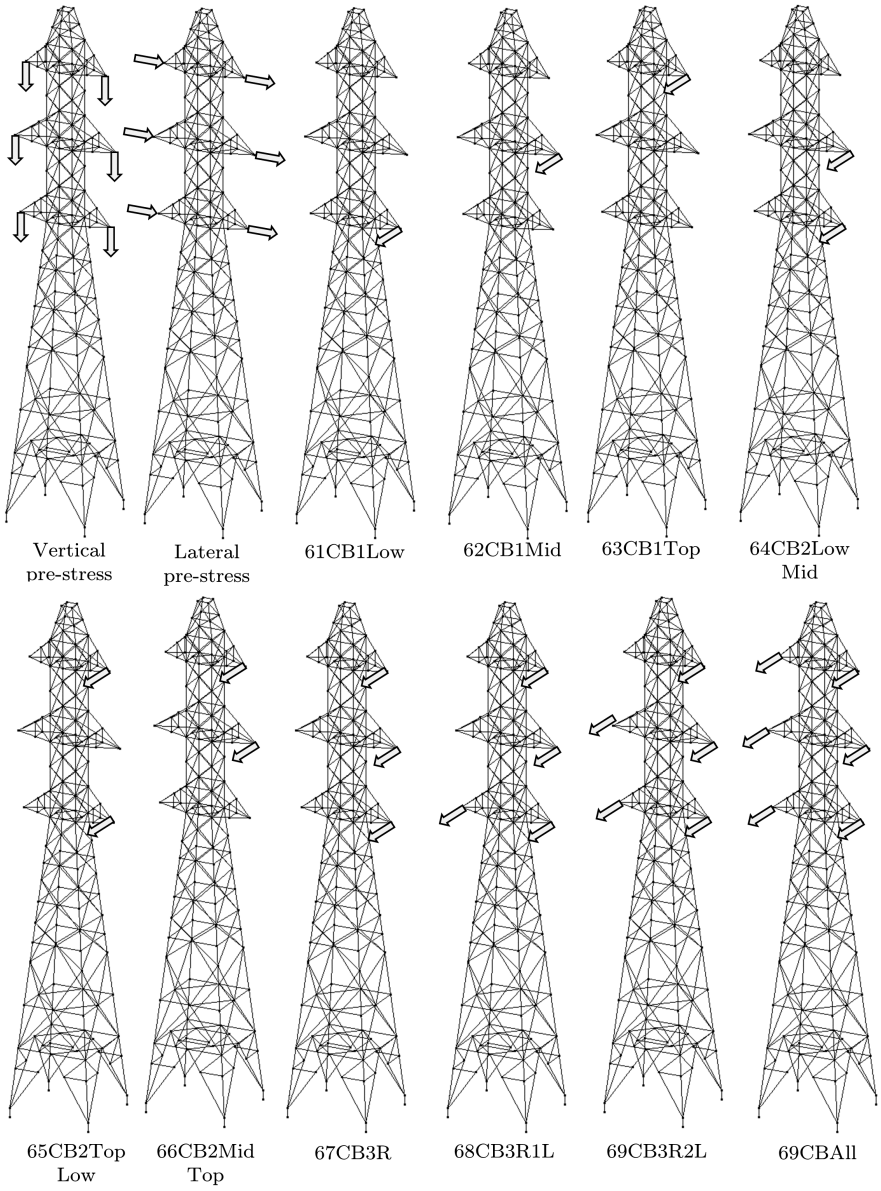

Figure 4.54: Alteration scenarios on the numeric model tower involving cables.

	#	Familiy	Tag	Description	Value
-	00	Reference	00Ref	Baseline reference pristine state	-
Global modification	01	Young Modulus	01YM-10	10% Young modulus reduction	180 GPa
	02		02YM-5	5% Young modulus reduction	185 GPa
	03		03YM-2	2% Young modulus reduction	190 GPa
	04		04YM-1	1% Young modulus reduction	195 GPa
	05		05YM-0.5	0.5% Young modulus reduction	198 GPa
	06		06YM+0.5	0.5% Young modulus increase	202 GPa
	07		07YM+1	1% Young modulus increase	205 GPa
	08		08YM+2	2% Young modulus increase	210 GPa
	09		09YM+5	5% Young modulus increase	215 GPa
	10		10YM+10	10% Young modulus increase	220 GPa
	11	Ambient temperature	11TP-30	Temperature	-30°C
	12		12TP-20	Temperature	-20°C
	13		13TP-10	Temperature	-10°C
	14		14TP-0	Temperature	0°C
	15		15TP+10	Temperature	10°C
	16		16TP+30	Temperature	20°C
	17		17TP+40	Temperature	30°C
	18		18TP+50	Temperature	40°C
	19		19TP+60	Temperature	60°C
	20		20TP+70	Temperature	70°C
Pre-stressing	21	Vertical pre-stress	21CW10	Vertical overload at 10% P_{crit}	17423 N
	22		22CW20	Vertical overload at 20% P_{crit}	34846 N
	23		23CW30	Vertical overload at 30% P_{crit}	52269 N
	24		24CW40	Vertical overload at 40% P_{crit}	69692 N
	25		25CW50	Vertical overload at 50% P_{crit}	87115 N
	26		26CW60	Vertical overload at 60% P_{crit}	104538 N
	27		27CW70	Vertical overload at 70% P_{crit}	121961 N
	28		28CW80	Vertical overload at 80% P_{crit}	139384 N
	29		29CW90	Vertical overload at 90% P_{crit}	156807 N
	30		30CW99	Vertical overload at 99% P_{crit}	172488 N
	31	Lateral pre-stress	31WA10	Lateral overload at 10% P_{crit}	969 N
	32		32WA20	Lateral overload at 20% P_{crit}	1937 N
	33		33WA30	Lateral overload at 30% P_{crit}	2906 N
	34		34WA40	Lateral overload at 40% P_{crit}	3875 N
	35		35WA50	Lateral overload at 50% P_{crit}	4844 N
	36		36WA60	Lateral overload at 60% P_{crit}	5812 N
	37		37WA70	Lateral overload at 70% P_{crit}	6781 N
	38		38WA80	Lateral overload at 80% P_{crit}	7750 N
	39		39WA90	Lateral overload at 90% P_{crit}	8719 N
	40		40WA97	Lateral overload at 97% P_{crit}	9397 N

Table 4.13: Model tower cases in the parametric study of the indicator.

	#	Familiy	Tag	Description	Associated value
Local modification	41	Member removal	41B1T0S0P	Trusses removed	S3R
	42		42B2T0S0P	Trusses removed	41 + S3L
	43		43B3T0S0P	Trusses removed	42 + E3L
	44		44B3T1S0P	Trusses removed	43 + S2R
	45		45B3T2S0P	Trusses removed	44 + S2L
	46		46B3T3S0P	Trusses removed	45 + E2L
	47		47B3T3S1P	Trusses removed	46 + S1R
	48		48B3T3S2P	Trusses removed	47 + S1L
	49		49B3T3S3P	Trusses removed	48 + E1L
	50		50BCorr	Corrosion analogy	SE loosen
Boundary modification	51	Elastic support	51ES2.5E7	Elastic boundary condition	2.50E7 N/m
	52		52ES3.0E7	Elastic boundary condition	3.75E7 N/m
	53		53ES3.5E7	Elastic boundary condition	4.00E7 N/m
	54		54ES4.0E7	Elastic boundary condition	4.50E7 N/m
	55		55ES4.5E7	Elastic boundary condition	4.75E7 N/m
	56		56ES6.0E7	Elastic boundary condition	5.25E7 N/m
	57		57ES7.0E7	Elastic boundary condition	5.50E7 N/m
	58		58ES8.0E7	Elastic boundary condition	6.00E7 N/m
	59		59ES9.0E7	Elastic boundary condition	7.50E7 N/m
	60		60ES1.0E8	Elastic boundary condition	1.00E8 N/m
Cable falls	61	Cable falls	61CB1Low	Unbalanced in-line load	1076 N
	62		62CB1Mid	Unbalanced in-line load	1076 N
	63		63CB1Top	Unbalanced in-line load	1076 N
	64		64CB2LowMid	Unbalanced in-line load	2153 N
	65		65CB2TopLow	Unbalanced in-line load	2153 N
	66		66CB2MidTop	Unbalanced in-line load	2153 N
	67		67CB3R	Unbalanced in-line load	3229 N
	68		68CB3R1L	Unbalanced in-line load	4305 N
	69		69CB3R2L	Unbalanced in-line load	5382 N
	70		70CBAll	Unbalanced in-line load	6458 N

Table 4.14: Model tower cases in the parametric study of the indicator (cont).

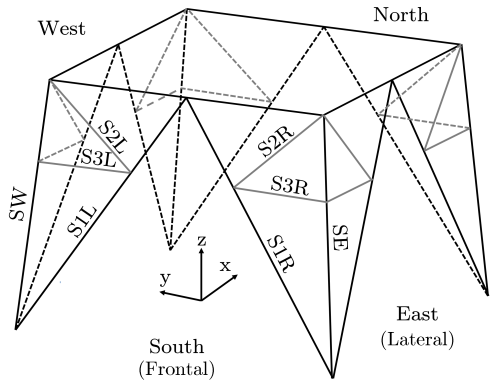

Figure 4.55: Bars removed in structural assessment scenarios.

4.2.3 Parameter sensibility

Parametric analysis involving the study of the influence of the frequency resolution is not executed for this second campaign as the previous section has demonstrated that it is, by far, the parameter with a lesser influence on the behaviour of the SCI in front of damage as long as reasonable Δf are kept. The stability requirement in frequency resolution is so loose that it is considered to be always granted by the acquisition resolutions commonly adopted in experimental analysis.

4.2.3.1 Driving point

In the numerical campaign on the aluminium plate, it is demonstrated that the selection of the driving point used to perform an EMA test (or to synthesize FRFs in parametric studies) plays a major role in the values of SCI indicators. Using observations made for the aluminium plate, the same methodology presented before is used to pick the optimal driving point that better reproduces the self-CFDAC of a virtual EMA involving all driving points and all excited points (a CFDAC indicator generated using the full mobility $\mathbf{H}(\omega)$ matrix). The methodology proposed picks as the driving point, the one whose auto-CFDAC better resembles the full mobility matrix CFDAC. Again, the quantification parameter used to establish the degree of similarity between CFDACs is the 1-PCC so the lowest value indicates the most representative driving point of the full inertance matrix.

Two tested planes in the structure, frontal and lateral, are independently analysed to obtain the most suitable driving point individually. Each of these two analysis is done considering only FRFs series corresponding to the points and directions characteristic of each testing plane. CFDACs are generated using a bandwidth of 400 Hz with a frequency resolution of Δf = 0.5 Hz. Results for this first analysis are shown in figures 4.56 and 4.56 for the frontal and lateral planes respectively. As it can be observed, the most representative point of the frontal plane is point 43 in that same face whereas point 58 of the lateral face is the most representative for that second plane. However, experimental feasibility arguments arise when trying to extrapolate these conclusions to a real scenario (such as the downscaled model of the tower to be constructed and tested in laboratory conditions).

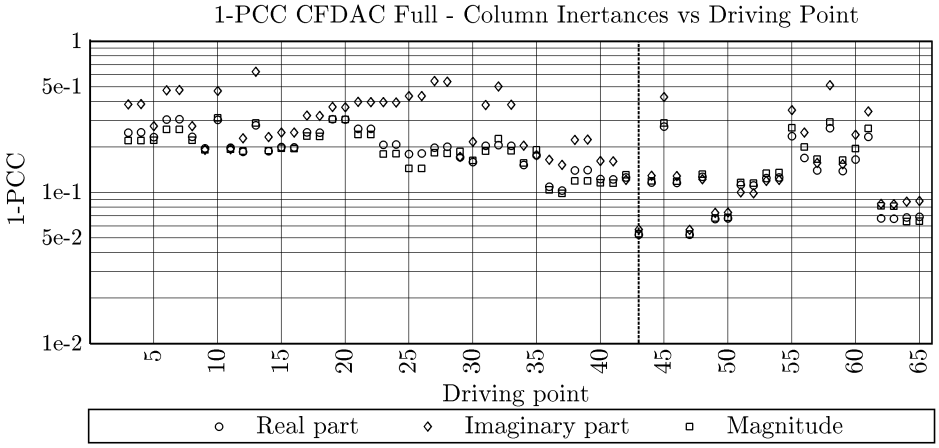

Figure 4.56: Numerical sub-sampled mesh for X direction.

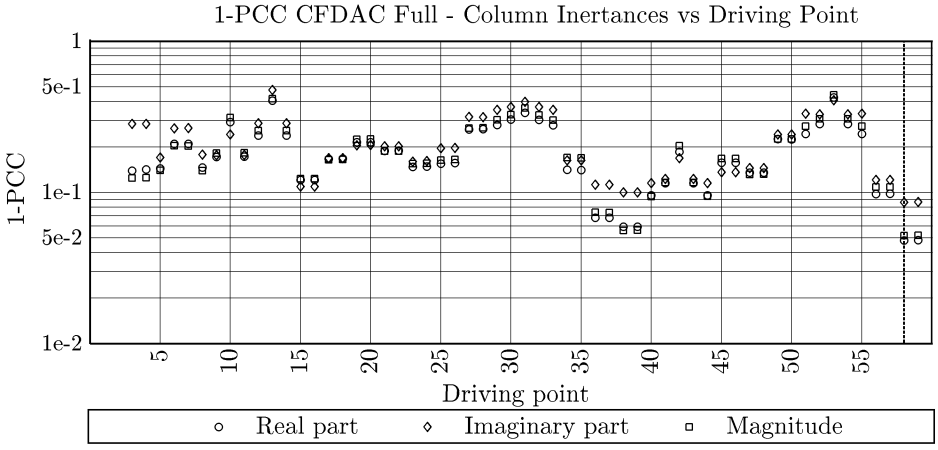

Figure 4.57: Numerical sub-sampled mesh for Y direction.

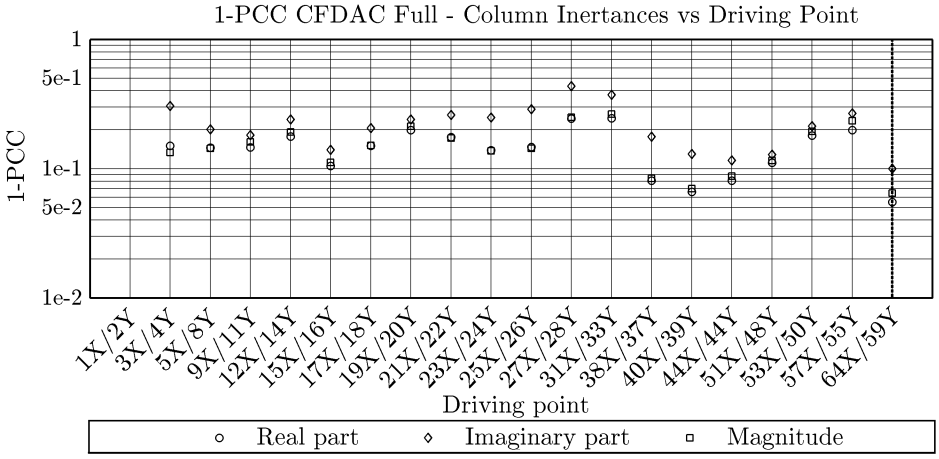

Figure 4.58: Numerical sub-sampled mesh for combined X and Y directions.

Real application of the methodology demands the inclusion of practicality arguments in the discussion. Although performing two separate test on the two different planes using the respectively best driving point as the reference is possible, this methodology is aimed to be implemented in a real in-field scenario (ambient excitation instead of EMA is the distant goal but out of scope of this investigation). So then, economy arguments suggest to use only one acquisition reference point which captures information in the two directions. This is the numerical equivalent of positioning a 2-axis accelerometer on any of the shared points of the two tested planes and avoiding the use of two accelerometers. So then, potential locations for the reference driving point are reduced to the shared nodes between the two planes.

If the same optimal driving-point selection methodology is applied but considering data series for both two planes altogether, and possible reference locations are limited to the shared nodal line between the two planes, results in figure 4.58 show that the optimal driving point is located in the position 64X/59Y.

Figure 4.59 shows the influence of the driving point pair selected in the SCIs. On the other hand, the same results are shown in figure 4.60 as relative values to the results corresponding to the optimal driving point pair 64X/59Y. Observing the results. the same conclusion exposed for the aluminium plate is drawn for the model tower. The driving point plays a major role in the value that the structural alteration indicator adopts but no clear tendency is observed. So then non-optimal driving points include a dispersion that can not be quantified *a prori*. It is desirable to select driving points that better reproduce theoretical maximum modal visibility achieved by using the full mobility matrix.

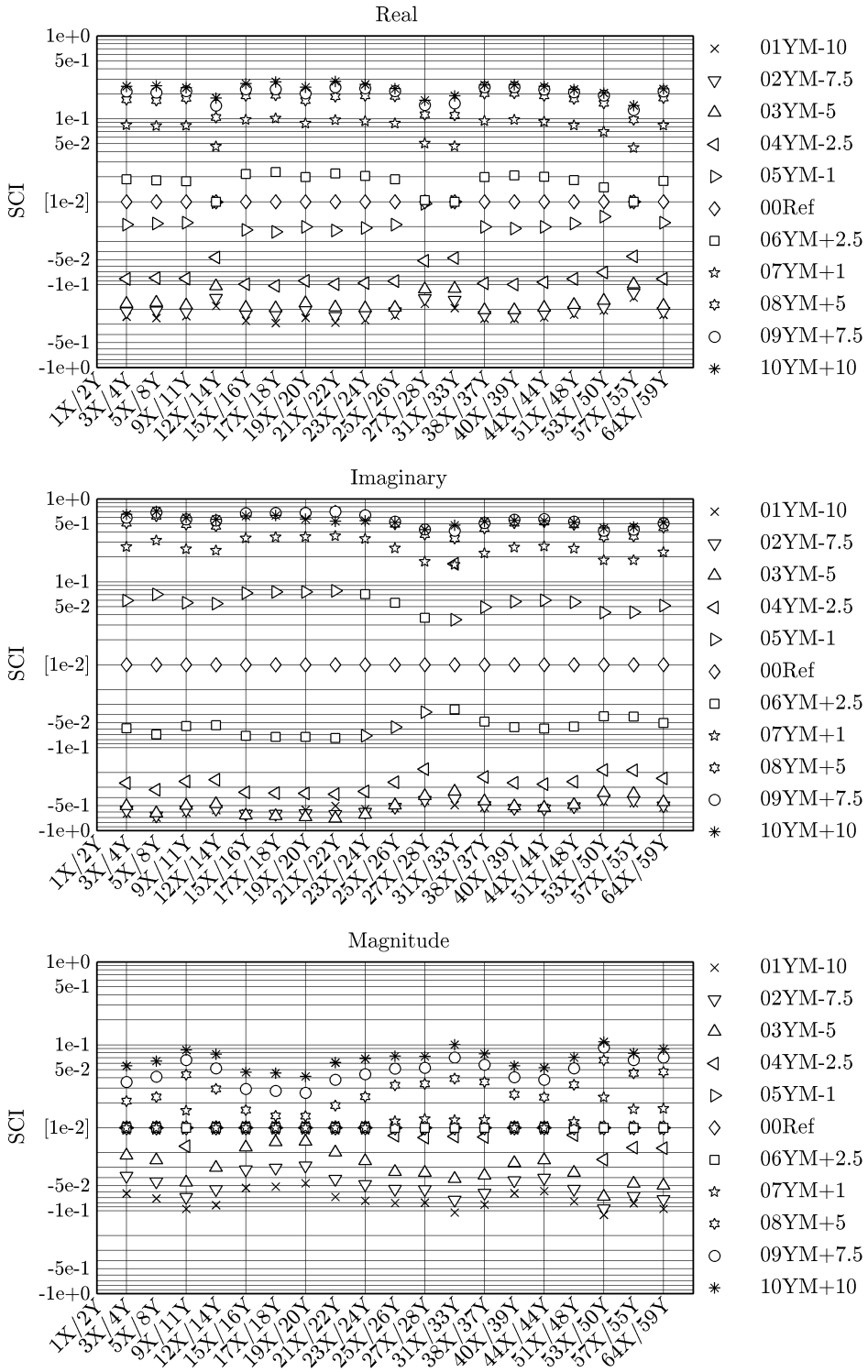

Figure 4.59: Scaled Tower. SCIs vs driving points.

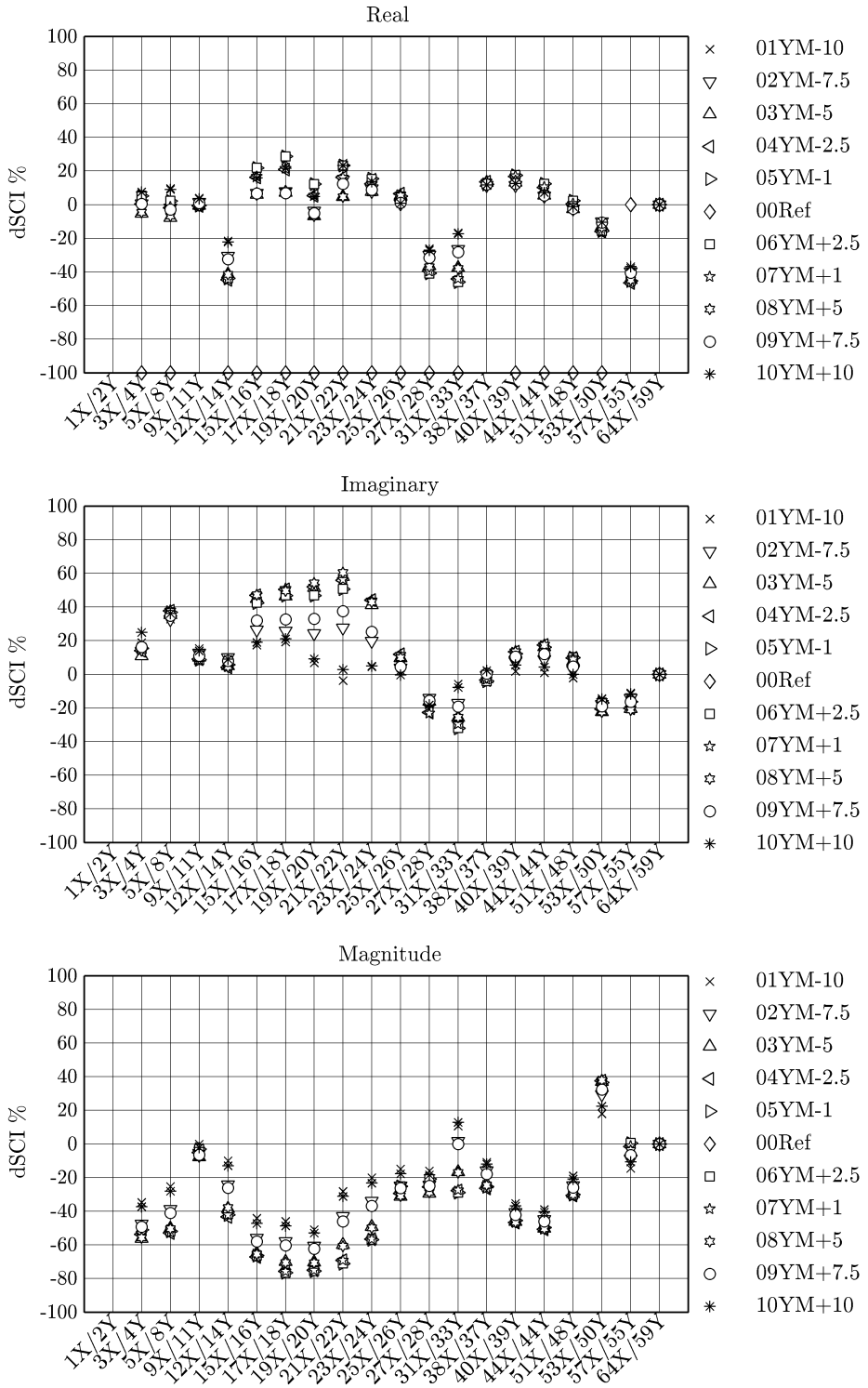

Figure 4.60: Scaled Tower. SCIs variations vs driving points.

4.2.3.2 Mesh density

Parametric analysis studying the influence of the number of acquisition points in the SCI indicators uses sub-meshes shown in table 4.15. CFDACs are generated using a frequency range of 400 Hz, with a frequency resolution of $\Delta f = 0.5$ Hz and driving points 64X/59Y as references for the FRFs corresponding to both planes in the structure studied.

The initial sub-sampled mesh from Ansys is selected so it includes all major nodes connecting main truss elements in the structure. For the mesh-dependent parametric study, another sub-set onf increasingly coarser meshes are used to reduce the amount of geometrically distributed data series available. The nodes in the sub-meshes here presented have been hand-picked following the same criteria that would be used if an EMA would have to be done with reduced number of acquisitions. Although surely subjective, experience in the execution of EMA is always a key point in assuring that acquisitions present the higher information-to-effort ratio. Sub-mesh tagged 36X30Y is equivalent to the experimental mesh used to execute EMA test on the built downscaled power transmission tower. Nodes in each sub-mesh are referred per each of the two planes of interest in the tower.

Mesh ID	**Dir**	**Nodes IDs**
3X3Y	X	34 43 60
	Y	33 40 55
5X5Y	X	16 23 34 43 60
	Y	16 23 33 40 55
10X10Y	X	9 14 15 22 27 34 38 43 52 60
	Y	9 14 15 22 27 33 40 55
24X24Y	X	3 4 9 11 12 14 15 16 19 20 23 24 27 28 30 34 40 41 43 47 53 54 56 60
	Y	3 4 9 11 12 14 15 16 19 20 23 24 27 28 29 33 38 39 40 44 49 50 51 55
36X30Y	X	3 4 9 11 12 14 15 16 19 20 23 24 27 28 30 31 33 34 38 39 40 41 43 44 46 47 51 52 53 54 56 57 59 60 64 65
	Y	3 4 9 11 12 14 15 16 19 20 23 24 27 28 29 33 36 37 38 39 40 44 47 48 49 50 51 55 58 59
42X36Y	X	3 4 9 11 12 14 15 16 17 18 19 20 21 22 23 24 25 26 27 28 30 31 33 34 38 39 40 41 43 44 46 47 51 52 53 54 56 57 59 60 64 65
	Y	3 4 9 11 12 14 15 16 19 20 23 24 27 28 29 30 33 35 36 37 38 39 40 43 44 45 47 48 49 50 51 52 55 57 58 59
50X42Y	X	3:1:5 8:1:9 11:1:12 14:1:31 33:1:35 38:1:44 46:1:48 51:1:57 59:1:61 64:1:65
	Y	3:1:4 9:1:12 14:1:16 19:1:20 23:1:24 27:1:30 32:1:41 43:1:52 54:1:59
65X59Y	X	1:1:65
	Y	1:1:59

Table 4.15: Sub-sampled meshes in the numerical study of the model tower.

Results depicted in figure 4.61 as real values of the SCIs do not show apparent variation in front of the mesh density. Figure 4.62 exposes the same results in relative form to the reference full 65X59Y mesh. The analysis of the relative variation of the SCIs in front of the number of points available for the CFDAC computation in the figure shows that the indicator is almost insensitive to variations in the mesh density once the 36X30Y density mesh is surpassed.

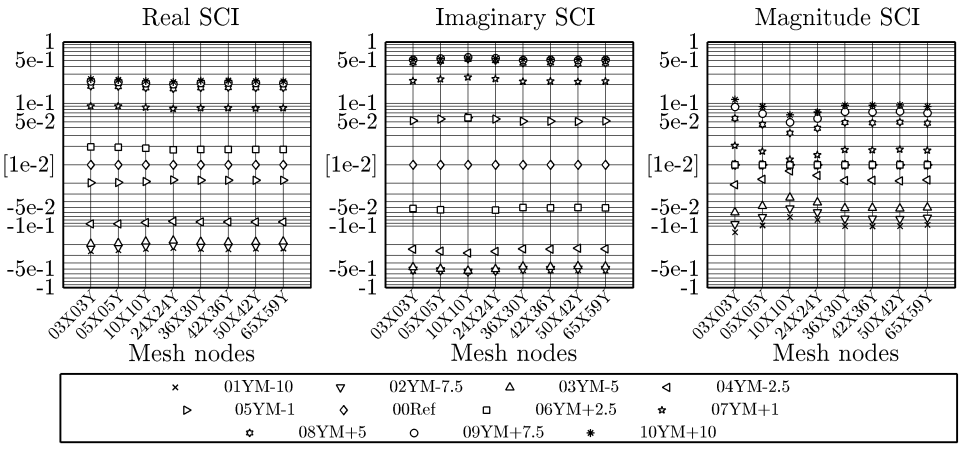

Figure 4.61: SCIs vs mesh density. FEM scaled tower. BW = 400Hz, Δf = 0.5Hz, DP64X/59Y

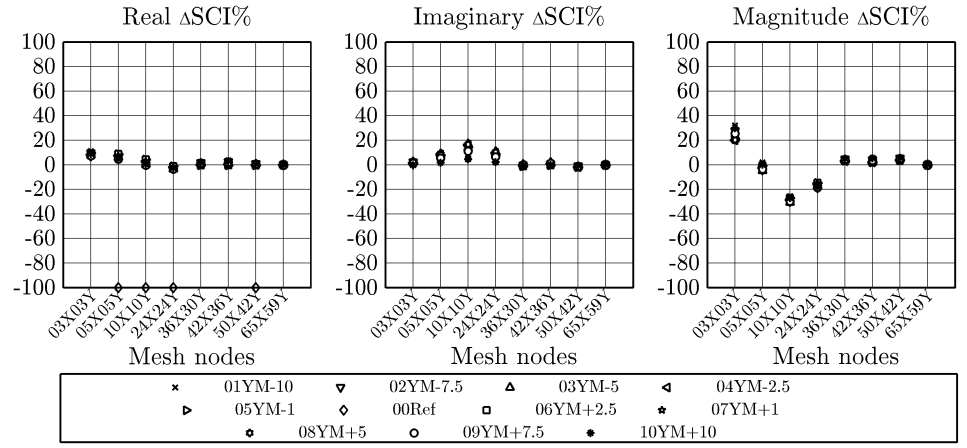

Figure 4.62: SCI shift vs mesh density. FEM scaled tower. BW = 400Hz, Δf = 0.5Hz, DP64X/59Y

If results are compared to the aluminium plate, the model tower shows an increased stability of its indicators in front of the mesh density. This is imputed to the fact that fewer points are required to describe the modal shapes (and thus, the spectral shapes) of the tower. In the plate cases, it is always needed to use a relative large amount of points to accurately describe mode shapes. As this requirement is less strict for this structural typology, coarser meshes assure relatively stable SCI values.

4.2.3.3 Bandwidth

Sensibility of the SCI indicators in front of the bandwidth is done for a range comprised between 25 Hz and 400 Hz in 25 Hz steps. Frequency resolution is kept at $\Delta f = 0.5$ Hz, and the full 65X59Y mesh with driving point 64X/59Y is used to compute the CFDACs involved in the analysis.

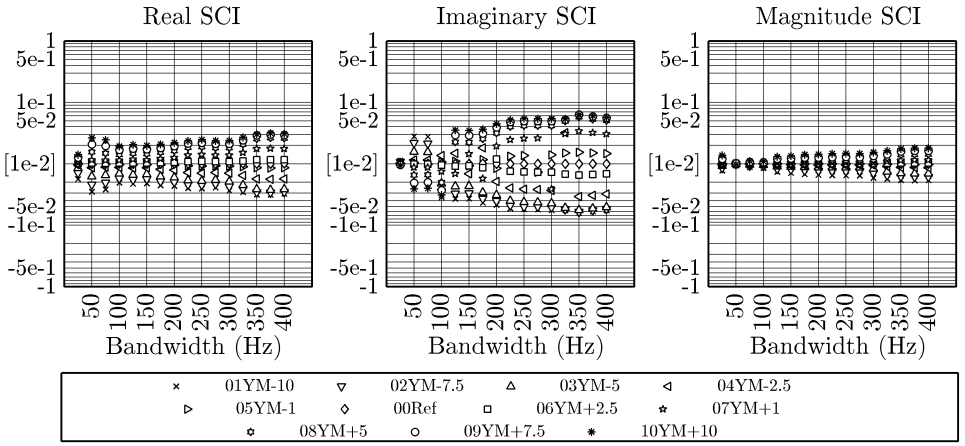

Figure 4.63: SCIs vs bandwidth. FEM scaled tower. 65X59Y mesh, $\Delta f = 0.5$ Hz, DP64X/59Y

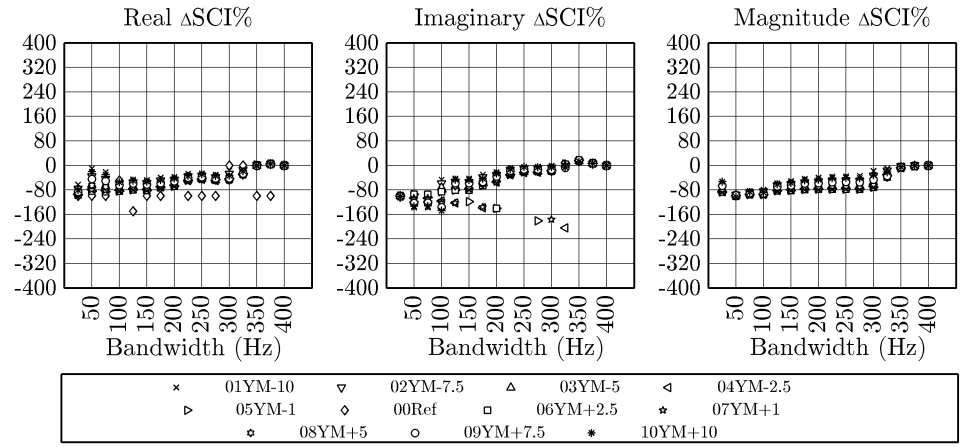

Figure 4.64: SCI shifts vs bandwidth. FEM scaled tower. 65X59Y mesh, $\Delta f = 0.5$ Hz, DP64X/59Y

Observing figures 4.63 and 4.64 it becomes clear that the structural typology influences the bandwidth sensibility of the SCI indicator, specially when comparing this results with the aluminium plate ones. In that other structure, a monotonic growth is observed in front of the maximum frequency of interest. This correlation, however, is less direct in this numerical analysis. This fact is attributed to the coarser mode density in the range for the scaled tower. The plate previously studied presents a greater amount

of mode shapes in the bandwidth studied. As the change in this parameter has less impact on the modal density in FRFs, this dependency is less noticeable for this structural typology.

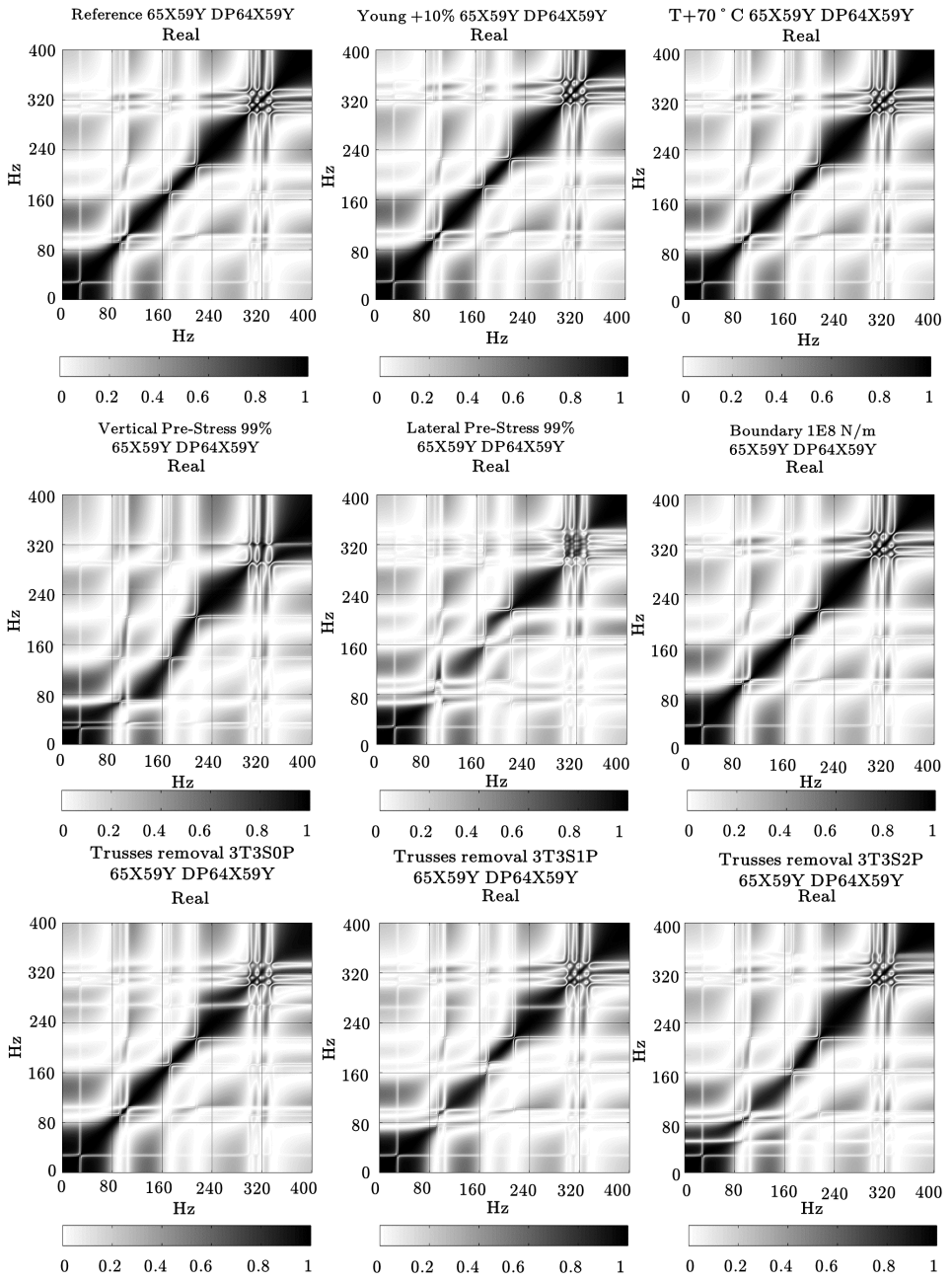

Figure 4.65: FEM model tower. CFDAC vs damage typology (pt.1)

In a real structure application, mode richness is expected to be very poor as both ambient excitation and acquisition hardware costs limit the relatively clean bandwidth that can be adequately captured. With this in mind, bandwidth dependency of the SCIs is expected to be much more favourable (towards stabilization as the maximum frequency of interest grows) in real application scenarios.

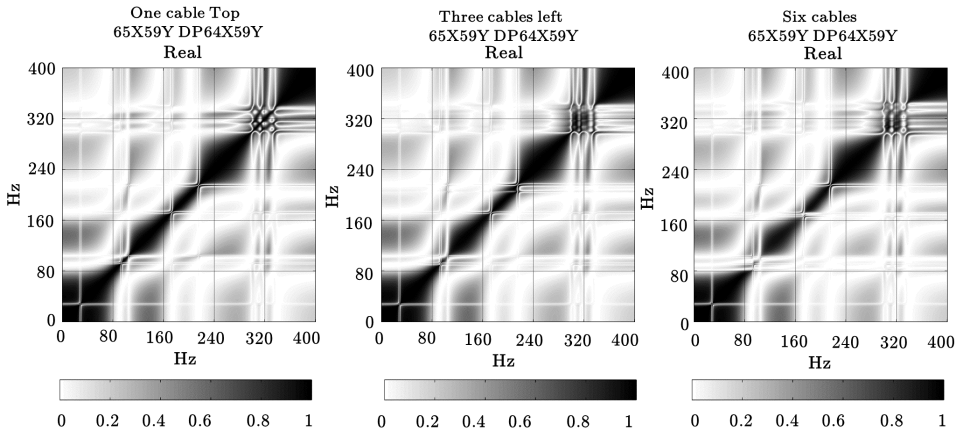

Figure 4.66: FEM model tower. CFDAC vs damage typology (pt.2)

4.2.4 Structural modification assessment

For the numerical campaign involving the scaled model tower, it is decided to drop the correlation of the SCI indicators with the residual stiffness out of the investigation. For the aluminium plate, the measurement of the residual stiffness of the structure is a relatively easy task to perform from an experimental point of view. So then a direct experimental to numeric comparison of the relationship between SCIs and residual stiffness is an affordable task to address. However, the measurement of the experimental stiffness on a latticed structure is far from being so straight-forward. This kind of measurement would require the use of auxiliary supporting structures to apply controlled loads and to install the displacement measuring gauges. In addition, the numerical numerical model of the tower is very different from the real dynamics of the prototype observed, so numerical to experimental comparison of SCIs is neither addressed. The tasks addressed in this section are then reduced to the observation of the behaviour of the real part of the CFDAC matrices as structural changes are introduced in the structure and to the observation of the evolution of the SCIs indicators as alterations progress in the already exposed families.

4.2.4.1 Damage typology and the CFDAC

This section describes the qualitative changes observed in the real part of the CFDAC matrices when altered states are compared to the reference intact conditions. Again, the real part of the CFDAC is selectd to be shown as it contains more information that the imaginary part of the same indicator. The analysis here presented is executed for a total bandwidth of 400 Hz, with a frequency resolution of 0.5 Hz, using the full 65X59Y mesh and keeping the driving point in position 64X/59Y

Figures 4.65 and 4.66 shown the influence of structural alterations in the real part of the CFDAC. The first observation that can be done is that the diagonal structure in the CFDAC matrices is much thicker that the one observed for the aluminium plate. This is the result of the modal density, which is much scarce in the scaled tower. This fact allows the modal correlation between spectral regions close to a resonance to show correlation in wider regions than in the aluminium plate does.

The alterations corresponding to the modification of the Young modulus present a tendency very similar to the already observed with the aluminium plate. That tendency appears as a global shift in the diagonal structure of the CFADC towards the positive triangular sub-matrix for Young modulus increases and towards the negative triangular sub-matrix when the Young modulus is lowered. This behaviour is exactly parallel to the one observed for the Young and thickness modifications in the aluminium plate. Thermal effects have no apparent effect on the CFDAC. This observation is latter confirmed when analysing these cases using the SCI indicators.

Vertical pre-stresses appear in the CFDAC as a general lowering in the diagonal structure of the CFDAC plus and accentuated degradation in the region around 160 Hz. Lateral pre-stresses show a more drastic pattern causing a general lowering in the diagonal structure of the CFDAC plus a general and noticeble loss of correlation up to 240 Hz. Removal of tertiary and secondary trusses have a residual (but noticeable effect) in the CFDAC causing the appearence of little de-coherence lines, for example the one that can be observed around 280Hz in the case 3T3S0P. As pimary diagonal trusses are removed the effect starts to be more and more noticeable with shifts in the diagonal of the CDFDAC around 160 Hz. Unbalances due to the removal of cables are hardly noticeable in the whole spectrum of the CFDAC except for the regions around the 320 Hz segment. In that region a complex pattern is present, even for reference cases. This is usually the case when multiple local modes of individual trusses appear in the analysis. In this regions of the spectra, the unbalanced loads cause that the complex pattern becomes even richer in terms of de-coherence lines. This can be attributed to the fact that initially symmetric local modes become unsymmetrical and

split up in the spectral map.

4.2.4.2 Damage typology and the SCI

In this section the tendencies of the SCI indicators are shown per each of the structural modification families for the model downscaled tower. This results allow to follow the evolution of structural alterations as a progression with tags C1 to C11 referring to each of the cases in each family. The correspondences for cases of each structural alteration family are shown in table 4.16.

Family of Young modulus alteration shows a trend consistent with the damage introduced in the structure. Negative values of the SCI correlate well with lowering of the Young modulus value. In a similar way, increases in the Young modulus adequately correlate with positive values of the SCI indicators. The family of thermal pre-stresses are always below the detection threshold, which is considered to be at an absolute value of SCIs of about 1E-2. This value has been set in the experimental campaign involving the aluminium plate as the closest potency of 10 below SCIs achieved in repeatability tests. Vertical and lateral pre-stressing families also present a consistent trend, showing damage when second order terms appear in the structure. Minimum vertical pre-stress detectable is 10% of the axial buckling load whereas the lateral pre-stress detection limit is around a 30% of the lateral buckling load.

The family of trusses removal presents a specially interesting behaviour. The removal of tertiary and secondary trusses (as depicted in figure 4.55) has the effect of increasing the natural frequencies in the system so the SCI indicators show reinforcement of the structure. That can be explained considering that these trusses mostly contribute in terms of mass to the structure, so its removal decreases the total mass of the system, so natural frequencies slightly increase. However, the removal of the primary diagonal members have the expected effect of decreasing the natural frequencies of the system and thus, the SCI indicators show negative values indicating damage. The family consisting of the modification of the boundary condition presents the expected behaviour: hardening of the boundary stiffness shows reinforcement in the SCI indicators whereas softening of the elastic support shows damage in the SCIs.

The family of structural unbalances caused by the breaking of cables presents disperse trends in real and imaginary parts and in magnitude indicators. Conclusions can not be elaborated based on those trends except that the SCIs indicators are capable of noticing that *something* has happened in the structure, acting as an detection alarm. The sign is not consistent with the expected behaviour which was to present similar trends to the lower stages of lateral buckling family cases.

As it is shown for the aluminium plate, the real part SCI indicator is much more linear in front of alterations introduced in the structure whereas the imaginary part indicator is much more sensible. Same conclusion is extracted from these results that both parts can be used in damage detection with different objectives: whereas the real SCI can be used to establish a damage progression that can be related with the amount of damage accumulated, the imaginary part SCI can be used as an early detector of changes in the system due to its increased sensibility. It is additionally observed that small quantities of alteration in the structure also invalidate the sign decision algorithm for the SCI indicator. This observation could be the source for the dispersion observed in the results concerning the family of cable losses analogy although it is not demonstrated in this investigation.

Despite this, the indicators proposed show remarkable sensibility in front of the structural alteration scenarios proposed. Besides this, the indicators are capable of discerning reinforcements from damages with notable accuracy when observing cases corresponding to an increase of the Young modulus of the material and to the stiffening of the elastic boundary condition. An interesting observation is made concerning the ability of the indicators in detecting operational conditions close to the buckling failure envelope of the structure, both in vertical and transverse directions. Finally, this first parametric analysis shows that the indicators proposed are insensitive to changes in environmental temperature, a beneficial characteristic for in-service applications in harsh climates.

Case	Young modulus	Temperature	Vertical pre-stress	Horizontal pre-stress	Members removal	Elastic Support	Cables break
C1	01YM-10	11TP-30	00Ref	00Ref	00Ref	51ES2.5E7	00Ref
C2	02YM-5	12TP-20	21CW10	31WA10	41B1T0S0P	52ES3.0E7	61CB1Low
C3	03YM-2	13TP-10	22CW20	32WA20	42B2T0S0P	53ES3.5E7	62CB1Mid
C4	04YM-1	14TP0	23CW30	33WA30	43B3T0S0P	54ES4.0E7	63CB1Top
C5	05YM-0.5	15TP10	24CW40	34WA40	44B3T1S0P	55ES4.5E7	64CB2LowMid
C6	00Ref	00Ref	25CW50	35WA50	45B3T2S0P	00Ref	65CB2TopLow
C7	06YM+0.5	16TP30	26CW60	36WA60	46B3T3S0P	56ES6.0E7	66CB2MidTop
C8	07YM+1	17TP40	27CW70	37WA70	47B3T3S1P	57ES7.0E7	67CB3R
C9	08YM+2	18TP50	28CW80	38WA80	48B3T3S2P	58ES8.0E7	68CB3R1L
C10	09YM+5	19TP60	29CW90	39WA90	49B3T3S3S	59ES9.0E7	69CB3R2L
C11	10YM+10	20TP70	30CW99	40WA97	50BCorr	60ES1.0E8	70CB3R3L

Table 4.16: Structural modification scenarios corresponding to each family for the model tower

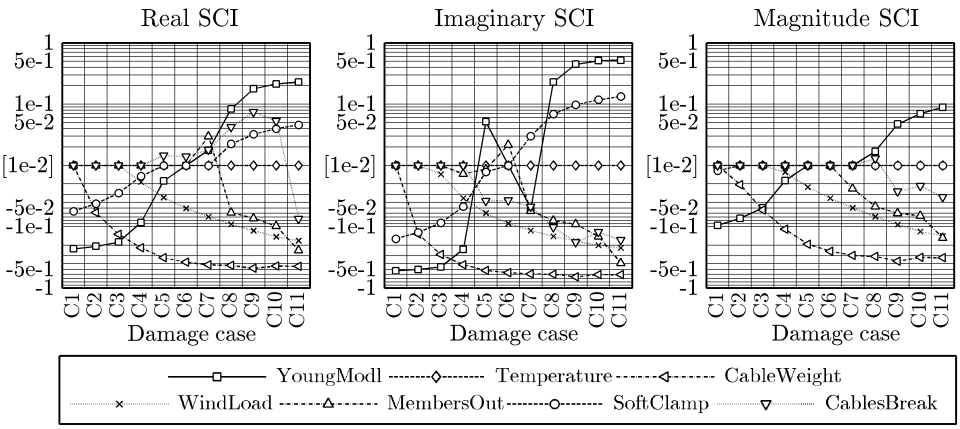

Figure 4.67: SCI vs numerical damage scenarios

5. Experimental approach

Previous chapters have demonstrated the feasibility of utilizing the proposed SCI indicator as a structural alteration indicator using synthesized frequency response functions extracted from FEM numerical modal analysis. This chapter deals with the analysis of the behaviour of the same indicators when applied to experimentally acquired real vibration data. These experimental series are captured using the experimental modal analysis technique with a roaming hammer procedure and, thus adopt the form of inertance transfer functions. Real residual side-effects in experimental scenarios are very difficult to model and to incorporate in purely numerical parametric analysis. This final part of the investigation aims to evaluate the influence of experimental uncertainties on the proposed indicator so resolve the mentioned issue. The experimental investigation is performed for three real structures and a series of intentionally applied structural alterations on them: a square aluminium plate with 1-edge clamped boundary conditions, a downscaled model of a latticed power transmission tower and a final campaign on a real scale latticed power transmission tower in a real in-service scenario.

5.1 Aluminium plate

The first experimental campaign deals with the investigation on the behaviour of the SCI indicator applied to spectral data obtained from EMA tests on a square clamped aluminium plate and its correspondent structural alteration scenarios. Configurations used for testing try to reproduce some of the numerical cases analysed in the parametric analysis in terms of material, geometry, boundary conditions, experimental acquisition mesh used, acquisition parameters, damage scenarios and sensibility dependences. To reproduce as accurately as possible the numerical campaign procedure, the residual stiffness of the plate is also evaluated.

5.1.1 Experimental set-up

Two experimental specimens are tested which correspond to those already exposed in section4.1.1.1. The reader is encouraged to review that discussion concerning the FEM modelling of the square aluminium plate to have a complete description of the specimen involved in this analysis. These two base specimens are again referenced in table 5.1 for clarity. All damage progression scenarios are applied to these two baseline specimens.

ID	Material	Young (GPa)	width (mm)	height (mm)	thickness (mm)	mass (g)
PAL1	Al-T5083	69.0	300.0	300.0	5.0	1199.1
PAL2	Al-T5083	69.0	300.0	300.0	5.0	1202.6

Table 5.1: Experimental specimens

Specimens are always clamped on the same edge. This is enforced by graphically marking the plate orientation and base clamping position. Three mechanical clamps are fixed to an optical monolithic testing bench with a tightening torque of 50 N/m. The clamps are not directly mounted on the plate as two auxiliary steel mounts in the bottom and top of the clamping act as force distributors and contributing to ensure a well distributed clamping reaction along all the edge. The clamping surface includes all the width of the plates and extends for 26 mm inwards from the edge. This configuration is equivalent to the one used in the numerical analysis previously discussed.

Experimental modal analysis tests are executed with a roaming excitation technique on the 81 node already exposed mesh with an excitation hammer (Figure 4.2). Driving point is located at position 30, as the numerical analysis shows that this location is the one that better resembles the modal visibility equivalent to a full transfer matrix OMA-like test. However, locations 5 and 18 are also utilized as driving points in order to study the sensibility of the reference acquisition position in the results of the SCI indicator.

Vibration acquisition hardware used in the aluminium plate campaign is provided by the manufacturer Bruel& Kjaær. Equipment available include a DAQ spectrum analyser Bruel& Kjaer LAN-XI Type 3160-A-042 (S/N 3160-105238) connected via an ethernet link with RJ45 connectors to a 64-bit Windows 7 Laptop Computer running Pulse Reflex v21.0 acquisition software. A Bruel& Kjær model 4519-003 piezo-capacitive accelerometer with integrated voltage transducer (S/N 62645) is used to acquire vibration data. Excitation is done with the aid of a miniature impact hammer with piezo-capacitive load cell with integrated voltage transducer Bruel& Kjær 8204 (S/N 58096). All the connections to the sensors are done with low-noise double-

screened coaxial 10-32 UNF to BNC cables.

Stiffness is also measured in this experimental campaign. The force application position is the same where the displacement is measured and corresponds to node 5 in the experimental mesh (30 mm from the most distant edge from the clamping on symmetry line of the setup -150mm from lateral edges-). The load is applied with the aid of a rotary machining mill support equipped with a rotational lever. The housing in the support is used to incorporate a machined steel shaft to which a resistive load cell screwed to its lower end. The remaining free end of the load cell is then screwed to a machined head with a semispherical steel tip of diameter 16 mm and hardness HRC 42. This rounded tip attacks node 5 in the aluminium plate. The load cell used is a HBM-U9C-200N (S/N 202310059). Displacement is measured in the uppermost part of the steel shaft which stands out the exporting structure. Axial stiffness of the shaft is considered to be enough to withstand a test load of 200 N without introducing additional deformation to the tested cantilevered aluminium plate. The displacement is measured using an HBM-WI +/-5 mm induction LVDT (S/N 201810209) supported by a magnetic base attached to the testing bench. Both sensors are connected with a 4 wire cable ended in a VGA 15-Pin to a HBM MX-840B DAQ (S/N 0009E5008384). The acquisition module is linked to the same 64-bit Windows 7 computer running the acquisition software HBM Cataman Easy AP v4.2 using a Cat-5 ethernet cable with a RJ45 connector. As both the vibration DAQ and the static sensors DAQ share the same communication interface to the computer, the use of an ethernet hub becomes necessary.

Figure 5.1: Experimental setup for aluminium plate tests.

The maximum frequency of interest is set to coincide with the maximum frequency synthesized in the parametric numeric analysis of the plate,that is, 3200Hz. Frequency

resolution is set at Δf desired 0.5 Hz, a resolution fine enough to assure stability in the SCIs as already demonstrated numerically. This acquisition parameters require to sample a total of 6400 spectral lines which at the same time require to capture a total of 16384 samples in the time domain. This number of samples requires to use a 14-bit buffer to accumulate data and a sampling frequency of $f_s = 8192$Hz. This results in an acquisition window of 2 seconds. The force signal from the hammer is acquired using a rectangular window function whereas the accelerometer series is weighted with an exponential window function that reduces experimental noise in sampled signals. Static measurements used to determine the stiffness are sampled at a frequency of 50Hz. The whole experimental set-up is shown in figure 5.1 and depicts one of the structural alteration scenarios.

5.1.2 Experimental campaign

Three families of structural alterations have been decided to be reproduced experimentally from numerical reference tests. These three families include: a subset of the crack analogy family, of the stringer reinforcement family and of the holes family. Cases experimentally reproduced are shown in table 5.2. Each case is identified by the same reference number utilized in the numerical study to facilitate case identification. Several reference undamaged cases have been also incorporated in the experimental campaign in order to study repeatability thresholds and the influence of the driving point. Some of the experimentally tested structural alteration scenarios are depicted in figure 5.2.

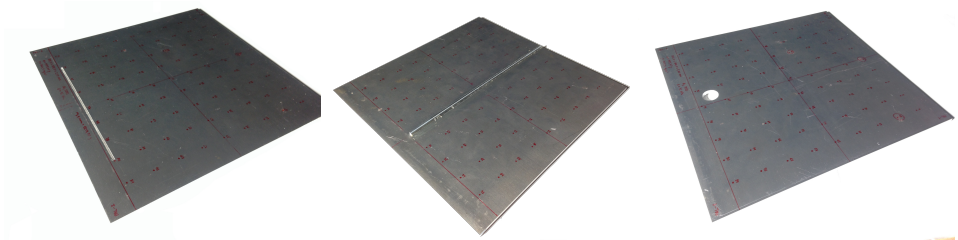

Figure 5.2: Experimental damage scenario. Left: 30C180, Mid: 40S5.0, Right: 47H25.

A total of 10 reference test in pristine conditions are executed before the application of structural modifications. Most of the cases share the same driving point and are utilized to establish the test-retest reliability thresholds in the experimental campaign, human effect in the tests and the influence of slight variations in boundary conditions on the results. Additional tests are also performed changing the reference driving point (which is numerically determined to be point 30) to serve as references when studying the influence of the selected driving point in the SCIs. These alternative driving points include DP5, worst-case driving point, and DP18, which presents a

intermediate modal visibility between optimal and worst case references.

Cracks are simulated by machining a 2mm wide slot with the corresponding length to each of the damage scenarios considered. The slot is positioned in such a way that one of its longer edges is coincident with the experimental mesh line defined by nodes 73 and 81. As nodes are exactly on the edge of the slots, the impacts required to perform EMA tests are done approximately at a 1 mm distance of original mesh locations. The other parallel edge of the slot is located 2mm outwards the same mesh line defined by nodes 73 and 81. The slot is laterally located so its central point is coincident with the symmetry axis of the plate. The 2mm width of the slot is selected to be coincident with the element size used in the numerical simulations. Machining of the slot is done with the aid of a CNC milling cutter.

Stringers are incorporated as a 4mm wide, 5mm thick, 270mm long aluminium bar. The material used is the same as the main body of both plates. The stringer is symmetrically attached to the plate using commercial epoxy resin and letting it cure whilst mechanically clamped to guarantee perfect adhesion. The stringer is mounted on the symmetry line of the plate (the 4mm aluminium rod in the center extends for 2mm in each direction from the symmetry line). The total length of this reinforcement (270 mm) is coincident with the distance between the free edge of the plate and the 73-81 nodal line. Nodes 5, 14, 23, 32, 41, 50, 59, 68, 77 coincide with the directive line of the stringer. Progression of structural modifications involving the stringers is achieved by machining the stringer once attached to the desired thickness with a 2mm milling cutter. As machining could introduce debounding in the interface between the two components, after each machining step, the adhesion is carefully inspected visually using high intensity light, manual verification of the resistance of the union and checking for self-hitting interferences when preliminary impacted with the test hammer. Results of the experimental campaign show that this procedure has been enough to guarantee the integrity of the bounding. Corrective actions planned to repair the union if damage would have been observed would have included the complete removal of the stringer using a sharp blade, the cleansing of the surfaces with chemical solvents and the adhesive reattachment of the specimens using the same clamping procedure previously exposed.

The family of damages including hole diameter progression is also machined on the plate using appropriate size drilling bits. Holes are always cut with origin in the ortocenter of element formed by nodes 67, 68, 76 and 77 of the experimental mesh. The damage stage corresponding to the complete removal of the element (forming a square aperture) is also machined using a CNC milling cutter with a 2 mm diameter tool.

	ID	Specimen	DP	Description
References	00Ref1-DP30	PAL1	30	Clean plate
	00Ref2-DP30	PAL1	30	Same as EP-Ref1-DP30. Test-retest reliability
	00Ref3-DP30	PAL1	30	Set-up re-set. Boundary repeatability
	00Ref4-DP5	PAL1	5	Same as EP-Ref3-DP30.
	00Ref5-DP18	PAL1	18	Same as EP-Ref3-DP30.
	00Ref6-DP30	PAL2	36	Plate reversed. Symmetric to DP30
	00Ref7-DP30	PAL2	30	Clamp remounted. Boundary repeatability
	00Ref8-DP30	PAL2	30	Same as EP-Ref7-DP30. Test-retest reliability
	00Ref9-DP5	PAL2	5	Same as EP-Ref7-DP30.
	00Ref10-DP18	PAL2	18	Same as EP-Ref7-DP30.
Cracks	22C8-DP30	PAL1	30	Crack 8mm
	25C20-DP30	PAL1	30	Crack 20mm
	26C40-DP30	PAL1	30	Crack 40 mm
	27C60-DP30	PAL1	30	Crack 60 mm
	22C100-DP30	PAL1	30	Crack 100 mm
	29C140-DP30	PAL1	30	Crack 140 mm
	30C180-DP30	PAL1	30	Crack 180 mm
	30C180-DP5	PAL1	5	Crack 180 mm
	30C180-DP18	PAL1	18	Crack 180 mm
Stringers	32S1.0-DP30	PAL1	30	Stringer 1mm
	34S2.0-DP30	PAL1	30	Stringer 2mm
	36S3.0-DP30	PAL1	30	Stringer 3mm
	38S4.0-DP30	PAL1	30	Stringer 4mm
	40S5.0-DP30	PAL1	30	Stringer 5mm
Holes	43H5-DP30	PAL2	30	Circular hole D5 mm
	44H10-DP30	PAL2	30	Circular hole D10 mm
	45H15-DP30	PAL2	30	Circular hole D15 mm
	46H20-DP30	PAL2	30	Circular hole D20 mm
	47H25-DP30	PAL2	30	Circular hole D25 mm
	50HS30-DP30	PAL2	30	Square hole A30 mm
	50HS30-DP5	PAL2	5	Square hole A30 mm
	50HS30-DP18	PAL2	18	Square hole A30 mm

Table 5.2: Experimental tests executed on aluminium plates

5.1.3 Repeatability thresholds

This section addresses the repeatability that can be obtained in experimental controlled conditions. This analysis serves as a tool to asses the detection thresholds for the indicator and the influence of uncertainties caused by test operator an by slight

differences in the boundary conditions.

The repeatability analysis is done using the experimental analysis data from Reference cases. Reference cases 1 to 10 are included in the analysis. Although cases 5, 6, 9 and 10 refer to tests that use a different reference driving point for acquisition, they have also been included in this discussion to preliminary shown the influence of the driving point in the degree of correlation between experimental CFDACs.

The quantifying index of the degree of correlation between experimental CFDACs is, again, the Pearson Correlation Coefficient that has already been exposed in equation 3.14. Values of PCC near unity show almost perfect correlation, values around zero, total lack of correlation. The results of all cross correlation between experimental CFDACs are shown in figure 5.3.

The observation of figure 5.3 leads to the conclusion that very high values of test-retest reliability can be obtained. When comparing Ref1 to Ref2 values of 0.98 for the real part and 0.96 for the imaginary part are obtained. Comparison of cases Ref7 and Ref8 give human repeatabilities of 1.00 for the real part and 0.99 for the imaginary part. So then, in conclusion, if the tests are made carefully enough, the tester influence can be minimized and even eliminated as a dispersion source.

However the influence of the boundary condition is much more important. Comparison of tests Ref2 an Ref3, whose transition includes a remounting of the clamping in the plate, leads to repeatability values of 0.95 and 0.86 for the real and imaginary parts respectively. The great dispersion caused by the change of boundary conditions is also observed when comparing cases Ref6 to Ref7 which lead to repeatability values of 0.93 and 0.79 for the real and imaginary parts of the CFDAC respectively. This observation leads to the the assessment that this indicator is capable of detecting slight changes in the boundary conditions and thus, these cases should not be considered reference repeatability cases but a kind of structural alteration where the clamping condition undergoes a change.

So then, the structural alteration threshold is set considering the values obtained for the plates in the human repeatability analysis. The minimum detection threshold is then established as PCC = 0.96 (correspondent to PCC between imaginary parts of CFDACs corresponding to Ref1 to Ref2 comparison). The translation of this value to the SCI implies that SCI values with an absolute value below 0.04 are considered to be under the detection threshold. For practicality, all SCI plots in this investigation are shown in the interval of absolute values between 0.01 and 1 for scaling consistency and in a positive/negative logarithmic Y-scale to ease the reading of small SCI values.

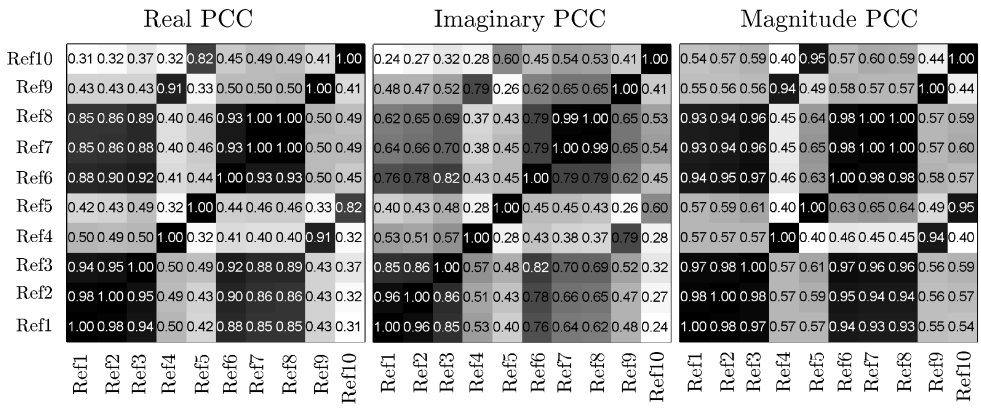

Figure 5.3: Pearson Correlation Coefficients for CFDACs for reference cases

5.1.4 Parameter sensibility

EMA tests performed on the aluminium plate in controlled laboratory conditions results in low noise level FRFs that can be used to develop a sensibility analysis similar to the one done using FEM synthesized. The quality of the experimentally acquired signals on the aluminium plate allows to propose a numerical to experimental comparison of results that is used to validate the conclusions extracted from the numerical campaign. Generally speaking, this is not the case as EMA acquisitions on real in-service structures present a lot of residual noise of even influence of the boundary conditions which make the correlation with numerical models an arduous task.

The experimental sensibility analysis on the aluminium plate and its intentionally applied structural alteration scenarios is done accounting for the influence of the driving point, the influence of the mesh density, the influence of the frequency resolution and the influence of the total bandwidth used to compute the SCIs indexes. This experimental analysis tries to reproduce the numerical campaign on the plate. However, as the real application of damages (by machining defects in the plate) is not a reversible procedure, only a limited subset of degradation and reinforcement states are studied.

Experimental modal analysis tests are executed following the same experimental set-up and acquisition parameters shown in section 5.1.1.

5.1.4.1 Driving point

The influence of the driving point is studied by generating CFADCs corresponding to cracks and holes damages (See table 5.2 30C180-DP30, 30C180-DP5, 30C180-DP18,

30C180-DP30, 30C180-DP5, 30C180-DP18) and to their respective reference cases (Ref8-DP30, Ref9-DP5, Ref10-DP18). Results shown in this section are computed for a total bandwidth of 3200 Hz, with a frequency resolution of $\Delta f = 0.5$ Hz, and a total number of 81 acquisition points or the FRFs.

Figure 5.4 shows a comparative between experimentally determined SCIs (in black) and its numeric equivalent determined in chapter 4 (in grey). Square markers correspond to the SCI determined for the real part of the CFDAC, triangles to the SCI related to the imaginary part and round markers refer to the SCI of the magnitudes of the CFDACs.

The first observation that can be done is that the experimental results closely correlate with the numerically obtained ones. The sign of the SCI indicators is correctly assigned for these cases. The SCI corresponding to the imaginary part is always bigger in absolute value, followed by the real part SCI and by the magnitude SCI. This observation is consistent with previous discussions that showed that the imaginary SCI is the most sensitive in front of damage of them. Additionally it can be identified that the driving point selected have some influence in the value adopted by the SCIs and, thus, it is desirable to systematize its election. Driving point selection procedure already presented in the numerical campaign serves as a tool to objectify this driving point selection. SCIs corresponding to the hole detection using the magnitude of the CFDAC are under the detection threshold.

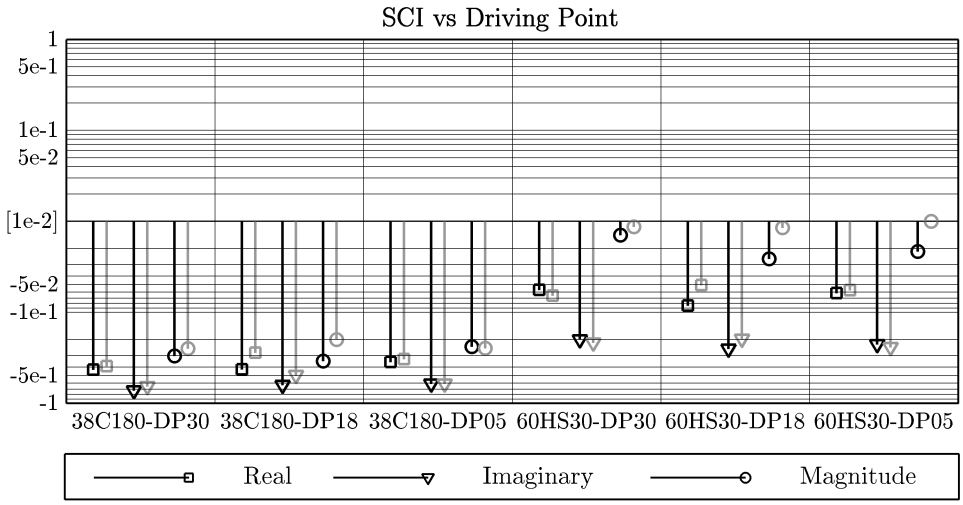

Figure 5.4: Experimental sensitivity of the SCI to driving point

Comparing the experimental trend of SCI indicators in front of driving point changes with the dispersion observed for the SCIs in the numerical analysis, it becomes clear that real effects in the signals induce a beneficial stabilization effect in the SCI values. Noise and other experimental effects in FRFs cause that SCIs computed for different driving points in using experimental data are much less disperse that the numerically analysed ones. Driving point uncertainty seems to be smaller than suggested by numerical synthesis analysis. However, it is recommended to apply the already presented optimal driving point selection methodology for prudence.

5.1.4.2 Mesh density

In experimental applications, reduction of the number of acquisition points has a big impact on time and monetary costs of the data acquisition campaign. The influence of the number of FRFs used to construct the CFDACs and the SCIs is investigated with the aid of the same sub-meshes used in the numerical campaign and depicted in table 4.7. All FRFs used in this segment acquired for a total bandwidth of 3200 Hz, with a frequency resolution of $\Delta f = 0.5$ Hz, and keeping the driving point in position DP30. Results as a function of the mesh density are shown in figures 5.5 to 5.7 corresponding to each of the three experimental families of structural alterations analysed.

The SCI sign decision algorithm appears to fail when small amounts of alteration are present in the structure, as it can be observed in the initial progression stages of the crack analogy family and hole family. This behaviour seems to be independent of the mesh density. In a very similar way to the observations made in the numerical campaign, the SCI values seem to stabilize around 40 source FRFs. The sign dispersion in the crack family is attributed due to the fact that when small amounts of damage are present in the structure little experimental uncertainties (such as the boundary conditions) can slightly shift the diagonal structure in the CFDAC. On the other hand, the numerical campaign has already shown that the sign decision algorithm in hole scenarios fails. In those numerical cases, dispersion in the sign of the SCIs is also observed. This phenomena is strengthened when dealing with experimental series. This behaviour is mostly caused by the small amount of shift in the CFDAC caused by holes. The convergence threshold of 40 acquisition points is coincident with observations made in the numerical analysis of SCI indicators.

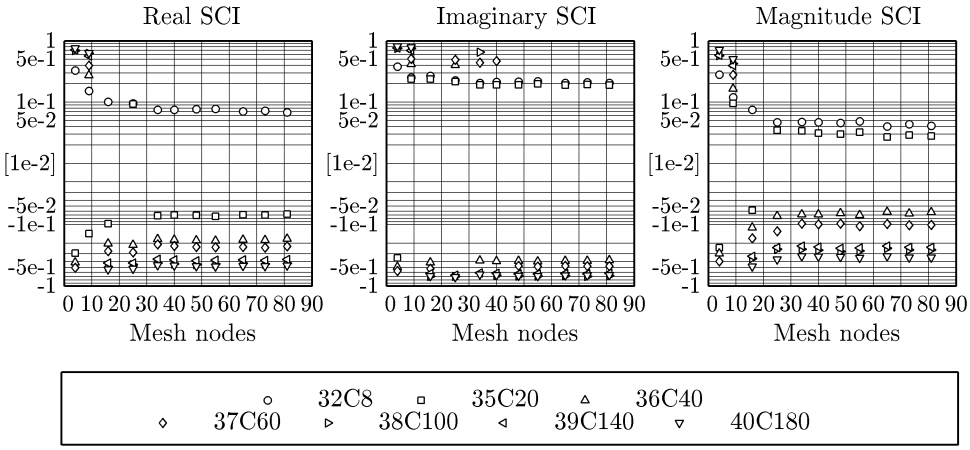

Figure 5.5: Experimental sensitivity of the SCI to the mesh density. Crack family

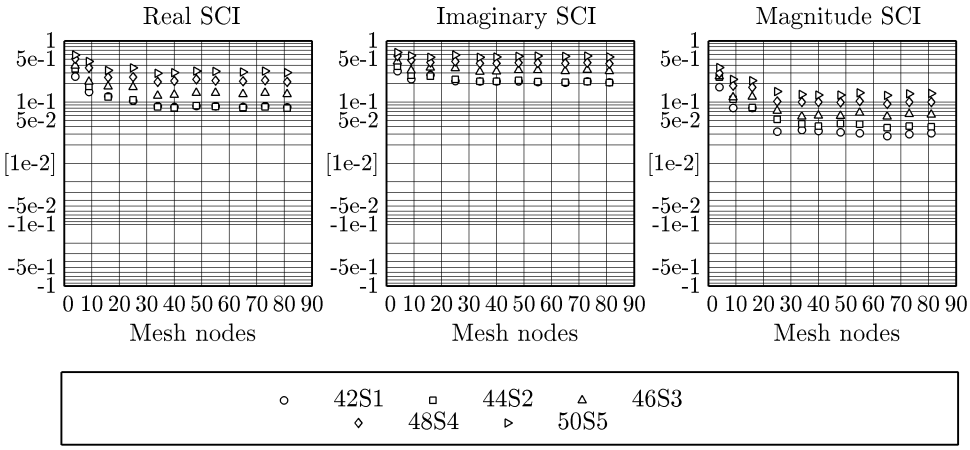

Figure 5.6: Experimental sensitivity of the SCI to the mesh density. Stringer family

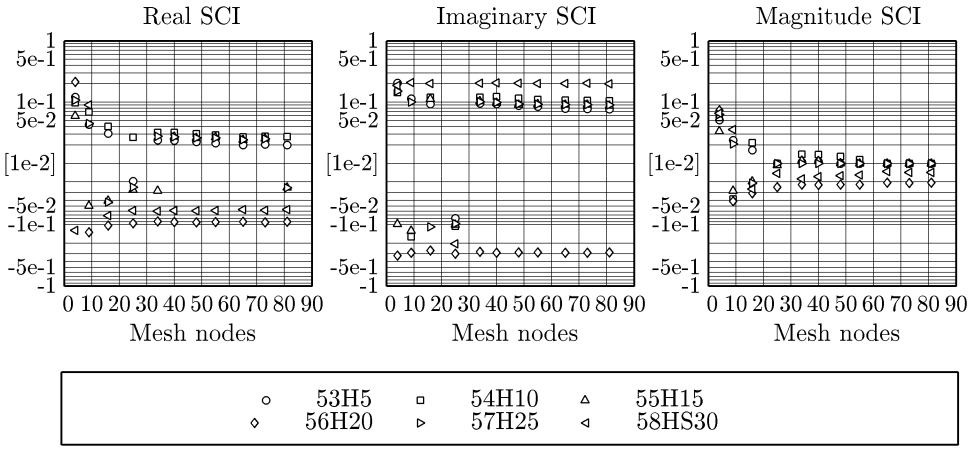

Figure 5.7: Experimental sensitivity of the SCI to the mesh density. Holes family

5.1.4.3 Frequency Resolution

The influence of the Δf used to sample the FRFs which later form the CFDAC and the SCIs is investigated by sub-sampling originally acquired EMA FRFs with modified stepping between samples. All FRFs used in this segment acquired for a total bandwidth of 3200 Hz, with an original Δf of 0.5 Hz, a 81-node mesh of acquisitions and the driving point set in position DP30. Frequency resolutions analysed in the numerical parametric analysis are reproduced in this experimental approach by sub-sampling original FRFs with Δf equal to 1, 2, 4, 6, 8, 12, 14 and 16 Hz. If the sub-sampling ins not a perfect multiple of the original series, the subsets are truncated in the last value smaller than 3200 Hz.

Results as a function of the mesh density are shown in figures 5.8 to 5.10 corresponding to each of the three experimental families of structural alterations analysed. Results are shown in a relative scale referenced to the original $\Delta f = 0.5$Hz resolution and show that the SCI indicators start to undergo dispersion for Δf equal or greater that 4Hz in the worst case scenario corresponding to the crack analogy family. Although the other two families corresponding to stringers and holes present a relative increased stability in front of frequency resolution changes, a Δf of 2Hz is adopted as the uppermost acceptable value for frequency sampling.

In conclusion, these observations allow to reduce the number of bits in the buffer acquisition hardware thus reducing the cost of the equipment required in an in-field application. This observations are consistent with the conclusions extracted in the numerical parametric study on the aluminium plate including changes in the frequency resolution of FRF signals.

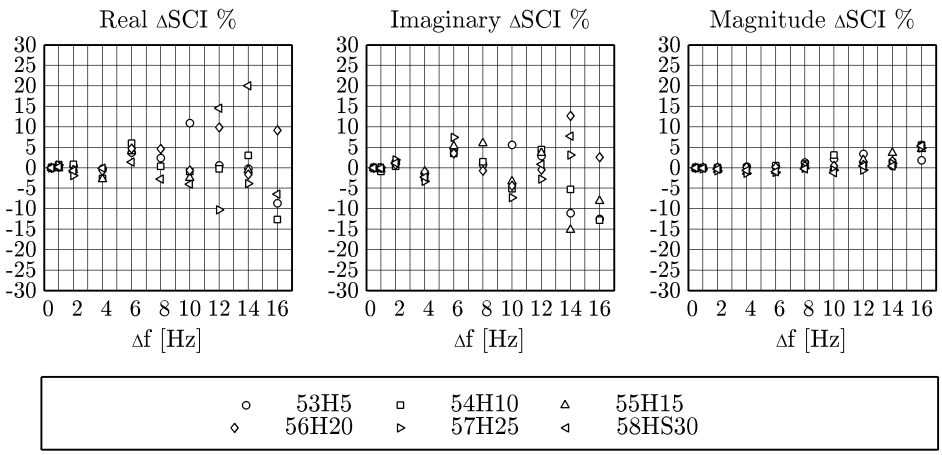

Figure 5.8: Experimental sensitivity of the SCI to the frequency resolution. Crack family

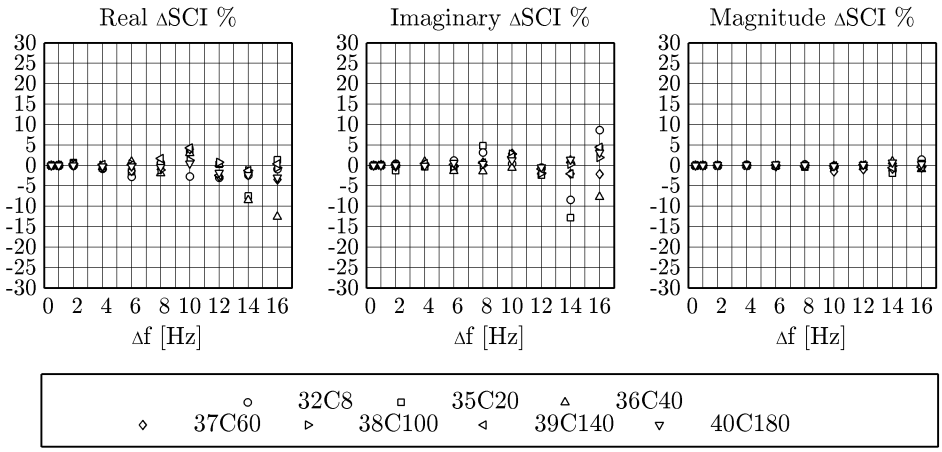

Figure 5.9: Experimental sensitivity of the SCI to the frequency resolution. Stringer family

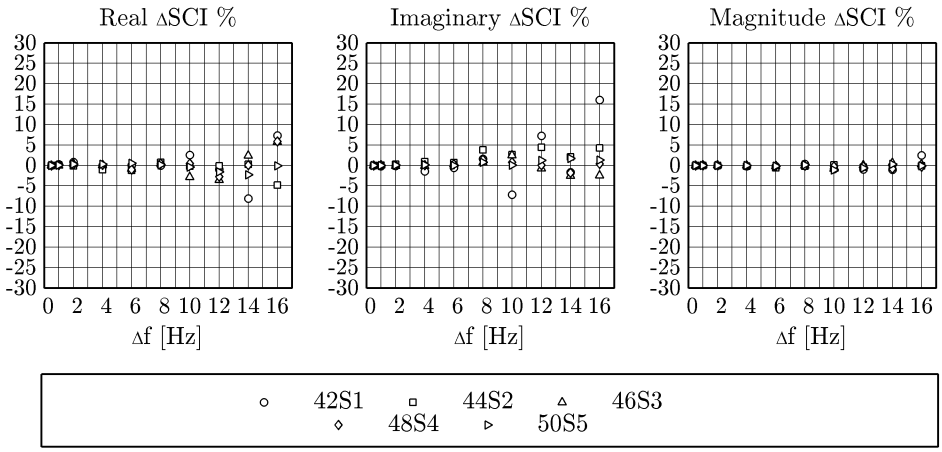

Figure 5.10: Experimental sensitivity of the SCI to the frequency resolution. Holes family

5.1.4.4 Bandwidth

The influence of the maximum frequency of interest in the bandwidth for the FRFs used to construct the CFDAC and the SCIs is investigated using the same sub-stepping than that in the numeric campaign: from 400 Hz to 3200 Hz in 400 Hz steps. All FRFs used in this segment are acquired with a frequency resolution of $\Delta f = 0.5$ Hz, and keeping the driving point in position DP30. Results as a function of the mesh density are shown in figures 5.11 to 5.13 corresponding to each of the three experimental families of structural alterations analysed.

When observing the results in the figures, a first conclusion can be drawn regarding the influence of the bandwidth in hte SCIs indicators. In these experimental cases the indicator seems to present a much more stable tendency as the bandwidth is increased

compared to the results obtained in the numerical chapter if this investigation. The reader is reminded that the numerical cases showed a monotonic increasing tendency in the SCIs indicators as bandwidth was increased while in these experimental scenarios the tendency is observed to be to stabilization around a limit value. This behaviour is explained due to the nature of experimental acquisitions. In a real scenario it is very difficult to excite and measure higher frequencies and modes of mechanical systems (for example, consider an impact hammer with a limited excitation bandwidth, or a shaker, that also is spectrally bounded to a range of interest, or even natural excitation, wih the narrower band of excitation of the mentioned examples). This causes that upper sections of FRFs become much fuzzier when experimentally captured than in a numeric case. The CFDACs generated with these fuzzier signals are then much fuzzier in the higher parts of the spectral correlation. Those fuzzier regions do not significantly contribute to the PCC correlation as their values tend to be smaller or even zero. This physical effect, that was not originally modelled in the numerical campaign, acts a soft bound in the SCI indicators convergence.

A second aspect that can be observed is the reduced accuracy in the sign decision algorithm for the SCI specially when small bandwidths are used and little structural alteration is present in the structure. This is same observation has been already exposed in previous discussions but is in this parametric analysis again reproduced. This fact is specially apparent in the hole damaged scenarios. or this last family magnitude SCIs are below the detection threshold. However, the real and imaginary parts SCIs are capable of detecting anomalies although the sign of the alteration is not always well estimated.

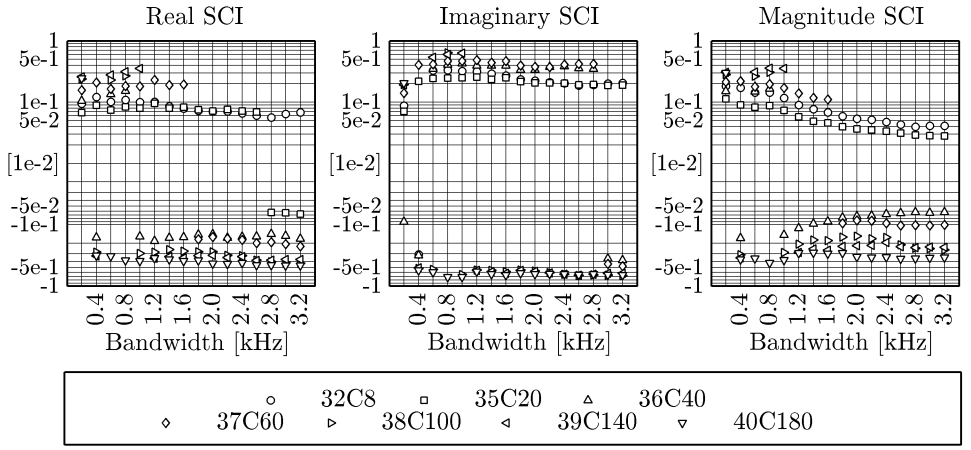

Figure 5.11: Experimental sensitivity of the SCI to the bandwidth. Cracks family

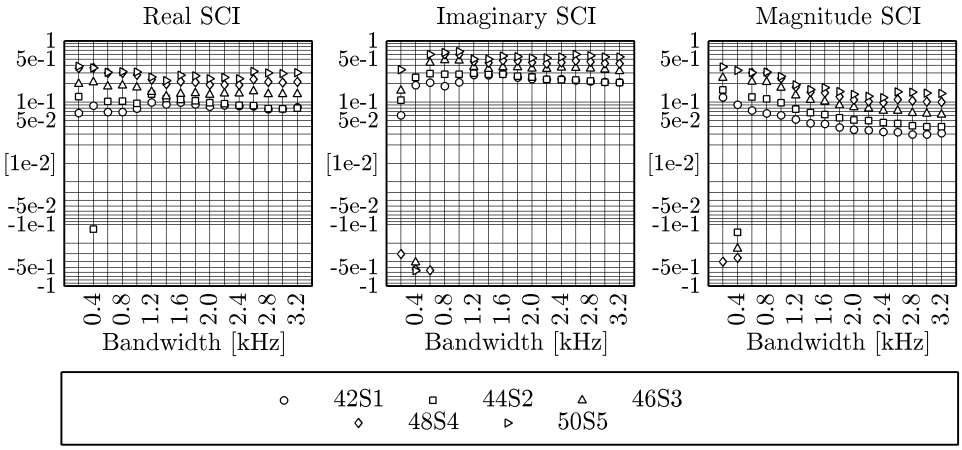

Figure 5.12: Experimental sensitivity of the SCI to the bandwidth. Stringer family

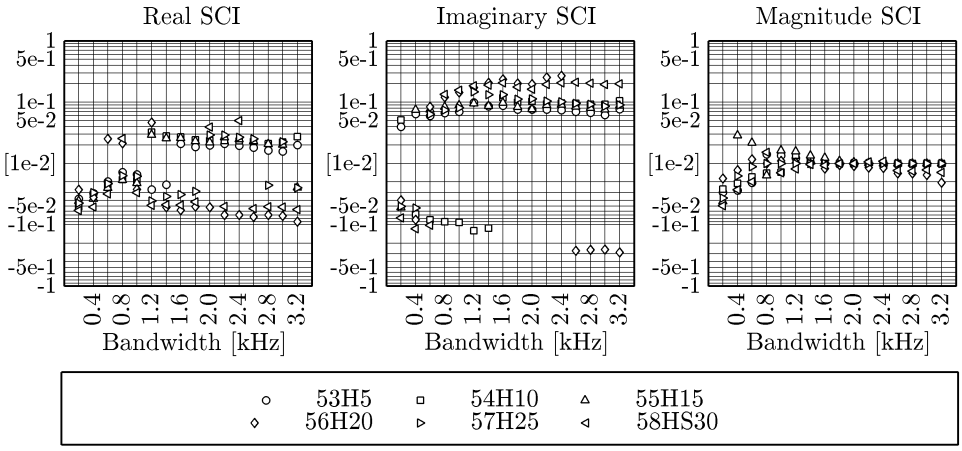

Figure 5.13: Experimental sensitivity of the SCI to the bandwidth. Holes family

5.1.5 Structural modification assessment

As the experimental campaign on the aluminium plate tries to reproduce the numerical study presented first, the same analysis analysing the influence of damage in the real part of the CFDAC and on the SCI is presented in this section. In addition, as residual stiffness can be readily measured using the experimental set-up already exposed in this chapter, the relationship between this magnitude and the SCI indicators is also presented. These informations are complemented with a numerical-to-experimental correlation of the indicators computed.

5.1.5.1 Damage typology and the CFDAC

The CFDACs that are analysed in this section are generated from FRFs acquired up to a maximum frequency of interest of 3200 Hz, a Δf of 0.5 Hz, setting the reference

driving point at location 30 and using the full 81 FRFs available. Only some representative cases of each damage family are shown to identify the degradation mechanism in the CFDAC caused by each alteration typology. The real part of the CFDACs corresponding to certain alteration scenarios are depicted in figure 5.14.

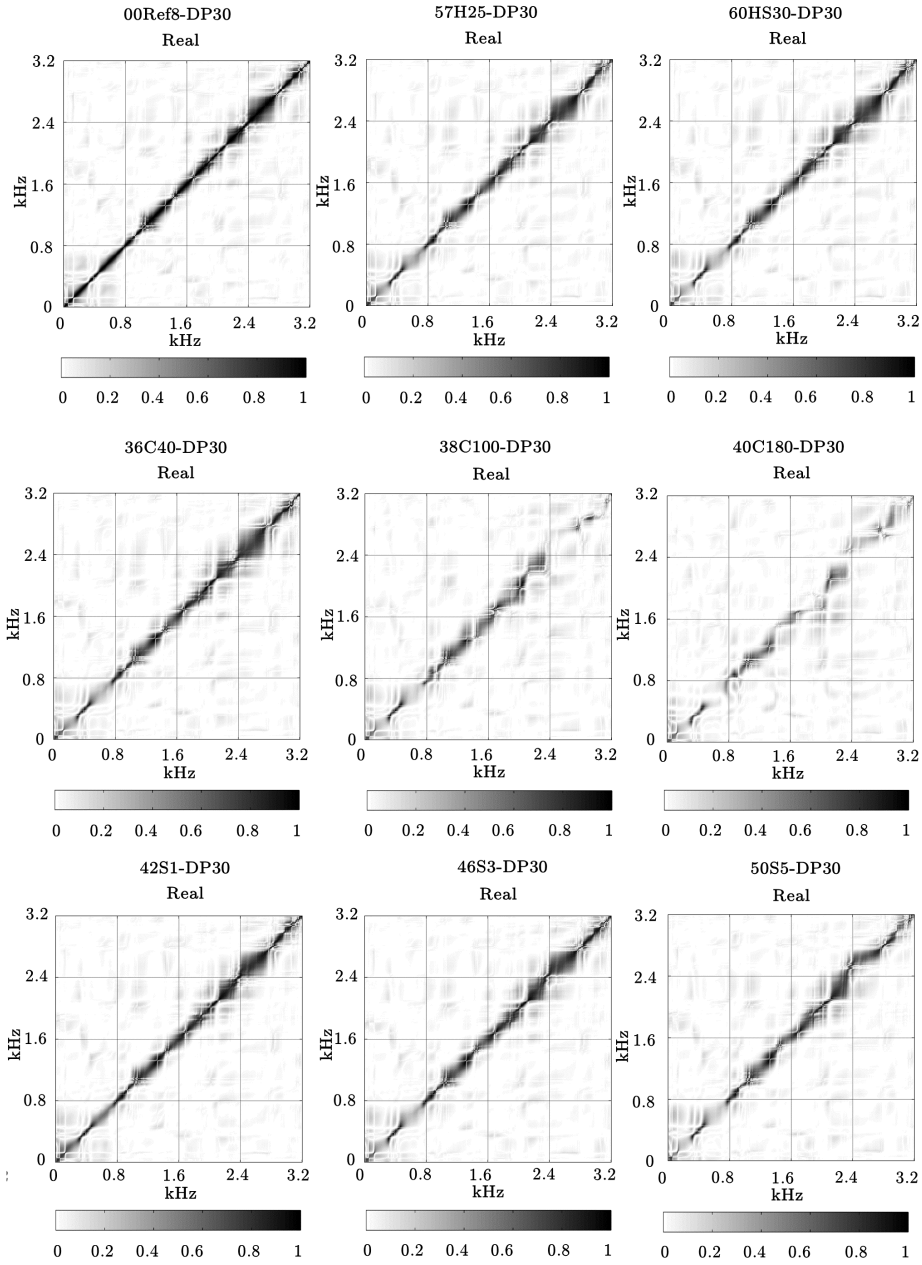

Figure 5.14: Real part CFDAC vs structural alteration typology. 3.2 kHz, $\Delta f = 0.5$ Hz, 81 node mesh, DP30

Observing CFDAC alterations caused by cracks, namely cases C40, C100 adn C180, it can be observed that as the crack length progresses, the degradation mechanism in the CFDAC slightly changes. For low values of crack lengths, the diagonal structure of the CFDAC dilutes at low frequencies of 600 Hz. For large slots, such as in case C100, the degradation mechanism changes showing distortion in all the frequency range and almost a lack of correlation above 2400 Hz. Case C180 shows a very similar degradation in the CFDAC to the one observed for case C100.

The modifications consisting in the reinforcement of the structure with a stringer, it can be seen in the figures that the structural alteration is translated to the CFDAC by showing an upper shift in the diagonal lobes in hte diagonal structure of the CFDAC around 2400 Hz. Influence of the holes can not be observed at first sight although a general decreasing in the CFDAC correlation is observed in the whole diagonal structure of the indicator. This loss of correlation appears as a blurring in the values in the CFDAC diagonal.

The degradation mechanisms observed in the CFDAC are very similar to the observations done in the numerical analysis of the plates. CFDAC shift presents a greater potentiality in damage classification and identification that SCIs as the patter in the degradation is characteristic of the structural alteration typology analysed. Advanced pattern recognition algorithms using image condensation tools and supervised machine learning algorithms such as artificial neural networks or support vectors machines could be applied to the CFDAC condensed information to clearly identify the structural alteration mechanism undergoing.

5.1.5.2 Damage typology and the SCI

The next analysis is made to identify the effect of structural alteration typology on the SCI indicator. Again, the FRFs used to generate the indicators are captured up to a maximum frequency of interest of 3200 Hz, with a Δf of 0.5 Hz, setting the reference driving point at location 30 and using the full 81 FRFs available. The experimental results are compared with the numerical results obtained in the previous numerical campaign.

Figure 5.15 shows a comparative between experimentally determined SCIs (in black) and its numeric equivalent determined in chapter 4(in grey) for each of the structural alteration families in hte experimental campaign. Square markers correspond to the SCI for the real part of the CFDAC, triangles to the imaginary part SCI and round markers to the magnitude SCI.

In general, results show a good correlation between numeric and experimental results

for the stringer an crack families. As already identified before, low values of damage in the crack family causes that slight variations in the boundary conditions alter the results. This dispersion is specially clear in cases C8 and C20. Once this aspect is considered, stringer cases and crack analogy cases shows good correlation in sign and magnitude with the typology and direction of the structural modification introduced in the system. Holes family again shows dispersion in its results as it has been shown before. As these cases introduce little alteration to the structure, slight modifications in the experimental conditions greatly alter the results. The results in the SCIs for the hole families are probably more related to changes in the clamping conditions that changes in the structure itself.

5.1.5.3 Residual stiffness and the SCI

The last analysis using experimental data from EMA tests on the aluminium plates is done in order to relate residual stiffness with the proposed SCI indicators in a parallel fashion as already done in the initial numerical campaign. Again, the FRFs used to generate the indicators are captured with a Δf of 0.5 Hz, setting the reference driving point at location 30, using the full 81 FRFs available and ranging the bandwidths of interest from 400 Hz to 3200 Hz is 400 Hz steps. These indicators are correlated with the experimental static stiffness in each altered structural condition.

The fist task addressed is to compare the experimental static stiffness with the numeric stiffness measured in equivalent locations. The result of this comparison is shown in figure 5.16 as absolute values and as percentage shifts from the reference pristine condition. In general, numeric stiffness is slightly higher than the experimentally determined due to the ideal boundary conditions that cannot be accurately reproduced in an experimental set-up. Despite these small offsets, the linear relationship between the two sets of stiffness show an almost perfect correlation.

This results validate the numeric stiffness obtained from simulation. Additionally, the experimental SCIs have already been correlated with their equivalent numeric counterparts previously. The results of correlation between SCIs for each bandwidth and residual experimental stiffness are shown in figures 5.17 to 5.19 for each of the experimentally tested structural alteration families. Again, the sign decision algorithm is not accurately enough for the small cracks cases and for the holes families. The discussion about this issue is already exposed in previous section 5.1.5.2. This phenomenon is more unfavourable if small bandwidths are used for SCI computation. In general, the correlation between residual stiffness and SCIs is consistent with the expected behaviour once these significant discordances are identified.

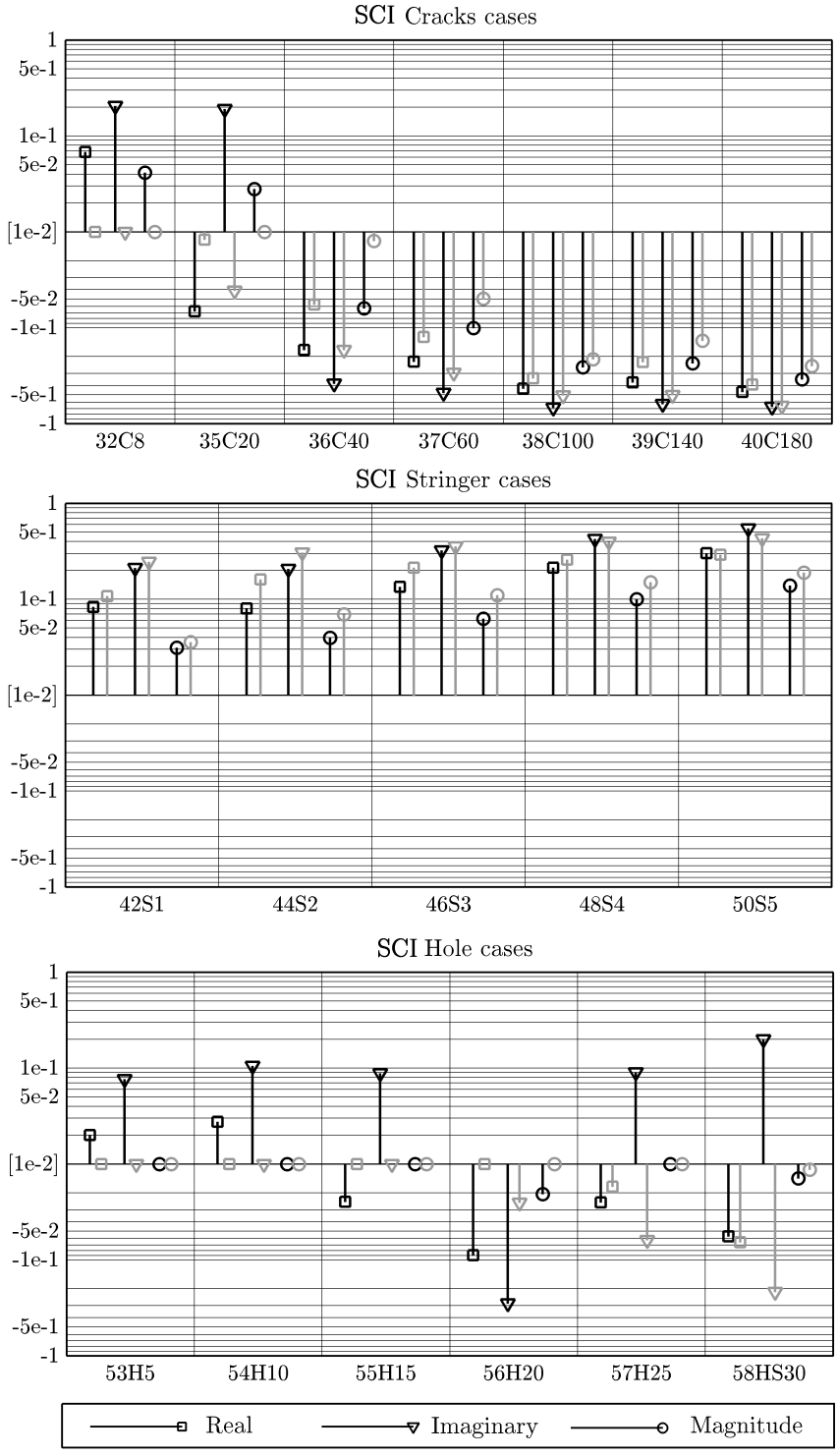

Figure 5.15: Experimental to numeric comparison of the SCI evaluated for DP30, BW = 3200 Hz, $\Delta f = 0.5$ Hz, 81 nodes mesh. In black, experimental results, in gray, correspondent numeric cases.

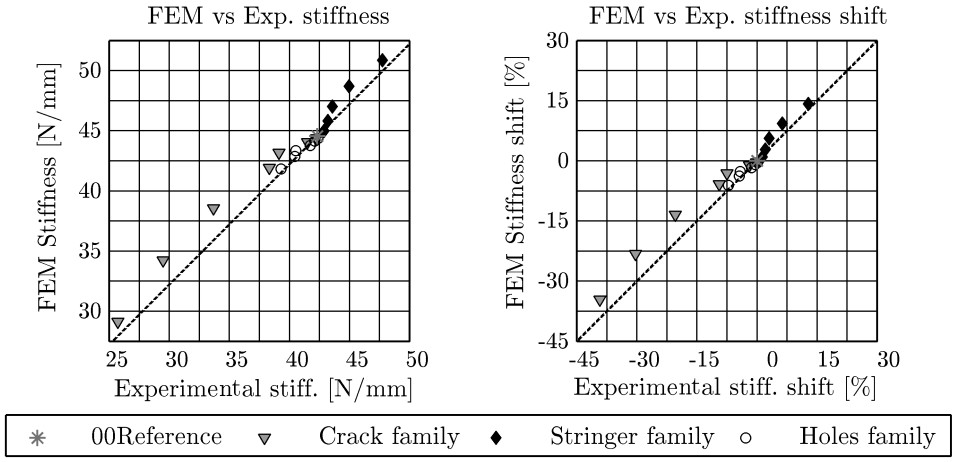

Figure 5.16: Experimental vs. numerical stiffness.

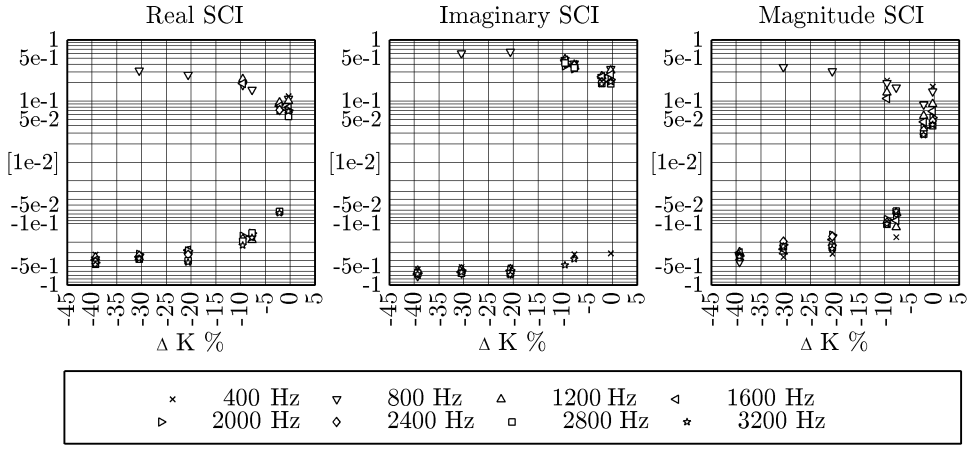

Figure 5.17: Experimental residual stiffness shift vs experimental SCIs for different bandwidths evaluated for DP30, $\Delta f = 0.5$ Hz, 81 nodes mesh. Cracks

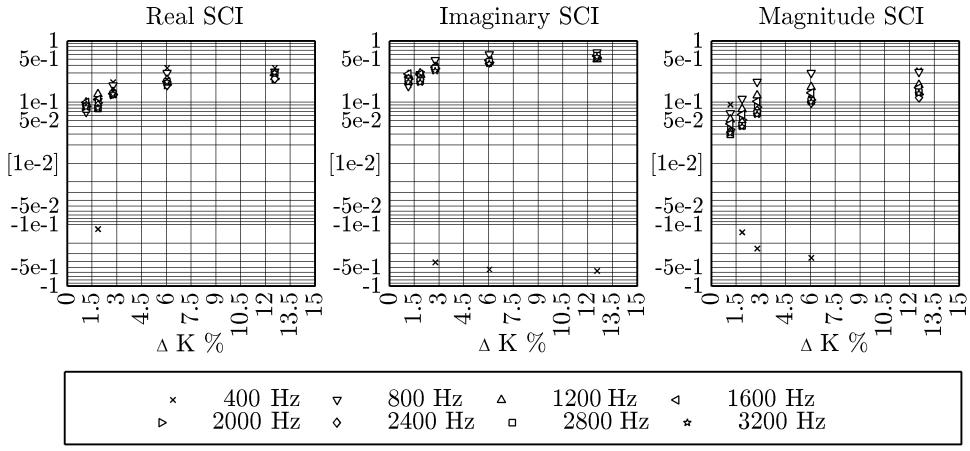

Figure 5.18: Experimental residual stiffness shift vs experimental SCIs for different bandwidths evaluated for DP30, $\Delta f = 0.5$ Hz, 81 nodes mesh. Stringers

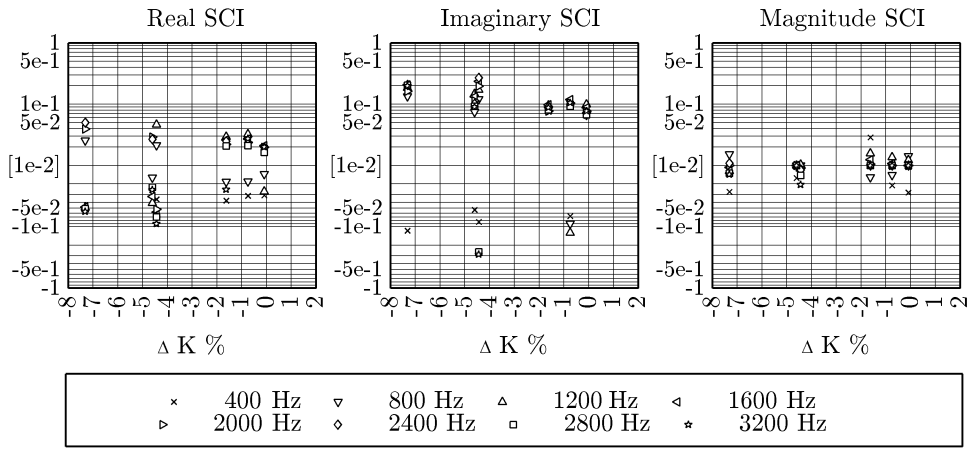

Figure 5.19: Experimental residual stiffness shift vs experimental SCIs for different bandwidths evaluated for DP30, Δf=0.5 Hz, 81 nodes mesh. Holes

5.1.6 Comparing experimental SCIs with DRQ and ΔODS

In this section SCI indicators generated from experiments are compared to DRQ and ΔODS indicators from bibliography. Results are depicted in figure 5.20. The reader is encouraged to backtrack to section 4.1.5 to review conclusions there presented as similar observations apply for the experimentally calculated indicators.

Experimental comparison slightly differs from the numerical one. Observing the test-retest reliability experiments corresponding to Ref7 and Ref8 it becomes clear that the ΔODS indicator presents a big drawback when used in structural modification assessment. Although it is the index with a highest sensitivity to damage, this receptivity is so high that even tosses alteration detection for cases with very hight test-retest reliabilities such as the two exposed. This fact, combined with the relative scaling of its values justify the discarding of this indicator in structural alteration detection (false positives would be commonplace). Imaginary and real part SCIs presents higher sensitivity to structural changes that the DRQ as already observed in the numerical campaign with the added perquisite of being capable of discerning reinforcements from degradations.

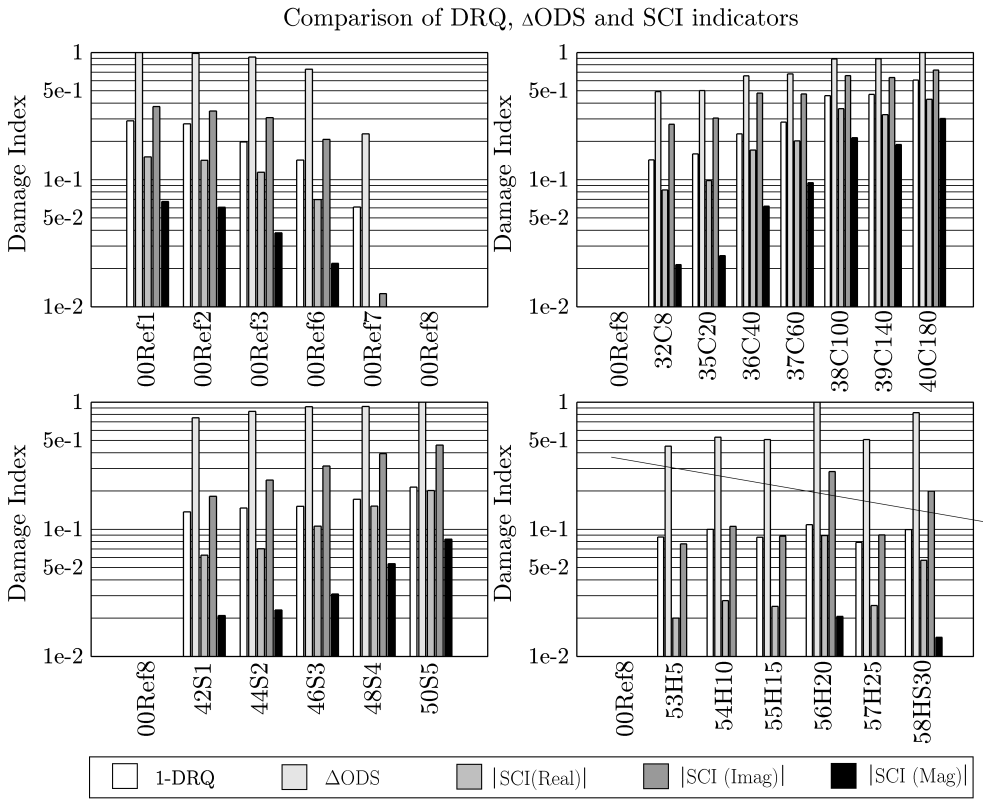

Figure 5.20: Comparison of DRQ, ΔODS and SCI indicators.

5.2 Model latticed tower

Experimental investigation of SCI indicators include an experimental campaign on a 1:12 downscaled model of a latticed tower built in the LITEM laboratory. Intentional and equivalent to structural alterations scenarios are introduced to the pristine structure and evaluated through the proposed indicator. The procedure is equivalent to the one used in the numerical numerical campaign of the FEM model of the tower. Experimental results allows to evaluate the influence of mechanical noise and non-idealised connectors of the structure (boundary conditions, screw-nut unions, riveted unions, flexible clampings and self interference of members). A critical discussion of the results obtained from simulations and from experimental acquisitions is finally exposed.

5.2.1 Experimental setup

The construction of the 1:12 prototype is executed following the geometry, simplifications and considerations already exposed in section 4.2.1.1. To avoid redundancy the reader is redirected back there for completeness of the discussion here presented.

The model tower was constructed following the 3D CAD model of the simplified 1:12 downscaled GE19 2-circuit LA455 110 kV tower by the author of this investigation with the support of the LITEM research group. The CAD software used to visualize and measure the geometry during construction is CIMNE's GiD 11.0. All the members of the structure are manually cut from preformed L profile rods and drilled to the adequate dimensions to fit the joining elements. Joints between elements are done using M5 high strength steel, with nuts and washers in both sides of the screwed unions. All screws and nuts are tighten to a torque of 8 Nm as torques near 10 Nm wear the screw thread out. In some specially tight locations, M5 steel rivets are used as joining elements as it is not possible to fit the screw head or the nut in the region. More details of the structure are given in section 4.2 concerning the geometry used in the modelization of the numerical model.

The model tower is built in two separate segments that are later assembled together. These two sub-assemblies consist in a lower part with variable width cross section, and an upper part, with constant cross section from where the tower arms extend. The two sub-assemblies are constructed from the initial skeleton formed by the four main columns of the structures and the eight companion horizontal members. This results in a truncated pyramid (for the lower sub-assembly) and an upper sub-structure with an octahedron shape. The lower section of the structure is built atop the initial

concrete base in which an auxiliary square steel structure is embedded. This embedded structure has 4 short L profiles standing out vertically to which the truncated pyramid substructure is screwed to assure perfect aligning. Vertical symmetry is achieved by the use of four bubble levels and a gravity plumb that is carefully checked until pointing to the centrer of the base square is achieved. The initial alignment is kept in place with the aid of screw clamps and thereafter, a drill is used to create the holes that house the M5 screws. The initial skeleton for the upper part is much easier to align correctly as the orthogonality of the members and faces allow to use set-squares as aligning tooling. Once the main components of the structure are set in place, additional horizontal and diagonal reinforcements are sequentially mounted on the structure. Final construction step involves the assembly of the two substructures. Again, the use of a gravity plumb and multiple bubble levels becomes mandatory. An auxiliary bridge crane is used to lift the upper sub-structure. Screwed clamps are used to temporary fix the upper sub-assembly in place. Holes are drilled to house M5 screws that fix both structures. Some constructive details of the structure are shown in figure 5.21.

Figure 5.21: From left to right and top to bottom: Completed prototype, arm of the tower, riveted union, screwed union and connection between the structure and the concrete base.

As already mentioned in the numerical chapter of this investigation (4.2), two different alternatives are used for the concrete base acting as the supporting element for the structure. The initial base to which the supporting steel skeleton is embedded consist of a fully filled concrete block of 1000x1000x200 mm on an elastomeric support. The

improved boundary condition, used to conduct the second series of experimental tests consist of the same base concrete block without the elastomeric bed and with wedges around all the contact perimeter.

This experimental investigation includes suspended cables in the experimental set-up. Dynamic interaction between cables and the lattice structure is not numerically modelled so this experimental approach allows to have an insight in its influence in the structural dynamics response of the system. The cables are supported by two clamping substructures mounted on two steel vertical columns in the laboratory. These clamps are assembled from U-profiles and keep in place by pressure and friction generated by M30 screws, nuts and washers. Material used in the cables is twisted multi-threaded aluminium, with a total diameter of 15 mm. Cables are attached to the column clamps using screwed tensors hooked to horizontal bar supported in the clamps. Cables are then buckled through shackles of screwed tensors and fixed over themselves with screwed staples. Wires are initially suspended from the tower arms using the same kind of screwed tensors mounted on cable clamps. Some of theses details can be reviewed in figure 5.22. The whole experimental set-up is also shown in figure 5.23.

Figure 5.22: From left to right and top to bottom: Isolated structure without cables, wired structure, wire clamping detail, cable staple and tensor, continuity union in the wires and cable connection to the tower.

Figure 5.23: Elastic boundary conditions experimental model tower set-up.

Experimental modal analysis tests executed for this first configuration are always performed for two directions of the tower, namely lateral and frontal tests planes. The accelerometer is positioned on a shared location between the two planes (and keeping corresponding direction for both planes tested). The experimental mesh used is one of the sub-sampled meshes from the full FEM grid, 36X30Y. This mesh includes nodes for the two directions of the model tower and is depicted in figure 4.46. Driving point F23/L22 adopted as the reference for all experimental modal analysis tests is depicted in figures 5.22 and 5.23 with a white arrow. Although the numeric analysis suggests that the most convenient driving point would have been F35/L30, the execution of the experimental modal tests is previous to the developement of the optimal driving point selection methodology. However, and if graph shown in figure 4.58 is revisited, point 44X/44Y (corresponding to the experimental F23/L22) shows the fourth best degree of correlation respect the ideally best driving point (which is numeric 64X/59Y and experimental F36/L30) and with a value very close to the second and third ones. Although the selection of the experimental driving point was initially done with a trial-error approach, further application of the finer-tuned already exposed driving point selection methodology shows that the initial informed guess, although not being perfect, is accurate enough. As results are found to be consistent, the experimental campaign is considered to be significant enough to extract valid conclusions.

The second experimental campaign with modified boundary conditions uses the same

geometry and concrete base than in the initial one. Dirving point is decided to be left in the same F23/L22 location as in the first experimental campaign for consistency. Further changes introduced besides boundary conditions include the substitution of the aluminium cables by vegetal fibre torsioned ropes. These ropes are tied in one of its free ends to a clamp attached to a laboratory shelf whereas the other free edge is put on a near-frictionless support (made of polished stainless steel) on the moving head of an electromechanical traction/tension testing machine. Weights of 5 kg are tied to each of these other free ends on the quasi-frictionless support so the tension on the ropes can be controlled (this was not the case on the initial campaign with aluminium cables, where the tension of the cables was not controlled but only tighten to similar torques on the screw tensors). The connecting element between the ropes and the arms of the tower is also substituted by segments of chain with a carabiner in its lower end in which the rope rests. Some of these details corresponding to the second set-up are shown in figure 5.24. A general overview of the setup is shown in figure 5.25.

Experimental modal analysis hardware consist of vibration acquisition equipment by the manufacturer Bruel & Kjaær. Hardware used include a DAQ Type 3050-B-060 connected via an ethernet link to a 32-bit architecture Windows XP Laptop Computer running Pulse LabShop v13.1.0.246 acquisition software. The model of accelerometer used is 4370-V with a type 2646 capacity-to-current analogue amplifier and with a mounting magnet. EMA is made in terms of roaming excitation with impact hammer model 8206-003. All the connections to the sensors are done with low-noise double-screened coaxial 10-32 UNF to BNC cables. Post-process aimed to extract the complete modal model from the raw EMA captured data is made using the software by Vibrant Technologies ME'Scope VES v4.1

Acquisition parameters are set so a total number of 1600 spectral lines are available in the FRF series, with a frequency resolution of Δf = 0.25 Hz so a total number of 4096 samples in the temporal domain (12-bit buffer) are needed. Bandwidth is selected to range up to 400 Hz as it is near this upper limit where noise starts to dominate signals and resonant peaks become fuzzy in the FRF spectra. Sampling, then, is determined to be f_{sampl} = 1024 Hz with an acquisition window of 4 seconds. An exponential window is used to reduce noise on the accelerometer channel whereas the impact hammer is sampled with a rectangular window.

5.2.2 Experimental campaign

The objective of the experimental campaign is to obtain a set of FRFs for each of the damage progression stages so correspondent CFDACs can be generated. Some repeatability tests are also done in order to set the repeatability thresholds on the structure after the damage application. Two different experimental campaigns have been performed, each of them corresponding to one of the two presented boundary conditions. For each of the campaigns, several configurations with and without cables are tested. Unwired altered configurations are always compared to its unwired reference and wired modification scenarios are always compared to wired references. This way, altered states with cables are never compared to the states without cables.

Figure 5.24: From left to right and top to bottom: General view of the wedged boundary conditions set-up, inclination of the rope lines, attachment of ropes to arms, detail of the link, weights hanging on the ropes, knotted edge of the ropes.

Figure 5.25: General view of the wedged BC prototype tower set-up

Cables have considerable influence on the FRFs acquired specially in terms of noise introduction and harmonic multiplicity around purely structural modes. So then, unwired states allow to evaluate the capabilities of the SCI indicator on structural modification detection without the increase of noise and complexity introduced by the cable coupling. Damage scenarios tested during the experimental campaign are depicted in table 5.3. Damage typologies are shown in figure 5.26 for their first apparition in the elastic boundary support campaign.

		Case	Name	Description
Elastic boundary condition (Dir. X and Y)	Unwired	C0A	Reference1	Reference condition before intervention
		C1	MiddleTruss	Removal of an horizontal truss in the 5th floor in the frontal plane
		C2	SecondaryTruss	Removal of secondary and tertiary reinforcements in the first floor
		C3	PrimaryTrussL	Removal of primary left diagonal reinforcement in the frontal plane
		C4	PrimaryTrussLR	Removal of primary left and right diagonal reinforcements in the frontal plane
		C5	CorrosionAnalog	Unscrewing of the frontal plane right link between the tower and base
		C6	IceAnalog	Addition of 10 kg in each arm to simulate ice overweight
		C0B	Reference2	Reference condition after intervention
	Wired	C0A	Refrence1	Reference condition before intervention
		C1	PrimaryTrussL	Removal of primary left diagonal reinforcement in the frontal plane
		C2	PrimaryTrussLR	Removal of primary left and right diagonal reinforcements in the frontal plane
		C3	CorrosionAnalog	Unscrewing of the frontal plane right link between the tower and base
		C4	IceAnalog	Addition of 5kg in each half-wire to simulate ice accretion in the cables
		C5	WindAnalog	Rope pulling from the top with α ∼25 to the normal of the frontal plane. 25 kg
		C6	1FallenWire	Top right cable (reference frontal plane) detached
		C7	3FallenWire	3 right cables detached
		C8	1PullingWire	Top right cable unsymmetrical. Pulling in one direction. Unknown force
		C0B	Reference2	Reference condition after intervention
Wedged boundary condition (Dir. X)	Unwired	C0A	Reference1	Reference condition before intervention
		C1	SecondaryTruss	Removal of secondary and tertiary reinforcements in the first floor
		C2	PrimaryTrussL	Removal of primary left diagonal reinforcement in the frontal plane
		C3	PrimaryTrussLR	Removal of primary left and right diagonal reinforcements in the frontal plane
		C4	CorrosionAnalog	Unscrewing of the frontal plane right link between the tower and base
		C0B	Reference2	Reference condition after intervention
	Wired	C0A	Reference1	Reference condition before intervention
		C1	SecondaryTruss	Removal of secondary and tertiary reinforcements in the first floor
		C2	PrimaryTrussL	Removal of primary left diagonal reinforcement in the frontal plane
		C3	PrimaryTrussLR	Removal of primary left and right diagonal reinforcements in the frontal plane
		C4	CorrosionAnalog	Unscrewing of the frontal plane right link between the tower and base
		C5	WindAnalog	Rope pulling from the top. α ∼45 to the normal of the frontal plane. 25 kg
		C6	1FallenWire	Mid right cable (reference frontal plane)detached
		C7	3FallenWIre	3 right cables detached
		C8	1PullingWire	Top right cable unsymmetrical. Pulling in one direction. Unknown force
		C0B	Reference2	Reference condition after intervention

Table 5.3: Damage progression stages. Prototype tower.

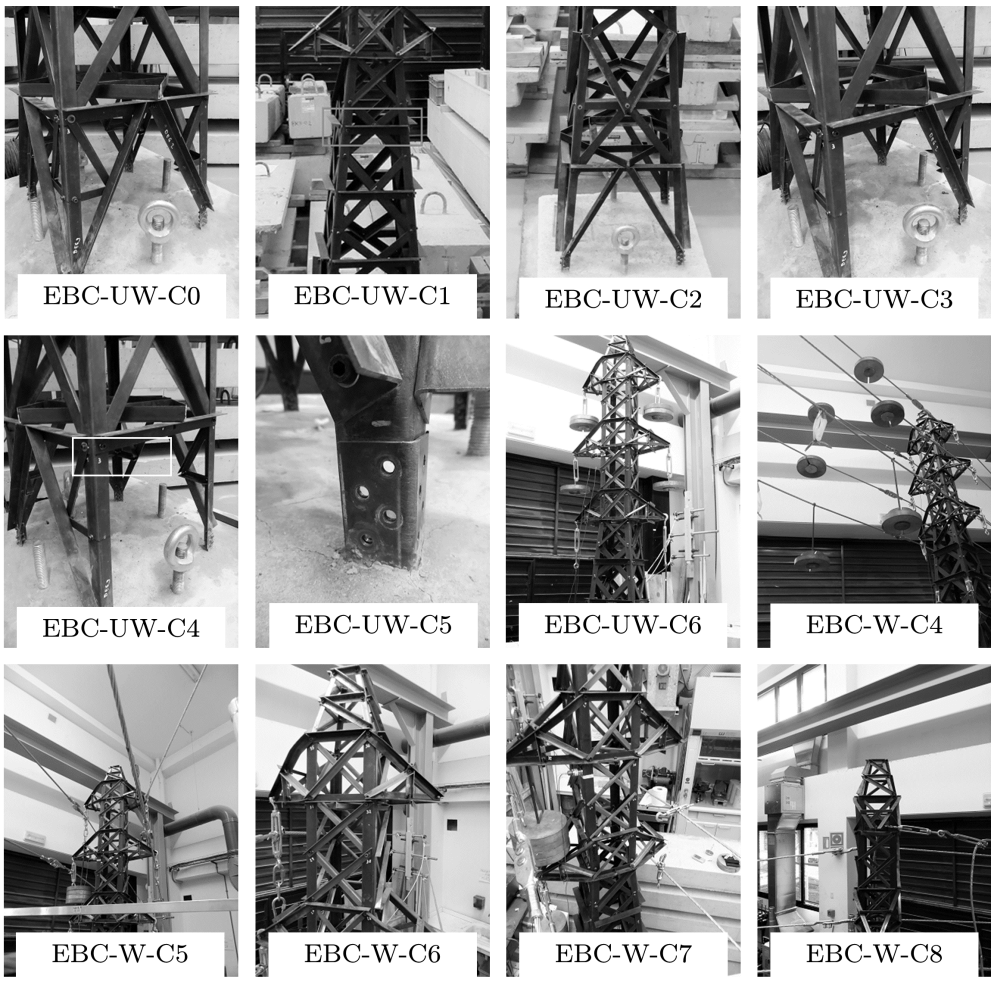

Figure 5.26: Experimental structural alterations applied on the model tower.

5.2.3 Parameter sensibility

Parametric analysis using experimental FRFs is performed for the experimental damage stages shown in previous section. These cases correspond to four acquisition campaigns: the first with an elastic boundary condition and no cables, the second with an elastic boundary condition and cables, the third with wedged boundary conditions and no cables, the last with wedged boundary condition and cables.

The only parameter studied in this section is the bandwidth as other parameters have already been demonstrated to be either of small importance or either controllable to convergence if certain requirements are met. All experimental acquisitions are performed using the same parameters. A total bandwidth of 400 Hz is selected to be

sampled with a frequency resolution of $\Delta f = 0.5$ Hz. Cases tested using the elastic boundary condition include data from the two tested planes of the structure, namely the frontal an lateral one. These first two families of experimental damage cases include 36 FRFs acquired for the frontal plane with driving point set at position F24 and 30 FRFs for the lateral plane with driving point L22. So then, the SCI and CFAC indicators for the first two experimental campaigns are generated from a total number of 66 FRFs with driving points set at positions F24/L22. Cases corresponding to the two families that use wedged boundary conditions are only sampled for the frontal plane, so the only 36 FRFs are available to the computation of the indicators. In these two last families driving point is also kept at location F24 of the frontal plane. 36F30L experimental acquisition mesh and driving point pair F24/L22 are depicted in figure 4.46.

Numerical campaign results show that the hypothetical best position to position both driving points is point 64X/59Y of the full numerical mesh. This point corresponds to position F35/L30 of the experimental mesh. The driving points were originally chosen by trial and error by probing the point which showed better modal visibility to the naked eye (a common practise when executing EMA tests aimed to extract modal models). The optimal driving point decision methodology was developed much later in this investigation than the execution of all the tests in the experimental campaign. Experimental database of the model tower used in this investigation was originally purposed to a damage detection methodology involving conventional modal-domain derived damage indicators.

When the optimal driving point methodology showed that the driving points used in the experimental campaign was not the one with most modal visibility it was initially considered to repeat the whole four experimental campaigns. However, and due to the fact that the used driving point couple was the fourth best one (and almost equal to the third and second pairs), it was decided that effort-to-gain ratio of repeating the whole four campaigns was not enough to justify its repetition and that valid conclusions could be extracted from the indicators generated from already available FRFs with sub-optimal driving points.

5.2.3.1 Bandwidth

The study of the influence of the bandwidth in the SCI indicators for each of the four experimental campaigns is done for a range of maximum frequencies between 25 Hz and 400 Hz in 25 Hz steps. These discretization is the same used in the numerical campaign involving the model tower. Results for the four campaigns are shown in

figures 5.27 to 5.30.

Discussion in this section tries to uniquely address the convergence trend of the results. For most of the cases it becomes apparent that the SCI indicators seem to stabilize at bandwidths equal or grater that 200 Hz. This trend is not strictly true for all cases but can be adopted as a general descriptor of all the series present in the results. Again, and is a similar fashion of what is is observed in the numerical to experimental comparison of the indicators for the aluminium plate, this trend is much beneficial than the monotonically growth tendency that is observed in the bandwidth sensibility analysis for the aluminium plate. This is justified by the less modal richness of the tower in the range studied (as already stated in the numerical parametric analysis). Additionally, experimental acquisition of FRFs also introduce considerations regarding the excitation on the structure. In a real acquisition scenario, low frequencies are usually better captured and described than higher ones. Although this could potentially lead to enhaced stability properties of the indicator due to high frequencies contributing less to the PCC correlation, the relative narrow bandwidths involved in this study suggest that this phenomena can be put aside the discussion for the model tower cases.

The sign in the SCI indicators is not consistent with the damages introduced in the structure. In the aluminium plate experimental campaign, these inaccuracies were attributed to the masking effect causing by boundary conditions alterations over the real structural modifications introduced. In the cases here analysed this factor is much more important as the boundary condition with the ground is observed to be at least, inconsistent. Boundary conditions in the model tower are observed to be the biggest distortion source in this investigation and thus, completely distorts the sign decision algorithm for the SCI indicator. However, absolute values of the indicators are representative of the amount of damage present in the structure as, for example trusses removal and corrosion analogy cases in figure 5.27 show reasonable correlation between its increasingly growing SCI indicators and the severity of damages in this stages. Convergence threshold is decided to be set at a bandwidth of 200 Hz. This value is used in further discussions regarding the influence of the damage typology on the SCI indicators.

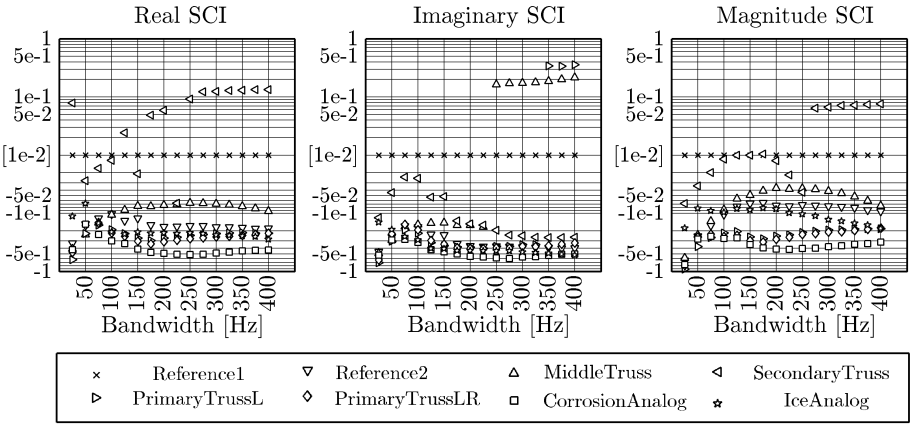

Figure 5.27: SCI indicator for the elastic boundary unwired campaign versus bandwidth.

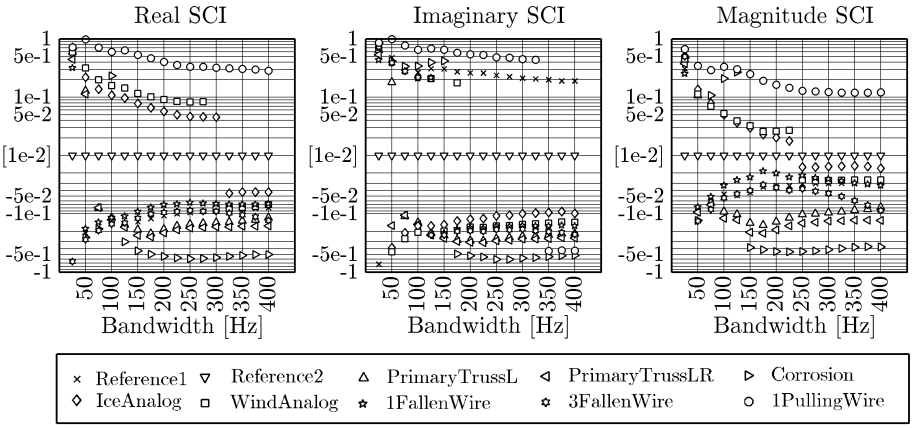

Figure 5.28: SCI indicator for the elastic boundary wired campaign versus bandwidth.

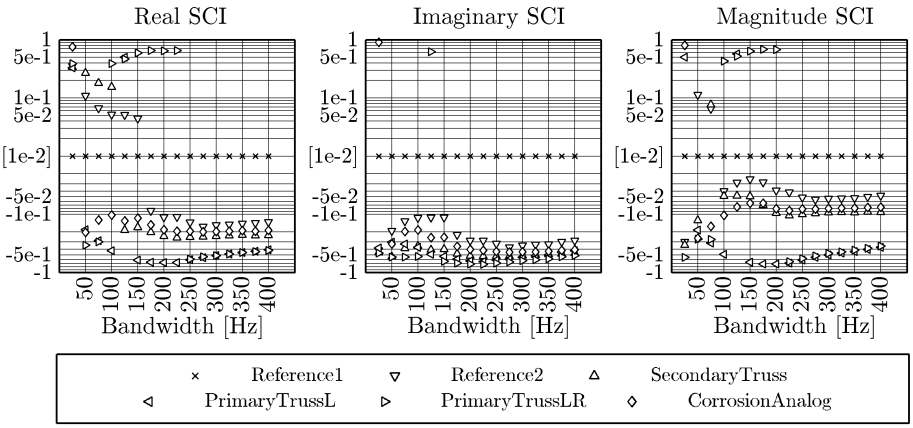

Figure 5.29: SCI indicator for the wedged boundary unwired campaign versus bandwidth.

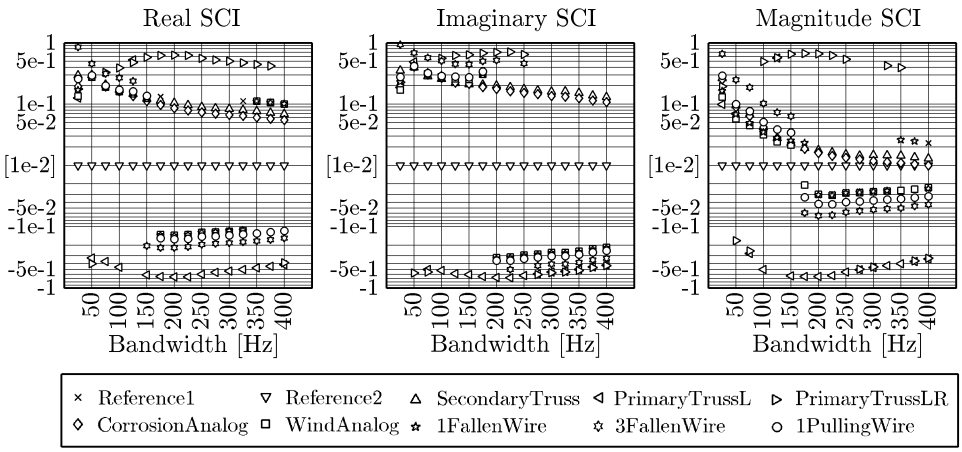

Figure 5.30: SCI indicator for the wedged boundary wired campaign versus bandwidth.

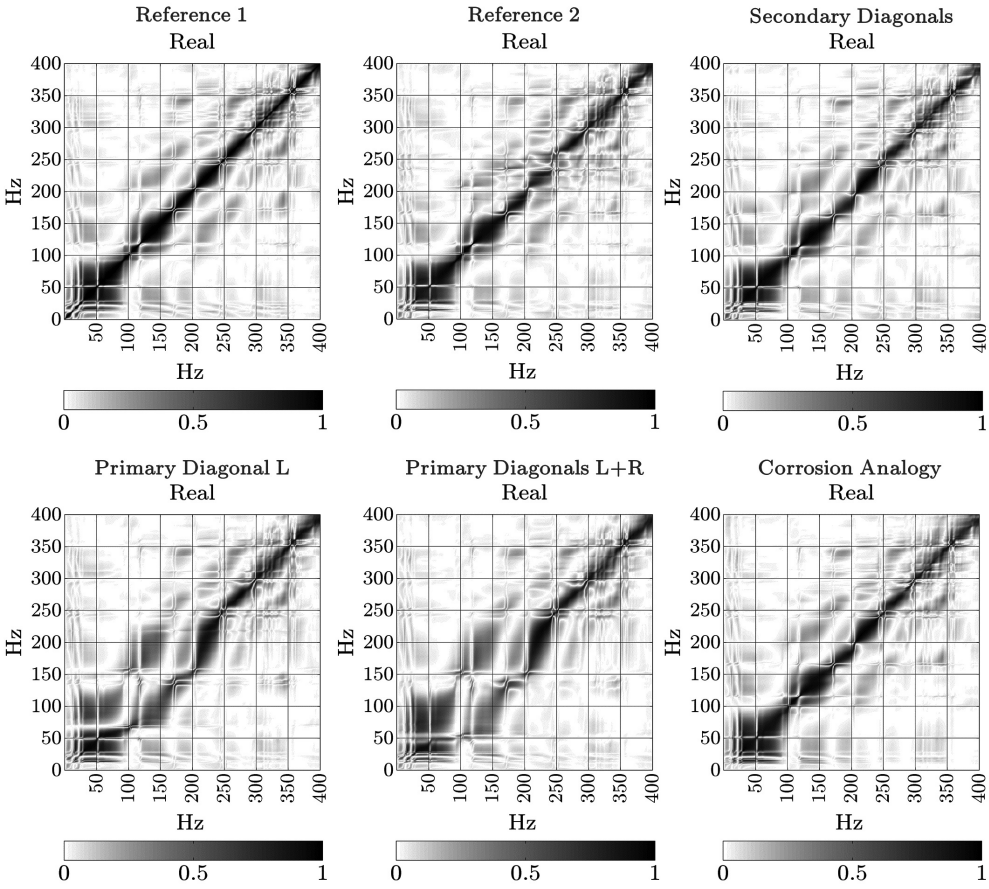

Figure 5.31: Evolution of the real part of the CFDAC for damage scenarios in wedged boundary unwired campaign. 36F mesh, DPF23, $\Delta f = 0.5$ Hz, BW = 400 Hz

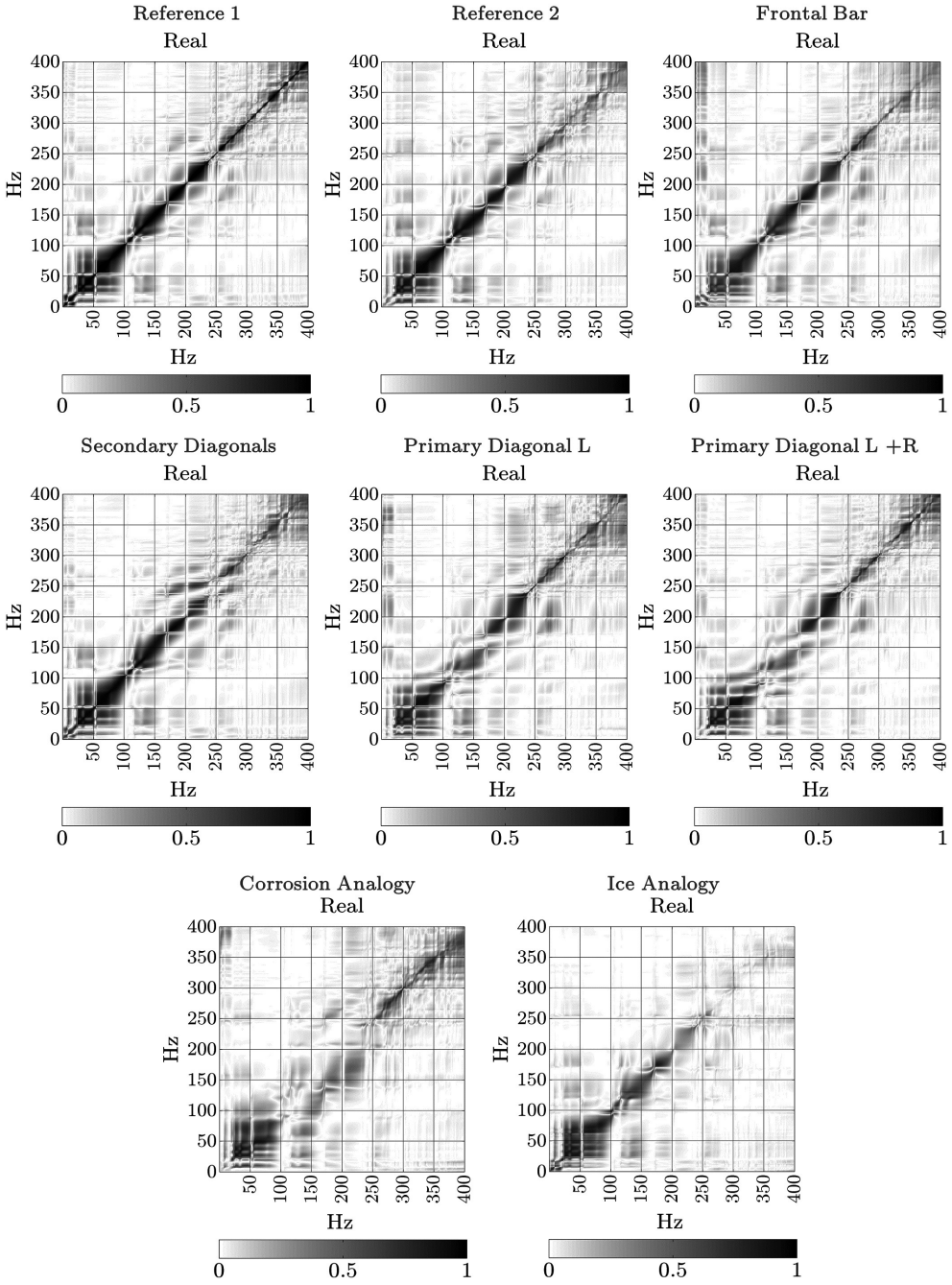

Figure 5.32: Evolution of the real part of the CFDAC for damage scenarios in elastic boundary unwired campaign. 36F30L mesh, DPF23L22, $\Delta f = 0.5$ Hz, BW = 400 Hz

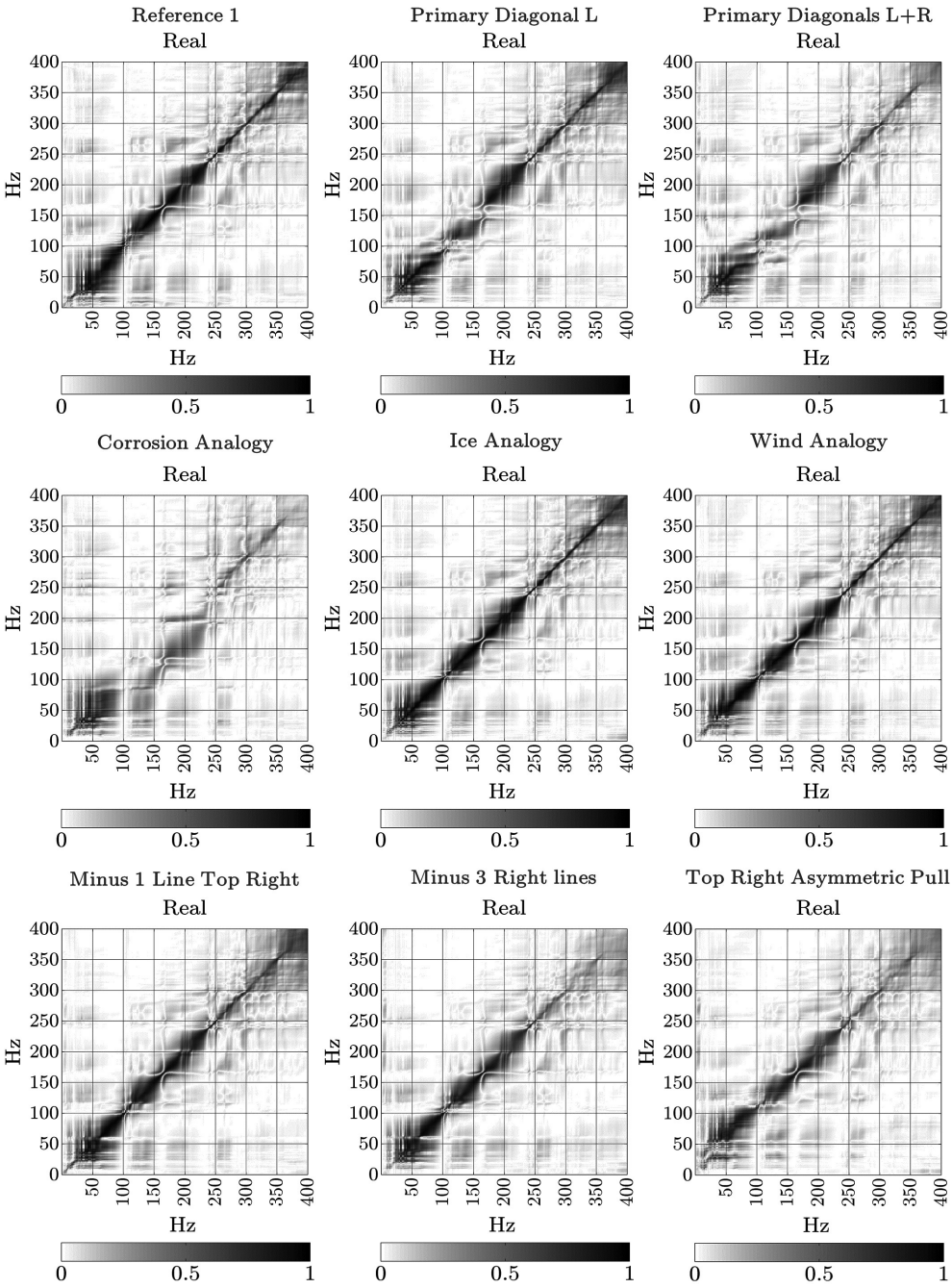

Figure 5.33: Evolution of the real part of the CFDAC for damage scenarios in elastic boundary wired campaign. 36F30L mesh, DPF23L22, $\Delta f = 0.5$ Hz, BW = 400 Hz

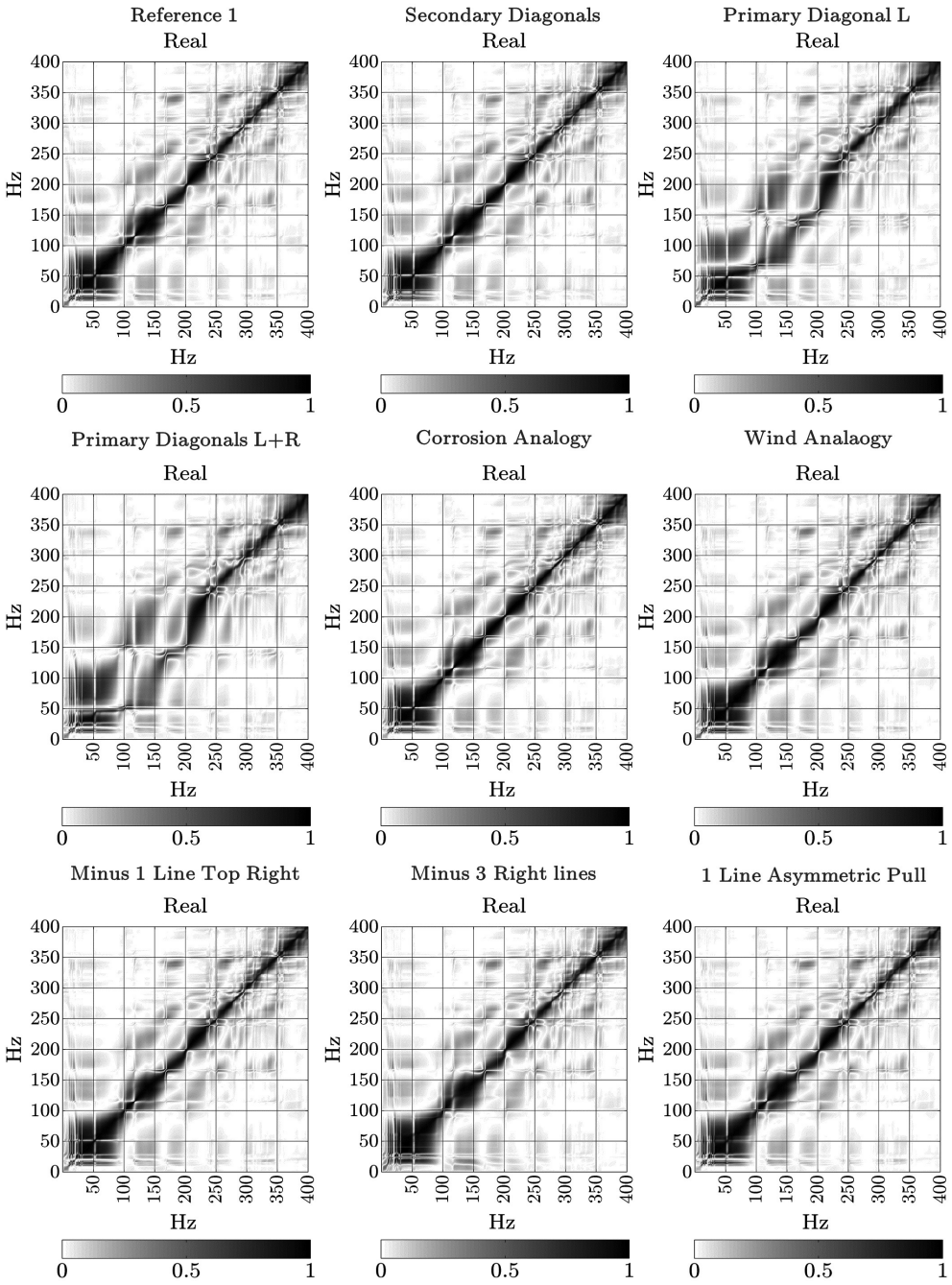

Figure 5.34: Evolution of the real part of the CFDAC for damage scenarios in wedged boundary wired campaign. 36F mesh, DPF23, $\Delta f = 0.5$ Hz, BW = 400 Hz

5.2.4 Structural modification assessment

This section shows the correlation between damage typologies and the real part of the CFDAC and the SCI indicators. Results are shown for the four experimental campaigns.

5.2.4.1 Damage typology and the CFDAC

Real parts of the CFDACs here shown are calculated from the full data series available for each case in each experimental campaign, so the full 400 Hz bandwith is utilised to compute these matrix indicators. Results are shown in figures 5.32 to 5.34 for the four experimental campaigns.

Focusing on the results for the unwired elastic boundary condition campaign in figure 5.32, it becomes clear that all structural modifications except the removal of the frontal bar are clearly translated to degradations in the diagonal structure of the real CFDACs. Removal of the secondary an tertiary reinforcements is specially visible in degradations around the 250 Hz region in the CFDAC.This shift however, introduces an increased correlation in the positive triangular sub-matrix of the real CFDAC. This indicates that the removal of these bars slightly reduce the mass in the structure buts its effect in the modal stiffness is of less importance. Primary diagonal removal cases are clearly shown as stiffness reductions in the CFDACs in spectral regions around 200 Hz. Corrosion analogy case introduces a distortion in all frequencies in the range visualized whereas added weight simulating vertical overloads in the structure causes a loss of correlation in the CFDAC for higher frequencies between 200 Hz and 400 Hz.

Cases in the second experimental campaign corresponding to the tests with elastic boundary condition and wires are shown in figure 5.33. In general, the presence of cables introduce noise and harmonic duplication of fundamental modes around their original locations. This is shown in the CFDAC matrices as enhaced correlation regions around the main diagonal structure, so the whole CFDAC matrix becomes fuller outside the diagonal. Cases involving the removal of bars show a similar tendency to the exposed in previous paragraph. However, noise in the FRFs and consequently, in the CFDACs slightly masks this observation. Wind analogy case (with a rope pulling with a 250 N force from the top of he tower) causes little alteration in the CFDAC shown as an alteration in the correlation lobes at 200 Hz. Damage cases including the effect of cable falls blur the CFDAC matrix in the range of 250 Hz to 400 Hz.

Results for the unwired wedged boundary condition campaign in figure 5.31 are very similar to those in campaign 1. However, in this case, improved boundary conditions

causes that the amount of shift in the CFDACs is shown even clearer than in that first campaign. The corrosion analogy in this family of cases however, show little to non-existent degradation. It is hypothesized that although all screws in the right leg of the frontal plane that link the tower to the concrete base are removed, construction stresses on the structure or even reduced dimensional tolerances cause that the leg gets blocked and rests completely linked to the support, effectively acting as in its pristine condition.

Results for the experimental campaign using wedged boundary conditions and cables (figure 5.34) show results very similar for the trusses removal scenarios to the previous campaign. The main differences with elastic support and wired campaign appear for the cases of cable falls and wind analogy. Naked eye observation makes very difficult to identify alterations in the CFDACs for these cases.

5.2.4.2 Damage typology and the SCI

SCI indicators here shown are calculated from the full data series available for each case in each experimental campaign with a convergence bandwidth of 200 Hz identified in section 5.2.3.1. SCIs corresponding to real parts, imaginary parts and magnitudes of the CFDACs are depicted as squares, triangles and circles in figures 5.35 to 5.38.

SCIs corresponding to the first elastic support unwired campaign (figure 5.35) show that the repeatability test should not be considered as such, as the damage indicator shows a considerable amount of discorrelation. This is mostly due to the possible change in boundary conditions or even due to structural changes accumulated during the damage progression. Although case representing the removal of the two main diagonal trusses of the first level shows a wrong sign (due to the fact that CFDAC shift is so global that the even CFDAC positive semi-matrix is altered), the correlation between the alteration and SCI indicators presents a consistent trend.

SCIs corresponding to the second elastic support wired campaign (figure 5.36) shows similar results to the unwired equivalent one. In this case Reference 2 is selected as the baseline comparison reference state as SCI indicators computed with it better correlate with damages than the ones generated using Reference 1 as the baseline. Again, the sign decision algorithm shows mixed accuracy. Cases representing wind analogies and falls of cables also show values of SCIs above the detection thresholds. Results for third and fourth experimental campaigns on the unwired and wired tower with wedged boundary conditions (figures 5.37 and 5.38) show results very similar to the ones with the elastic boundary conditions.

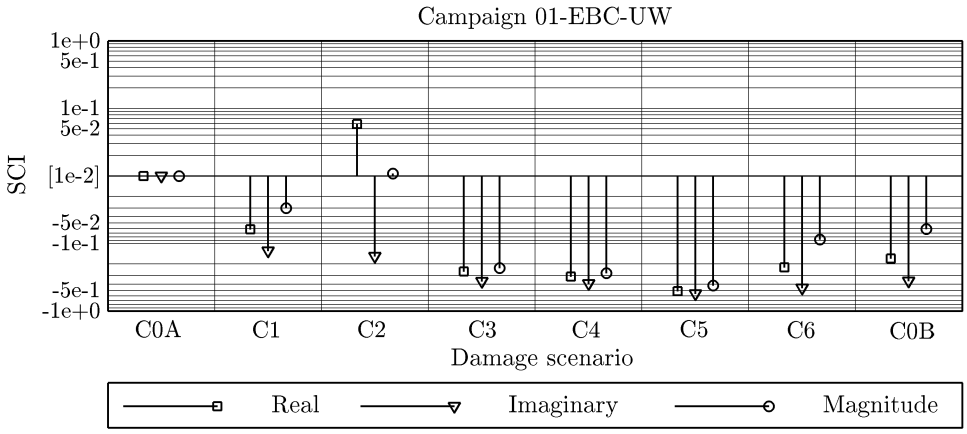

Figure 5.35: SCI indicator for the elastic boundary unwired campaign. BW = 200 Hz.

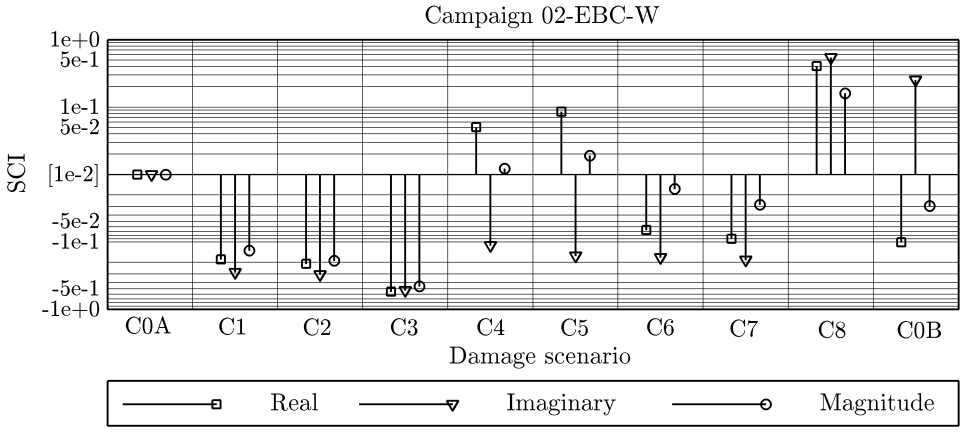

Figure 5.36: SCI indicator for the elastic boundary wired campaign. BW = 200 Hz.

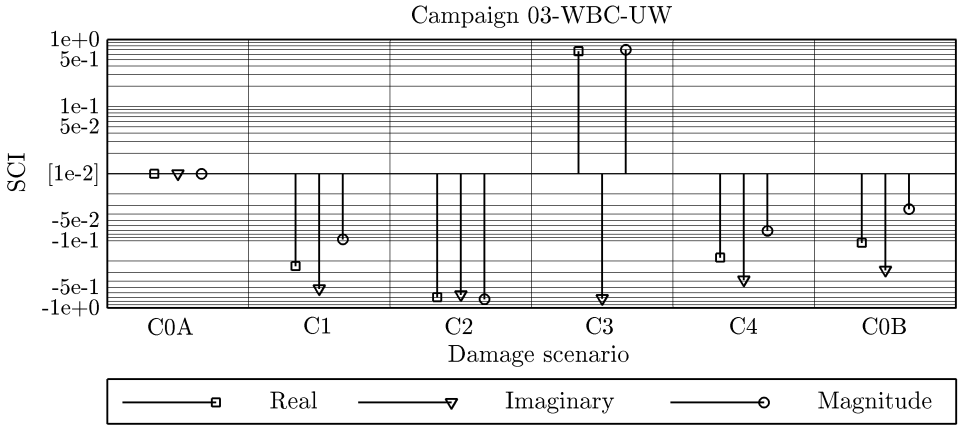

Figure 5.37: SCI indicator for the wedged boundary unwired campaign. BW = 200 Hz.

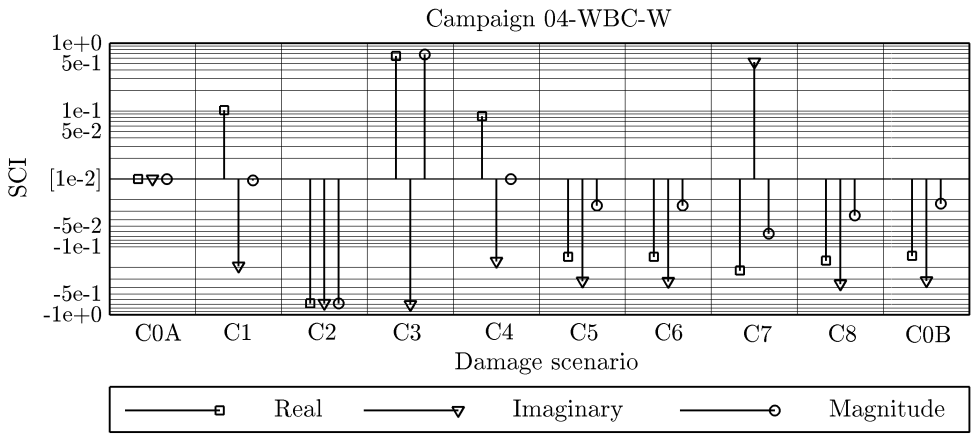

Figure 5.38: SCI indicator for the wedged boundary wired campaign. BW = 200 Hz.

Observation of results leads to the conclusion that the SCI absolute values (the PCC correlation of CFDACs) are not specially sensitive to boundary conditions. As already observed, real part SCI is somewhat more linear in front of alterations introduced in the structure whereas SCI corresponding to the imaginary part is generally slightly more sensitive.

5.3 Full-scale latticed tower

Final step of the research involve the use of the proposed indicator to the evaluation of damage in a real scale, in-service conditions, latticed power transmission tower to which certain artificial degradations are introduced. Experimental measurements on the field structure are taken using the EMA technique so proposed indicators can be computed. Two differentiated stages will be taken in this final discussion.

In first place, relationship between spectral indicator and modal residual stiffness is extracted from a range of frequencies in which experimental acquired FRFs are clear and with few noise making modal post-process possible. This process is parallel to each of the previously proposed tasks serving as a reference to get the correlation between the SCI and residual modal stiffness in the range selected

In second and final place, degradation using the indicator is evaluated in all the range available in the experimental FRFs even for frequency ranges where experimental noise make the application of modal post-processing techniques not viable. This is the final and main goal of this whole research: evaluating the SCI as an indicator of damage without the use of any kind of modal post-processing.

5.3.1 Experimental setup

The full scale test campaign is executed on real in-field plant consisting of three medium voltage latticed power transmission towers with discharged lines. The lines used in the installation are deployed used LA56 cables made of a 47AL1/8-ST1A alloy and with a cross section of S = 54.5 mm^2. Latticed towers belong to the OLMO-15-3T-H42 series with free distances of 30 m between each support giving a total length of 60 m. The metallic latticed towers are founded to the ground using a concrete block of 170x170x175 cm. Figure 5.39 shows some images regarding the installation of the towers: the initial vertical alignment, the foundation of the structures and the wiring of the latticed supports. The experimental mesh adopted is directly marked on the tower once installed. Geometry of the tower and experimental acquisition mesh are shown in figure 5.40.

Figure 5.39: Installation process of the full-scale power transmission towers.

Vibration acquisition hardware is by the manufacturer Bruel & Kjaær. Vibration equipment available include a DAQ Type 3050-B-060 connected via an ethernet link to a 32-bit architecture Windows XP Laptop running Pulse LabShop v13.1.0.246 acquisition software. The models of accelerometers used are 4370-V with a type 2646 capacity-to-current analogue amplifier and with mounting magnets. The Experimental Modal Analysis is made in terms of Roaming Excitation with impact hammers models 8206-003. All the connections to the sensors are done with low-noise double-screened coaxial 10-32 UNF to BNC cables. Driving point used in the experimental acquisitions is DP5 of the full-scale experimental mesh. EMA modal analysis tests are done using the roaming excitation technique using an articulated crane. Specialized in-heigh workers are trained to perform the impacts with the testing hammer on the structure. Some details of the experimental set-up are shown in figure 5.41.

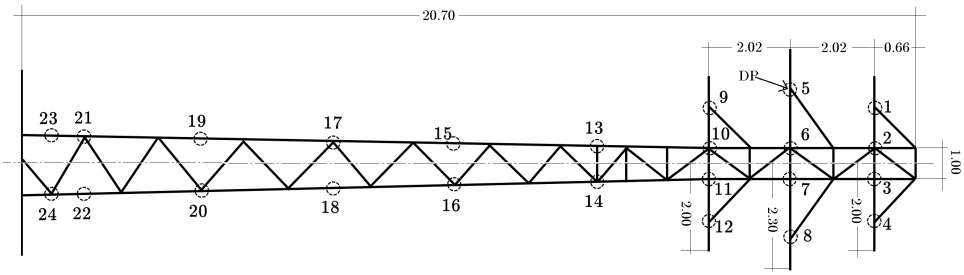

Figure 5.40: Geometry of the installed towers and experimental acquisition mesh. Dimensions in m

Figure 5.41: Top left, location of the accelerometer in point D5 of the experimental mesh. Top right, bottom left: crane used to access and test the structure. Bottom right: COMSA-EMTE worker performing the EMA impact on the tower.

5.3.2 Experimental campaign

The experimental campaign executed on the tower consist on a series of 6 intentionally applied damage scenarios to the tower and two additional reference cases, the first one corresponding to the initial pristine state of the structure after installation and the second one corresponding to the reassembled state once all damage scenarios have been applied to the structure. All tests are executed in the central latticed tower of the 3 support installation. Table 5.4 shows the damage progression stages.

The first damage applied to the structure consist in the loosening of the screws and nuts corresponding to the first level of complete diagonals of the structure. Figure 5.42 shows the existence of a first level of diagonals partially embedded in the concrete foundation. This first damage state loosens all the bars in the level immediately above these trusses.

Second stage of damage adds up to the first actuation on the structure. In this case, the diagonal trusses in the immediately above level are also loosen. The corrosion analogy case is reproduced by tightening again all the unscrewed bars and loosening the bars corresponding to the link between the tower and the support. 6 screws and nuts are loosen but not removed.

The last three cases include the unlinking of one of the mid cables from the structure (the left one facing geographical north), the addition of a 20 kg weight on the right middle arm of the pristine structure (again, facing geographical north) and the over tension of the middle left cable using a rope and a tension pulley.

ID	Case	Description
C0A	Reference1	Reference condition before intervention
C1	1stLevelDiagonals	Unscrewing of the nuts tightening all the first level diagonals
C2	2ndLevelDiagonals	Unscrewing of the nuts tightening all the first and second level diagonals
C3	CorrosionAnalog	Nuts of the diagonals re-tighten. With a frontal reference on the tested plane, unscrewing of the nuts of the left leg connecting the structure to foundation
C4	IceAnalogy	Addition of a 20 kg mass to each of the middle arms of the tower
C6	Minus1Line	Detachment of the right middle cable from the tower arm
C6	1LinePull	Overtension on the right middle cable of the tower with a levered spool tensor
C0B	Reference2	Reference condition after all degradation interventions

Table 5.4: Damage progression stages on the full scale tower.

Frequency response functions captured in this real scenario are much more noisy than the signals acquired in laboratory conditions. Figure 5.43 shows 2 signals for each of the two reference states of the tower corresponding to nodes 7 and 15 of the experimental mesh. As it can be observed, only the 0 Hz to 50 Hz range shows clear resonant peaks corresponding to modal frequencies. Information above 50 Hz does not show clear resonances. From a conventional modal analysis point of view, this would make the

spectral series above this threshold completely useless. However, spectral indicators proposed in this investigation allow to include such noise data in the damage indicator generation without loss of generality. So then, this full-scale experimental campaign serves as a tool to validate the initial hypothesis that spectral processing is much more flexible than conventional modal-derived damage indicators.

Figure 5.42: Damage scenarios tested in the full scale experimental campaign. From left to right and top to bottom, loosening of the first level diagonals, corrosion analogy, unlinking of the mid right cable, ice accretion analogy, cable overtension analogy.

5.3.3 Parameter sensibility

The parametric analysis addressed in this section includes only the study of the influence of the bandwidth in the damage indicators. This segment is faced only from an experimental standpoint so this is considered to be enough to extract valid conclusions on the suitability of the methodology in damage detection in real applications.

A total of 24 FRFs are available to generate the CFDAC, with a total acquisition bandwidth of 400 Hz, an acquisition frequency resolution of $\Delta f = 0.5$ Hz and setting the driving point in location 5 of the experimental acquisition mesh (Figure 5.40).

These acquisition conditions are exactly equivalent to the ones used in the model downscaled tower.

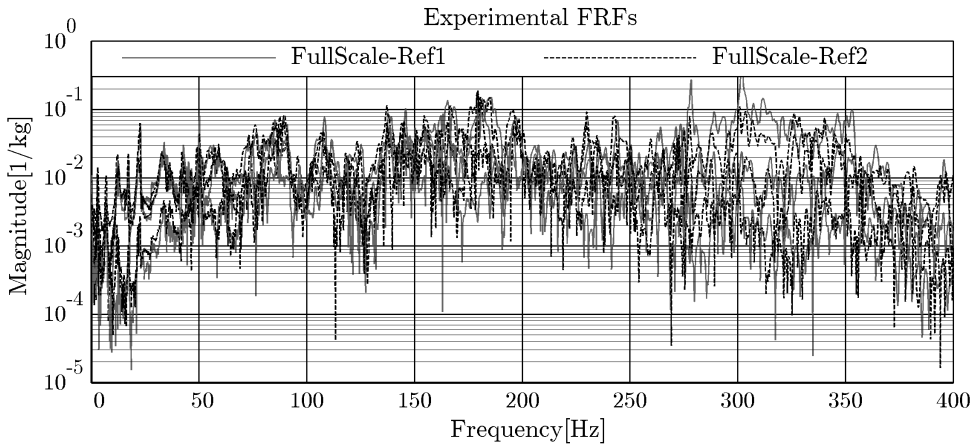

Figure 5.43: Example FRFs for the 1:1: real scale tower

5.3.3.1 Bandwidth

Bandwidth sensibility is studied by cutting the maximum frequency of interest in the original acquisitions and observing the evolution of the indicators. Bandwidth is ranged from 25 Hz to 400 Hz in 25 Hz steps. Results for each of the intentionally applied damage scenarios and bandwidths are shown in figure 5.44

Observing the figure at first sight, the sign decision algorithm for the SCI is observed to be inaccurate, as all damage stages should result in negative valued indicators (due to the presence of under-stiffness).

In second place, repeatability results (Reference2) show large values of structural alteration, although this is considered a pristine condition. However, this second reference state is measured after the application of all the campaign of intentional damages, so this shift in the reference results is considered to be significant of certain modifications accumulated by the structure after the campaign.

A third observation can be done regarding the behaviour of the indicators as frequencies of interest in the bandwidth increases. It seems reasonable to affirm that the indicators do not significantly diverge (except for the sign decision algorithm) when the bandwidth is increased. This result discredits the numerical behaviour observed for the aluminium and model tower, where the increase in bandwidth is observed to correlate with an increase in the SCI indicators. As already stated, this soft convergence behaviour is attributed to the fact that in real scenarios, excitation of high frequencies is increasingly more difficult to do so CFDAC in those regions dilute and therefore,

its contribution to the SCI correlation becomes less and less important.

Last but not least, no clear correlation between the amount of damage and the value of the SCI indicators is observed in these experimental results. This is specially clear when following the trends of the damage case correspondent to the removal of one of the levels of diagonal trusses and the case corresponding to the removal of two diagonal levels. Values corresponding to both cases appear in arbitrary pistons in the SCI scale, so then, gradation in the severity of damage is not clear.

Be that as it may, the SCI indicators always clearly show structural degradation for all cases.

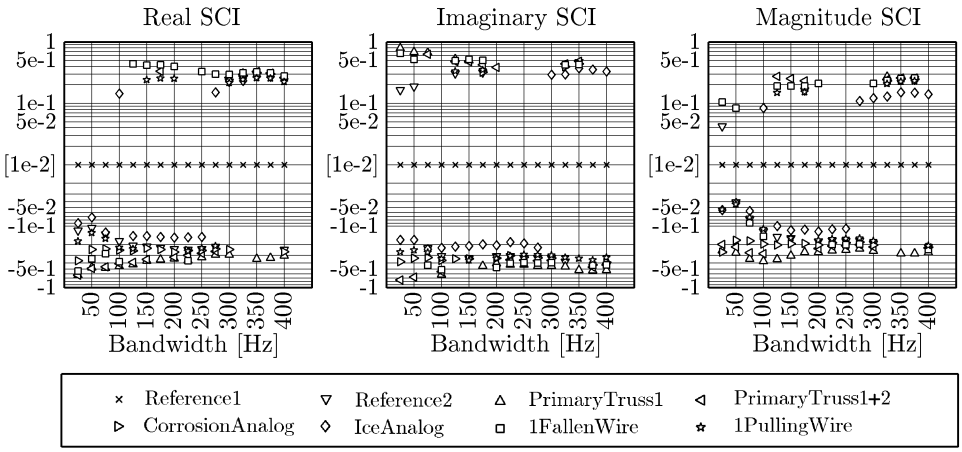

Figure 5.44: Evolution of the SCI indicator for the damage scenarios in the full scale tower as a function of the bandwidth

5.3.4 Structural modification assessment

Analysis of the influence of the damage typologies on the CFDAC and on the SCI indicators is done for a bandwidth of 200 Hz. This value has been hand-picked as the first bandwidth analysed where a relative convergence in the indicator is achieved and avoiding high frequency regions where the sign decision algorithm for the SCI starts to fail. All other acquisition parameters are the same already exposed in section 5.3.3.

5.3.4.1 Damage typology and the CFDAC

The visual analysis of the real part of the CFDAC in figure 5.45 is much more difficult than for the experimental cases of both the aluminium plate and the scaled tower due to the heavy presence of noise in the signals. Although the detailed observation of

each case do not shown clear distortions in the CFDAC diagonal structure above the general noisy distortions, some general affirmations can be done.

The first observation to be made is that the diagonal structure in the CFDAC matrix is much thinner than in the plate and scaled tower cases. This fact is related with the modal density in the spectral range of interest. As more modes are present in the range, correlation intervals between them reduce and thus so does the diagonal main correlation diagonal of the CFDAC.

Cases corresponding to the loosening of one and two level of diagonal reinforcements show a characteristic distortion in spectral regions between 0 Hz and 50 Hz. This segment is where the pure modal resonances where identified in first place. So then, these distortions are representative of the modification in the natural modes caused by the unscrewing of these diagonal trusses. Other damage scenarios present fuzzy distortions without clear tendencies. The only common characteristic that can be identified is the general blurring in the diagonal structure of the CFDAC showing some kind of correlation loss. Elaboration of conclusions for CFDACs computed from noisy FRFs is a much more estimative task.

5.3.4.2 Damage typology and the SCI

The analysis of the SCI indicators for each damage introduced in the structure casts similar results to the ones showed in the bandwidth sensibility analysis. Figure 5.46 shows SCIs corresponding to the real part, imaginary part and magnitude of CFDACs as squares, triangles and circles, respectively for a total bandwidth of 100 Hz. Although a cut frequency of 200 Hz has been selected to show results corresponding to the CFDAC matrices, the 100 Hz bandwidth threshold has been hand-picked in this case as it is the most significant region in the spectra which shows visible resonances. Upper frequencies are not considered to contribute with significant modal information to the results so are discarded. This limitation in the bandwidth is also supported by the fact that the convergence analysis shows similar values of SCIs computed for 100 Hz and 200 Hz.

Sign decision algorithm is not reliable for some of these cases. This is specially clear for the removal of diagonals in the first and second levels. This is mostly due to the great presence of noise in the CFDACs which artificially introduces correlation regions in the sub-triangular matrices in the two sides of the main diagonal structure distorting, this way, the sign decision algorithm. A second observation can be drawn regarding the quantification of the amount of damage present in the structure. as the values for the SCI indicators are very similar for all alterations introduced in the structure.

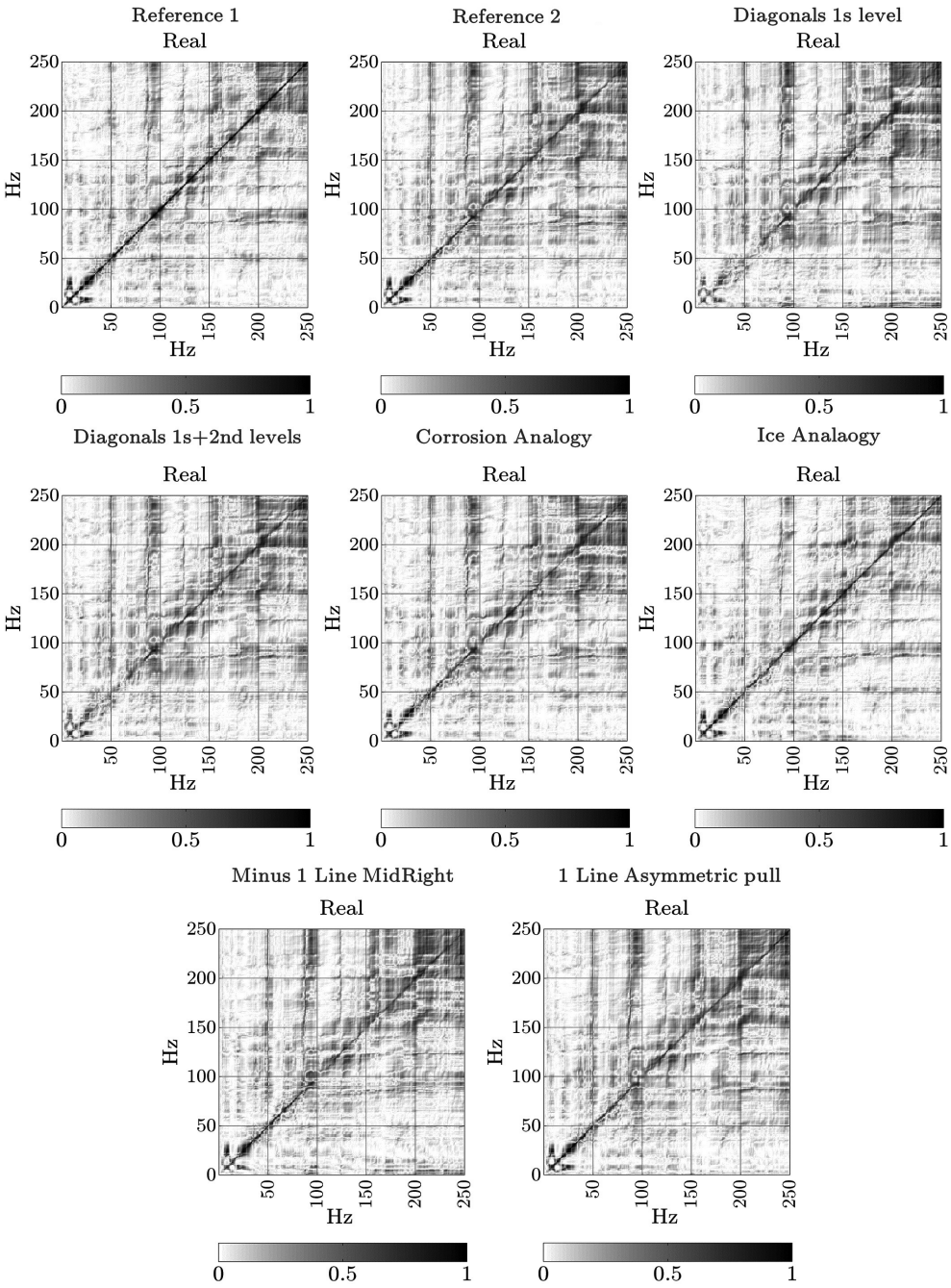

Figure 5.45: Evolution of the real part of the CFDAC for damage scenarios in full-scale experimental campaign. 24p mesh, DP5, $\Delta f = 0.5$ Hz, BW = 250 Hz

For this specific case, the indicator is considered to be capable of damage detection but not damage quantification. SCI indicators adequately reproduce the accumulation of damage for the loosening of diagonal elements (C1 and C2) and also for the loosening on the link to the ground (C3). However, ice analogy case (C4), the 1-line removal case (C6) and the pulling-wire case (C6) show degradation index very close to the repeatability values (C0B). However, these low repeatability, far from being an indication of an hypothetical and unfavourable hypersensitivity of the indexes, can be interpreted as an indication of the accumulated structural alteration along the experimental campaign, from the starting state to the final condition of the structure after invasive manipulation.

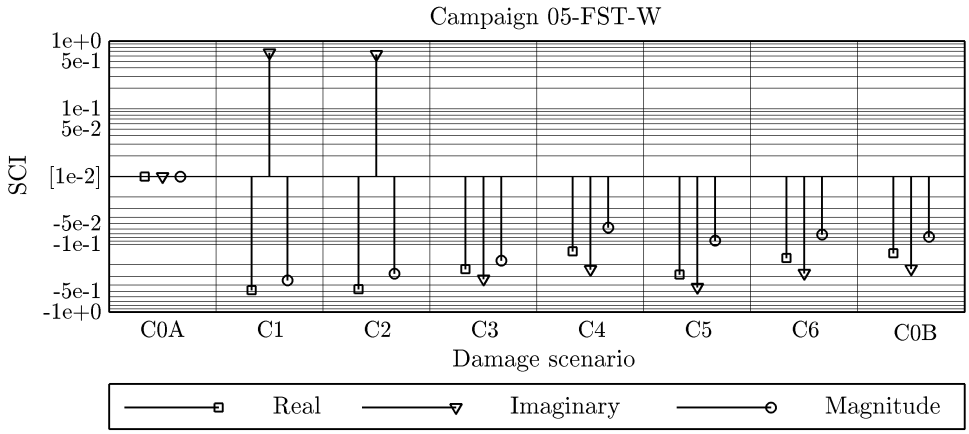

Figure 5.46: Evolution of the SCI indicator for the damage scenarios in the full scale tower for BW = 100 Hz

Although experimental data acquired in this operational scenario is far more noisy than laboratory acquisitions, it has been demonstrated that the methodology presented, once significant ranges of the spectra are selected, can be used to successfully trace structural alterations in a full-scale latticed power transmission tower. Additionally, this full scale experimental campaign has served to show the enhanced stability behaviour of the indicators in front of bandwidth due to the influence of real effects such as high frequency low geometrical resolution of modes and narrow band excitations in those same regions. This methodology, despite not univoquely quantifying the amount of accumulated alteration in the structure, can be qualitatively used to trace the changes in structural performance in the structure during its operational life.

6. Final remarks

6.1 Summary

This document presents an investigation on vibration-based spectral-domain structural alteration indicators derived from experimentally determined input-output inertance response functions of mechanical systems aimed to detect, quantify and discern damage from reinforcement in structures. Spectral-domain data allows to retain most of the information of a vibrating system whilst easing up the interpretation of the physical phenomena behind. Additional benefits include the avoidance of overcomplexities introduced by modal-domain derived condensation and fitting techniques and other counterintuitive forms of domain transformation.

Initial hypothesis of this investigation is that structural alteration in a system can be traced and correlated with spectral-domain-derived indicators, namely the complex frequency domain assurance criterion CFDAC, and the spectral correlation indexes, SCIs. This initial hypothesis translates to the demonstration that global change in the CFDAC (evaluated through SCIs) is a measure of the change in stiffness in the structure whereas the pattern of the discorrelation in the diagonal signature of the CFDAC is characteristic of the structural alteration typology undergoing.

The final goal of this investigation is to apply the proposed structural alteration indicators to a real system in an operational environment. To do so, a characterization of the spectral indicators is presented and discussed. The investigation on indicators consist of an initial parametric analysis in front of common acquisition parameters performed on a simple structural component, namely a square 1-edge-clamped aluminium plate. This numeric sensibility analysis is later validated with equivalent experimental tests on the same structural element. The investigation progresses by assessing structural alterations in the same plate both numerically and experimentally over a multitude of structurally modified cases. CFDAC behaviour in front of

structural changes is qualitatively discussed whereas SCIs trends are quantitatively assessed. An investigation of the same indicators is later faced to try and evaluate their structural assessment performance in more complex structures, such as a 3D latticed power transmission tower. A simplified parametric analysis is then executed, both numerically and experimentally in a downscaled power transmission tower. Immediately before confronting structural assessment in a real-scale latticed power transmission tower, an assessment of the structural state of the downscaled tower is carried out using both numerical models and an experimental testing prototype. Conclusions extracted from this extensive characterization work are used to evaluate the structural integrity of a latticed real-scale tower over a set of intentionally applied structural alteration scenarios.

6.2 Findings

This section presents the main discoveries based on observations made during the analysis of results in this investigation. Only significant observations to the advance of current state-of-the-art knowledge are presented, thus leaving aside observations related to other standard techniques. In this line of though, observations related with experimental modal analysis and synthesis of FRFs are not addressed as they act as auxiliary tools to the development of the core of this research.

The CFDAC complex matrix indicator comparing pristine sets of FRFs to altered ones shows alteration in its initially perfectly symmetrical diagonal signature when alteration is present in the mechanical system. Global alterations, such as modification of material characteristics or specimen geometry, result in a linear shift in CFDACs. This give rise to affirm that the global shift in the CFDAC matrix is an indicator of the change in the global stiffness of the structure. Local alterations and boundary condition changes introduce non-linear shifts in the CFDAC matrix, thus showing that the pattern in the shift in the CFDAC is an indicator of the alteration typology present in the mechanical system.

The global shift in the CFDAC matrix can be successfully quantified using spectral correlation indicators (SCIs), which are based in the Pearson correlation coefficient (PCC) between a pristine-to-pristine CFDAC and a pristine-to-altered CFDAC, for their real parts, imaginary parts and magnitudes separately. The use of the PCC is rooted on structural similarity arguments concerning image cognition. Mean values of upper and lower pristine-to-altered CFDAC sub-triangular matrices have been used to estimate the direction of degradation (reinforcement and damage) with relative success. Narrow bandwidths, small amounts of alteration, or boundary conditions

inconsistencies degrade the precision of the sign-estimation algorithm. The methodology presented would benefit from an increase in the robustness of the sign decision technique.

Test-retest experimental reliability of SCIs is very high in controlled laboratory conditions, thus allowing relative low threshold values for alteration detection (about $|SCIs| \geqslant 0.02$). Repeatability tests however, also show that the indicators are very sensitive to small changes in the boundary conditions, so even for a test-retest with a reassemble of the clamping boundary conditions, indicators show alteration above the reliability threshold. This sensitivity can be either incorporated in the characteristic detection threshold or considered as a change in the mechanical characteristics of the system. In this investigation, the later approach is adopted as in-service structures would never incorporate reassembling of the supports, so then, this scenario should be interpreted as a structural degradation.

SCIs indices present some dependencies on acquisition and sampling parameters that converge to stable values once certain requirements are met. This stability requirements studied for the driving point used in acquisitions, for the number of independent FRFs used to generate the CFDAC (nodes sampled or mesh density), for the frequency resolution of sampled series and for the total bandwidth used in the computation of the indicators. Numerical investigation shows that the driving point introduces a random dispersion that cannot be characterized. To address this issue, an auxiliary method for optimal driving point selection is proposed. However, experimental investigation of the influence of driving point shows that this dispersion is less important due to real effects such as limited bandwidth excitation, little drifts from the ideal sampling mesh locations and small differences in geometry that modify nodal lines in mode shapes.

An optimal driving point methodology is proposed based on the correlation of a pristine-to-pristine CFDAC composed of all FRFs which conform the full inertance matrix with pristine-to-pristine CFDAC composed by FRFs in one of the columns in the full inertance matrix corresponding to a virtual driving point EMA test. Pearson correlation coefficient between these two CFDACs is a measure of how similar is each EMA test CFDAC to a full inertance matrix CFDAC. If this second full inertance CFDAC is considered to present the maximum modal visibility for a given acquisition mesh, the driving point which results in higher values of correlation is the one which gives the EMA test with the optimal driving visibility.

For the experimental investigation on the 1-edge-clamped square aluminium plate and for the prototype downscaled tower, frequency resolution influence appears to be the less important of all parameters studied. Once the resolution is set at 4 Hz or lower,

results for the SCI indices diverge by less than a 1% respect the reference computed ones (correspondent to a resolution of 0.5 Hz). Mesh density sensibility also presents a clear stability threshold. However, convergence limits are different depending on the typology of structure studied. Both numerical and experimental investigation on the aluminium plate show that the convergence limit can be estimated to be at 40 nodal samplings. Denser meshes up to the 81-node reference result in stable values of the indicators. On the other hand, mesh density stability requirements for the model tower are identified to be around 30 nodes for each of the two planes studied. Concretely, 36 nodal acquisitions for the frontal plane and 36 for the lateral one are identified as suitable convergence limits. However, dispersion due to mesh density is much lower for cases studied in the model tower parametric analysis. This fact is justified by the lower modal density of the tower which allows to accurately capture operational deflection shapes in range with less spatial resolution. So then, regions of increased correlation in the CFDAC do not appear as frequently as it happens with the aluminium plate and the SCI indices present increased stability in font of mesh density.

Bandwidth influence is heavily impacted by real effects present in experimental acquisition that are not included when numerically synthesizing FRFs. As a result, numerical investigation shows a strong dependency between indicators and the bandwidth selected to compute them, both for the aluminium plate and for the downscaled tower. However, this dependency is greatly relaxed and even converged when using experimental series. Experimental investigation shows convergence trends in SCIs as bandwidth is increased. For the aluminium plate, this convergence tendency seems to appear for bandwidths above 2800 Hz, for the downscaled prototype tower, the convergence limit is identified at 200 Hz and for the full scale tower, convergence is estimated to appear around 250 Hz. This effect is attributed to the inability to excite upper modes in structures with the same amount of energy that lower ones, to the increased damping at higher frequencies, which reduces the amplitude response of those modes, and to the reduced accuracy in the geometrical description of mode shapes at high frequencies, which introduces regions of high correlation in the CFDAC matrix and contributes to the stabilization of the indicators.

SCI indicators are very sensitive to changes in damping of structures. As damping changes are a common indicator of structural degradation, this enhanced sensitivity can be taken advantage of in structural assessment. On the other hand, indicators are quite stable in front of acquisition random noise up to values with maximum amplitudes of order 5% of the maximum peak value of FRFs. Common ratios for experimental testing are usually below the 1% peak value threshold.

Comparing experimental to numerical alteration scenarios on the aluminium plate, the

indicators present good correlation although numerically derived SCIs tend to show lower values (in absolute magnitude) that experimentally derived ones. However, the absolute values of the indicators can hardly be related with the total amount of alteration in the structure, as different alteration mechanisms result in similar values of the indicators. However, when focusing in the progression of structural shifts inside the same family, a clear correlation exist between the modified parameters and the values adopted by the indicators.

Imaginary SCIs present the greatest sensibility in front of alteration of all indicators proposed this investigation, even more than other similar indicators presented in literature such as DRQ. Real SCIs present sensitivities slightly inferior to DRQ indicators whereas magnitude SCI is the less sensitive of the four, even below the DRQ indicator. Real SCIs present the most linear tendency between alteration progression and values adopted. On the other hand, magnitude SCI shows a decreased linear correlation with structural alterations studied. This differential behaviour leads to the proposal of the imaginary SCIs as early detection indexes whilst real SCI could be used as long term alteration progression trend indicators. Decreased sensitivity and linearity of magnitude SCI indicators could be useful in specially noisy acquisition scenarios with volatile operational conditions (such as extreme wind variability).

In general, residual stiffness shift and indicator progression present reasonable correspondences, with losses of stiffness corresponding to negative SCI values and gains to positive SCI values. Static stiffness is not univocally related with values in the SCI indicators but depends on the structural alteration typology studied. Specially interesting is the comparison of thickness and Young modulus modification families where the relationship between residual stiffness shift and SCI indicators is fairly similar. Other structural alteration families present different trends between those variables. This observation could eventually be used to characterize the typology of alteration if those two parameters could be determined altogether.

However, while residual stiffness is evaluated in a fixed node of the structure, which is simultaneously loaded and sampled, SCI are global indicators of the structure evaluated for the whole geometrical domain of the system. This raise the question whether this comparison is meaningful at all. Inertances are inverse to dynamic stiffness response functions, so then, the static stiffness of a structure measured between a loaded and a sampled point is exactly equal to the 0 Hz component of the dynamic stiffness function excited at the loaded point with driving point located at the sampled node. However, experimental determination of 0 Hz FRF functions is usually not feasible as these spectral regions are the ones with more accumulated noise and DC components in acquisitions. Bearing in mind that inertance functions are referred to a common

driving point, estimation of the static stiffness would have been more significant at that location. However, results shown allow to successfully identify general trends in SCIs to residual stiffness correlation.

It has also been demonstrated that the methodology proposed for a plate can be applied to different typologies of structures, such as latticed 3D structures, as long as adequate convergence thresholds are determined. The methodology does not rely on any geometrical consideration so its extension to any kind of vibrating system is straightforward, even with different sensing technologies or characteristic bandwidths used. The geometry of the system impacts the modal density in the system and bandwidth of interest to capture enough amount of natural modes. Once stability requirements are met, the work-flow here presented can be applied to any mechanical system.

Indicators studied have been shown to be very sensitive in front of alteration in boundary conditions. When supports slightly change, the sign-decision algorithm is likely to be dominated by the direction of the shift in the boundary conditions. Although this phenomena arises as a very noticeable effect in this investigation, real structures hardly suffer from boundary condition modifications, and even if that happens, this is a clear indicator of the loss of structural performance in the system. Conclusively, despite noticeably disrupting results for the experimental model tower, this behaviour is considered to be beneficial when dealing with in-service systems.

Additionally, it has been numerically demonstrated that the indicators are sensible to operational conditions which are close to the buckling load safety envelope of the structure. This collapse mechanism is the most common failure cause in latticed structures. So then, early detection of buckling limit approximation is a promising feature of this spectral domain derived approach.

Lastly, although this investigation is focused on the quantification of the global shift in the CFDAC using correlation indicators, this indicator presents further potentiality in damage classification. Numerical and experimental investigation have shown that the pattern in the CFDAC shift is a revealing characteristic of the alteration mechanism undergoing. However, as this observation has been made from a qualitative point of view, further investigation is required to fully confirm this observation.

6.3 Limitations

Current investigation relies on the use of input-output measurements experimentally acquired using experimental modal analysis or resynthesized from modal models using

polynomial expansions. However, in-field implementation of the indicators would require to use output-only data measured in an operational environment, as a real plants cannot rely on active excitation with instrumented actuators. So then, conclusions in this investigation are not directly translatable to industrial applications, as further investigation using operational acquisition would be needed

In this research, it has been numerically proven that the indicators proposed are sensitive to second order instability effects when the structure approaches its buckling load envelope. However, conclusions have only been extracted from FEM derived results. Further experimental investigation on the subject is needed to experimentally validate this results.

Analysis presented have only been performed for limited bandwidths, both for the aluminium plate and experimental towers. Although real effects (such as narrow band excitation, insufficient spatial resolution at higher frequencies and higher noise-to-signal rations at upper parts of the spectral domain) seem to have a positive impact on the influence of bandwidth in the indicators, limited bandwidths used in this investigation makes categorical assessment on its dependence a bold endeavour. In addition, seemingly appropriate stability thresholds for bandwidths used in the experimental segments involving the prototype tower and the full-scale one have been hand-picked based on observation of trends. More advanced approaches, such as percentage convergence of the error could systematize this procedure. Trends in this investigation, however, seem clear enough to permit the manual technique used.

Finally, discussion on CFDAC behaviour in front of different structural alteration typologies has been addresses from a qualitative and cognitive point of view based on observation. Affirmations made rely on naked-eye analysis of the images generated and thus are non-exhaustive and meant to be taken only from a descriptive standpoint. In-depth analysis of CFDACs matrices requires the use of advanced image processing tools, which is by far, out of the scope of this investigation.

6.4 Contributions

One of the more general contributions of this research is the extensive database of modal testing results that has been generated to perform this investigation. This extensive database includes frequency response functions determined for a variety of structural alteration scenarios on a square 1-edge-clamped aluminium plate, on a modelled downscaled power transmission tower and on a full-scale latticed power transmission tower.

A second general development of this research is the computation tool aimed to calculate CFDAC indicators from frequency response functions. Althoug this tool was originally developed in the Matlab scripting language, it has been furtherly ported to C language to allow future applications in industrial scenarios.

However, the main contribution of this research is the understanding and characterization of the CFDAC in the correlation between pristine an altered states in structural assessment through statistical condensation using the Pearson correlation coefficient, completely avoiding modal post-process. The CFDAC degradation pattern is indicative of the typology of alteration present in the structure. The total shift in CFDAC evaluated through the SCI indices can be used as a univocal and stable parameter to detect structural alteration and its sign in a structural system.

Condensed SCI indices present similar behaviour with improved sensibility than other indicators proposed in literature, improved stability in front of acquisition parameters and improved repeatability characteristics if compared with the accumulated variation of response functions. Additionally, condensed indexes are capable of discerning degradations from reinforcements in most of the analysed cases. Real and imaginary SCIs are preferred over magnitude SCIs in structural alteration progression monitoring and early detection respectively.

However, the biggest implication of this investigation arises from the observed potentiality of the CFDAC complex matrix indicator to be used by itself in structural assessment. Changes in the structural similarity of the main diagonal signature of the indicators are directly related with global and local changes. Those changes however have only been discussed qualitatively in this investigation.

6.5 Future works

Immediate extension of the methodology here presented would involve the application of the CFDAC correlation through SCIs to the localization of structural alterations. To do so, it is proposed to generate locally distributed CFDACs, each corresponding to an experimental element defined by three or four nodes of the acquisition mesh. Each node has an associated FRFs measured with driving point located in a certain reference point. Each local CFDAC then, would measure the *stiffness visibility* of each experimental element respect the driving point used. By correlating locally distributed pristine CFDACs to altered ones, the relative direction between the driving point and the local damage can be estimated. This methodology, however, presents a main drawback in localization. If a local defect is present close to the reference point, all

elements behind that local alteration and on the same line radius to the reference would show alteration, as FRFs measure the relative dynamic stiffness between nodes and the driving point.

To overcome that limitation, the full inertance matrix would be required, measuring all nodes respect all driving points. This way, local CFDACs could be generated from relative FRFs in the nodes composing each element, this time not measured from a common driving point, but corresponding to pairs of nodes in each experimental element. As a matter of exemplification, in an experimental quadrilateral element defined by four nodes, there exist 6 lines possible to connect nodes in pairs (4 sides and 2 diagonals). Those lines define FRFs excited in one node and measured in the correspondent companion node. These 6 independent 6 FRFs could be used to compute locally distributed CFDAC, that could be used to generate correspondent locally distributed SCIs. With this approach, limitations arising from *stiffness visibility* can be overcome.

Although technically possible, input-output measurement of the full inertance matrix (using accelerometers and impact hammers or electrodynamic shakers) is a costly and difficult task in experimental tests even in controlled laboratory conditions. The challenges multiply when attempting this complex acquisition task in a real operational environment. Recent trends in modal analysis of operational structures rely on the operational modal analysis technique (OMA) which uses only output accelerations on a system to estimate modal parameters from Fourier-transformed acceleration series. The matrix of transfer functions between acquisition points is then referred as transmissibility matrix and it is a linear combination of elements in the inertance matrix with unknown external excitation vectors. This technique allows to obtain a full inertance-like matrix. Modal frequencies and dampings can be accurately estimated as long as the unknown external forces excite the modes in the frequencies of interest (for low ranges in the spectral domain, this is common). The main drawback of the technique is its inability to accurately estimate modal masses in the system. However, the CFDAC operator works by non-dimensionalizing the product of response functions with their magnitudes at each spectral line. As magnitude of FRFs are dominated by the relative mobility of nodes and modal masses of each mode, the CFDAC can be used in transmissibility functions without loss of generality (as long as enough modes are excited by operational forces).

The use of OMA also makes possible to deploy the proposed damage indicators in real acquisition scenarios using output-only measurements. However, due to the noisy nature of in-service sampling, it would be needed to perform a new parametric analysis and sensibility study on the proposed indices. In real application, one accelerometer

has to be mounted in each acquisition point, limiting the amount of spatial resolution due to costs concerns. On the other hand, the possibility of estimating all tranmissibility response functions in the full matrix gives added location potentiality to the system.

One of the concluding remarks of this investigation is that the CFDAC seems a promising tool to classify structural alteration based on the pattern of the shift identified in the CFDAC diagonal structure. It is proposed to rule the statistical quantification of the CFDAC out and bet on advanced image processing and pattern recognition and classification tools. Specially interesting is the deep learning paradigm. Deep learning (performed by deep neural networks, DNN) is a discipline of unsupervised machine learning that use a sequence of sub-algorithms to extract or transform information. Deep learning is heir of artificial neural network developments with added layers of artificial intelligence that expand the abilities of the system with graphic modelling, pattern recognition and signal processing tools.

7. Related publications

7.1 Peer-reviewed articles

- M. A. Pérez, A. Manjón, J. Ray, R. Serra-López. Experimental assessment of the effect of an eventual non-invasive intervention on a Torres guitar through modal testing. *Journal of Cultural Heritage*,1209(1):1-136, 2015. JCR:Q3-Material Sciences, IF:1.533.

7.2 Conference articles

- M.A. Pérez, R. Serra-López, L. Gil. Structural damage assessment of power transmission towers using dynamic experimental data. *Proceedings of the International Conference on Structural Engineering Dynamics.* Lagos, Portugal, July 2015.
- M.A. Pérez, R. Serra-López, L. Gil. Static and dynamic characterization of a guitar soundboard along successive stages of construction.. *Proceedings of the International Conference on Structural Engineering Dynamics.* Lagos, Portugal, July 2015.
- M.A. Pérez, J. Pernas-Sánchez, J. A. Artero-Guerrero, R. Serra-López, J. López-Puente, L. Gil. Analysis of the effect of high velocity impact of ice spheres upon the static and dynamic response of carbon/epoxy laminates. *ICCS18: 18th International Conference on Composite Structures Lisbon, Portugal, June 15-18, 2015.* Lisbon, Portugal, June 2015.

7.3 Oral presentations

- M.A. Pérez, R. Serra-López, L. Gil. Damage detection in power transmission towers using an unsupervised Structural Health Monitoring system. *Congress of Advances*

in Vibrations. Porto, Portugal. March 2015.

- M.A. Pérez, R. Serra-López, L. Gil. Dynamic assessment of truss structures using Hybrid Simulation. *Congress of Advances in Vibrations*. Porto, Portugal. March 2015.
- M.A. Pérez, A. Manjón, R. Serra-López. Mechanics of the classical guitar. *WoodMusICK Opening Conference, Paris (France), 27-28th of February 2014: proceedings & poster presentation abstracts*. London, Royal College of Music.

8. References

[1] X. Crehuet. Temporal de neu a les comarques gironines. *Territori. Observatori de projectes i debats terriorials de Catalunya*, 2010. Accessed: 2017-04-17.

[2] Achmad Widodo and Bo-Suk Yang. Support vector machine in machine condition monitoring and fault diagnosis. *Mechanical Systems and Signal Processing*, 21(6):2560–2574, 2007.

[3] Nuno M M Maia, Raquel A B Almeida, Antonio P V Urgueira, and Rui P C Sampaio. Damage detection and quantification using transmissibility. *Mechanical Systems and Signal Processing*, 25(7):2475–2483, 2011.

[4] António P V Urgueira, Raquel A B Almeida, and Nuno M M Maia. On the use of the transmissibility concept for the evaluation of frequency response functions. *Mechanical Systems and Signal Processing*, 25(3):940–951, 2011.

[5] R. P C Sampaio, N. M M Maia, R. A B Almeida, and A. P V Urgueira. A simple damage detection indicator using operational deflection shapes. *Mechanical Systems and Signal Processing*, 72-73:629–641, 2016.

[6] R. Pascual, J. C. Golinval, and M. Razeto. A Frequency Domain Correlation Technique for Model Correlation and Updating. *15th International Modal Analysis Conference (IMAC XV)*, pages 1–7, 1997.

[7] S. R. Hall. The effective management and use of structural health data. In *Proceedings of the 2nd International Workshop on Structural Health Monitoring*, pages 265–275, 1999.

[8] Seth S Kessler, S Mark Spearing, and Constantinos Soutis. Damage detection in composite materials using Lamb wave methods. 11:269–278, 2002.

[9] Charles R Farrar and Keith Worden. An introduction to structural health monitoring. *Philosophical transactions. Series A, Mathematical, physical, and engineering sciences*, 365(1851):303–315, 2007.

[10] Srinivasan Gopalakrishnan, Sathyanarayana Hanagud, and Massimo Ruzzene. *Computational techniques for structural health monitoring.*

[11] E. P. Carden. Vibration Based Condition Monitoring: A Review. *Structural Health Monitoring*, 3(4):355–377, 2004.

[12] Gyuhae Park, Daniel E Muntges, and Daniel J Inman. Self-monitoring and self-healing jointed structures. In *Key Engineering Materials*, volume 204, pages 75–84. Trans Tech Publ, 2001.

[13] Anders Rytters. *Vibration Based Inspection of Civil Engineering Structures.* PhD thesis, 1993.

[14] Charles R Farrar and Kerry M Cone. Vibration testing of the I-40 bridge before and after the introduction of damage. Technical report, Los Alamos National Lab., NM (United States), 1994.

[15] Charles R Farrar, Scott W Doebling, and David A Nix. Vibration–based structural damage identification. *Philosophical Transactions of the Royal Society of London A: Mathematical, Physical and Engineering Sciences*, 359(1778):131–149, 2001.

[16] Rune Brincker, Lingmi Zhang, and Palle Andersen. Modal Identification from Ambient Responses using Frequency Domain Decomposition, 2000.

[17] Spilios D Fassois and John S Sakellariou. Time-series methods for fault detection and identification in vibrating structures. *Philosophical Transactions of the Royal Society of London A: Mathematical, Physical and Engineering Sciences*, 365(1851):411–448, 2007.

[18] Michael I Friswell. Damage identification using inverse methods. *Philosophical Transactions of the Royal Society of London A: Mathematical, Physical and Engineering Sciences*, 365(1851):393–410, 2007.

[19] Ajit Mal, Sauvik Banerjee, and Fabrizio Ricci. An automated damage identification technique based on vibration and wave propagation data. *Philosophical Transactions of the Royal Society of London A: Mathematical, Physical and Engineering Sciences*, 365(1851):479–491, 2007.

[20] Wieslaw J Staszewski and Amy N Robertson. Time-frequency and time-scale analyses for structural health monitoring. *Philosophical transactions. Series A, Mathematical, physical, and engineering sciences*, 365(1851):449–477, 2007.

[21] Hoon Sohn, Charles R Farrar, Francois Hemez, and Jerry Czarnecki. A Review of Structural Health Monitoring Literature 1996 2001. *Third World Conference*

on Structural Control, pages 1–7, 2002.

[22] Shigeru Izumi, Izumi Yamada, and Masayuki Izumi. Vibration Monitor for Rotating Machines Using Average Frequency Technique. *Journal of Nuclear Science and Technology*, 16(6):441–445, 1979.

[23] Subhasis Nandi, Hamid Toliyat, Xiaodong Li, and Others. Condition monitoring and fault diagnosis of electrical motors-a review. *Energy Conversion, IEEE Transactions on*, 20(4):719–729, 2005.

[24] Marie Gaudard and Philip J Ramsey. Introduction to Statistical Quality Control. *Technometrics*, 39(3):331–332, 1997.

[25] Charles R Farrar and Nick a J Lieven. Damage prognosis: the future of structural health monitoring. *Philosophical transactions. Series A, Mathematical, physical, and engineering sciences*, 365(1851):623–632, 2007.

[26] Keith Worden, Charles R. Farrar, Graeme Manson, and Gyuhae Park. The fundamental axioms of structural health monitoring. *Proceedings of the Royal Society A: Mathematical, Physical and Engineering Sciences*, 463(April):1639–1664, 2007.

[27] Charles R Farrar and Keith Worden. *Structural Health Monitoring a Machine Learning Perspective*. 2013.

[28] Peter J Shull. *Nondestructive evaluation: theory, techniques, and applications*. CRC press, 2002.

[29] Y. Y. Hung, Y. S. Chen, S. P. Ng, L. Liu, Y. H. Huang, B. L. Luk, R. W L Ip, C. M L Wu, and P. S. Chung. Review and comparison of shearography and active thermography for nondestructive evaluation. *Materials Science and Engineering R: Reports*, 64(5-6):73–112, 2009.

[30] T Warren Liao and Yueming Li. An automated radiographic NDT system for weld inspection: Part IIFlaw detection. *Ndt & E International*, 31(3):183–192, 1998.

[31] Cristina Goidescu, Hélène Welemane, Christian Garnier, Marina Fazzini, Romain Brault, Elodie Péronnet, and Sébastien Mistou. Damage investigation in CFRP composites using full-field measurement techniques: Combination of digital image stereo-correlation, infrared thermography and X-ray tomography. *Composites Part B: Engineering*, 48:95–105, 2013.

[32] M Michaloudaki, E Lehmann, and D Kosteas. Neutron imaging as a tool for the non-destructive evaluation of adhesive joints in aluminium. *International*

journal of adhesion and adhesives, 25(3):257–267, 2005.

[33] M J Lovejoy. *Magnetic particle inspection: a practical guide*. Springer Science & Business Media, 2012.

[34] Henry A Sodano. Development of an automated eddy current structural health monitoring technique with an extended sensing region for corrosion detection. *Structural Health Monitoring*, 6(2):111–119, 2007.

[35] S. Bagavathiappan, B. B. Lahiri, T. Saravanan, John Philip, and T. Jayakumar. Infrared thermography for condition monitoring - A review. *Infrared Physics and Technology*, 60:35–55, 2013.

[36] Daniel Post. Optical Interference for Deformation Measurements–Classical, Holographic and Moire Interferometry. In *Mechanics of Nondestructive Testing*, pages 1–53. Springer, 1980.

[37] G. De Angelis, M. Meo, D. P. Almond, S. G. Pickering, and S. L. Angioni. A new technique to detect defect size and depth in composite structures using digital shearography and unconstrained optimization. *NDT and E International*, 45(1):91–96, 2012.

[38] Hock C Tan, Olubayo O R Famiyesin, and Mohammed S E Imbabi. Dynamic deformation signatures in reinforced concrete slabs for condition monitoring. *Computers & Structures*, 79(26):2413–2423, 2001.

[39] Shizeng Lu, Mingshun Jiang, Qingmei Sui, Yaozhang Sai, and Lei Jia. Damage identification system of CFRP using fiber Bragg grating sensors. *Composite Structures*, 125:400–406, 2015.

[40] Junliang Dong, Byungchil Kim, Alexandre Locquet, Peter McKeon, Nico Declercq, and D.S. Citrin. Nondestructive evaluation of forced delamination in glass fiber-reinforced composites by terahertz and ultrasonic waves. *Composites Part B: Engineering*, 79:667–675, 2015.

[41] Marco a. Pérez, Lluís Gil, Montserrat Sánchez, and Sergio Oller. Comparative experimental analysis of the effect caused by artificial and real induced damage in composite laminates. *Composite Structures*, 112(1):169–178, 2014.

[42] Roman Růžek, Radek Lohonka, and Josef Jironč. Ultrasonic C-scan and shearography NDI techniques evaluation of impact defects identification. *NDT and E International*, 39(2):132–142, 2006.

[43] X Wang, Y Lu, and J Tang. Damage detection using piezoelectric transducers and the Lamb wave approach: I. System analysis. *Smart Materials and*

Structures, 17(2):025033, 2008.

[44] J. C. Dodson and D. J. Inman. Thermal sensitivity of Lamb waves for structural health monitoring applications. *Ultrasonics*, 53(3):677–685, 2013.

[45] Konstantin J. Schubert and Axel S. Herrmann. On the influence of moisture absorption on Lamb wave propagation and measurements in viscoelastic CFRP using surface applied piezoelectric sensors. *Composite Structures*, 94(12):3635–3643, 2012.

[46] Ming Hong, Zhongqing Su, Qiang Wang, Li Cheng, and Xinlin Qing. Modeling nonlinearities of ultrasonic waves for fatigue damage characterization: Theory, simulation, and experimental validation. *Ultrasonics*, 54(3):770–778, 2014.

[47] Harsh Baid, Christoph Schaal, Himadri Samajder, and Ajit Mal. Dispersion of Lamb waves in a honeycomb composite sandwich panel. *Ultrasonics*, 56:409–416, 2015.

[48] A. R. Clough and R. S. Edwards. Characterisation of hidden defects using the near-field ultrasonic enhancement of Lamb waves. *Ultrasonics*, 59:64–71, 2015.

[49] Piotr Nazarko and Leonard Ziemianski. Damage detection in aluminum and composite elements using neural networks for Lamb waves signal processing. *Engineering Failure Analysis*, 69:97–107, 2016.

[50] Zenghua Liu, Kunming Sun, Guorong Song, Cunfu He, and Bin Wu. Damage localization in aluminum plate with compact rectangular phased piezoelectric transducer array. *Mechanical Systems and Signal Processing*, 70-71:625–636, 2016.

[51] Xu Baochun, Yuan Shenfang, Wang Mulan, and Qiu Lei. Determining impact induced damage by lamb wave mode extracted by EMD method. *Measurement: Journal of the International Measurement Confederation*, 65:120–128, 2015.

[52] B.S. Ben, B.a. Ben, K.a. Vikram, and S.H. Yang. Damage identification in composite materials using ultrasonic based Lamb wave method. *Measurement*, 46(2):904–912, 2013.

[53] Nitesh P. Yelve, Mira Mitra, P. M. Mujumdar, and C. Ramadas. A hybrid method based upon nonlinear Lamb wave response for locating a delamination in composite laminates. *Ultrasonics*, 70:12–17, 2016.

[54] Pedro Ochôa, Virgínia Infante, José M. Silva, and Roger M. Groves. Detection of multiple low-energy impact damage in composite plates using Lamb wave techniques. *Composites Part B: Engineering*, 80:291–298, 2015.

[55] Natalie Rauter, Rolf Lammering, and Tim Kühnrich. On the detection of fatigue damage in composites by use of second harmonic guided waves. *Composite Structures*, 152:247–258, 2016.

[56] Wongi S. Na. Distinguishing Crack Damage from Debonding Damage of Glass Fiber Reinforced Polymer Plate using a Piezoelectric Transducer based Nondestructive Testing Method. *Composite Structures*, 159:517–527, 2016.

[57] Nitesh P. Yelve, Mira Mitra, and P.M. Mujumdar. Detection of delamination in composite laminates using Lamb wave based nonlinear method. *Composite Structures*, 159:257–266, 2016.

[58] Ming Hong, Zhu Mao, Michael D. Todd, and Zhongqing Su. Uncertainty quantification for acoustic nonlinearity parameter in Lamb wave-based prediction of barely visible impact damage in composites. *Mechanical Systems and Signal Processing*, 82:448–460, 2015.

[59] V. Y. Senyurek. Detection of cuts and impact damage at the aircraft wing slat by using Lamb wave method. *Measurement: Journal of the International Measurement Confederation*, 67:10–23, 2015.

[60] G. Giridhara, V. T. Rathod, S. Naik, D. Roy Mahapatra, and S. Gopalakrishnan. Rapid localization of damage using a circular sensor array and Lamb wave based triangulation. *Mechanical Systems and Signal Processing*, 24(8):2929–2946, 2010.

[61] Y. J. Yan, L. Cheng, Z. Y. Wu, and L. H. Yam. Development in vibration-based structural damage detection technique. *Mechanical Systems and Signal Processing*, 21(5):2198–2211, 2007.

[62] Wei Fan and Pizhong Qiao. Vibration-based Damage Identification Methods: A Review and Comparative Study. *Structural Health Monitoring*, 10(1):83–111, 2011.

[63] Scott W. Doebling, Charles R. Farrar, Michael B. Prime, and Daniel W. Shevitz. Damage identification and health monitoring of structural and mechanical systems from the changes in their vibrational characteristics: a literature review.

[64] O S Salawu. Detection of structural damage through changes in frequency: a review. *Engineering structures*, 19(9):718–723, 1997.

[65] Y. Zou, L. Tong, and G.P. Steven. Vibration-Based Model-Dependent Damage (Delamination) Identification and Health Monitoring for Composite Structures a Review. *Journal of Sound and Vibration*, 230(2):357–378, 2000.

[66] Theodorus Hendricus Ooijevaar. *Vibration based structural health monitoring of*

composite skin-stiffener structures. 2014.

[67] J.-T. Kim and N. Stubbs. Crack Detection in Beam-Type Structures Using Frequency Data. *Journal of Sound and Vibration*, 259(1):145–160, 2003.

[68] C. M. Harris. *Shock and Vibration Handbook*, volume 45. 1977.

[69] Marco a. Pérez, Lluís Gil, and Sergio Oller. Impact damage identification in composite laminates using vibration testing. *Composite Structures*, 108(1):267–276, 2014.

[70] Roger Serra-Lopez and Marco A. Pérez Martínez. Report of the SIDTE project. Technical report, 2013.

[71] a. Messina, E. J. Williams, and T. Contursi. Structural Damage Detection by A Sensitivity and Statistical-Based Method. *Journal of Sound and Vibration*, 216:791–808, 1998.

[72] MacIej Radzieński, Marek Krawczuk, and Magdalena Palacz. Improvement of damage detection methods based on experimental modal parameters. *Mechanical Systems and Signal Processing*, 25(6):2169–2190, 2011.

[73] C S Kraaij. Model updating of a clamped'-free beam system using FEMTOOLS. 2007.

[74] Dora Foti, Mariella Diaferio, Nicola Ivan Giannoccaro, and Michele Mongelli. Ambient vibration testing, dynamic identification and model updating of a historic tower. *NDT & E International*, 47:88–95, 2012.

[75] Sjs Hakim and Ha Razak. Frequency Response Function-based Structural Damage Identification using Artificial Neural Networks-a Review. *Research Journal of Applied Sciiences, Engineering and Technology*, 7(9):1750–1764, 2014.

[76] Shuncong Zhong, S. Olutunde Oyadiji, and Kang Ding. Response-only method for damage detection of beam-like structures using high accuracy frequencies with auxiliary mass spatial probing. *Journal of Sound and Vibration*, 311(3-5):1075–1099, 2008.

[77] Mark J Schulz, Ahmad S Naser, Sunil K Thyagarajan, Travluss Mickens, and PF Pai. Structural Health Monitoring using frequency response functions and sparse measurements. (February):760–766, 2014.

[78] Ward Heylen and Stefan Lammens. FRAC: a consistent way of comparing frequency response functions. In *Proceedings of the Conference on Identification in Engineering Systems*, pages 48–57, 1996.

[79] C. Zang, M. I. Friswell, and M. Imregun. Structural Health Monitoring and Damage Assessment Using Measured FRFs from Multiple Sensors, Part I: The Indicator of Correlation Criteria. *Key Engineering Materials*, 245-246(October 2015):131–140, 2003.

[80] M. Palacz and M. Krawczuk. Vibration Parameters for Damage Detection in Structures. *Journal of Sound and Vibration*, 249(5):999–1010, 2002.

[81] Degalhal Mallikarjuna Reddy and Seetharaman Swarnamani. Application of the FRF curvature energy damage detection method to plate like structures. *World Journal of Modelling and Simulation*, 8(2):147–153, 2012.

[82] M. M. R. Taha. Wavelet Transform for Structural Health Monitoring: A Compendium of Uses and Features. *Structural Health Monitoring*, 5(3):267–295, 2006.

[83] Norden E Huang, Zheng Shen, Steven R Long, Manli C Wu, Hsing H Shih, Quanan Zheng, Nai-Chyuan Yen, Chi Chao Tung, and Henry H Liu. The empirical mode decomposition and the Hilbert spectrum for nonlinear and non-stationary time series analysis. In *Proceedings of the Royal Society of London A: Mathematical, Physical and Engineering Sciences*, volume 454, pages 903–995. The Royal Society, 1998.

[84] Norden E Huang, Zheng Shen, and Steven R Long. A new view of nonlinear water waves: The Hilbert Spectrum 1. *Annual review of fluid mechanics*, 31(1):417–457, 1999.

[85] Jn Yang, Y Lei, S Lin, and N Huang. Hilbert-Huang based approach for structural damage detection. *Journal of engineering mechanics*, 130(1):85–95, 2004.

[86] K. Worden and G. Manson. The application of machine learning to structural health monitoring. *Philosophical Transactions of the Royal Society A: Mathematical, Physical and Engineering Sciences*, 365(1851):515–537, 2007.

[87] Hoon Sohn, Jerry A. Czarnecki, and Charles R. Farrar. Structural Health Monitoring Using Statistical Process Control. *Journal of Structural Engineering*, 126(11):1356–1363, 2000.

[88] Ronald E Walpole, Raymond H Myers, Sharon L Myers, and Keying Ye. *Probability and statistics for engineers and scientists*, volume 5. Macmillan New York, 1993.

[89] Christopher M Bishop. *Neural networks for pattern recognition*. Oxford university press, 1995.

[90] Robert Hecht-Nielsen. Theory of the backpropagation neural network. In *Neural Networks, 1989. IJCNN., International Joint Conference on*, pages 593–605. IEEE, 1989.

[91] David Kriesel. A Brief Introduction to Neural Networks. page 244, 2007.

[92] M Mehrjoo, N Khaji, H Moharrmi, and A Bahreininejad. Damage detection of truss bridge joints using Artificial Neural Networks. *Expert Systems with Applications*, 35(3):1122–1131, 2008.

[93] Luca Facchini, Michele Betti, and Paolo Biagini. Neural network based modal identification of structural systems through output-only measurement. *Computers & Structures*, 138:183–194, 2014.

[94] X. Fang, H. Luo, and J. Tang. Structural damage detection using neural network with learning rate improvement. *Computers & Structures*, 83(25-26):2150–2161, 2005.

[95] Stephan Ebersbach and Zhongxiao Peng. Expert system development for vibration analysis in machine condition monitoring. *Expert Systems with Applications*, 34:291–299, 2008.

[96] F G A Albermani and S Kitipornchai. Numerical simulation of structural behaviour of transmission towers. *Thin-walled Struct.*, 41(2):167–177, 2003.

[97] Soheil Dadras Eslamlou and Behrouz Asgarian. Methods of determining the critical areas of transmission towers due to sudden removal of members. *Case Studies in Engineering Failure Analysis*, 2015.

[98] H Yasui, H Marukawa, Y Momomura, and T Ohkuma. Analytical study on wind-induced vibration of power transmission towers. *J. Wind Eng. Ind. Aerodyn.*, 83(1):431–441, 1999.

[99] Ronaldo C. Battista, Rosângela S. Rodrigues, and Michèle S. Pfeil. Dynamic behavior and stability of transmission line towers under wind forces. *Journal of Wind Engineering and Industrial Aerodynamics*, 91(8):1051–1067, 2003.

[100] Qingguo Fei, Honggang Zhou, Xiaolin Han, and Jiang Wang. Structural health monitoring oriented stability and dynamic analysis of a long-span transmission tower-line system. *Eng. Fail. Anal.*, 20:80–87, 2012.

[101] Mayumi Takeuchi, Junji Maeda, and Nobuyuki Ishida. Aerodynamic damping properties of two transmission towers estimated by combining several identification methods. *Journal of Wind Engineering and Industrial Aerodynamics*, 98(12):872–880, 2010.

[102] Li Pengyun, Lin Jiedong, Nie Ming, Zhong Wanli, and Huang Anguo. Dynamic Response of Power Transmission Towers under Wind Load. *Energy Procedia*, 17:1124–1131, 2012.

[103] Li Qin, Junjian Yuan, and Wei Li. Random wind-induced response analysis of transmission tower-line system. *2012 International Conference on FUture Energy, Enviroment and Materials*, 16(PART C):1813–1821, 2011.

[104] T G Mara and H P Hong. Effect of wind direction on the response and capacity surface of a transmission tower. *Eng. Struct.*, 57:493–501, 2013.

[105] Hong N. Li, Wen Long Shi, Guo X. Wang, and Lian Guang Jia. Simplified models and experimental verification for coupled transmission tower-line system to seismic excitations. *Journal of Sound and Vibration*, 286(3):569–585, 2005.

[106] Gang Wu, Changhai Zhai, Shuang Li, and Lili Xie. Effects of near-fault ground motions and equivalent pulses on Large Crossing Transmission Tower-line System. *Engineering Structures*, 77:161–169, 2014.

[107] J. Kaminski, J.D. Riera, R.C.R. de Menezes, and Letícia F.F. Miguel. Model uncertainty in the assessment of transmission line towers subjected to cable rupture. *Engineering Structures*, 30(10):2935–2944, 2008.

[108] Fengli Yang, Jingbo Yang, and Zifu Zhang. Unbalanced tension analysis for UHV transmission towers in heavy icing areas. *Cold Regions Science and Technology*, 70:132–140, 2012.

[109] Byoung-Wook Moon, Ji-Hun Park, Sung-Kyung Lee, Jinkoo Kim, Taejin Kim, and Kyung-Won Min. Performance evaluation of a transmission tower by substructure test. *J. Constr. Steel Res.*, 65(1):1–11, 2009.

[110] Tao Yin, H. F. Lam, H. M. Chow, and H. P. Zhu. Dynamic reduction-based structural damage detection of transmission tower utilizing ambient vibration data. *Engineering Structures*, 31(9):2009–2019, 2009.

[111] H. F. Lam, J. H. Yang, and Q. Hu. How to install sensors for structural model updating? *12th East Asia-Pacific Conference on Structural Engineering and Construction*, 14:450–459, 2011.

[112] Qiang Xie and Li Sun. Failure mechanism and retrofitting strategy of transmission tower structures under ice load. *Journal of Constructional Steel Research*, 74:26–36, 2012.

[113] Qu Cheng-Zhong and Lian Xu-Wei. Damage identification for transmission towers based on HHT. *Energy Procedia*, 17:1390–1394, 2012.

[114] De Silva, Clarence W Frontmatter, and Clarence W De Silva. *Vibrations. Foundamentals and Practise*. 2000.

[115] Andreas H. Schellenberg, StephenA. Mahin, and Gregory L. Fenves. Advanced Implementation of Hybrid Simulation. Technical report, Pacific Earthquake Engineering Reasearch Center, University of California, Berkeley, 2009.

[116] Zhou Wang, Alan C Bovik, Hamid R Sheikh, Student Member, Eero P Simoncelli, and Senior Member. Image Quality Assessment : From Error Visibility to Structural Similarity. 13(4):1–14, 2004.

[117] Peter Avitabile. Experimental Modal Analysis. A simple non-mathematicacl presentation. *Sound and Vibration*, (January):1–11, 2001.

[118] Peter Avitabile. Back to basics - Curve fitting. *Experimental Techniques*, 1999.

[119] Peter Avitabile. Back to basics - Curve fitting extended. *Experimental Techniques*, 1999.

[120] Peter Avitabile. Back to basics - Mode shapes from one H column. *Experimental Techniques*, 1999.

[121] Peter Avitabile. Back to basics - Operation Deflection Shapes vs Mode Shapes. *Experimental Techniques*, 1999.

[122] Peter Avitabile. Back to basics - About Structural Dynamic Modification. *Experimental Techniques*, 2000.

[123] Peter Avitabile. Back to basics - Single Value Decomposition. *Experimental Techniques*, 2001.

[124] Peter Avitabile. Back to Basics - Modal Space. *Experimental Techniques*, (June):17–18, 2002.

[125] Peter Avitabile. Back to basics - In our own little world. In *Experimental Techniques*, volume 36, pages 1–2, 2003.

Annexes

A. Parametric analysis

This annex presents additional results for the numeric parametric studies on the SCI indicators omitted in the general discussion of the thesis for concision. The speech in the main sections discusses results for all structural alteration progression families but only results for a reference structural alteration family are shown (Young modulus alteration for both the FEM aluminium plate and for the FEM scaled tower). This chapter aims to complement the data omitted in those sections.

First section in this annex shows results for all parametric analysis performed on the FEM-modelled aluminium plate and for the remaining structural alteration families that have not been explicitly shown in correspondent chapter. Comprehensive results for all the structural modification families are shown depicting influence of driving points, mesh density, frequency resolution, bandwidth, damping and noise. The second section in this annex show equivalent results for the numerical campaign executed on the FEM scaled tower.

A.1 Numeric SCI Sensitivity: Aluminium Plate

A.1.1 Driving point

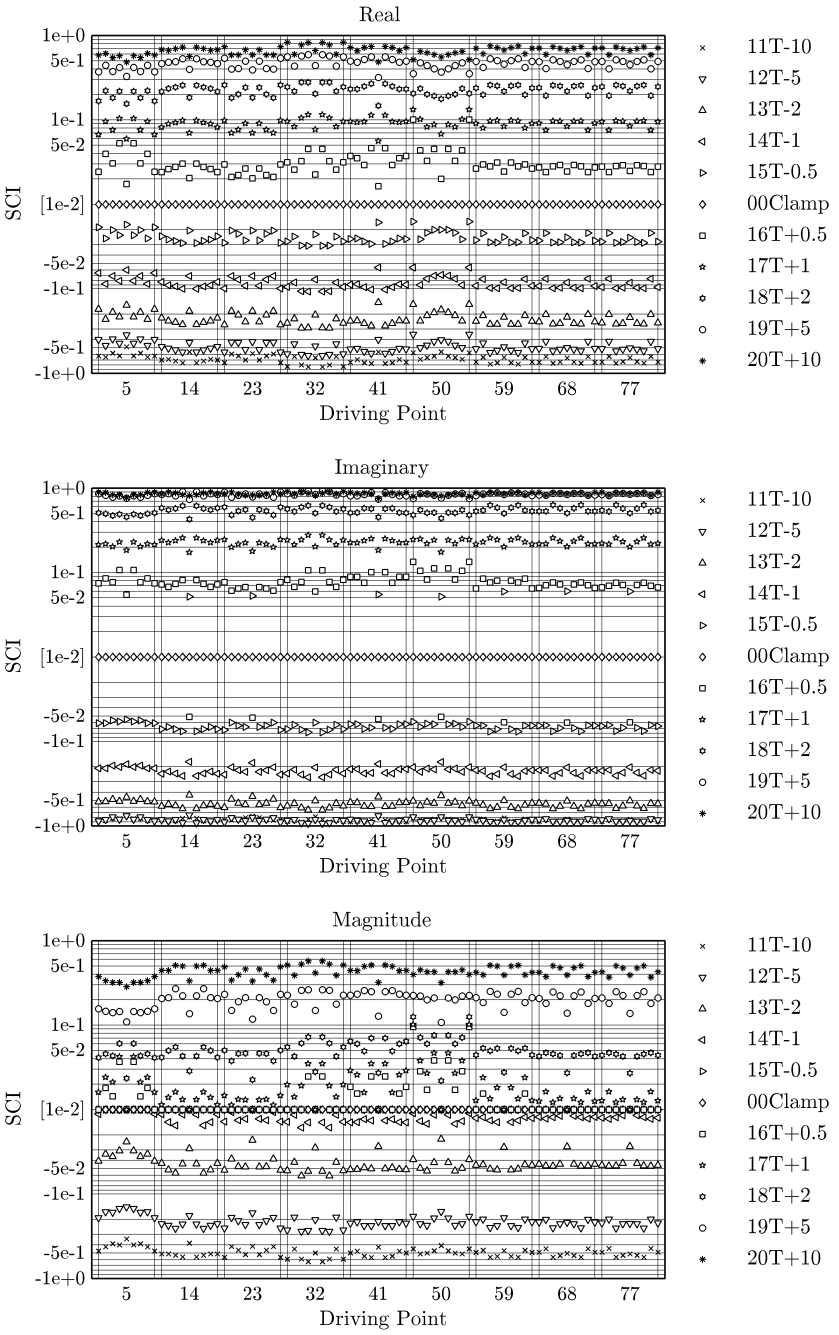

Figure A.1: SCI vs driving point. Thickness. 81 nodes, DP30, BW = 3200 Hz.

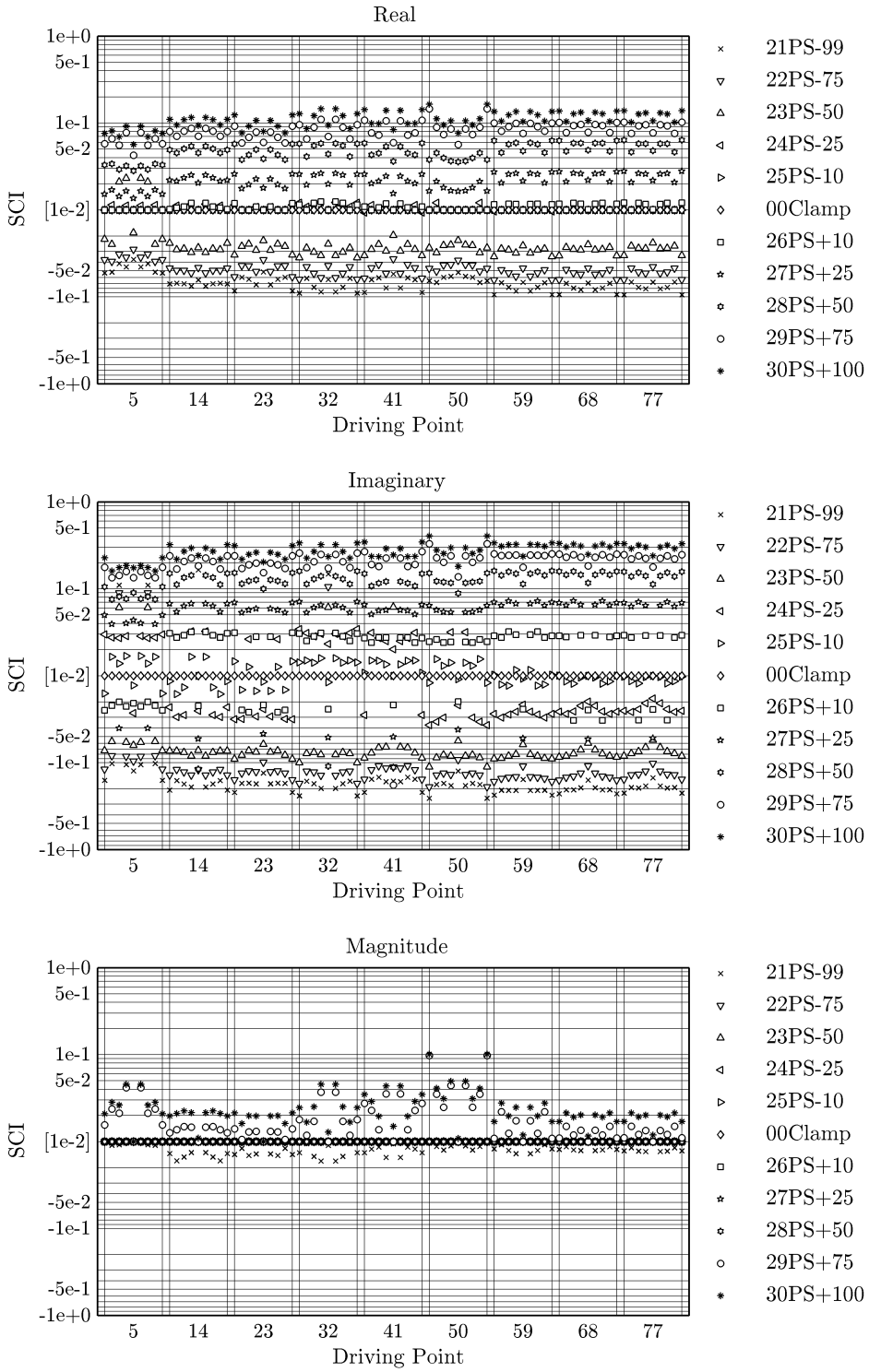

Figure A.2: SCI vs driving point. Pre-stress. 81 nodes, DP30, BW = 3200 Hz.

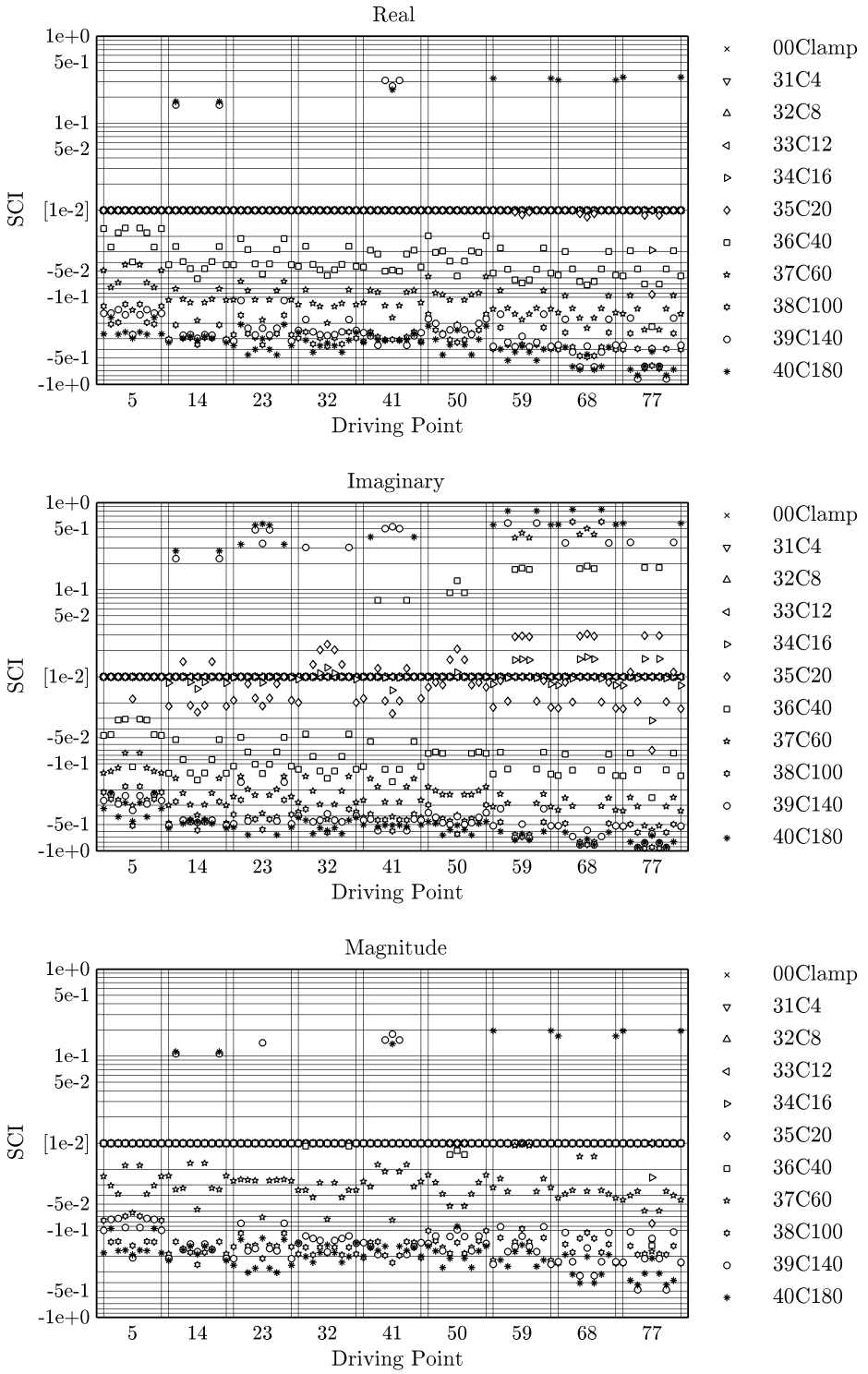

Figure A.3: SCI vs driving point. Cracks. 81 nodes, DP30, BW = 3200 Hz.

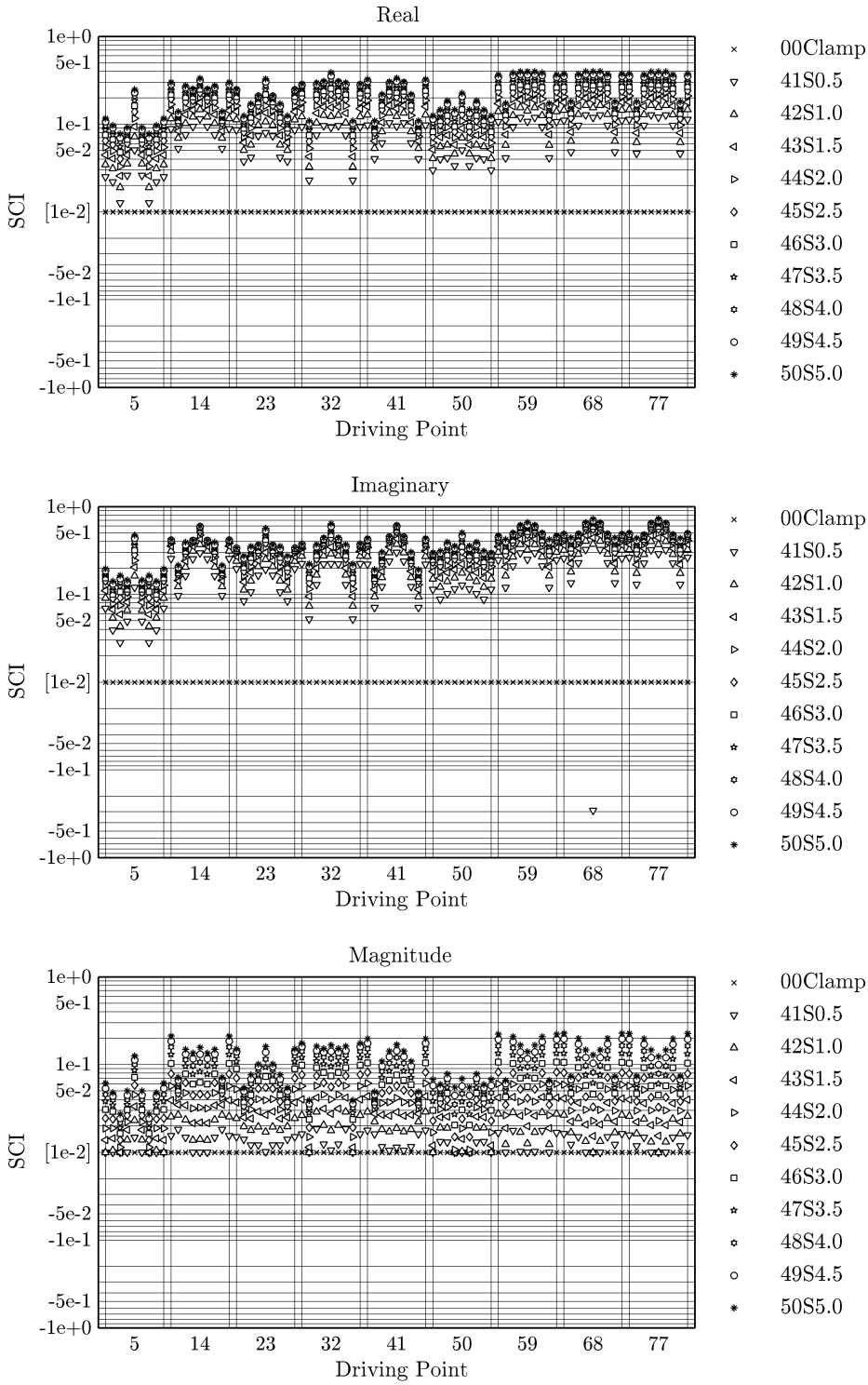

Figure A.4: SCI vs driving point. Stringers. 81 nodes, DP30, BW = 3200 Hz.

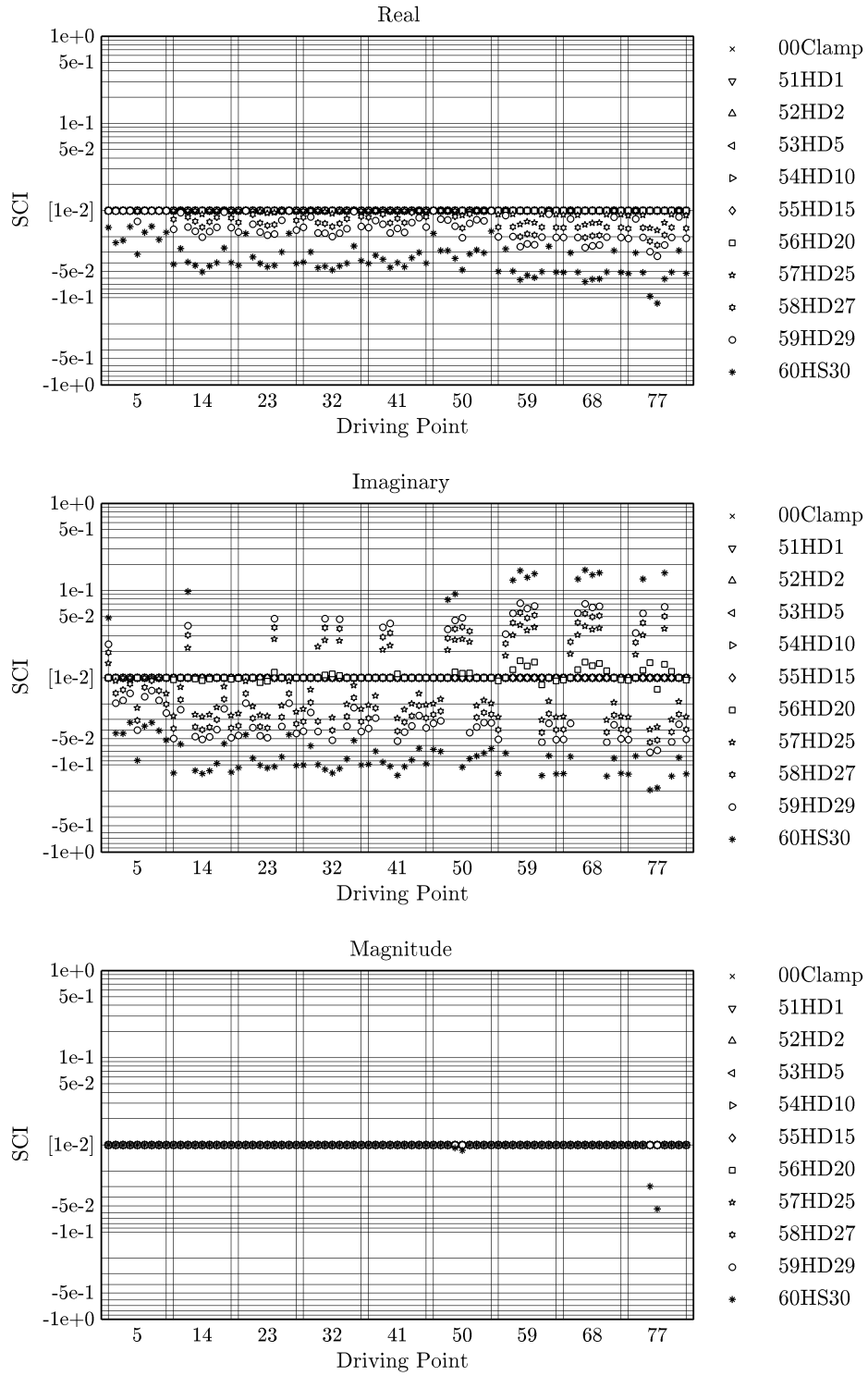

Figure A.5: SCI vs driving point. Holes. 81 nodes, DP30, BW = 3200 Hz.

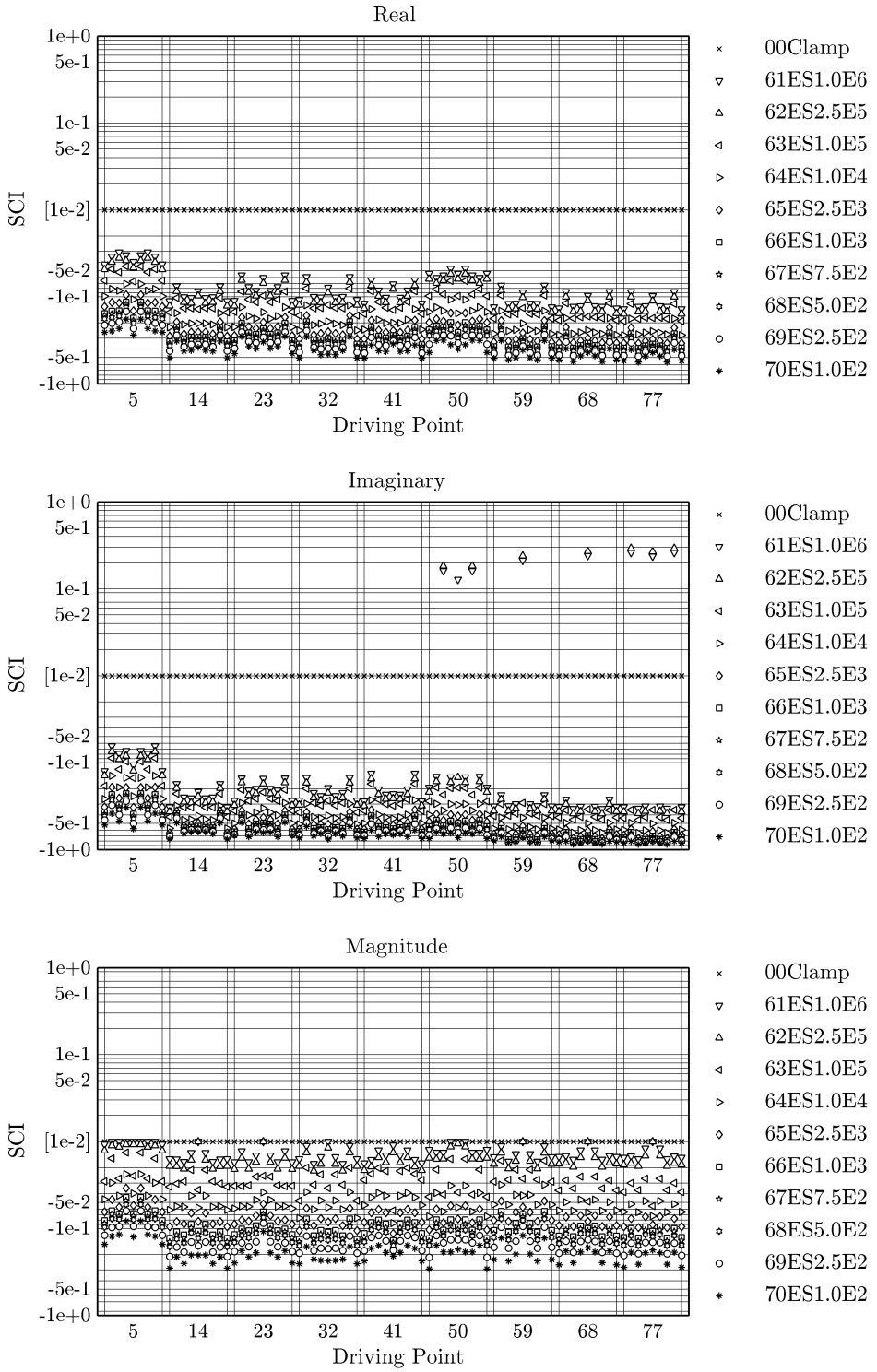

Figure A.6: SCI vs driving point. Elastic clamping. 81 nodes, DP30, BW = 3200 Hz.

A.1.2 Mesh density

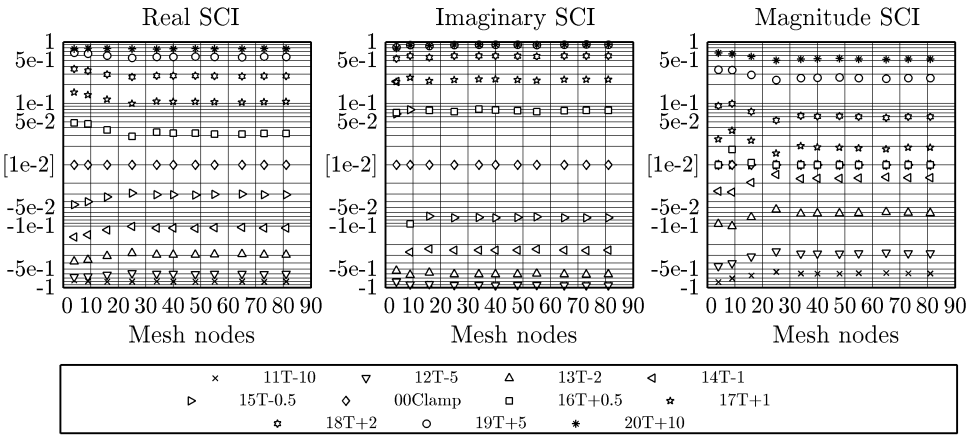

Figure A.7: SCI vs mesh density. Thickness. 81 nodes, DP30, BW = 3200 Hz.

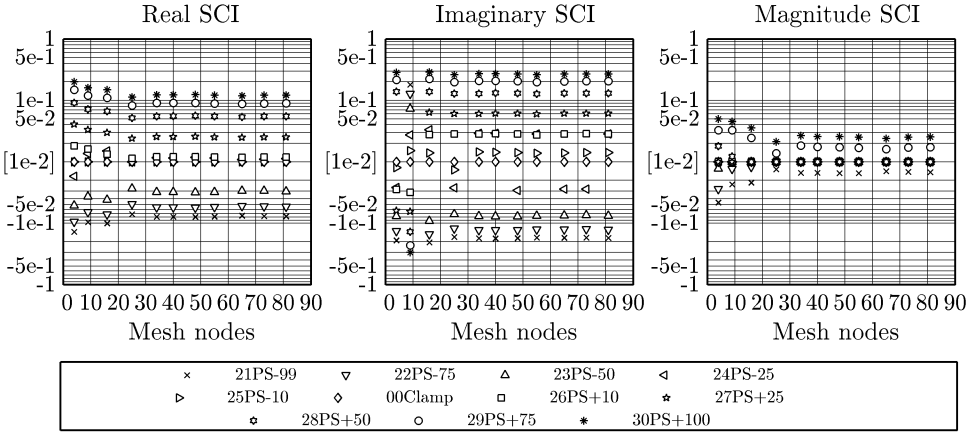

Figure A.8: SCI vs mesh density. Pre-stresses. 81 nodes, DP30, BW = 3200 Hz.

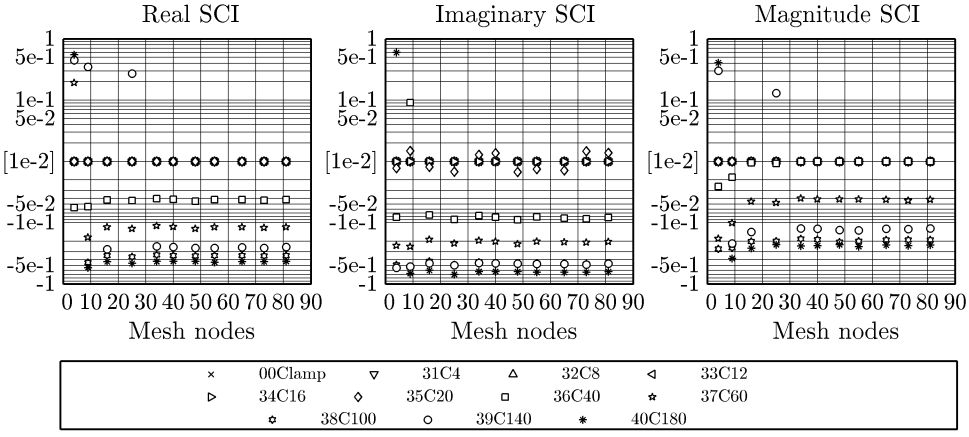

Figure A.9: SCI vs mesh density. Cracks. 81 nodes, DP30, BW = 3200 Hz.

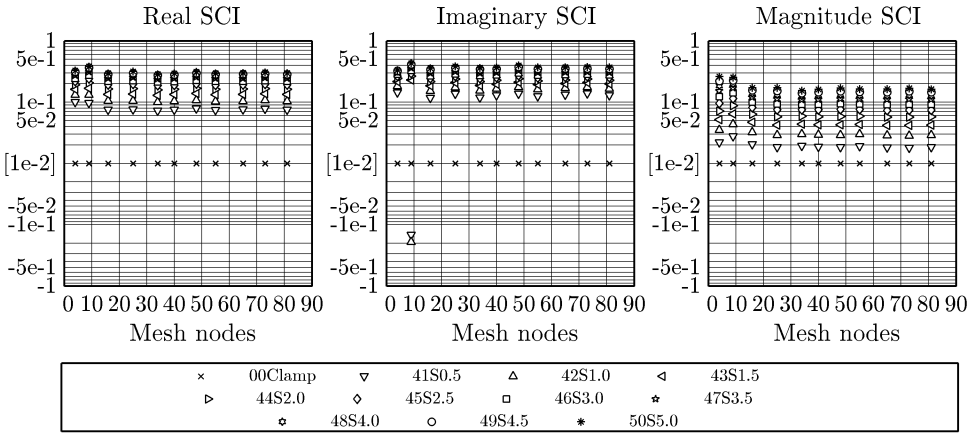

Figure A.10: SCI vs mesh density. Stringers. 81 nodes, DP30, BW = 3200 Hz.

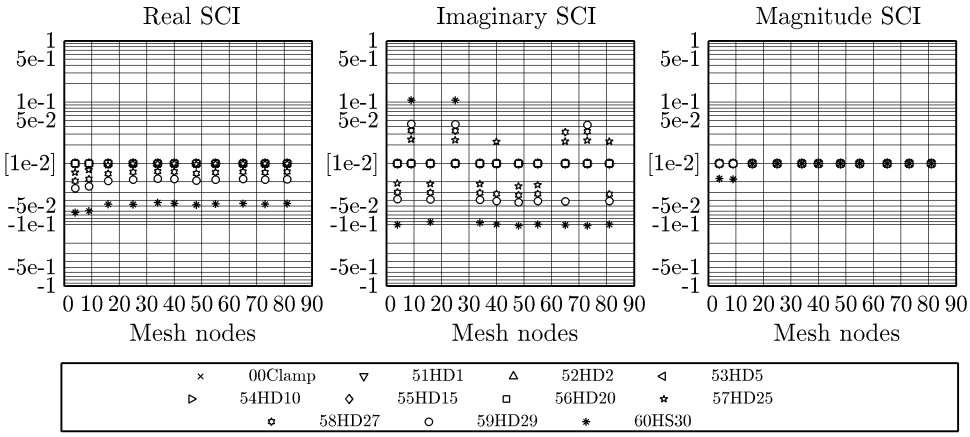

Figure A.11: SCI vs mesh density. Holes. 81 nodes, DP30, BW = 3200 Hz.

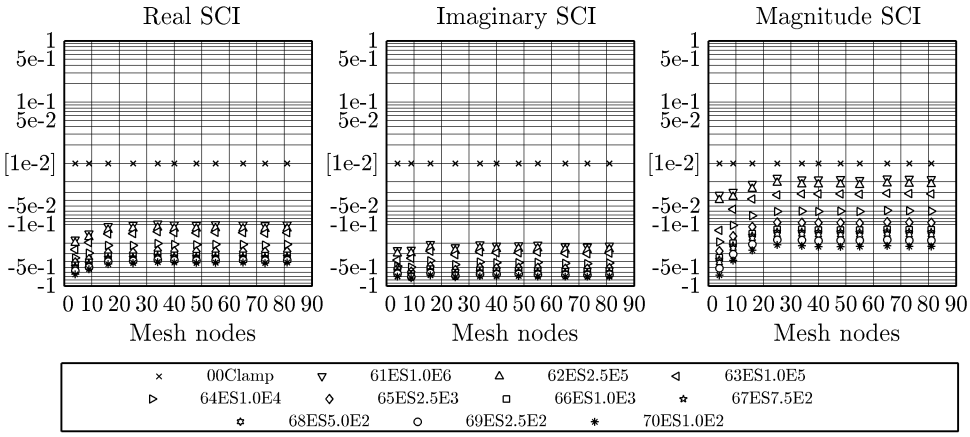

Figure A.12: SCI vs mesh density. Elastic clamping. 81 nodes, DP30, BW = 3200 Hz.

A.1.3 Frequency resolution

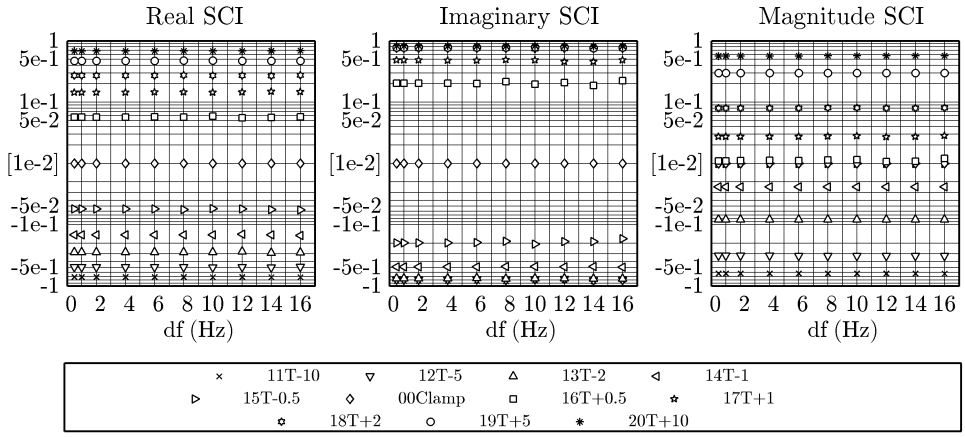

Figure A.13: SCI vs freq. resolution. Thickness. 81 nodes, DP30, BW = 3200 Hz.

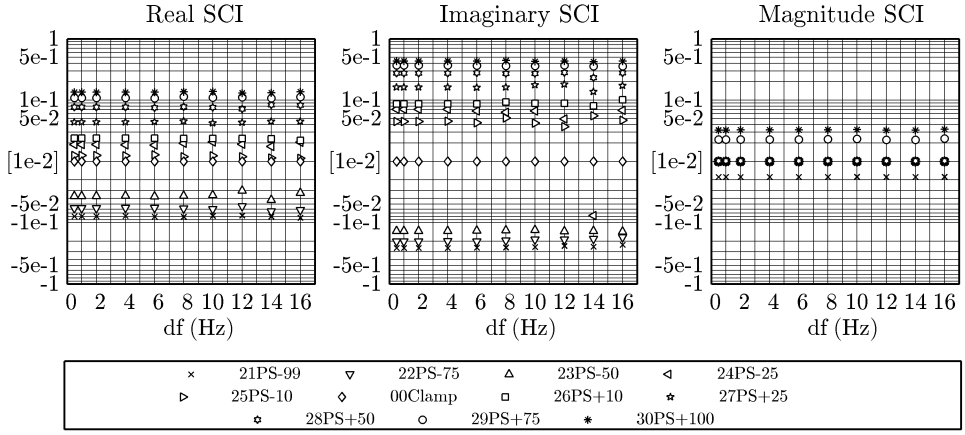

Figure A.14: SCI vs freq. resolution. Pre-stresses. 81 nodes, DP30, BW = 3200 Hz.

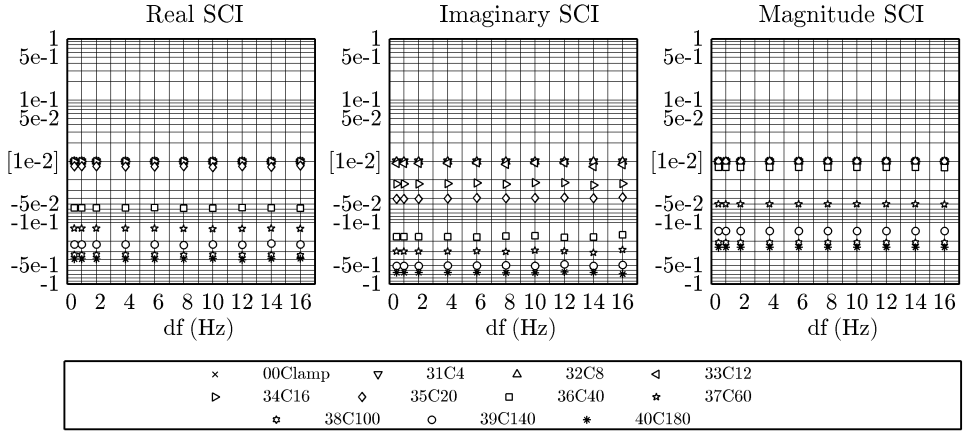

Figure A.15: SCI vs freq. resolution. Cracks. 81 nodes, DP30, BW = 3200 Hz.

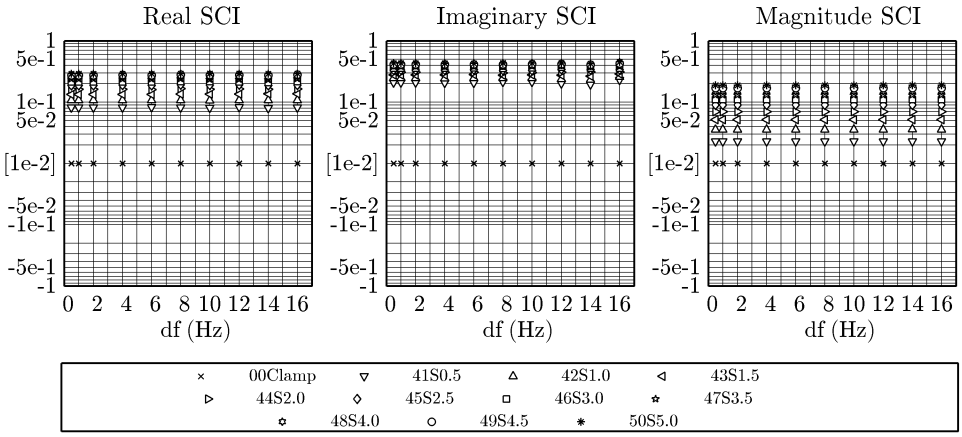

Figure A.16: SCI vs freq. resolution. Stringers. 81 nodes, DP30, BW = 3200 Hz.

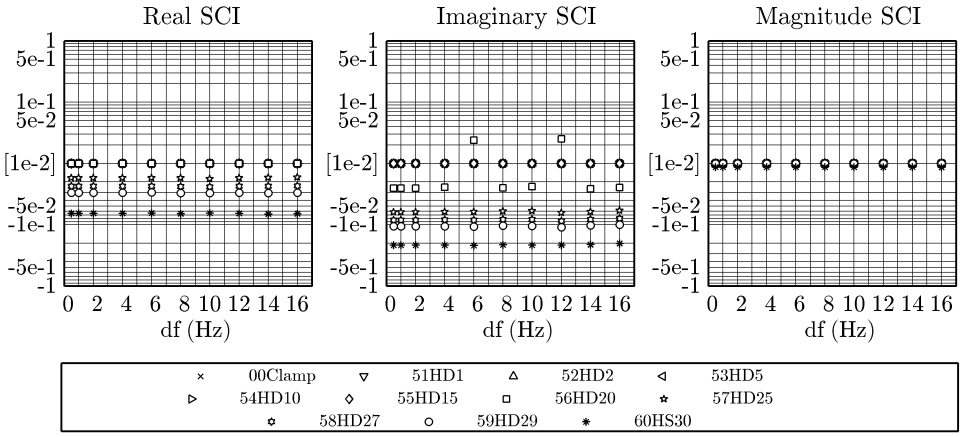

Figure A.17: SCI vs freq. resolution. Holes. 81 nodes, DP30, BW = 3200 Hz.

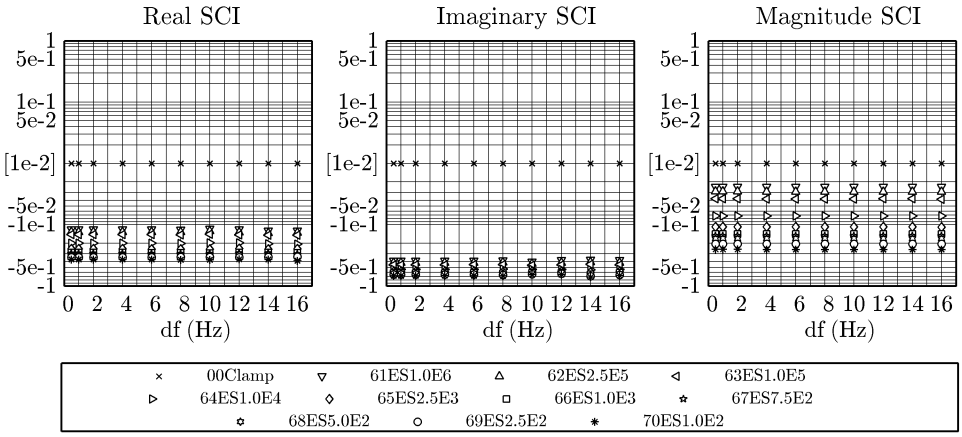

Figure A.18: SCI vs freq. resolution. Elastic clamping. 81 nodes, DP30, BW = 3200 Hz.

A.1.4 Bandwidth

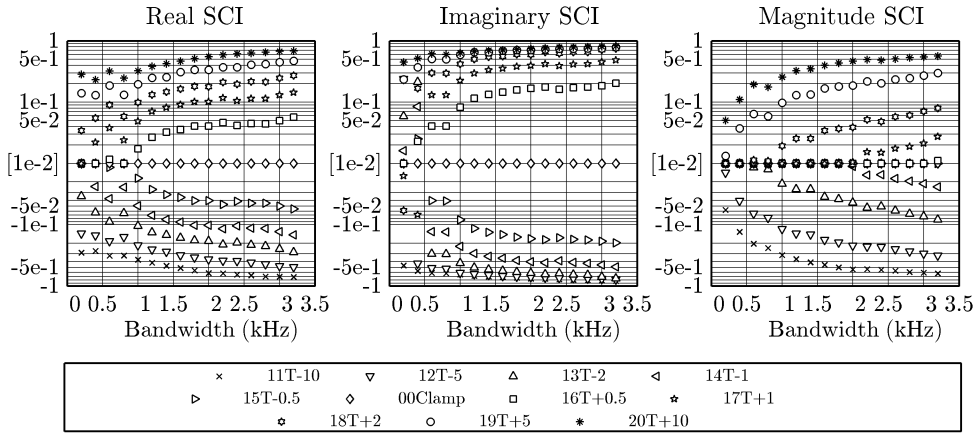

Figure A.19: SCI vs frequency range. Thickness. 81 nodes, DP30, $\Delta f = 0.5$ Hz

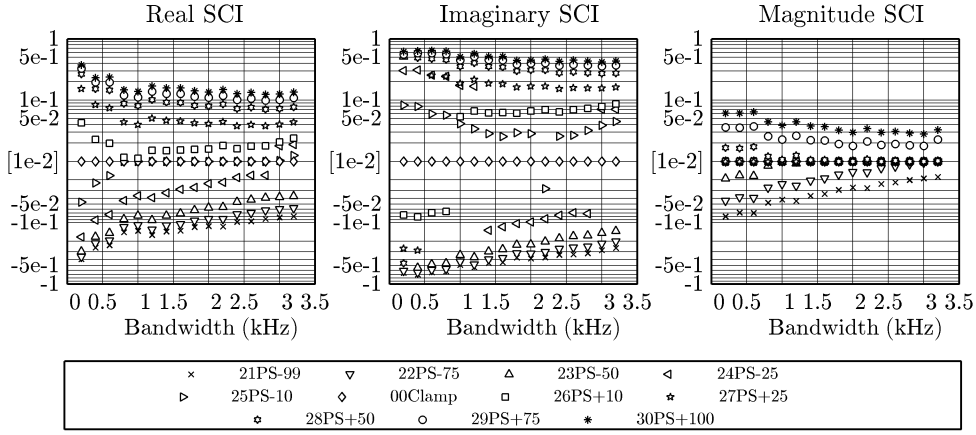

Figure A.20: SCI vs frequency range. Pre-stresses. 81 nodes, DP30, $\Delta f = 0.5$ Hz

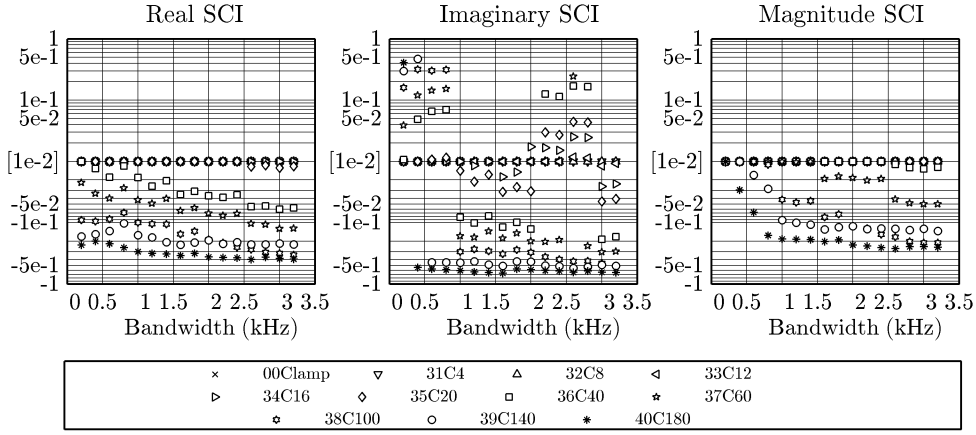

Figure A.21: SCI vs frequency range. Cracks. 81 nodes, DP30, $\Delta f = 0.5$ Hz

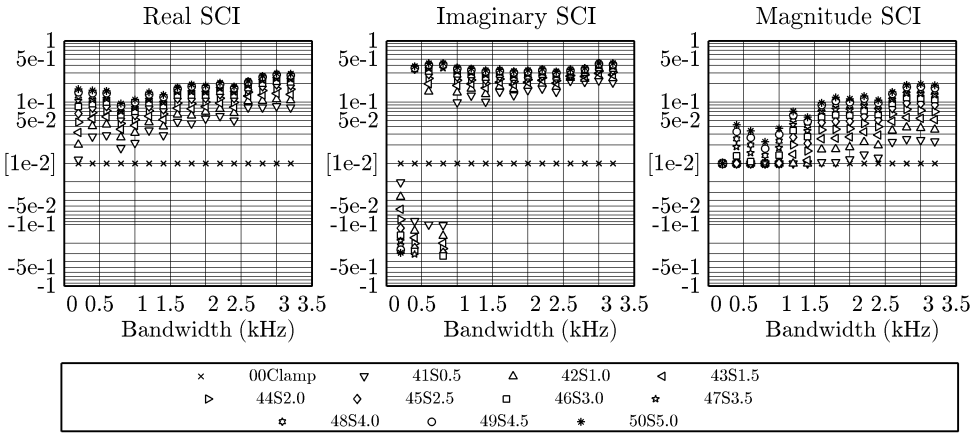

Figure A.22: SCI vs frequency range. Stringers. 81 nodes, DP30, $\Delta f = 0.5$ Hz

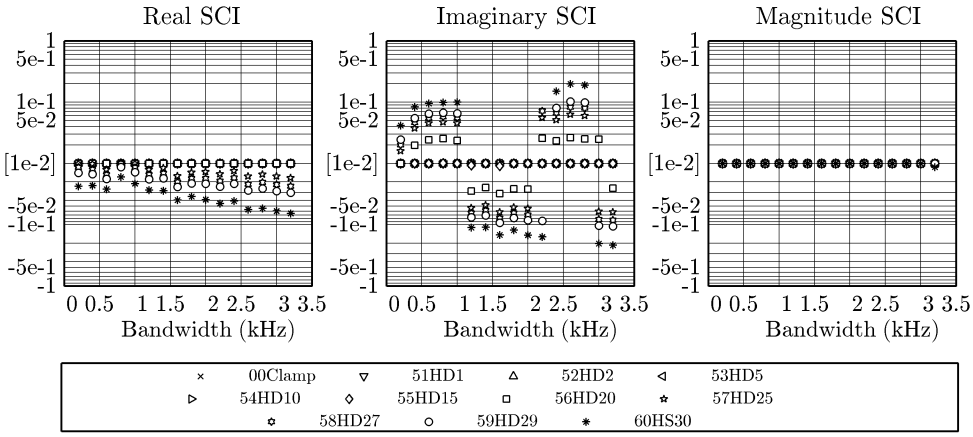

Figure A.23: SCI vs frequency range. Holes. 81 nodes, DP30, $\Delta f = 0.5$ Hz

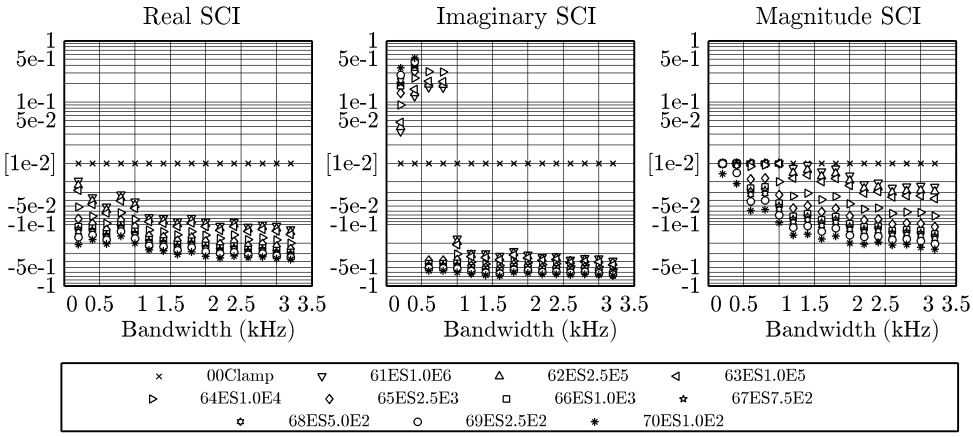

Figure A.24: SCI vs frequency range. Boundary conditions. 81 nodes, DP30, $\Delta f = 0.5$ Hz

A.1.5 Damping

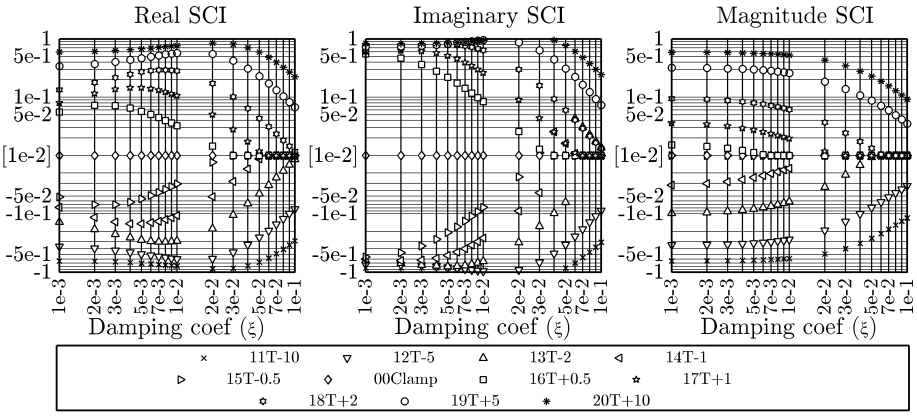

Figure A.25: SCI vs damping coeff.. Thickness. 81 nodes, DP30, BW = 3200 Hz, $\Delta f = 0.5$ Hz

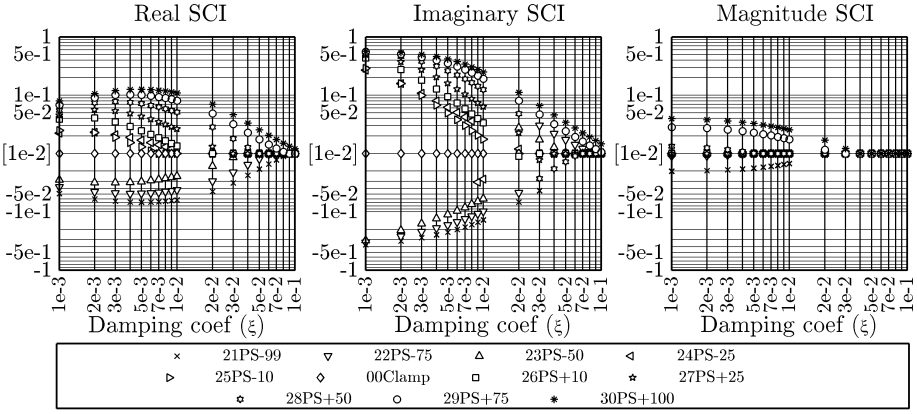

Figure A.26: SCI vs damping coeff.. Pre-stresses. 81 nodes, DP30, BW = 3200 Hz, $\Delta f = 0.5$ Hz

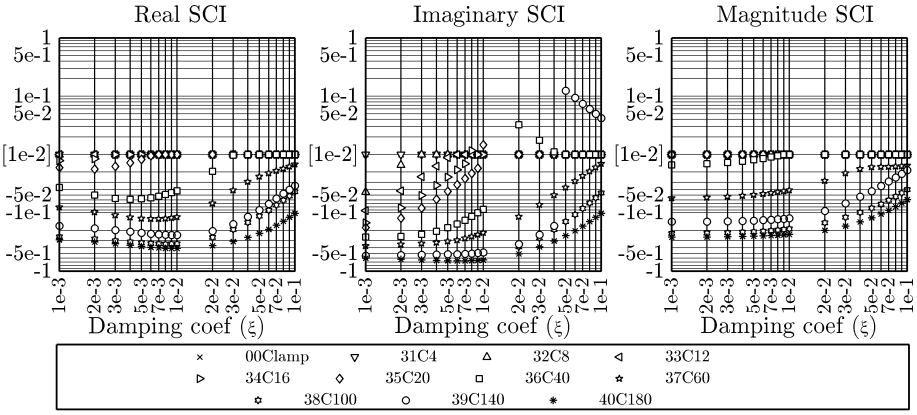

Figure A.27: SCI vs damping coeff.. Cracks. 81 nodes, DP30, BW = 3200 Hz, $\Delta f = 0.5$ Hz

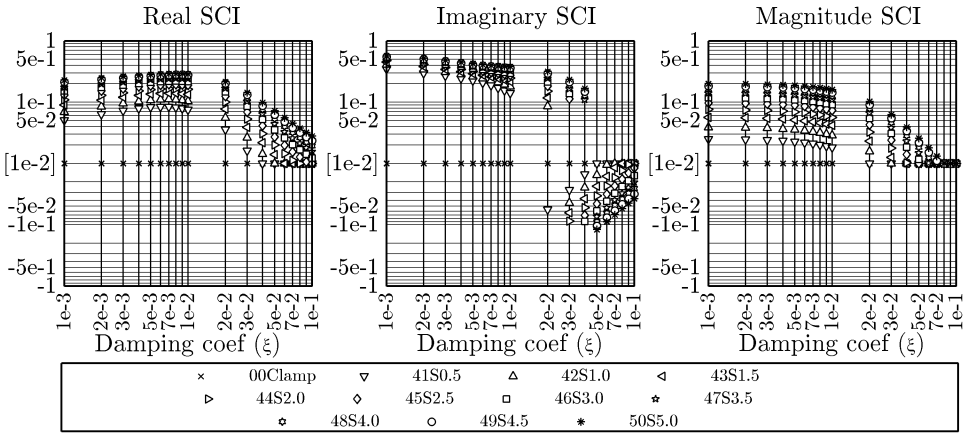

Figure A.28: SCI vs damping coeff.. Stringers. 81 nodes, DP30, BW = 3200 Hz, $\Delta f = 0.5$ Hz

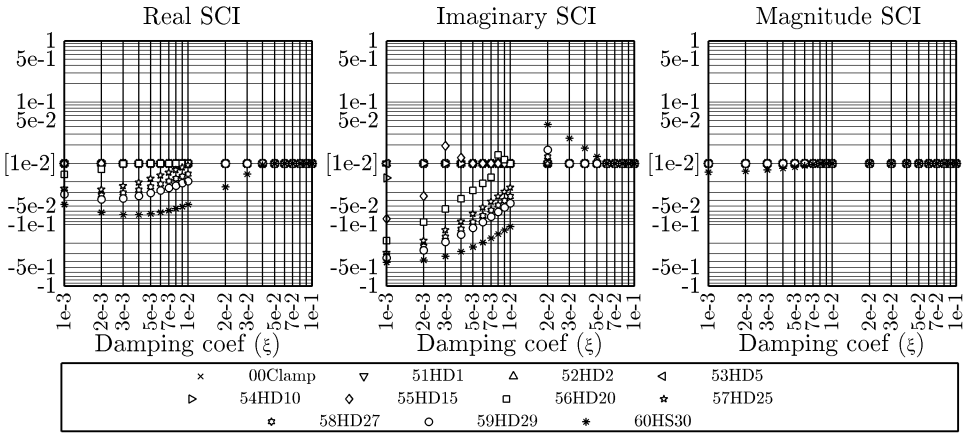

Figure A.29: SCI vs damping coeff.. Holes. 81 nodes, DP30, BW = 3200 Hz, $\Delta f = 0.5$ Hz

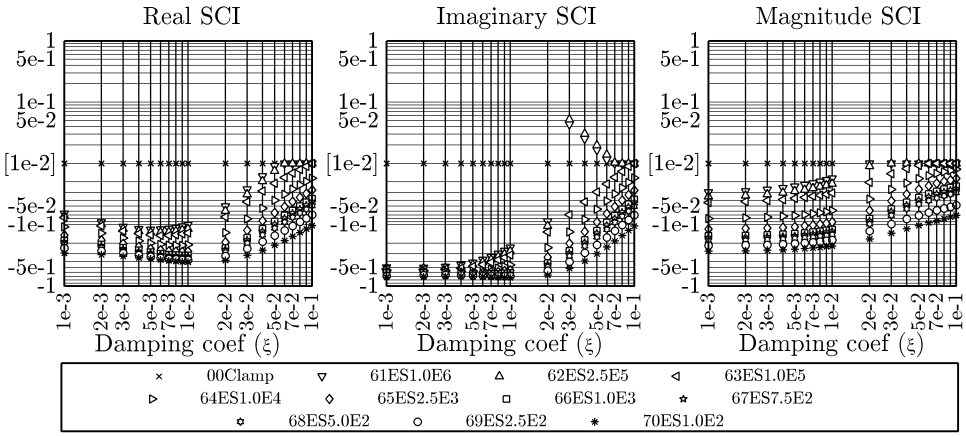

Figure A.30: SCI vs damping coeff.. Boundary conditions. 81 nodes, DP30, BW = 3200 Hz, $\Delta f = 0.5$ Hz

A.1.6 Noise

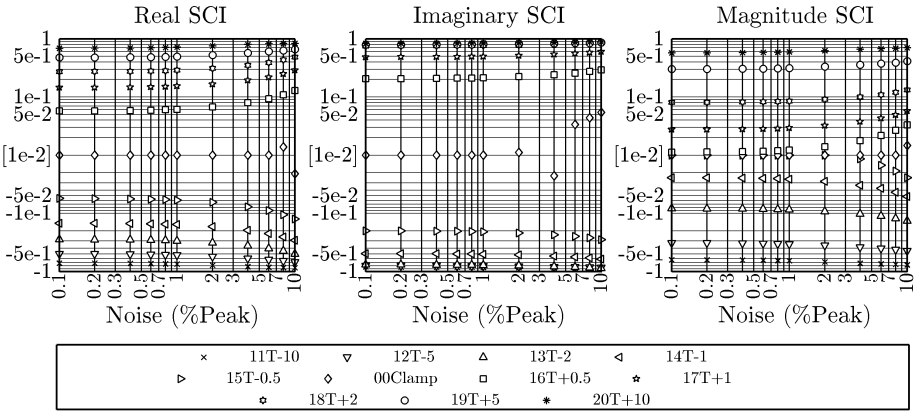

Figure A.31: SCI vs % peak noise. Thickness. 81 nodes, DP30, BW = 3200 Hz, $\Delta f = 0.5$ Hz

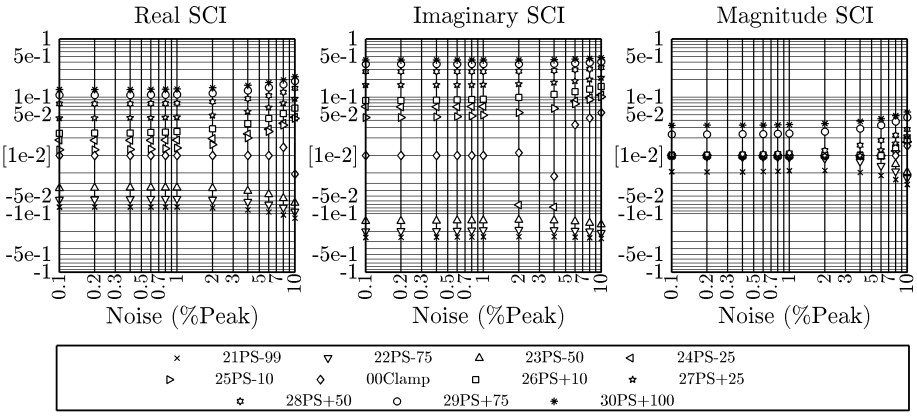

Figure A.32: SCI vs % peak noise. Pre-stresses. 81 nodes, DP30, BW = 3200 Hz, $\Delta f = 0.5$ Hz

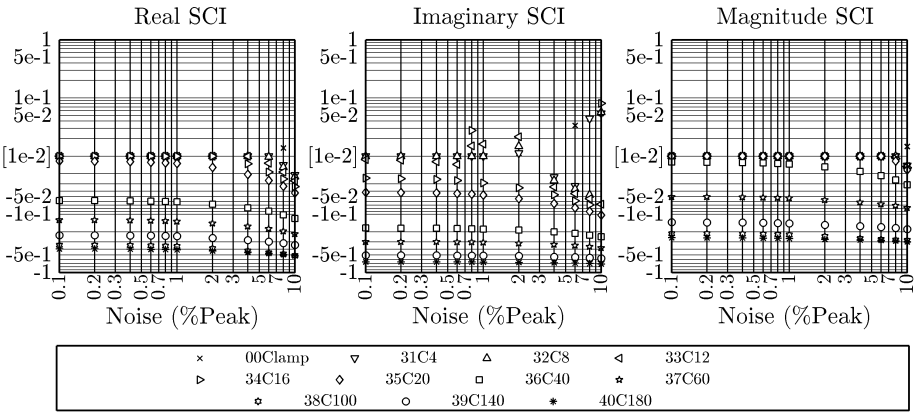

Figure A.33: SCI vs % peak noise. Cracks. 81 nodes, DP30, BW = 3200 Hz, $\Delta f = 0.5$ Hz

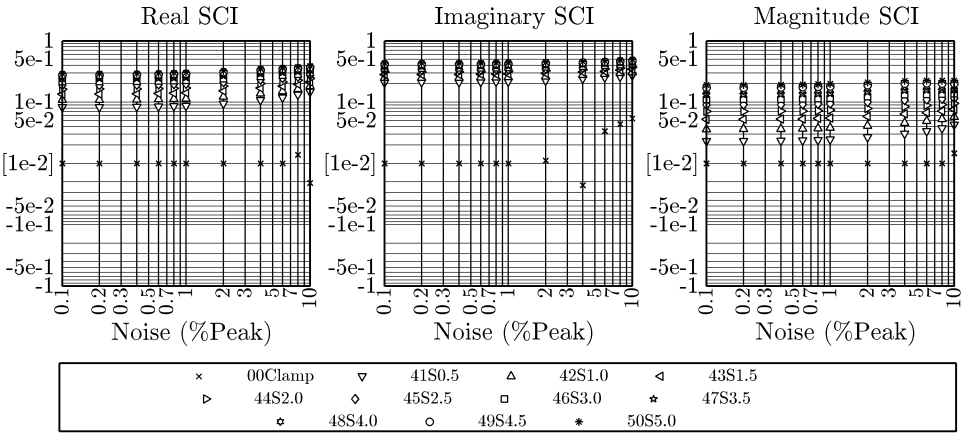

Figure A.34: SCI vs % peak noise. Stringers. 81 nodes, DP30, BW = 3200 Hz, $\Delta f = 0.5$ Hz

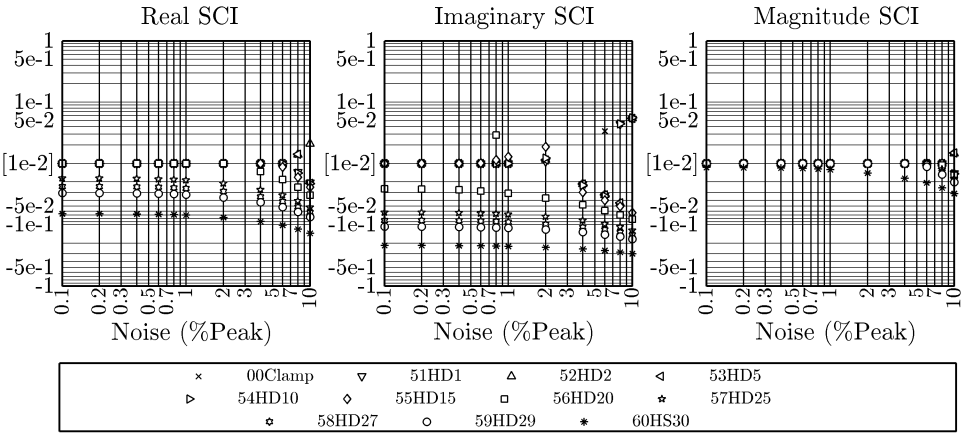

Figure A.35: SCI vs frequency range. Holes. 81 nodes, DP30, BW = 3200 Hz, Δf = 0.5 Hz

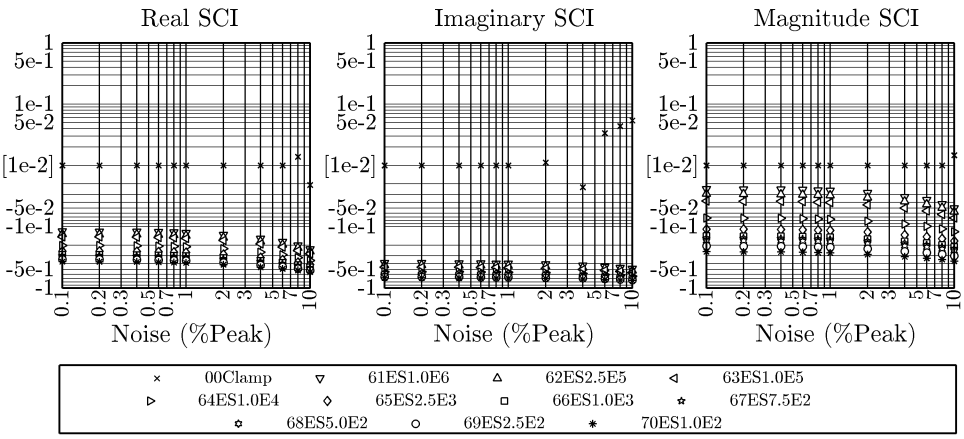

Figure A.36: SCI vs % peak noise. Boundary conditions. 81 nodes, DP30, BW = 3200 Hz, Δf = 0.5 Hz

A.2 Numeric SCI Sensitivity: Scaled Tower

A.2.1 Driving Point

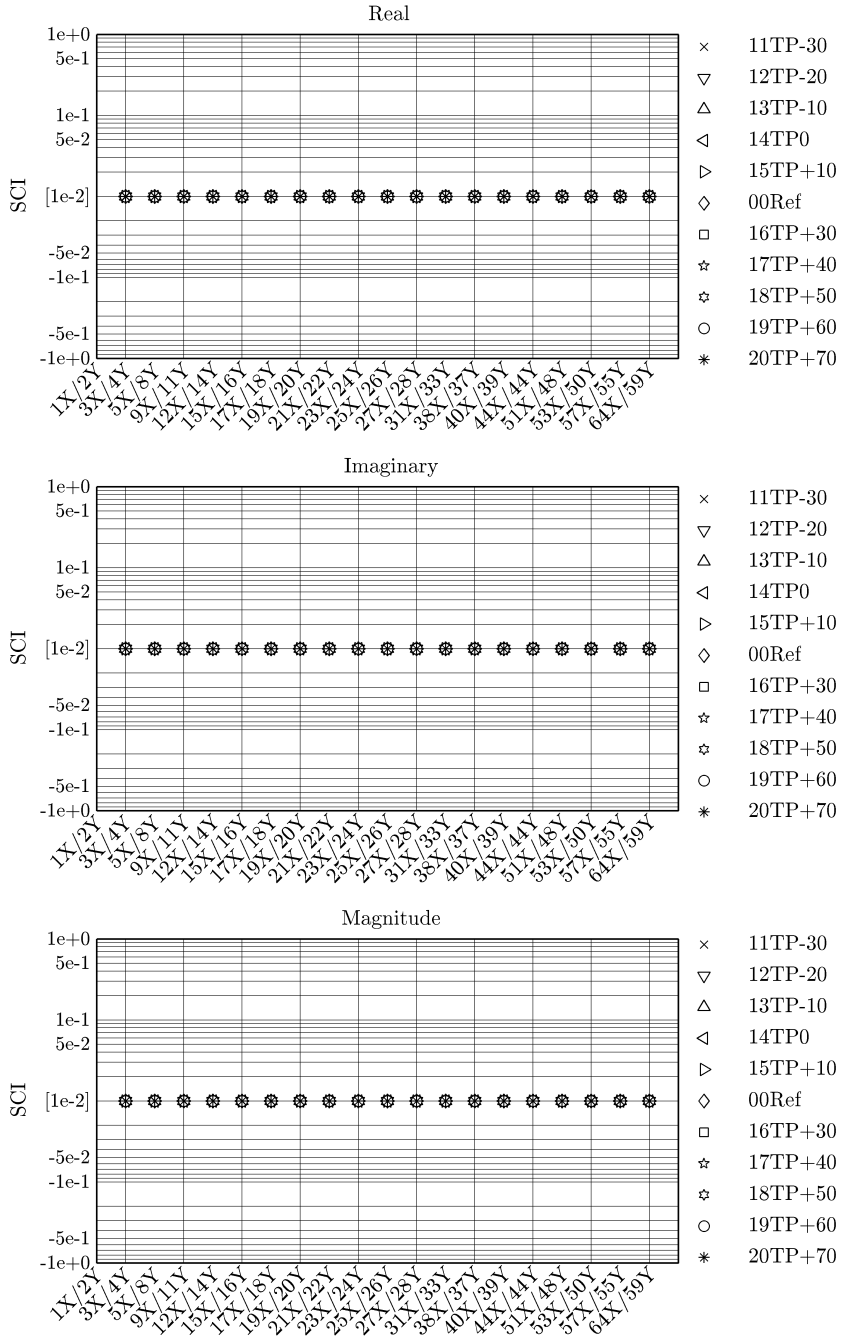

Figure A.37: SCI vs Driving point. Thermal pre-stresses. 65X59Y mesh, BW = 400 Hz, Δf = 0.5 Hz

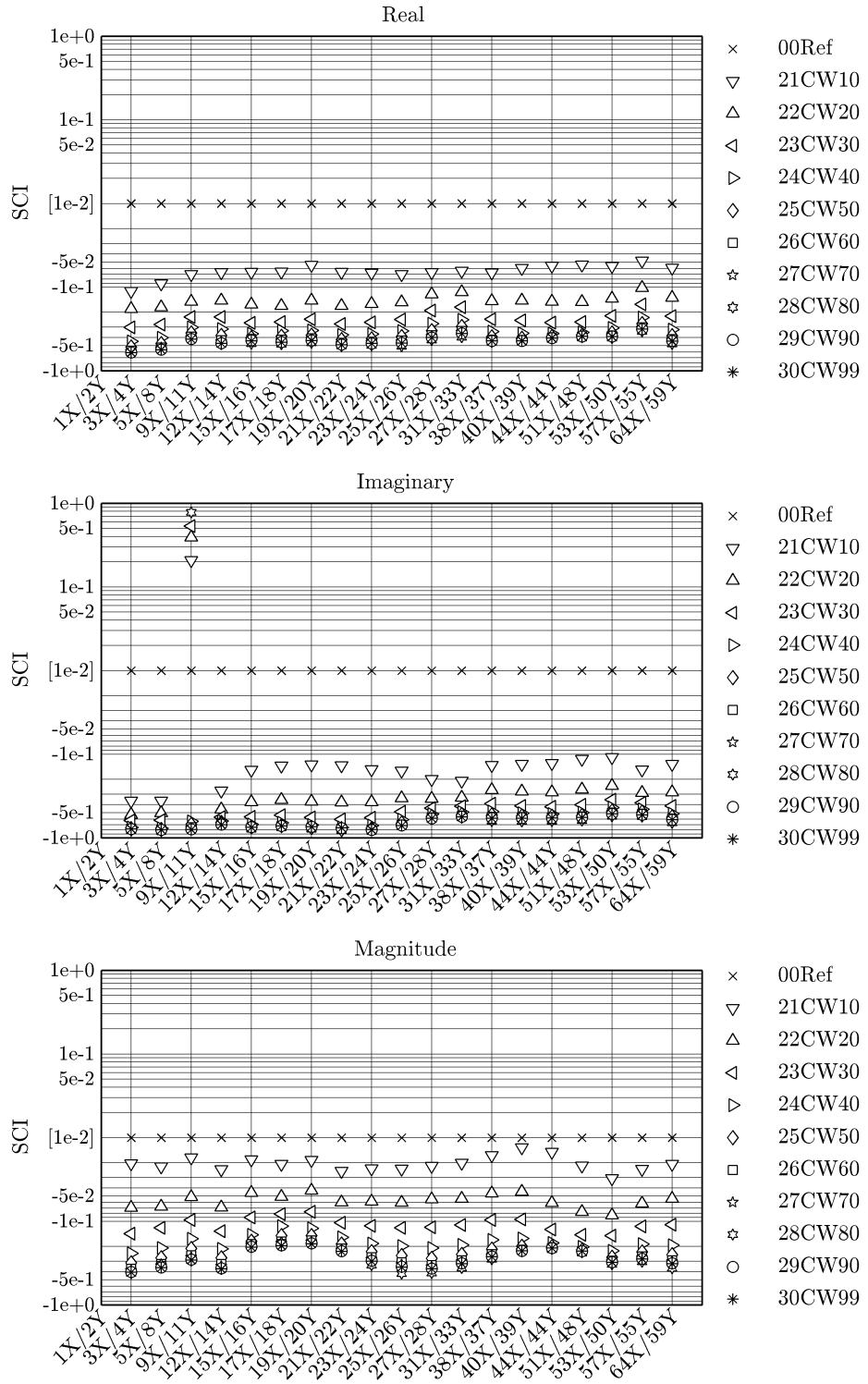

Figure A.38: SCI vs Driving point. Vertical pre-stresses. 65X59Y mesh, BW = 400 Hz, $\Delta f = 0.5$ Hz

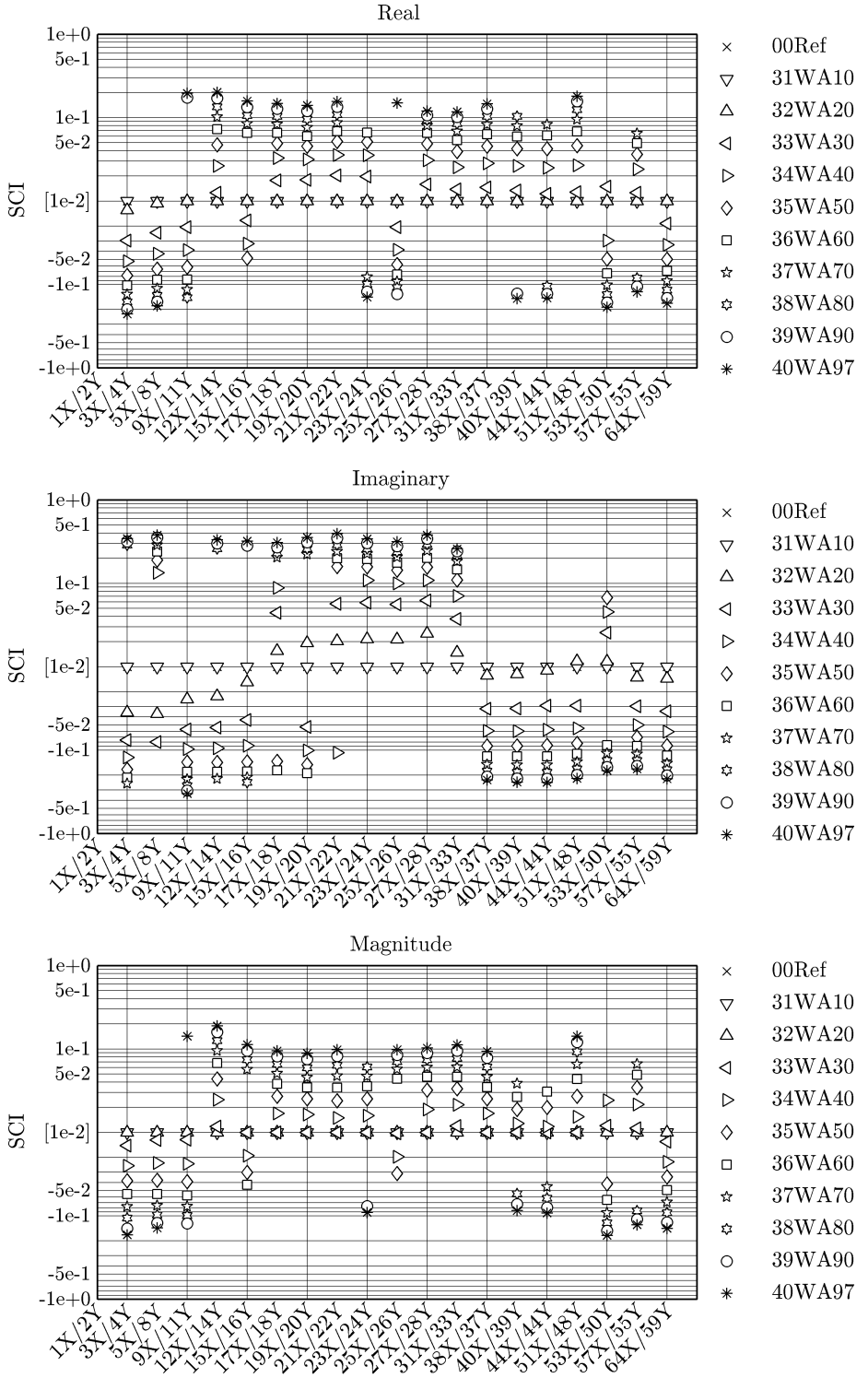

Figure A.39: SCI vs Driving point. Lateral pre-stresses. 65X59Y mesh, BW = 400 Hz, $\Delta f = 0.5$ Hz

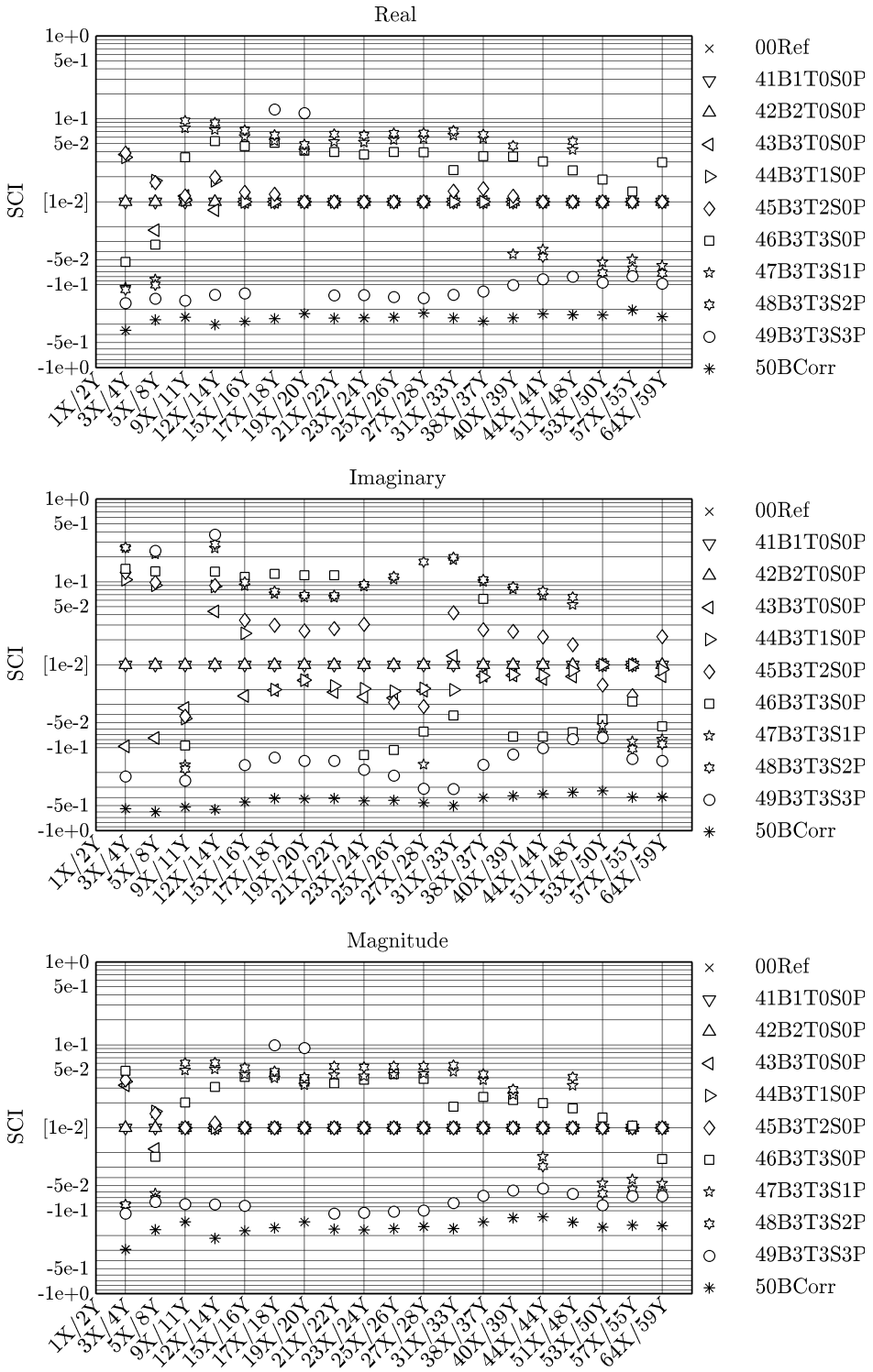

Figure A.40: SCI vs Driving point. Removal of members. 65X59Y mesh, BW = 400 Hz, $\Delta f = 0.5$ Hz

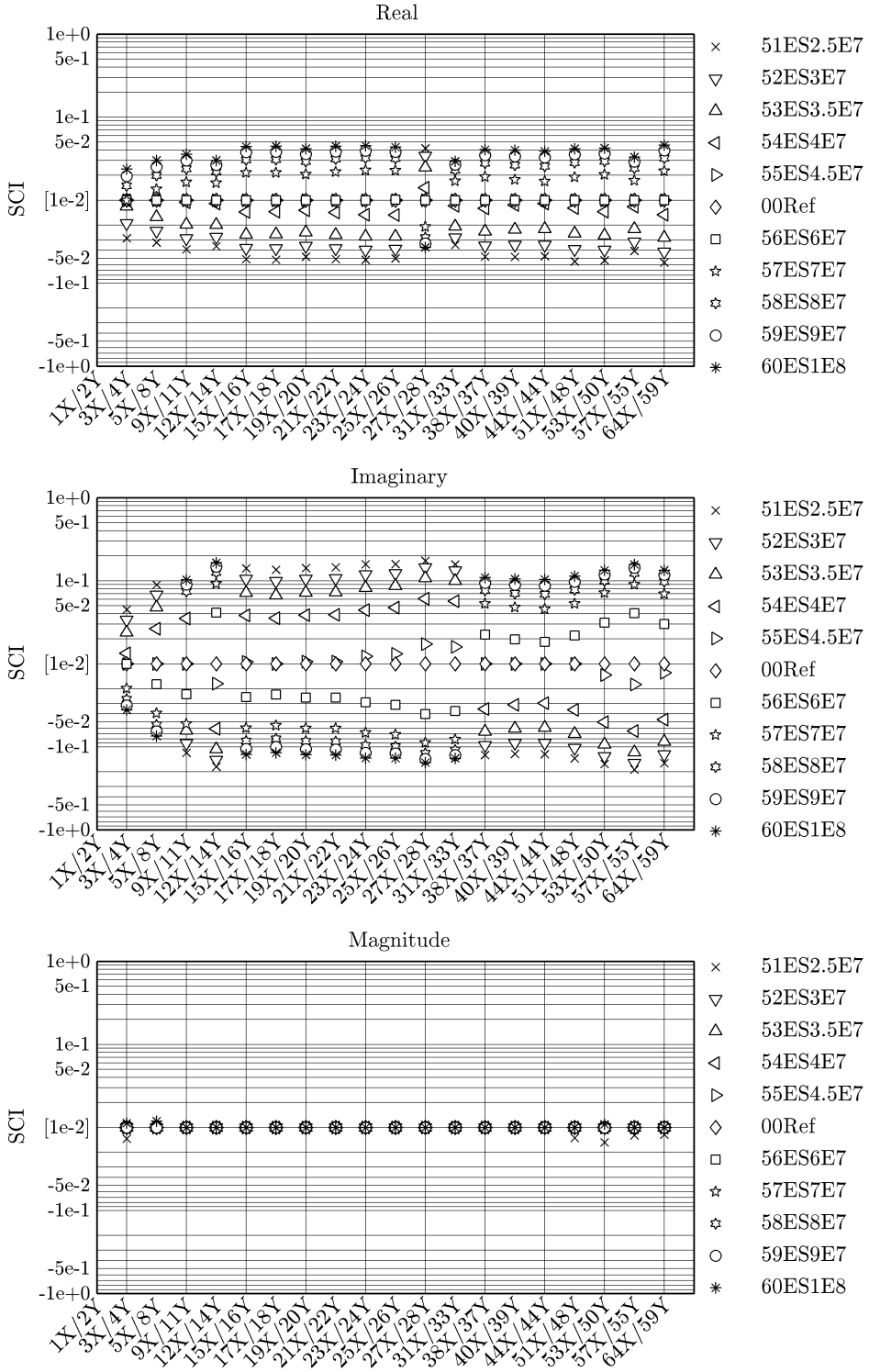

Figure A.41: SCI vs Driving point. Elastic support. 65X59Y mesh, BW = 400 Hz, $\Delta f = 0.5$ Hz

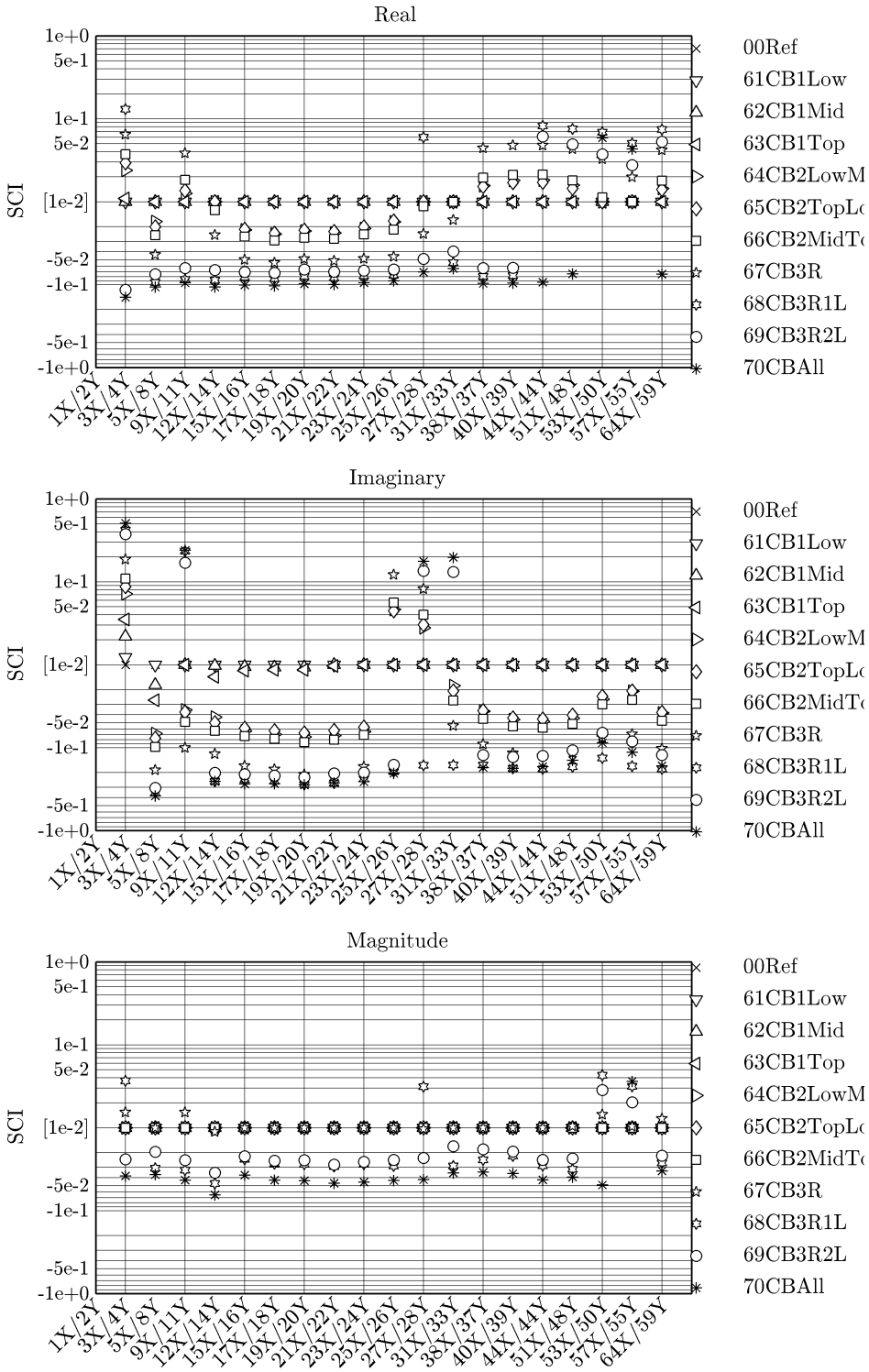

Figure A.42: SCI vs Driving point. Cable falls. 65X59Y mesh, BW = 400 Hz, $\Delta f = 0.5$ Hz

A.2.2 Mesh Density

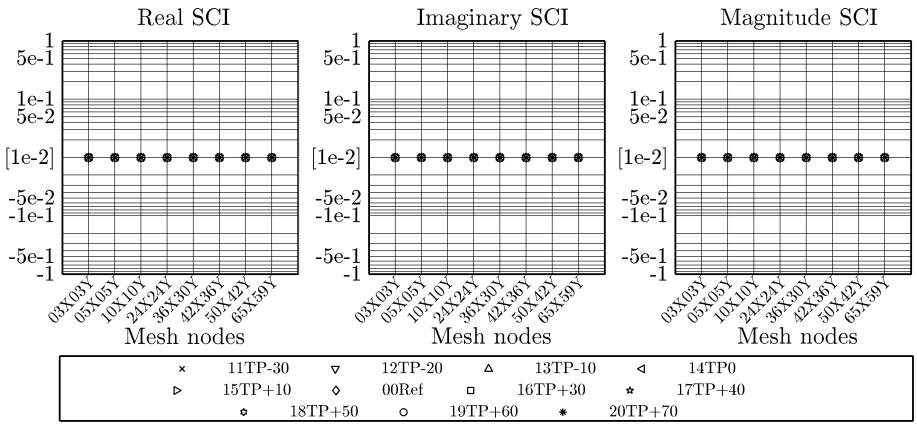

Figure A.43: SCI vs Mesh Density. Thermal pre-stresses. 65X59Y mesh, BW = 400 Hz, $\Delta f = 0.5$ Hz

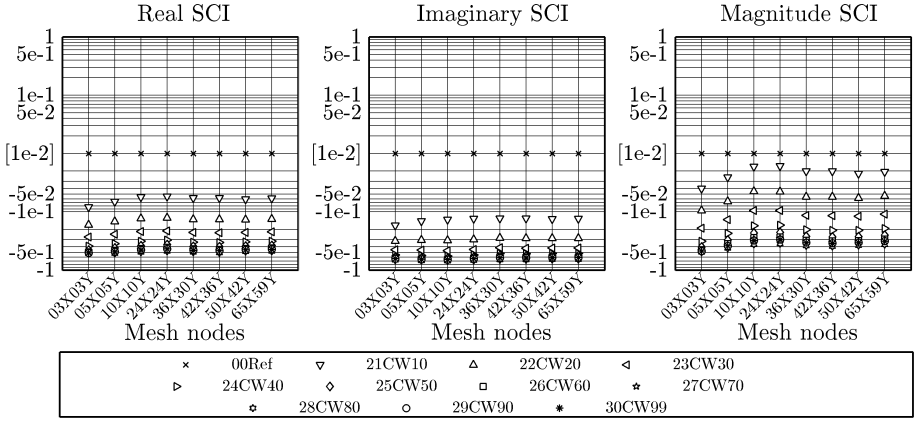

Figure A.44: SCI vs Mesh Density. Vertical pre-stresses. 65X59Y mesh, BW = 400 Hz, $\Delta f = 0.5$ Hz

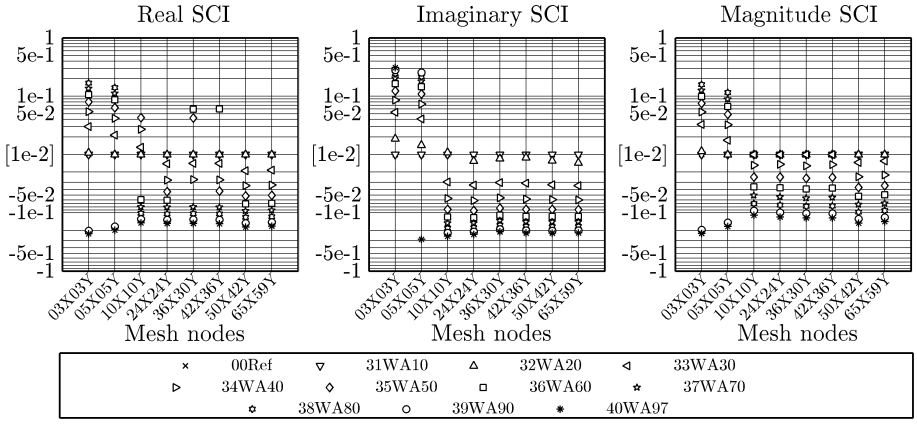

Figure A.45: SCI vs Mesh Density. Lateral pre-stresses. 65X59Y mesh, BW = 400 Hz, $\Delta f = 0.5$ Hz

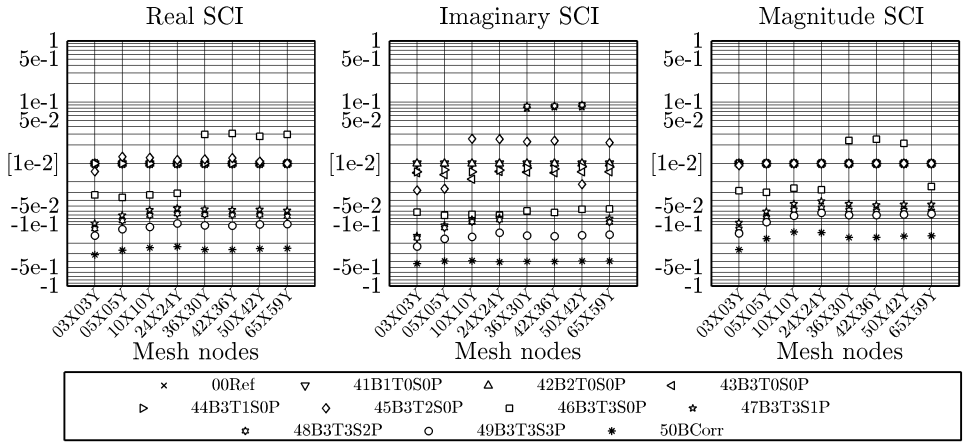

Figure A.46: SCI vs Mesh Density. Removal of members. 65X59Y mesh, BW = 400 Hz, $\Delta f = 0.5$ Hz

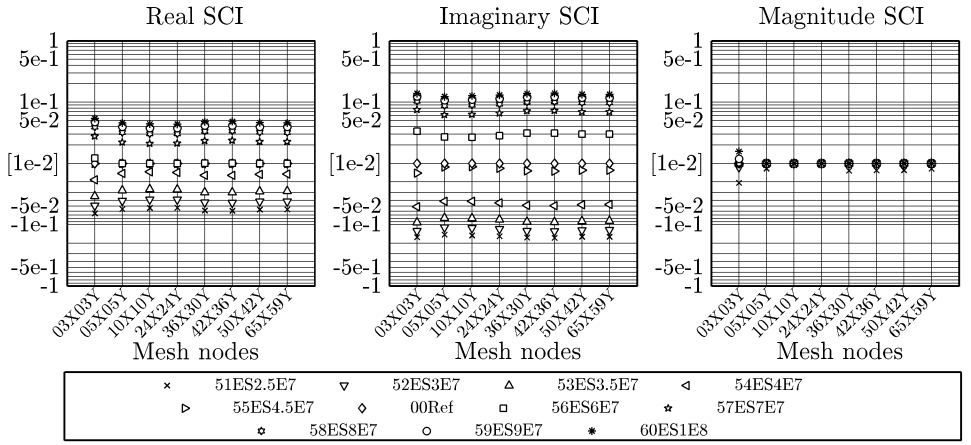

Figure A.47: SCI vs Mesh Density. Elastic support. 65X59Y mesh, BW = 400 Hz, $\Delta f = 0.5$ Hz

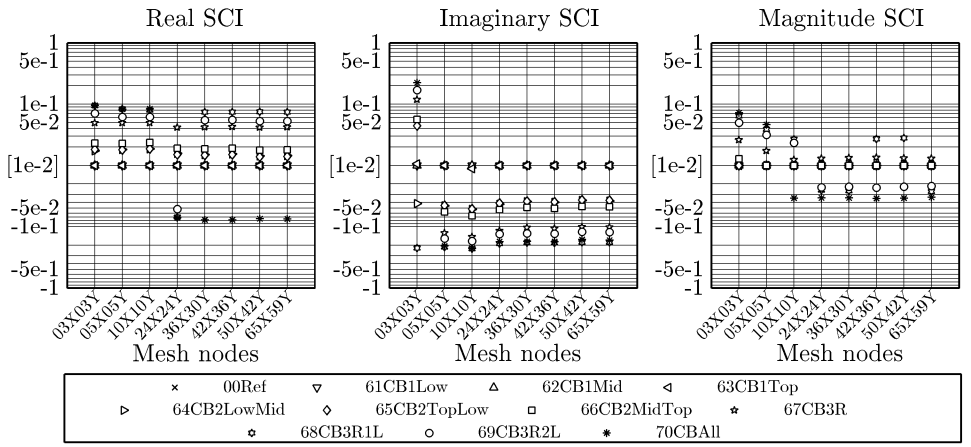

Figure A.48: SCI vs Mesh Density. Cable falls. 65X59Y mesh, BW = 400 Hz, $\Delta f = 0.5$ Hz

A.2.3 Bandwidth

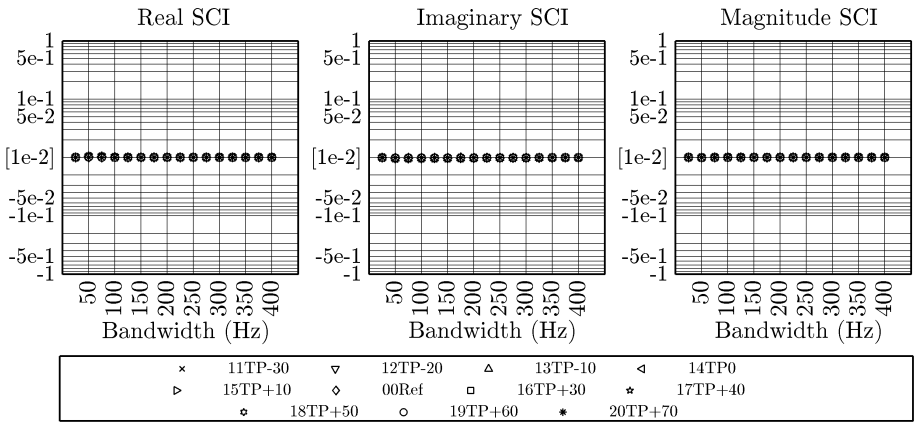

Figure A.49: SCI vs Bandwidth. Thermal pre-stresses. 65X59Y mesh, BW = 400 Hz, $\Delta f = 0.5$ Hz

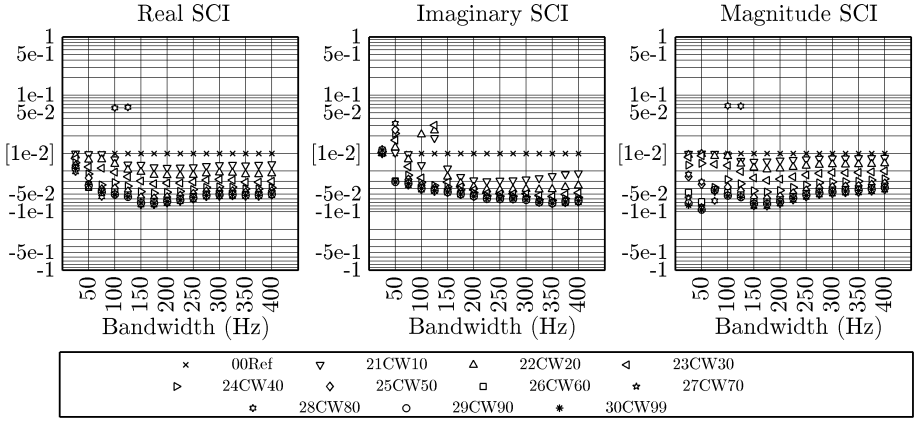

Figure A.50: SCI vs Bandwidth. Vertical pre-stresses. 65X59Y mesh, BW = 400 Hz, $\Delta f = 0.5$ Hz

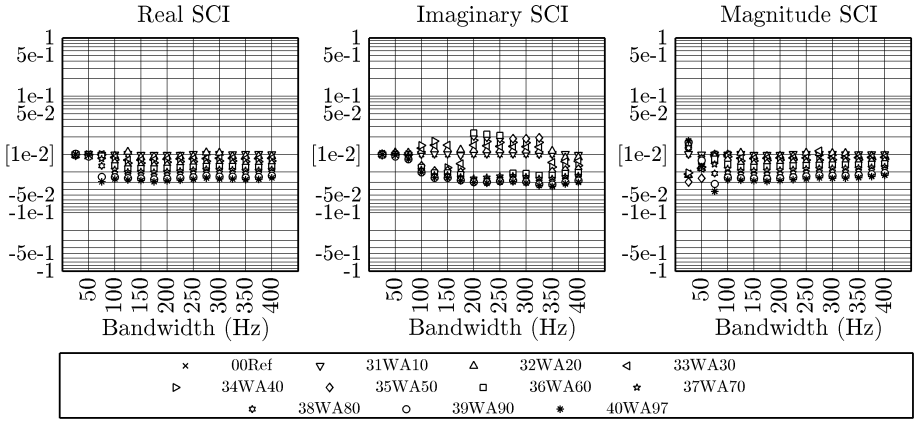

Figure A.51: SCI vs Bandwidth. Lateral pre-stresses. 65X59Y mesh, BW = 400 Hz, $\Delta f = 0.5$ Hz

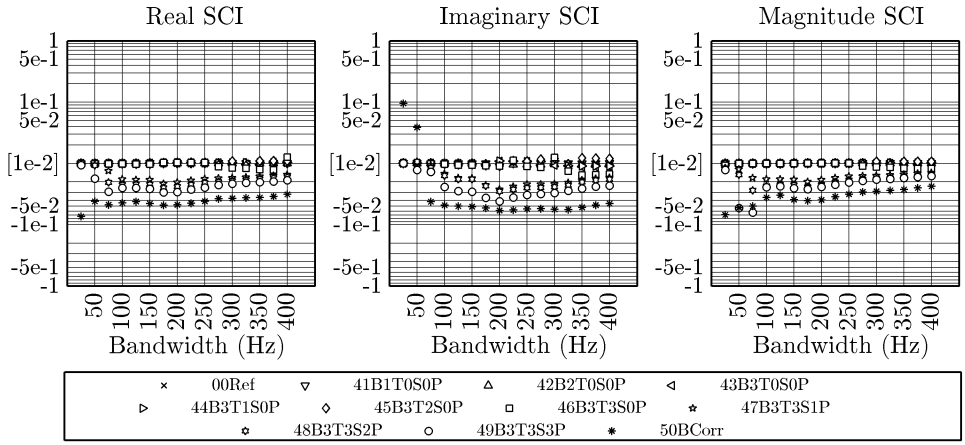

Figure A.52: SCI vs Bandwidth. Removal of members. 65X59Y mesh, BW = 400 Hz, $\Delta f = 0.5$ Hz

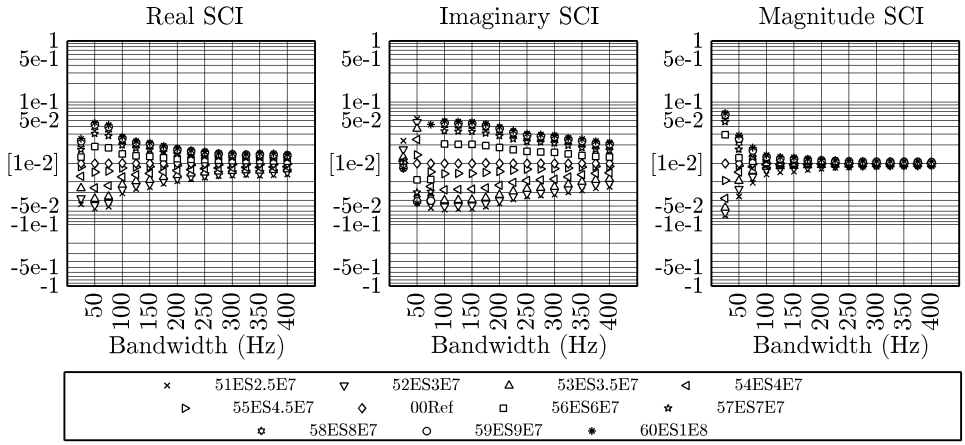

Figure A.53: SCI vs Bandwidth. Elastic support. 65X59Y mesh, BW = 400 Hz, $\Delta f = 0.5$ Hz

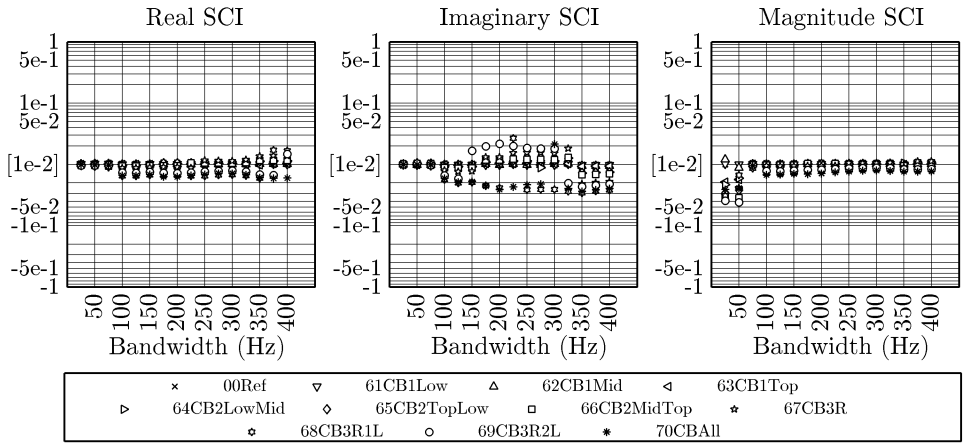

Figure A.54: SCI vs Bandwidth. Cable falls. 65X59Y mesh, BW = 400 Hz, $\Delta f = 0.5$ Hz

Structural health monitoring has been defined as the acquisition, validation and analysis of technical data to facilitate life-cycle management decisions. It is the result of a convergent path from many previous existing disciplines the two most influential being condition monitoring for rotary machinery and non-destructive testing. From all the possible technologies, vibration based structural health monitoring is the one which present a greater stage of maturity.

In this work, an integrated methodology for the evaluation of a spectral domain vibration based structural indicator for structural health monitoring is proposed. Results of this preliminary investigation show that spectral domain damage indicators present some advantages over modal domain and temporal domain based indicators such as convenient condensing procedures without loss of information through the Fourier transform, added post-process simplicity and enhanced sensitivity to degradation.

UNIVERSITAT POLITÈCNICA DE CATALUNYA
BARCELONATECH
Escola Superior d'Enginyeries Industrial, Aeroespacial i Audiovisual de Terrassa